IMPROVING RESIDUAL STRENGTH OF UNIDIRECTIONALLY REINFORCED PLASTIC LAMINATES BY METAL LAYERING

Von der Fakultät für Maschinenbau

der Technischen Universität Carola-Wilhelmina zu Braunschweig

zur Erlangung der Würde

eines Doktor-Ingenieurs (Dr.-Ing.)

genehmigte Dissertation

von:	Dipl.-Ing. Daniel Stefaniak M.Sc.
aus :	Bergisch-Gladbach
eingereicht am:	19.01.2017
mündliche Prüfung am:	20.03.2017
Gutachter:	Prof. Dr.-Ing. Michael Sinapius Prof. Dr.-Ing. Axel Herrmann

2017

Zusammenfassung

Bei Faserverbundwerkstoffen erfolgt die Anpassung der Materialeigenschaften mit Hilfe der gezielten Ausrichtung der Fasern in Hauptlastrichtung. Bei einachsiger Belastung wäre eine ebensolche Ausrichtung zwar wünschenswert, erhöht jedoch die Empfindlichkeit des Laminats gegenüber Schäden drastisch. Besonders kritisch ist insbesondere eine Drucklast auf einem Laminat, das vorher durch einen Stoß geringer Energie geschädigt wurde. Aus diesem Grund werden in fast allen praktischen Anwendungen zusätzliche Faserrichtungen vorgesehen, die die Steifigkeit und Festigkeit in der gewünschten Richtung jedoch reduzieren. Diese Laminate bilden damit die eigentliche Referenz, wenn es in der Materialentwicklung um den Vergleich von Werkstoffen geht. Fälschlicherweise werden hier oftmals die Eigenschaften von Laminaten mit unidirektionaler Faserausrichtung betrachtet.
Ziel dieser Arbeit ist es ein neues Materialsystem, sogenannte UD-CFK-Stahllaminate, hinsichtlich ihrer Eignung für eben diese besonderen einachsigen Lastfälle zu prüfen. Die Laminate bestehen aus einem Schichtaufbau von CFK und Stahlfolien. In der Arbeit wird zunächst theoretisch erörtert, dass bei Verwendung von weniger als etwa 12% Stahl, eine höhere spezifische Steifigkeit als mit der CFK-Referenz erreicht werden kann. Voraussetzung hierfür ist, dass die Restfestigkeit nach einer Schädigung durch eine bestimmte Stoßenergie nicht geringer ist als die Restfestigkeit, welche die CFK-Referenz bei gleicher Stoßenergie erzielt.
Da in den meisten Einsatzfällen jedoch nicht ausschließlich die Eigenschaften in Lastrichtung allein ausschlaggebend sind, wird der Druckstab als ein einfaches Anwendungsbeispiel betrachtet. Mit Hilfe einer Parameterstudie werden für unterschiedliche Stäbe und Lasten die Stabquerschnitte für jedes Material variiert, um für jedes Material den idealen Querschnitt festzustellen. Da bei dem Druckstab neben der Druckfestigkeit auch Knicken und lokales Beulen als Versagensfälle betrachtet werden, entsteht ein realistisches Anforderungsprofil bei dem neben den Laminatsteifigkeiten in der Ebene auch die Biegesteifigkeiten eine Rolle spielen. Da die Ergebnisse der Parameterstudie dieser Arbeit zeigen, dass es durchaus Szenarien gibt, in denen das UD-CFK-Stahllaminat einen Vorteil erzielen kann, werden die Erkenntnisse aus dem Lagenaufbau auf weitere Versuche übertragen.
Bevor hierfür jedoch Prüfkörper hergestellt werden, wird zunächst die Oberflächenvorbehandlung betrachtet. Dazu werden unterschiedliche Beiz- und Strahlverfahren untersucht. Auf Grundlage dieser Untersuchungen wird eine Vakuumsaugstrahlanlage entwickelt und für die Vorbehandlung der Stahlfolie verwendet. Zusätzlich werden die thermischen Eigenspannungen, die durch die hohe Aushärtetemperatur und die unterschiedlichen Wärmeausdehnungskoeffizienten der Materialien entstehen, abgeschätzt und Maßnahmen zu dessen Reduktion aufgezeigt.
Die anschließende Druckpüfung zeigt, dass die Drucksteifigkeit und Druckfestigkeit deutlich erhöht werden können, so dass auch eine höhere spezifische Drucksteifigkeit als bei der CFK-Referenz erzielt werden kann. Die Schäden nach Stoßenergien von 9, 12 und 16 J sind zwar größer als bei Proben aus CFK, die Restfestigkeit ist jedoch vergleichbar mit der Referenz. Bei den spezifischen Restfestigkeitskennwerten entsteht daher ein geringer Nachteil gegenüber CFK.
Zusätzlich wird aufgezeigt, dass mit Hilfe der Anordnung der Stahllagen Einfluss auf die Tiefe des Schadensabdrucks und auf das Versagensverhalten genommen werden kann. Denn werden die Metalllagen zum Beispiel eher außen angeordnet, so erzielt ein vorgeschädigter Körper ein deutlich weniger abruptes Druckversagen.

Abstract

Composite laminates are adjusted to the expected scenario by aligning their reinforcing fibers in load direction. Especially, when high specific uniaxial mechanical properties are aspired, notch and impact sensitivity properties, however, limit the fiber fraction in load direction drastically. Additionally, the thickness of equally orientated layers is limited to reduce crack distribution. Compression loading of a laminate, which have previously been impacted at a low impact energy, is particularly critical.

Therefore, the laminates suffer a loss of their lightweight potential due to residual strength evaluation. However, these laminates generate the reference for comparison with other material groups, although composites are often advertised with means of their unidirectional properties.

Recognizing these limitations, a new lay-up to increase the degree of capacity utilization of CFRP is analyzed in this thesis. The so-called UD-CFRP-steel laminates use a lay-up of CFRP and steel layers with a thickness below 0.08 mm to reduce the aforementioned disadvantages. At first, it is shown theoretically that when using less than 12% steel, a higher specific stiffness than by taking the CFRP reference is achievable. However, this only proves to be beneficial if the residual strength after an impact is comparable with the residual strength achieved by the CFRP reference after an impact of the same energy.

In the majority of applications, the exclusive consideration of uniaxial properties is not sufficient. Hence, struts under longitudinal compression load are regarded. When considering compression strength, local and global buckling, a strut provides a simple example in which not only the laminate's longitudinal strength and stiffness play an important role, but also the laminate's transverse stiffness and flexural bending stiffness. Therefore, a parameter study on different struts with different loads is performed to achieve the ideal cross section for each material system and loading scenario. For certain scenarios a weight-saving potential is realized by the UD-CFRP-steel lay-up compared to the reference laminate.

Before manufacturing test specimens, the surface treatment is regarded and a variety of pickling and grit blasting procedures are tested. Finally, a vacuum blasting machine is developed and used for the pre-treatment of the steel foils. Additionally, manufacturing experiments are performed to estimate the thermal residual curing stresses. In addition, methods for their reduction are presented.

The subsequent compression testing shows that the compression stiffness and strength is increased essentially in comparison to the CFRP reference. Thereby, the specific compression modulus is also increased.

Although the specimens indicate larger damage after being impacted at 9, 12 and 16 J, the residual compression strength is comparable to the CFRP reference. Hence, the specific residual compression strength of UD-CFRP-steel is lower.

Additionally one can conclude from the results, that the arrangement of a ply influences the dent depth and the load-displacement of the specimens. Damaged specimens with the metal layers oriented more to the outside, achieve a more ductile compression failure than CFRP or specimens with the metal layers orientated preferably more to the center of the specimen.

Acknowledgments

First of all I would like to thank Prof. Michael Sinapius for the supervision of my thesis and the valuable discussions over the time of preparation. My gratitude as well goes to Prof. Axel Hermann for the co-supervision.

In particular, I want to thank Prof. Christian Hühne not only as chairman of the thesis committee, but also for the fruitful collaboration over several years, for creating the work-environment to write this thesis and for providing tasks to grow with and develop on a personal level. I would also like express my gratitude to Dr. Boris Kolesnikov, who emphatically fought for the prosecution of any fiber metal laminate topic and provided the 'starting point' of the specific topic analyzed in this thesis.

Special thanks goes to my colleague and friend Dr. Erik Kappel for endless discussions regarding the topic of process-induced deformations, which fundamentally influenced this thesis and for sharing his exceptional knowledge of mechanics. Not forgetting the evenings in front of the white board, again trying to find the source for a certain phenomenon in composites manufacturing and the proof-reading of this thesis.

I would also like to thank Lennart Weiß for proof-reading and for being, together with Dr. Hardy Köke, a trigger to start with the 'pythonic way' of solving problems.

I would have not succeeded without the efforts and supports of Robert Prussak and Martin Kolotylo, who both helped preparing many of the specimens as part of their diploma theses. I am glad that both of you found your way to the DLR and now work hard on your own research. Several other 'students' also graciously supported my work, Daniel Osorio, Imke van Lessen, Martin Janssen and Martin Seide.

Further I would like to thank Mareike Stegmaier for the pre- and post-processing of many of the specimens and for her flexibility in terms of any special requirement.

I thank Arne Hindersmann for providing the possibility of discussions and answers in the field of composite manufacturing right next door.

I would also like to thank my father Istvan for always being a good listener and critical questioner. This helped me a lot to sort my mind and regain a general view of some special topics.

In general I would like to thank my father Istvan, my mother Eva and my brother Stefan for believing in me and for the enormous patience, which I know was required to get me to this point.

Finally, I would like to give a very special thanks to my wife Nina for encouraging me in academically hard times and tolerating long working days in academically good times. Although not in direct connection to this thesis, I would like to take the chance to thank you for your understanding concerning my unpredictable dedication to wavesailing and for just being like you are.

Stade, 2017

'*Clarity about what matters provides clarity about what does not.'*

- Cal Newport -

Deep Work: Rules for Focused Success in a Distracted World

Contents

Notations

List of symbols - latin letters

symbol	**unit**	**description**
a	mm	plate length
A_d	mm^2	damage area
A_{ij}	N/mm	coefficient ij of A-matrix
$Av(x)$	-	mean value of parameter x, notation used in test standards
A_s	mm^2	strut cross section
b	mm	plate width
c_{long}	kN/mm	spring stiffness from longitudinal consideration of the lay-up
c_{trans}	kN/mm	spring stiffness from transverse consideration of the lay-up
B_{ij}	N	coefficient ij of coupling stiffness matrix
d	mm	displacement
D	mm	diameter
D_{ij}	Nm	coefficient ij of bending stiffness matrix
$D_{C,ij}$	Nm	coefficient ij of bending stiffness matrix of composite layer
D_M	Nm	coefficient of bending stiffness matrix of metal layer
E_{11}	GPa	longitudinal tensile *Young‘s* modulus
E_c	GPa	compression *Young‘s* modulus of specimen
E_C	GPa	*Young‘s* modulus of the composite fraction
E_{c11}	GPa	longitudinal compression *Young‘s* modulus
E_{c22}	GPa	transverse compression *Young‘s* modulus
$E_{c,spec}$	MNm/g	specific compression *Young‘s* modulus
E_{glass}	MPa	*Young‘s* modulus in resin’s glassy state
E_{imp}	J	impact energy
E_L	GPa	*Young‘s* modulus of the laminate
$\hat{E}_{long,b}$	GPa	flexural bending stiffness in the longitudinal direction
$\hat{E}_{trans,b}$	GPa	flexural bending stiffness in the transverse direction
E_M	GPa	*Young‘s* modulus of the metal fraction
$E_{M,pl}$	GPa	ideal *Young‘s* modulus of the metal fraction in the plastic region
E_{pot1}	J	energy threshold for realistic energy
E_{pot2}	J	energy threshold for extremely improbable occurrence
E_R	GPa	reference *Young‘s* modulus
E_{rub}	GPa	*Young‘s* modulus in resin’s rubbery state
E_x	GPa	*Young‘s* modulus of an arbitrary layer in x-direction
$\overline{E_x}$	GPa	average laminate stiffness in x-direction
f_s	-	safety factor
F	N	load
g	m/s^2	gravitational acceleration

G_{glass}	GPa	shear stiffness in resin's glassy state
G_{rub}	GPa	shear stiffness in resin's rubbery state
h	mm	total specimen thickness
I	mm^4	moment of inertia
I_C	mm^4	moment of inertia of the composite layer
I_{circ}	mm^4	moment of inertia of circular strut
I_M	mm^4	moment of inertia of the metal layer
j_{gb}	-	global buckling safety factor
j_{lb}	-	local buckling safety factor
j_u	-	ultimate safety factor
j_y	-	yield safety factor
k	-	control variable for stress level in strut study
k_l	-	equivalent length factor
k_{max}	-	maximum number of loops in strut study
K	-	end-restraint coefficient
l	mm	length of specimen
l_d	mm	damage length
L_e	mm	effective strut length
L_s	mm	strut length
L_{sup}	mm	distance between support of 3-point bending specimens
m	-	buckling shape parameter
m_l	g	strut with lowest weight
m_k	g	strut weight in k-th calculation step
m_s	g	strut weight
M_x, M_y, M_{xy}	N	bending moments per unit length
M_x^T, M_y^T, M_{xy}^T	N	thermal bending moments per unit length
n	-	buckling shape parameter
n_k	-	cross section transformation factor of k-th layer
n_C	-	cross section transformation factor of composite layer
n_M	-	cross section transformation factor of metal layer
N	-	total number of layers
N_x, N_y, N_{xy}	N/m	in plane loads per unit length
N_x^T, N_y^T, N_{xy}^T	N/m	thermal in plane loads per unit length
$\widehat{N_{yy}}, \widehat{N_{xx}}$	N	axial forces acting on beam
$N_{buckl,loc,sq}^{ss}$	N	local buckling load (edges treated simply supported)
P_C	N	(in-plane) load in composite layer
P_M	N	(in-plane) load in metal layer
P_u	N	failure load
Q	N	transverse load
r	mm	striker radius
r_m	mm	midplane strut radius
r_s	mm	outer strut radius
R	mm	radius of material strip
R_{beam}	mm	radius obtained by beam theory

R_{OF}	mm	radius obtained by *Oel and Frechette* strain energy approach
R_{plate}	mm	radius obtained by plate theory
RS_{LL}	MPa	residual strength for limit load capability
RS_{UL}	MPa	residual strength for ultimate load capability
s	-	step size in strut study
S	mm^3	static moment
S_C	MPa	stiffness of the composite layer used in plane stress model
S_k	MPa	stiffness of the k-th layer used in plane stress model
S_M	MPa	stiffness of the metal layer used in plane stress model
t	mm	thickness/depth of indentation
t_C	mm	thickness of composite layer
t_k	mm	thickness of k-th layer
t_{lam}	mm	laminate thickness
$t_{lam,max}$	mm	maximum laminate thickness regarded in strut study
t_{lay}	mm	layer thickness
t_M	mm	thickness of metal layer
t_r	mm	repetitive layer thickness
$T_{cure,max}$	°C	maximum curing temperature
T_{op}	°C	operational temperature
T_{sf}	°C	stress free temperature
$P_{buckl,glob,sq}$	N	global buckling load for square cross sectioned strut
w	mm	inner strut/specimen width
w_c	mm	deflection of beam center
w_d	mm	damage width
w_h	mm	half outer strut width
w_s	mm	outer strut width
z	-	coordinate axis
$\hat{z}$	mm	position of layer interface with respect to neutral axis
z^*	mm	position of neutral axis

List of symbols - greek letters

symbol	unit	description
α	-	shell buckling shape parameter
α_{11}	10^{-6}/K	longitudinal coefficient of thermal expansion
α_C	10^{-6}/K	composite‘s coefficient of thermal expansion
α_L	10^{-6}/K	laminate‘s coefficient of thermal expansion
α_{L11}	10^{-6}/K	laminate‘s longitudinal coefficient of thermal expansion
α_M	10^{-6}/K	metal‘s coefficient of thermal expansion
α_x°, α_y°, α_{xy}°	10^{-6}/K	apparent thermal expansion coefficient
α_x^*, α_y^*, α_{xy}^*	1/mm	laminate’s thermal curvature
β	-	shell buckling shape parameter
γ	-	shear strain
Δl	mm	length difference

ΔP	K	load difference
ΔR	mm	radius difference
ΔT	K	temperature difference
$\Delta\alpha$	10^{-6}/K	difference in thermal expansion coefficient
$\Delta\epsilon_x$	-	difference in strain
ϵ_B	-	strain due to bending
$\epsilon_{C,R}$	-	residual strain in composite fraction
ϵ_{faceA}, ϵ_{faceB}	-	strain measured on face A or B, respectively
$\epsilon_{L,y}$	-	laminate‘s effective strain at yield limit
$\epsilon_{L,ult}$	-	laminate‘s effective strain at ultimate failure
$\epsilon_{M,0.2}$	-	effective strain at technical elastic limit
$\epsilon_{M,A}$	-	permanent strain after failure
$\epsilon_{M,R}$	-	residual strain in metal fraction
$\epsilon_{M,ult}$	-	effective strain at failure of the metal fraction
ϵ_{ult}	-	effective strain at failure
ϵ°_x, ϵ°_y, ϵ°_{xy}	-	apparent thermal expansion
κ_x, κ_{xy}	1/mm	curvatures of reference surface
λ_{cr}	-	critical buckling load parameter; eigenvalue
ν_{Cij}	-	composite’s *Poisson‘s* ratio in ij-plane
ν_{ij}	-	*Poisson‘s* ratio in ij-plane
ν_{kij}	-	*Poisson‘s* ratio in ij-plane of the k-th layer
ν_{Mij}	-	metal’s *Poisson‘s* ratio in ij-plane
ρ	g/cm^3	density
ρ_L	g/cm^3	laminate‘s density
ρ_R	g/cm^3	reference density
σ_{alt}	MPa	alternative stress level in strut
$\sigma_{buckl,glob}$	MPa	global buckling strength for square cross sectioned strut
$\sigma_{buckl,local,circ}$	MPa	local buckling strength for circular cross sectioned strut
$\sigma_{C,R}$	MPa	residual stress in composite fraction
$\sigma_{c,spec}$	kNm/g	specific compression strength
$\sigma_{c,ult}$	MPa	composites compression strength
$\sigma_{L,y}$	MPa	laminate‘s yield strength
$\sigma_{L,ult}$	MPa	laminate‘s ultimate strength
$\sigma_{M,0.2}$	MPa	technical elastic limit of metal fraction
$\sigma_{M,R}$	MPa	residual stress in metal fraction
$\sigma_{M,ult}$	MPa	metal‘s ultimate strength
$\sigma_{M,y}$	MPa	metal‘s yield strength
$\sigma_{p,0.2}$	MPa	technical elastic limit
σ_{ult}	MPa	yield strength
σ_v	MPa	equivalent stress
τ_{ij}	MPa	shear stress in ij-plane
$\tau_{ij,res}$	MPa	shear stress in ij-plane created by residual thermal stress
$\tau_{ij,test}$	MPa	shear stress in ij-plane created by test load
τ_{glass}	MPa	shear stress in resins’s glassy state

τ_{ILSS}	MPa	interlaminar shear strength
τ_m	MPa	maximum shear stress
τ_{rub}	MPa	shear stress in resin's rubbery state
τ_u	MPa	true shear strength
φ_M	%	metal volume fraction

List of abbreviations

ADL	allowable damage limit
Al	aluminum
ARALL	aramid fiber reinforced aluminum laminate
BSP	Boeing sol-gel Process
BVID	barely visible impact damage
CAI	compression after impact
CARALL	carbon fiber reinforced aluminum laminate
CFRP	carbon fiber reinforced plastic
CLC	combined loading compression
CLP	Ciba laser pretreatment
CLT	classical laminate theory
CT	computer tomography
CTE	coefficient of thermal expansion
DNS	double-notch shear
DSG	design service goal
FBG	fiber bragg grating
FEM	finite element method
FEP	fluorinated ethylene propylene
FML	fiber metal laminate
FRP	fiber reinforced plastic
GBS	grit-blast and silane process
GLARE	glass fiber reinforced aluminum laminate
HCCF	hydraulic composite compression fixture
HO	highly-orthotropic
HTS	high tenacity and strength
ILSS	interlaminar shear strength
IM	intermediate modulus
LL	limit load
LVI	low velocity impact
MRCC	manufacturer‘s recommended cure cycle
MVF	metal volume fraction
NDI	nondestructive inspection
PBS	percent bending strain
QI	quasi-isotropic
ROM	rule of mixture
RT	room temperature
ss	simply supported

St	steel
Ti	titanium
UD	unidirectional
UL	ultimate load
US	ultrasonic
voxel	volume element

1 Introduction

1.1 Background

In the aerospace industry in particular, carbon fiber reinforced polymer composites are being used more and more extensively. The high stiffness and strength to weight ratio and fatigue resistance make them attractive for large civil aircraft. However, there are significant differences in material behavior between carbon fiber reinforced plastic (CFRP) and metals. Besides anisotropic mechanical and thermal properties, CFRP shows more complex failure mechanisms. Additionally, mechanical impacts do not always lead to visually detectable damage. As no compromises concerning safety when compared to conventional metallic structures can be permitted in this field, an adapted certification process has been introduced. The concept of continued airworthiness of aircraft primary structures for fatigue and accidental damage is described in AMC25.571 [1] and supplemented by CS25.603 [2] for composite parts in particular. The general idea is to ensure that damage will be detected before its size becomes critical and to repair the damage to regain the part's original strength. As damage growth and damage visibility in CFRP is different, the certification rules lead to increased certification effort. For example, in compliance AMC25.571, one year of safe operation must be substantiated before certification of a metallic part. For a composite part, 1 to 1.5 times the design service goal (DSG) must be substantiated in order to comply with CS25.603. The DSG for today's large civil aircrafts is about 35 years.

Another drawback in addition to the complex and elongated certification process is that the composite's elastic properties cannot be exploited to their full potential due to the material's largely brittle behavior when considering detectability of damages. As a consequence, concerns about the effect of impacts on the performance of composite structures have been a factor in limiting the use of composite materials [3].

Paragraph 'c' of AMC25.571 prescribes a safe-life concept for undetectable damages and for structures susceptible to damage but not being inspectable. In consequence, this means that the structure needs to be capable of sustaining all applied (ultimate) loads while damage sizes remain smaller than the detectability threshold.

Therefore, additional to the high stiffness to weight ratio and fatigue resistance mentioned above, the composite material's suitability for a particular application additionally depends on its residual strength at a certain detectable damage size. In particular, uniaxially loaded parts with high stiffness needs - which preferably contain a high amount of uniaxially oriented fibers - suffer a loss of their lightweight potential due to this residual-strength requirement.

It seems obvious that the combination of metallic and fiber reinforced plastic in fiber metal laminate (FML) could be one possible way to overcome the weaknesses of its individual constituents. Research on FML to improve the material performance of the individual constituents and to overcome the disadvantages of the single materials has been ongoing for over 40 years. Fiber metal laminates investigated include aluminum alloys (aramid fiber reinforced aluminum laminate (ARALL), carbon fiber reinforced aluminum laminate (CARALL) and glass fiber reinforced aluminum laminate (GLARE)) as well as FMLs incorporating metal alloys such as titanium or steel. Although each of these material combinations has its own motivations, they can be subdivided into two major groups. The first group utilizes the fibers to overcome the weak fatigue performance of the metallic constituent. The most famous representative of this group is GLARE, which uses glass fiber reinforced polymers to improve the fatigue performance of aluminum. This material combination is used in the upper fuselage panels of the A380. The second group makes use of titanium or steel sheets to locally reinforce composite parts in order to increase the bolt bearing capacity [4–9].

Although GLARE was not intended to overcome the required additional certification effort of composites, it is the only laminated and therefore composite material, which can be covered by the damage tolerance approach under AMC25.571. This can be explained by damage detectability, as GLARE behaves a very similar way to monolithic aluminum in the case of accidental mechanical impact [10]. However, no approach has yet been reported in research, which utilizes fiber metal laminates to overcome the loss of CFRP's lightweight potential due to residual-strength requirements.

This work aims to evaluate whether metallic layers are suitable for overcoming this loss, especially for uniaxially loaded parts utilizing a large amount of uniaxially orientated fibers.

1.2 Objective

Today, design is focused on undamaged laminate properties although residual strength is the critical design parameter in many aerospace applications when using composite materials. Therefore, residual strength should be the major design variable.

The formulation of a universally valid method of evaluating whether additional metallic layers are suitable for overcoming the loss of composite materials with regard to residual strength requires a suitable assessment approach in combination with experimental characterization of the material properties. Unfortunately, the manufacture of such specimens is accompanied by certain manufacturing challenges which need to be overcome, especially with regard to layer adhesion and residual stresses. This leads to a multiplicity of solutions which are more or less complex, low or high in cost and more or less effective. For a universally valid evaluation, all these solutions and their associated parameters must be investigated and their impact on the command variable - the residual strength - must be described. Such an approach would require an enormous manufacturing and testing effort which may or may not be bear fruit.

Therefore, another procedure is applied whereby the goal is to verify the advantage of FML - with regard to residual strength - for a single application. This would justify any further and more detailed investigation in this field.

When performing such a target-orientated investigation on this novel material there is the risk of an unsatisfactory intermediate step, which at the end may prohibit a meaningful conclusion. For example, high residual stresses or an unsatisfactory surface treatment may generate a different failure mode and the real potential of the material combination could remain undiscovered. It is therefore necessary to develop and investigate the manufacturing methods just sufficiently to yield meaningful test specimens, to be able to derive further investigation requirements and to ascertain those manufacturing parameters with the highest impact on residual strength.

2 Approach, hypotheses and outline

The present chapter describes the main advantages and drawbacks of CFRP and introduces a novel approach to encountering the low damage tolerance properties of highly orthotropic laminates. The approach leads to the definition of a principle hypothesis and six hypotheses which affect the outline of the research performed in this work. The outline and structure of the present thesis are summarized at the end of this chapter.

Summary: Composite laminates, and especially CFRP, have been applied in many engineering fields due to their excellent strength to weight and stiffness to weight ratios. Most of the structural components made using composite laminates are subjected to impact loading during assembly and maintenance operations, or during service life [11]. For CFRP in particular, the material's capability of tolerating local failure is a critical property. In most cases the compound does not collapse immediately after the onset of failure but the failure accumulates, accompanied by permanent stress redistribution until functional break-down occurs. Even minor damage can cause considerable reduction in the structural integrity of composites. Therefore, their main drawback is their susceptibility to impact damage and manufacturing defects. Damage tolerance in metals is related to the propagation rate of a crack, whereas damage tolerance in laminated composites is dominated by their resistance to impact [12]. This impact damage includes delamination, fiber breakage and matrix cracking, which may result in premature structural failure at loads well below the designed strength of the structure. The damage induced by low-velocity impact is the most important aspect inhibiting the wide-spread use of laminated composites in industry [13]. Therefore, parts with high stiffness needs, in particular struts at risk of buckling or parts with high eigenfrequency requirements, suffer a loss of their lightweight potential due to residual-strength evaluation. Recognizing these limitations, a new lay-up to increase the degree of capacity utilization of CFRP is proposed in the following.

2.1 UD-CFRP-steel approach

In order to increase the damage tolerance properties of composites, different approaches are used on material and laminate scale, in practice and in research. The prevalent solution is to create tougher interlayers by adding thermoplastic particles to the thermoset resin. However, layers with deviant fiber orientation must be added to the laminate in most of the applications, whether needed for the load case or not. These additional layers are required in case of accidental damage or manufacturing defects. As they are not required for the loading scenario, they reduce the material's potential for exploitation with regard to strength and stiffness. This relation is discussed in more detail in chapter 3.

The approach to reducing the aforementioned disadvantages uses a new laminate lay-up with low metal layer thickness and low metal volume fraction. The literature provides evidence for the following assumptions. The metal layers replace ±45°- and 90°-plies. Hence, stiffness and strength in the 0°-direction are not reduced in comparison to the use of variant fiber directions, while residual-strength-after-impact is improved in comparison with purely unidirectional (UD) laminates [14, 15].

Additionally, based on classical laminate theory (CLT), transverse stiffness and strength are enhanced in comparison with unidirectional laminates. The longitudinal compression strength is increased as a consequence of the material combination and the 'in-situ'-effect due to the high number of alternating interfaces [16]. A fundamental idea is that in the case of impact or fracture, the metal layers deflect inter-fiber-fracture into delamination and serve as crack arrester layers, as shown in Figure 2.1. Various investigations have indicated that the formation of delaminations absorbs energy and leads to reduced fiber breakage [17–19].

The combination of CFRP and steel forms an FML. The approach at hand focuses in particular on parts with uniaxially loading and high stiffness needs. An extensive explanation of the reasoning for this restriction can be found in chapter 3.

Another limitation anticipated for the following hypotheses is that steel is used exclusively so that the stiffness of CFRP is not reduced. An explanation and comparison with other metals can also be found in chapter 3.

2.2 Methodical hypotheses

The previous explanations are based on state-of-research in the field of laminated composites. The following principle hypothesis and hypotheses are based on the previous assumptions and thereby summarize the questions which need to be answered in order to determine the main factors of influence in the function of the novel UD-CFRP-steel laminates. At the same time, the hypotheses address areas where further research may be taken up.

Principle hypothesis

Using thin steel layers in a carbon-fiber-reinforced epoxy laminates permits an increase in weight-specific stiffness with no reduction of compression strength after impact.

- **Hypothesis 1:** Steel volume fractions lower than 10% are required to permit the increase of the weight-specific stiffness and strength in a given direction in comparison with a carbon-fiber-reinforced epoxy laminate.

- **Hypothesis 2:** Damage tolerance requirements are likely to lower the exploitation of the CFRP material in the laminate lay-up.

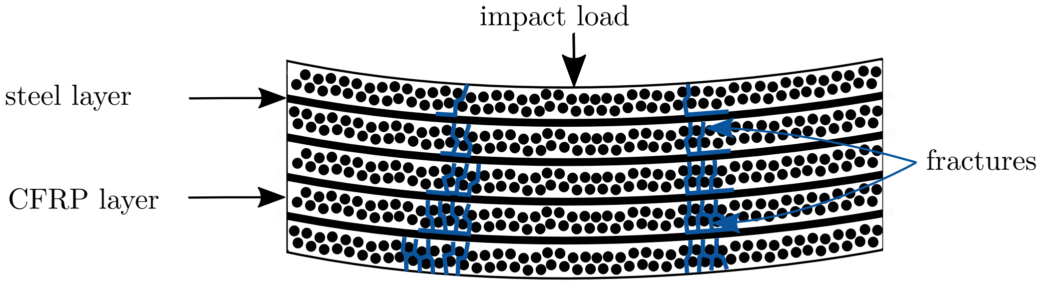

Figure 2.1: Deflection of inter-fiber-fracture into delamination at the interfaces between CFRP and steel

- **Hypothesis 3:** Due to the metal's time-dependent surface state, the overall treatment process exerts essential influence on the interlaminar shear strength of the UD-CFRP-steel laminates.

- **Hypothesis 4:** Contrary to prevalent assumptions, residual thermal stress is not a simple function of the difference between the cure and the operational temperature. Processing parameters such as pressure and temperature exhibit fundamental influence on residual thermal stress and thereby offer the possibility of stress reduction.

- **Hypothesis 5:** The insertion of steel layers in a CFRP-laminate decreases failure depth and consequently increases residual strength after impact.

- **Hypothesis 6:** The arrangement of the metal plies in a UD-CFRP-steel laminate has a major influence on failure geometry and strength after impact.

The hypotheses 1-6 are shown schematically on a cross section of a cap profile in Figure 2.2.

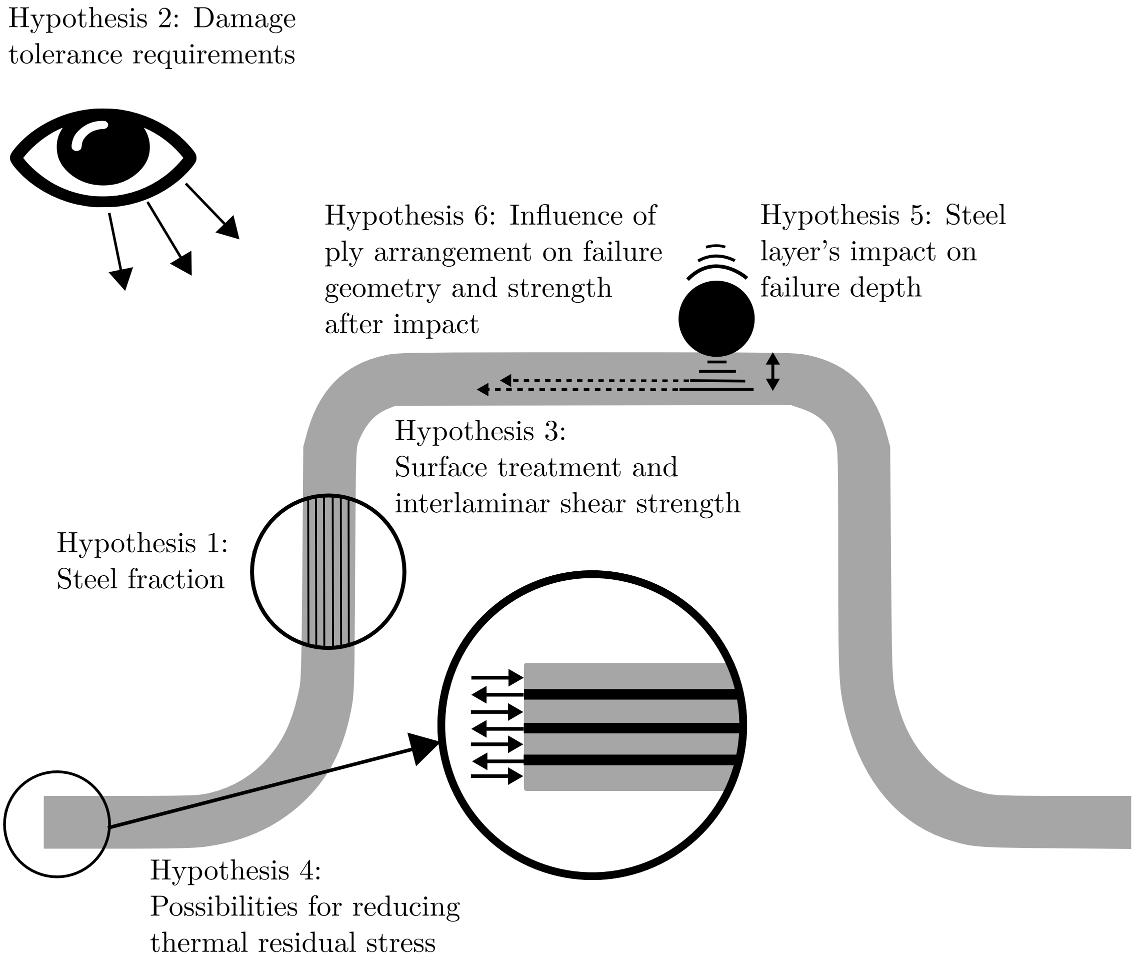

Figure 2.2: Schematic affiliation of all hypotheses shown on a profile cross section

2.3 Outline

The present work aspires to a clear composition with regard to chapters and hypotheses, see Figure 2.3.

The first two hypotheses are addressed in chapter 3 by an investigation of stiffness and strength properties depending on metal volume fraction. After narrowing down possible metal volume fractions, a more detailed consideration is performed. A parameter study is undertaken for axially loaded struts in order to get away from the typical comparison of uniaxial stiffness and strength.

Before meaningful specimens can be manufactured, the interface between the two constituents is regarded in chapter 4. Different surface treatments are investigated and a method for their determination is selected and adapted to the special characteristics of FML. The third hypothesis is also discussed in this chapter.

The second obstacle to overcome in CFRP-steel laminates is the thermal residual stress. The stress level must first to be evaluated to allow its consideration in the design process and methods to reduce the stress are also of interest. Both questions are addressed in chapter 5. The aim of this chapter is to identify the most promising and convenient approaches to lowering residual thermal stresses.

The present test standard for compression after impact tests is not applicable, as it comes with a certain specimen-size dependency. Therefore, a novel fixture for impact tests is developed and the related findings are presented in chapter 6 before different FML lay-ups are investigated with regard to their failure geometry and their compression strength after impact. Hypotheses 5 and 6 relate to these topics and are discussed at the end of this chapter. The failure geometry is assessed by ultrasonic inspection and x-ray computed tomography.

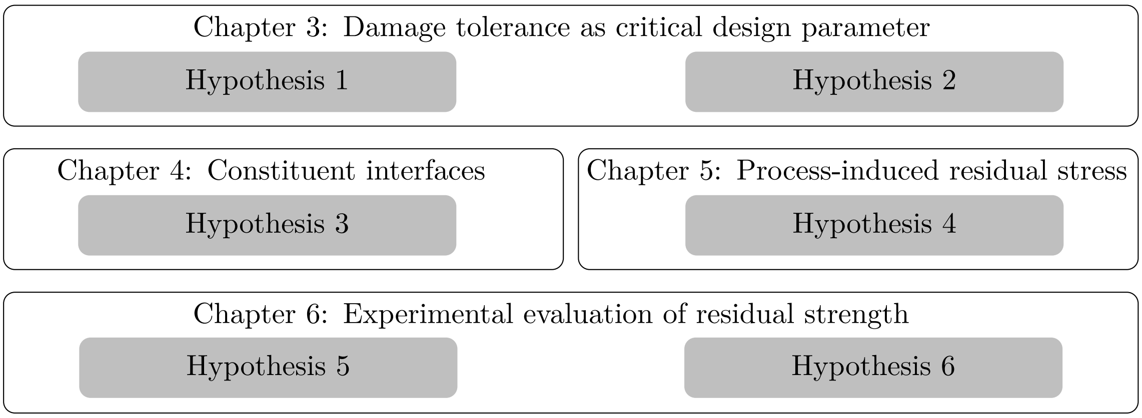

Figure 2.3: Thesis outline and affiliation of hypotheses

3 Damage tolerance as critical design parameter

Link to hypotheses: Hypothesis 1 and hypothesis 2 are examined in this chapter by means of regarding the weight specific stiffness and strength of UD-CFRP-steel laminates as a function of metal volume fraction and by investigating how damage tolerance requirements restrict the laminates considered.

Summary: This chapter first gives a résumé of design and safety philosophies in engineering, in particular the damage tolerance approach in aerospace engineering. In many applications these requirements drastically reduce the exploitation of fiber reinforced plastics. Profile structures with constant cross sections are identified as applications with the lowest possible exploitation of the composite's mechanical properties. The potential of Fiber Metal Laminates is then analyzed for these applications under consideration of their thermo-mechanical characteristics. An assessment methodology for struts is thus evolved based on an aeronautical framework application. Finally, a parameter study is executed for certain laminate stackings of UD-CFRP-steel, UD-CFRP-titanium, UD-CFRP-aluminum and pure CFRP with high strength and intermediate modulus fibers.

3.1 Literature review

The custom in ancient Rome that engineers had to stand under the bridge they had constructed the first time that it was actually used, may be considered as being the first safety philosophy in engineering. Since then, different philosophies have been refined by certification agencies in different branches.

Damage tolerance in aerospace applications

The first evidence for a damage tolerance philosophy in aerospace can be found in Leonardo Da Vinci's notebook on the design of flying machines [20]:

'In constructing wings, one should make one cord to bear the strain and a lower one in the same position so that if one breaks under strain, the other one is in position to serve the same function.'

Da Vinci is precisely describing a fail-safe concept. Before the establishment of the fail-safe philosophy, a **safe-life** approach was used, which limits the permitted operational life of a structure to ensure adequate fatigue life. Although this approach was found not to be economical for most use cases, it is still used in structures such as high-strength landing gear. An industrial **fail-safe** design philosophy for metallic structures was established in the 1960's. The idea was that damage introduced by fatigue loading could be detected before the retaining strength of the structure was reduced below a safe level [20]. This approach achieved acceptable safety levels and is more economical. The approach was then extended to include accidental damage and corrosion issues and, later, damage associated with manufacture and in-service use.

The **damage tolerance** philosophy evolved out of the safe-life and the fail-safe approaches [21] and has been included in the regulations since the 1970's. Nowadays, the concept of continued airworthiness of aircraft primary structures for large civil aircraft for fatigue and accidental damage is described in AMC25.571 [1]. This damage tolerance approach is easy to apply to aluminum structures, since deformation takes place in any practical case of accidental damage [10]. When damage is noticed during walk-around or inspection, its size is recorded and analytical methods provide the residual strength. With any possible damage size occurring, limit load capability needs to be justified.

Damage tolerance in composites

The safe-life approach is not considered appropriate for composites due to damage sensitivities and relatively flat fatigue curves. Instead, a damage tolerance approach is employed. Damage tolerance in the metallic structures traditionally used is mainly governed by usage-induced damage as fatigue and crack propagation. As composites do not suffer from fatigue to a comparable extent, the approach does not focus on usage-induced damage. Rather, in composites the damage that occurs during usage, i.e. impact, is more crucial [22]. In carbon fiber structures, mechanical impact does not lead to visually detectable damage in every case. Therefore, in composite aircrafts the AMC25.571 is supplemented by CS25.603 [2] and its provision AMC20 [23].

Following these rules, non-visible defects are considered while sizing the structure. Chapter 8 'Proof of structure – Fatigue and Damage Tolerance' of AMC20-29 claims an evaluation which shows that catastrophic failure due to fatigue, environmental effects, manufacturing defects, or accidental damage must be avoided throughout the operational life of the aircraft. Inspection intervals should therefore be established such that the damage will be detected between the time it initially becomes detectable and the time at which the extent of damage reaches the limits for required residual strength capability.

Compliance must be demonstrated to the agency, and there are different methods for doing so, as described for example in MIL-HDBK-17-3F [21]. The **'compliance with static strength requirements'** proposes the following means for complying with the regulations:

'It should be shown that impact damage that can be realistically expected from manufacturing and service, but no more than the established threshold of detectability for the selected inspection procedure, will not reduce the structural strength below ultimate load (UL) capability.' [21]

This relationship is graphically illustrated by the rectangle on the bottom left in Figure 3.1 as UL needs to be sustained in this area which is bounded by the threshold of detectability and realistic impact energy. Damage that exceeds the bounds of this rectangle is repaired with cosmetic or structural solutions to preserve or restore the structure's capability to withstand UL. The relationships for the top and right rectangles, but also for the bottom left rectangle, are additionally described by the **'compliance with damage tolerance requirements'**:

'Damage tolerance has to address the situation where, due to fatigue, corrosion or accidental damage occurrence, Ultimate Load strength capability may not exist and will have to be restored before the damage becomes critical.' [21]

Two different cases are identified within this means of compliance.

- For the top rectangle with visually detectable accidental impact, damage tolerance as per §25.571(b) is applied, which requires that the residual strength evaluation must show that the remaining structure is able to withstand limit load (LL) and any damage that lowers the residual strength below UL must be repaired when found. Additionally, the inspection interval needs to be defined in such a way that higher levels of safety are achieved than in metal practice. This is because, as a consequence of the non- or very slow growth of damage in composites, the residual strength could be sustained for a very long period below UL-capability. The top rectangle's upper threshold is defined as obvious damage which is detectable within a very small number of flights by walk-around.
- The right rectangle, but also the bottom left rectangle, contain visually undetectable damages and are therefore treated in accordance with §25-571(c). This paragraph demands a fatigue (safe-life) evaluation. The right energy cut-off level corresponds to extremely improbable events (less than 10^{-9} per hour) and is to be assumed in a risk analysis.

These two cases are accompanied by 'deterministic' and 'probabilistic methods', which define allowable damage limits (ADLs) while still meeting regulatory UL requirements and maintaining inspection intervals for the no-growth concept of composites. This includes two major relationships:

- The more likely the damage is, the sooner it should be detected.
- Higher residual strength – when strength capability is between UL and LL – allows longer inspection intervals.

The damage probability and energy assessment distinguishes between different sources of damage. The composite aircraft may be damaged during manufacturing, shipping or

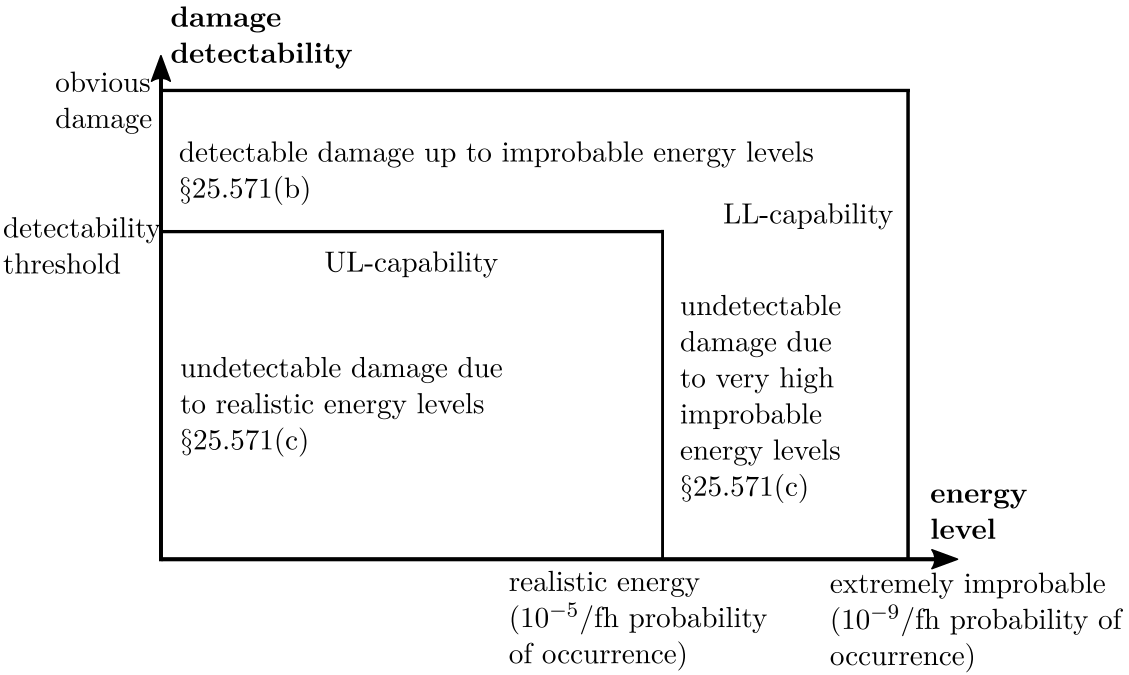

Figure 3.1: Damage detectability versus impact energy following compliance with static strength requirements (according to [21])

service. However, the primary focus is on low velocity impacts (LVIs) as these can cause significant damage that may not be clearly visible. Sources of such LVI damage are dropping tools and equipment, runway and ground debris, hail and collision with vehicles or other airplanes on ground [23].

For the damage tolerance approach, the detectability threshold – also called barely visible impact damage (BVID) is of primary interest. While BVID is subjective by nature, different values are defined in the literature. BVID is often defined as damage visible within a distance of 1 m. However, the threshold has to be defined depending on the part's accessibility and the inspection techniques applied.

As well as compliance with the regulations, inspection programs also need to achieve economic goals. Therefore, they often rely on combinations of frequent, relatively simple inspections on a large scale and less frequent, but more intense, examinations on local areas [21].

Four different inspection programs are thus distinguished in practice:

- Walk around - long distance visual inspection
- General visual inspection - careful visual examination with adequate lighting and appropriate access
- Detailed visual inspection - careful visual examination with inspection aids such as lenses or grazing light
- Special detailed inspection - inspection of specific locations with non-destructive procedures such as ultrasonics or x-ray.

3.2 Present chapter's structure

The aim of this chapter is to assess the suitability of UD-CFRP-steel as a structural material when damage tolerance requirements are present. The procedure thus deduced is shown in Figure 3.2.

As the diagram shown in Figure 3.1, which is currently used to explain the *compliance of damage tolerance* and is part of *AMC 20-29* [23], allows an ambiguous interpretation of the relationship between impact energy, damage size and residual strength, the following subchapter 3.3 introduces a novel three-dimensional perspective for a clearer representation. Additionally, stacking rules are discussed, as in fact their consideration is how the damage tolerance requirements are implemented in the present design process.

This means that any subsequent comparison of different materials is made with the stacking rules for composites in mind. Firstly, the unidirectional properties of pure CFRP lay-ups, pure metals and UD-CFRP-metals are discussed in subchapter 3.4. For the UD-CFRP-metals, a bilinear approach is used and presented in this subchapter. As shown in Figure 3.2, suitable metal volume fractions are discussed and then chosen for the UD-CFRP-metal laminates based on the unidirectional properties.

These metal volume fraction definitions serve as input for the following two subchapters 3.5 and 3.6, where the suitability of the materials is discussed on a more complex level. As especially composites in particular permit the tailoring of mechanical properties to a certain direction, a unidirectional comparison is not meaningful in any case. Therefore, longitudinally loaded struts serve as an application to asses the bidirectional properties of the material as the transverse properties of the material do have a significant influence on the buckling behavior of these structures. Firstly, the assessment method is discussed in subchapter 3.5 and then a parametric study is performed and discussed in the following subchapter 3.6. Finally, the connection to the hypotheses postulated in chapter 2 is then discussed in the last subchapter, 6.8.

3.3 Effect of damage tolerance on laminate design

The current approach utilized in the aerospace sector for laminate design is based on undamaged laminate properties; also residual strength is the critical design parameter in many applications. As a consequence, at present a laminate is first optimized to exhibit pristine properties and the resulting lay-up is subsequently examined to comply with the requirements in a damaged or defective state. *A.T. Nettles* demands a rethinking of this approach, as only an optimization process based on damaged laminate properties will lead to the desired goal [24]. A modified building block approach, based on compression after impact (CAI) specimens tested at BVID level, was investigated in the certification process of a helicopter tail boom and proved to be more cost efficient [25].
However, there is no information available in the literature which describes how to develop a material target-orientated for damage tolerance requirements following the present certification process. Stacking rules are therefore used in practice. By following these rules during the design process, it can be ensured in most cases that parts maintain the required residual strength when damaged.
Additionally, the current way of representing the relationship between detectability, impact energy and residual strength, as used in the Military Handbook [21] and in Figure 3.1, is inadequate. This two dimensional model tries to distinguish between different cases of residual strength in a diagram describing the relationship between impact energy and detectability. The Military Handbook also applies the model to laminates of different

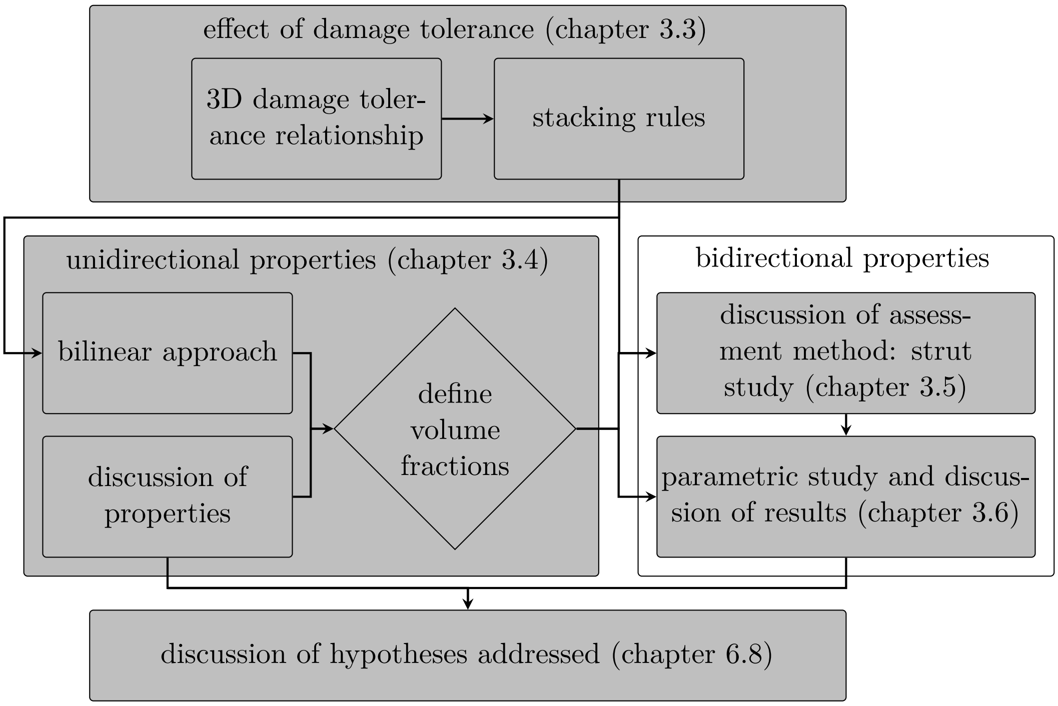

Figure 3.2: Flowchart describing the procedure pursued in chapter 3; individual subchapters marked in gray.

thicknesses. This leads to ambiguous interpretation in the two-dimensional diagram.
Therefore, first a 3D interpretation of the relationship between impact energy, residual strength and damage detectability is presented and then the common stacking rules are introduced.

Three-dimensional interpretation of damage tolerance relations

This novel perspective describes the relationship between the crucial parameters of impact energy, damage size and residual strength and allows the comparison of different materials concerning their damage tolerance properties. This model view consists of two cuboids generating a volume which contains unacceptable parameter combinations, see Figure 3.3. These cuboids are limited by six different planes indicated by colored lines. The gray lines indicate the two impact energy thresholds, the orange lines show the position of the visibility threshold based on damage size and the blue lines describe the residual strength properties connected with the Ultimate and Limit Load capabilities. The cuboid faces possess the associated colors. The six required values depend on the application. The gray-colored energy thresholds are a result of probability, in-service data and the part's accessibility. The orange-colored damage size for detectability is determined by tests at different lighting and mainly depends on the part's accessibility. The required residual stress levels for UL and LL capability can be calculated based on the different load cases and the part's design.
The blue top face of the upper cuboid represents the residual strength RS_{UL} and is limited by four edges, whereas the two edges describing the lower limits are not of any further interest. The cuboid's edge at the intersection between the blue and the gray face defines the threshold for the impact energy E_{pot1}. As long as there is no barely visible damage present, the strength must be above this edge. The other edge of interest is formed by the

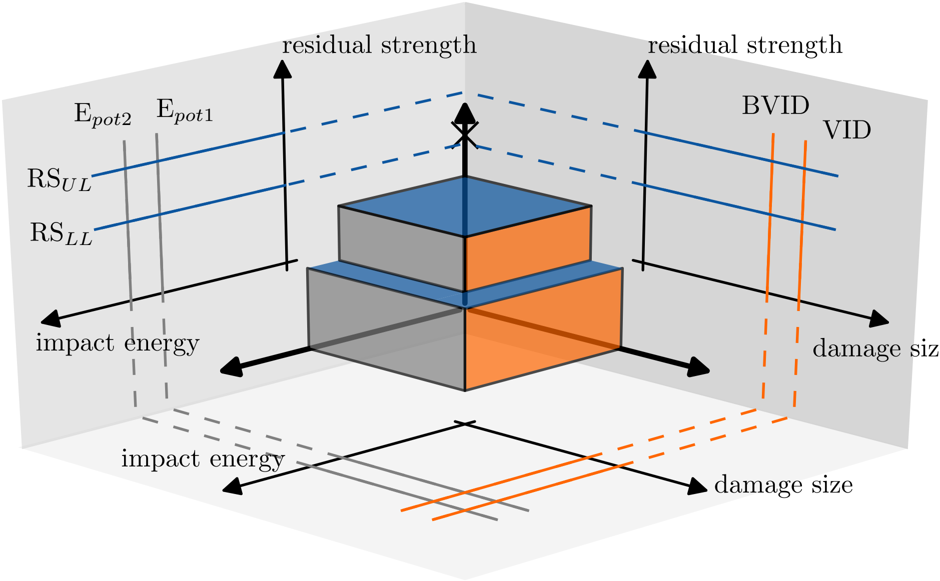

Figure 3.3: 3D damage tolerance relationship between the three fundamental damage tolerance parameters of impact energy, damage size and residual strength

line between the orange and the blue faces of the upper cuboid. This line represents the BVID and defines the threshold for those cases, where the residual strength falls below RS$_{UL}$ whilst the related impact energy is below E$_{pot1}$. In this case only those values which show at least an instance of barely visible damage and are outside the upper cuboid are valid.

The blue top face of the lower cuboid represents the residual strength RS$_{LL}$ and is also limited by four edges where two are of major interest. The line between the blue and gray faces defines the impact energy E$_{pot2}$. As long as there is no visible damage, the strength needs to be above this line. The edge between the orange and blue faces of the lower cuboid represents the threshold for those cases where the residual strength falls below RS$_{LL}$ whilst the related impact energy is below E$_{pot2}$. In this case only those values which show visible damage and are outside the lower cuboid are valid.

When performing CAI-tests at different impact energies, a graph can be generated in the 3D-domain, describing damage size and residual strength depending on impact energy. Graphs of this kind are shown in Figure 3.4 and Figure 3.5. The graph line starts at a point on the vertical axis depicting the undamaged strength value. The graph presents a solid black line and its projections in all three directions in space are presented by respective colored lines.

As soon as the graph line penetrates one of the cuboids by intersecting a blue face the laminate is not acceptable as this means that the residual strength of the specimens being impacted at a certain energy below that required is too low and there is no chance of detection as the related visibility level is not achieved. For a certain material, the only solution is to choose a thicker laminate. This would displace the residual strength which - in simplified terms - equals an increase in the initial strength value.

As shown by the projections, an ascending relationship is perceived between impact energy and damage size (see energy-damage size-plane projected to the bottom of the figure) and

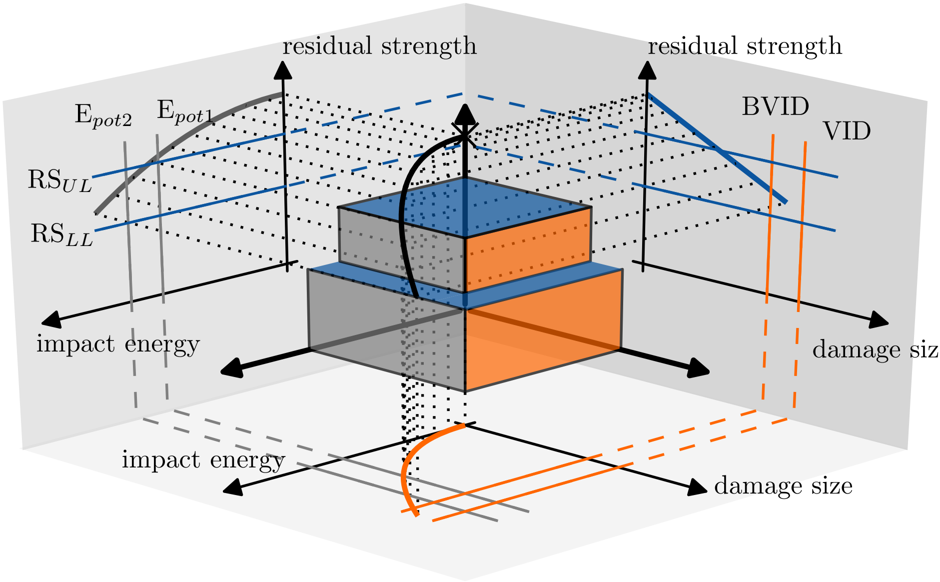

Figure 3.4: 3D damage tolerance relationship - acceptable material with undetectable damage requiring fatigue evaluation

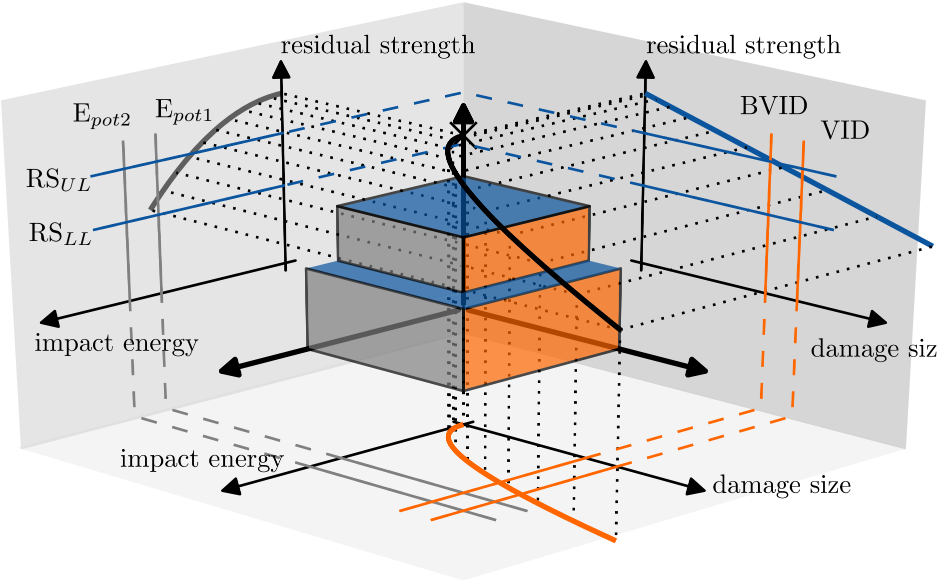

Figure 3.5: 3D damage tolerance relationship - acceptable material with undetectable damage requiring appropriate inspection interval definition

a declining relationship between impact energy and residual strength (see energy-residual strength-plane).

Basically, three different cases for valid relationships can be distinguished.

In the **first case**, the residual strength RS_{UL} is reached exactly by an impact energy E_{pot1} and the residual strength RS_{LL} is reached exactly by an impact with the energy E_{pot2}. At the same time, a BVID is achieved exactly with the energy E_{pot1} and a VID is achieved with E_{pot2}. In this particular case the graph line touches the forward upper corners of both cuboids and its projection on the bottom plane shows a diagonal connecting the origin with the two intercept points between the orange and the gray lines. Although such a relationship is hard to find in practice, this case subdivides the model into two major cases.

In the **second case**, shown in Figure 3.4, the graph line cuts the first residual strength threshold before it cuts the BVID threshold. The projection on the bottom plane stays left of the diagonal line discussed in the first case. This means that the graph line drops below RS_{UL}, representing the residual strength corresponding to UL, outside the cuboid and is therefore valid, but does not show any detectable damage. In this case, §25.571(c) must be applied, which means that a fatigue evaluation is required as damage may remain undetected. Economically, this means additional costs for certification, additional development time and increased non-recurring costs.

The **third case** is shown in Figure 3.5. Although the graph line falls below the residual strength threshold RS_{UL} at an impact energy below E_{pot1}, the laminate or part is valid because detectable damage is created as soon as the residual strength threshold is undercut. The projection of the graph on the bottom plane is on the right side of the diagonal, as discussed in case one, when it reaches the BVID threshold. In this case §25.571(b) is to be applied and the damage must be repaired in any case. Economically, some evaluation work must be carried out in order to define the inspection interval in such a way that equivalent safety is achieved to that which prevails with metallic structures is, but not as much experimental effort is required in preparation of the approval. Instead, recurring costs may be increased due to repair and potentially shorter inspection intervals.

Stacking rules

The definition of certain permitted lay-ups is one way to account for damage tolerance requirements in the design of a part. However, the most common process is the definition of so called ‘stacking rules’. The idea behind these rules is to avoid cost-intensive redesign loops due to compliance with damage tolerance requirements or mechanical and/or thermomechanical incompatibility. When following these rules, the part ought to be tolerant of damage in such a way that it fulfills the residual strength requirements defined later in the development process.

Hence, in applications exposed to any risk of an impact or manufacturing defect, stacking rules narrow down the possible lay-up arrangements and thereby reduce the material’s stiffness and strength exploitation in a certain load direction. The definition of a lay-up runs as a concurrent activity across design, stress and manufacturing engineering. Typical stacking rules account for manufacturing, damage tolerance, buckling and stress issues. Some common rules are given here, whereby for some applications they may be coexistent or incomplete [16]:

- the laminate must be balanced to prevent manufacturing distortions
- the stacking should be symmetrical with reference to the median axis to prevent deformation
- a minimum of 8% and a maximum of 67% of plies in each of the four basic directions is recommended to counter effects induced by different Poisson’s ratios
- different orientations of layers should be uniformly distributed
- minimizing the angle between adjacent plies to minimize inter-laminar shear is recommended
- grouping 45° and -45°-plies to minimize any mechanical coupling is recommended
- grouping of layers with similar orientation should be avoided in order to reduce micro-crack formation
- working plies should be placed away from the neutral axis to increase bending stiffness and improve buckling safety

3.4 Consideration of unidirectional properties

In the following, the properties of the different material groups are compared for the unidirectional case.

Firstly, the influence of the aforementioned stacking rules on pure CFRP laminates is discussed. Then, a bilinear approach is introduced for the FMLs in order to be able to compare the different material groups. Based on this approach, there follows a discussion of the laminate strength and stiffness depending on metal volume fraction. Finally, volume fractions are selected which are subsequently investigated in detail within this thesis.

Pure CFRP laminates following stacking rules

Following the aforementioned stacking rules to the utmost, a maximum of 65% plies in load direction is achievable for a given predefined laminate. Designing a 4 mm thick laminate with a given prepreg system with 0.13 mm ply-thickness, the created laminate lay-up is (62.5/25/12.5) and called highly-orthotropic (HO) laminate in the following. Quasi-isotropic (QI) laminates (25/50/25) are also widespread in practice and UD-laminates (100/0/0) are often referred to in theory. QI and UD-laminates are therefore also investigated. The laminate properties are calculated using the CLT [26] for moduli and the PUCK-2D [27] first ply failure criterion for compression strength. The relationship between compression stiffness and strength for these three lay-ups utilizing high tenacity and strength (HTS)- and intermediate modulus (IM)-fibers are presented in Figure 3.6. For both fiber types a significant drop in both values is apparent when increasing the amount of additional fiber directions. A QI-laminate of HTS-fibers reaches 40% of the stiffness and strength of its unidirectional counterpart. The loss for IM fibers is even more significant. For both properties, stiffness and strength, 38% of the value of the UD-laminate is achieved by a QI-laminate. The transverse laminate strength values of laminates of both fiber types are quite similar as it is a matrix-dominated laminate property. This results in a greater difference between longitudinal and transverse strength of IM-fiber laminates and explains the greater decrease when compared to HTS-fiber laminates. The transverse stiffness of HTS-fiber laminates is even slightly higher than the stiffness of IM-fiber laminates. This can be explained by the lower anisotropy of HTS-fibers. Therefore, the decrease in stiffness is also greater for IM-fiber than HTS-fiber when comparing QI-laminates with their unidirectional counterparts.

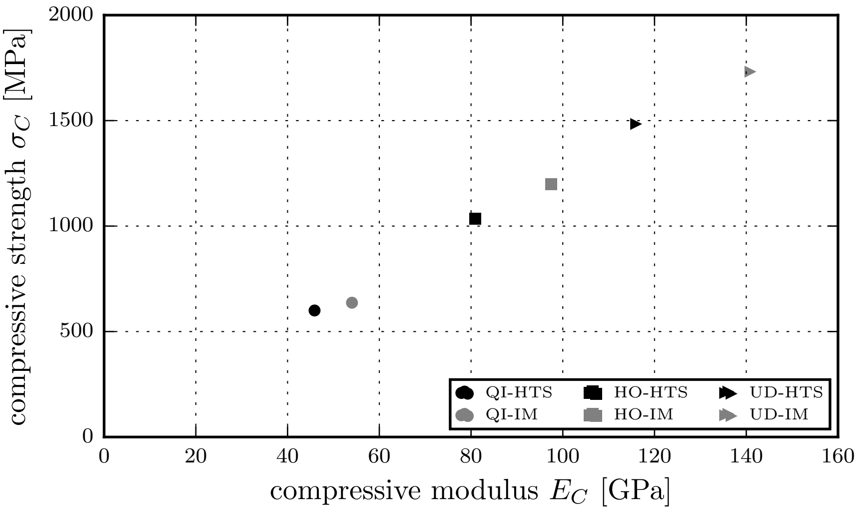

Figure 3.6: Relationship between compressive stiffness and strength of unidirectional (UD), highly-orthotropic (HO) and quasi-isotropic (QI) laminates of HTS and IM fiber reinforced Hexcel 8552 epoxy [28].

Bilinear approach for FMLs

As the two constituents, CFRP and steel, offer different strength and stiffness properties, a theory is required for the evaluation of the hybrid laminate's properties. Additionally, both materials show different coefficients of thermal expansion and in general the curing temperature of the resin is above operational temperature. Therefore, the residual stresses generated must also be considered. Suitable methods and theories are discussed and evaluated in chapter 5 at page 75. However, a simple approach is required to comprehensibly consider the residual stresses in the following parameter study as, depending on the metal volume fraction, the residual stress may essentially affect the material's load-bearing capacity. The bilinear approach is therefore presented in the following and then employed to examine the impact of the laminate's metal volume fraction on its stiffness, strength and capacity utilization.

For a narrow strip with fibers along its length and where the Poisson's effect is free to occur, the stress-strain relationship can be described by Hook's law for the one-dimensional case. This approach is applicable as the transverse stiffness of the fiber layer is very low and thus its restraint on the Poisson's effect is low as well. However, the approach neglects the restraining effect of the metal layer on the CFRP, especially for high metal volume fraction. The laminate's longitudinal stiffness E_L and the coefficient of thermal expansion (CTE) in the fiber direction α_L can be predicted by the rule of mixture (ROM) [16] as a function of the metal volume fraction φ_M (all following relationships are shown schematically and are additionally referenced by a Property number $Prop_n$ in front of the equations which describes each highlighted point in Figure 3.7):

$$Prop_1: \qquad E_L = E_M \varphi_M + E_C(1-\varphi_M) \tag{3.1}$$

$$\alpha_L = \frac{E_M \varphi_M \alpha_M + E_C \alpha_C (1-\varphi_M)}{E_L} \tag{3.2}$$

In this approach the yield stress $\sigma_{M,y}$ ($Prop_2$) of the metal is required, rather than the typically measured technical elastic limit $\sigma_{M,0.2}$ at 0.2% remaining strain and can be determined as follows:

$$Prop_2: \qquad \sigma_{M,y} = \sigma_{M,0.2} - \frac{0.002}{\frac{1}{E_{M,pl}} - \frac{1}{E_M}} \tag{3.3}$$

The required plastic stiffness of the metal $E_{M,pl}$ ($Prop_3$) is calculated by:

$$Prop_3: \qquad E_{M,pl} = \frac{\sigma_{M,ult} - \sigma_{M,0.2}}{\epsilon_{M,ult} - \epsilon_{M,0.2}} \tag{3.4}$$

which again requires effective elongation at the technical elastic limit $\epsilon_{M,0.2}$:

$$\epsilon_{M,0.2} = \frac{\sigma_{M,0.2}}{E_M} + 0.002 \tag{3.5}$$

Based on the permanent strain after failure $\epsilon_{M,A}$, the effective elongation of the metal at failure $\epsilon_{M,ult}$ ($Prop_4$) is:

$$Prop_4: \qquad \epsilon_{M,ult} = \frac{\sigma_{M,ult}}{E_M} + \epsilon_{M,A} \tag{3.6}$$

In the literature it is assumed that at cure temperature there are no internal stresses present and curing stresses are a function of curing temperature only [29]. Later investigations have shown these assumption not to be accurate [30–32], therefore, an additional stress-free temperature T_{sf} is defined to be lower than curing temperature $T_{cure,max}$. The residual cure strain of the metal layer $\epsilon_{M,R}$ ($Prop_5$) and the composite layer $\epsilon_{C,R}$ ($Prop_6$) are estimated with the help of the differential temperature ΔT between the stress free-temperature T_{sf} and the operational temperature T_{op}:

$$Prop_5: \qquad \epsilon_{M,R} = (T_{sf} - T_{op})(\alpha_L - \alpha_M) \tag{3.7}$$

$$Prop_6: \qquad \epsilon_{C,R} = (T_{sf} - T_{op})(\alpha_L - \alpha_C) \tag{3.8}$$

The required CTE of the laminate α_L can also be calculated with the help of the ROM as given in (3.2). When the residual strains after cure are known, the yield strength $\sigma_{L,y}$ ($Prop_8$) and the ultimate strength $\sigma_{L,ult}$ ($Prop_{10}$) of the laminate can be predicted with the corresponding elongations $\epsilon_{L,y}$ ($Prop_7$) and $\epsilon_{L,ult}$ ($Prop_9$).

$$Prop_7: \qquad \epsilon_{L,y} = \frac{\sigma_{M,y}}{E_M} - \epsilon_{M,R} \tag{3.9}$$

$$Prop_8: \qquad \sigma_{L,y} = E_L\epsilon_{L,y} = \big(E_M\varphi_M + E_C(1-\varphi_M)\big)\Big(\frac{\sigma_{M,y}}{E_M} - \epsilon_{M,R}\Big) \tag{3.10}$$

$$Prop_9: \qquad \epsilon_{L,ult} = \frac{\sigma_{C,ult}}{E_C} - \epsilon_{C,R} \tag{3.11}$$

$$Prop_{10}: \qquad \sigma_{L,ult} = \sigma_{L,y} + E_{L,pl}(\epsilon_{L,ult} - \epsilon_{L,y}) \tag{3.12}$$

$E_{L,pl}$ ($Prop_{11}$) describes the plastic stiffness of the laminate after passing the yield point of the metal:

$$Prop_{11}: \qquad E_{L,pl} = E_C(1-\varphi_M) + E_M\varphi_M = E_C(1-\varphi_M) + \varphi_M\frac{\sigma_{M,ult} - \sigma_{M,0.2}}{\epsilon_{M,ult} - \epsilon_{M,0.2}} \tag{3.13}$$

The thicker lines and associated coordinate system represent the relationship for the laminate. Therefore, two additional coordinate systems are placed on the abscissae, showing the constituent metal and fiber reinforced plastic (FRP) parts. Their displacement to the laminate's coordinate system equals the residual strain of each constituent in the hybrid laminate.

Stiffness and strength depending on metal volume fraction and curing stress

For a specific combination of FRP and metal, the laminate's stiffness and yield strength are significantly influenced by the constituent's volume fraction. In the following, this relationship is investigated for steel (St), titanium (Ti) and aluminum (Al) in combination with HTS-fiber and IM-fiber reinforced epoxy. The material data for each specific material is summarized in Table 3.1. AS4 is a widespread HTS fiber and IM7 a common IM fiber in the aerospace industry. The strength of the steel material in particular is high as a consequence of work hardening in the cold rolling process. All examinations follow the narrow strip assumptions described above with fibers aligned in the considered direction only.

Figure 3.8 and 3.9 show the relationships between volume fraction and tensile elastic modulus as well as volume fraction and weight-specific elastic modulus, respectively. At 0% metal volume fraction all graph lines meet in two single points representing the stiffness E_{11} of pure CFRP for HTS-fibers and IM-fibers. Accordingly, at 100% metal volume fraction the graph lines meet at three points, representing the stiffness of steel, titanium

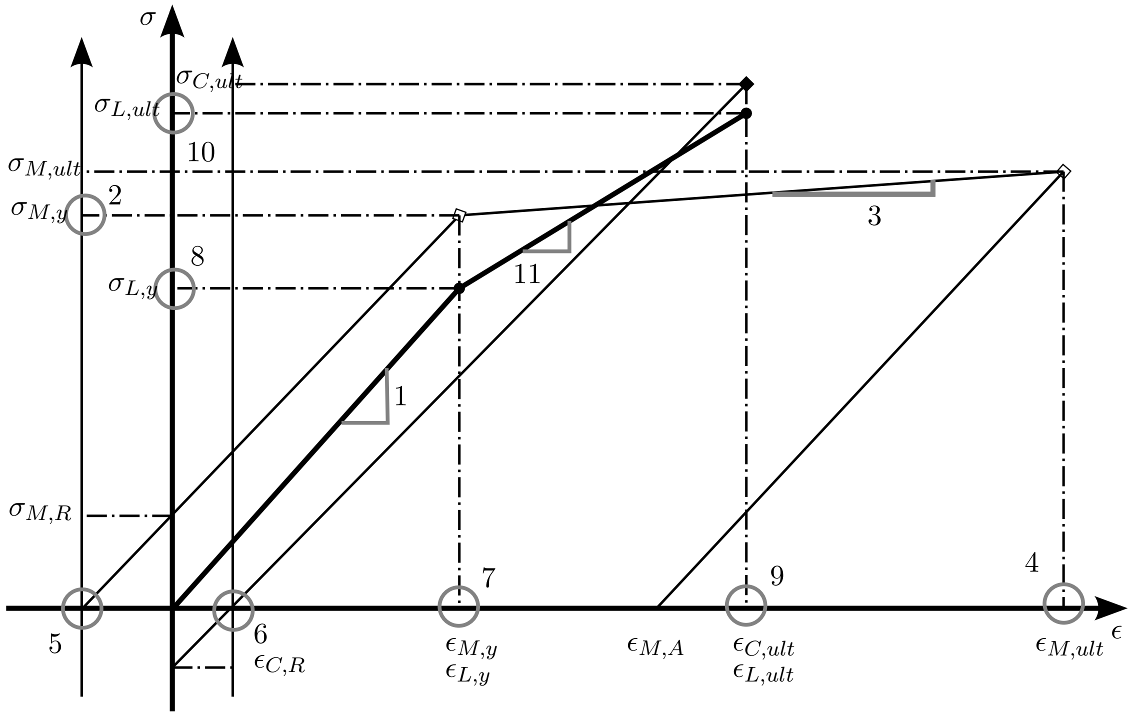

Figure 3.7: Bilinear stress-strain behavior of Fiber-Metal-Laminates for the one-dimensional case. Arabic numbers indicate reference properties

and aluminum. Significant stiffness differences can be observed even for low metal volume fractions, whereas the weight-specific elastic moduli are more similar. Although the compressive stiffness of CFRP is lower than for a tensile load, as shown in Table 3.2, the relationship is comparable with those presented in Figures 3.8 and 3.9, and hence is not shown separately.

However, considering yield strength, a distinction between tensile and compressive loads is essential as different phenoma are present. The tensile yield strength $\sigma_{L,y}$ of laminates composed of CFRP-HTS and different metals is shown in Figure 3.10.

As soon as there is any metal added to the laminate, the strength (as yield strength is considered relevant) decreases in comparison with pure CFRP-HTS. The reason for this effect is that the effective elongation at the technical elastic limit $\epsilon_{M,0.2}$ of steel, titanium and aluminum is lower than the ultimate elongation of CFRP-HTS. By adding a low amount of metal, the total stiffness does not change much but the elongation to the yield point decreases significantly. As a consequence, the laminate yield strength for low metal fractions is low, although the selected steel has similar yield strength to the ultimate strength of CFRP-HTS.

With increasing steel fraction the laminate's yield strength $\sigma_{L,y}$ converges towards the yield strength of pure steel. Titanium and aluminum show a lower strength than CFRP-HTS. This leads to a decrease in the laminate's yield strength $\sigma_{L,y}$. As a consequence of the tensile stress in the metallic layers, the laminate's tensile yield strength is lowered since the elastic limit of the metal component is regarded as the crucial limit. When aiming for low metal volume fractions, the consideration of residual stress becomes even more essential. This relationship is shown in Figure 3.10 at room temperature for a system cured at 180°C. The graphs which do not consider the residual cure stress are marked with an additional '-NR'. With lower metal volume fraction an increased amount of the

Table 3.1: Material data for FML constituents at room temperature (RT)

material	ultimate strength σ_{ult}	yield strength $\sigma_{p0.2}$	tensile modulus E_{11}	CTE α_{11}	density ρ	failure strain ϵ_{ult}
[-]	[MPa]	[MPa]	[GPa]	[10^{-6}/K]	[g/cm^3]	[%]
CFRP 8552/AS4	1928 [33]	-	132 [34]	0.28 [35]	1.59 [28]	-
CFRP 8552/IM7	2212 [33]	-	162 [33]	-0.35 [36]	1.57 [28]	-
steel 1.4310	2060 [37]	1980 [37]	190 [37]	16.4 [37]	7.9 [37]	5 [37]
titanium 15-3-3-3	1370 [37]	1290 [37]	116 [37]	8.6 [37]	4.78 [37]	2.4 [37]
aluminum 7075	510 [38]	434 [38]	71 [38]	23.4 [38]	2.81 [38]	5 [38]

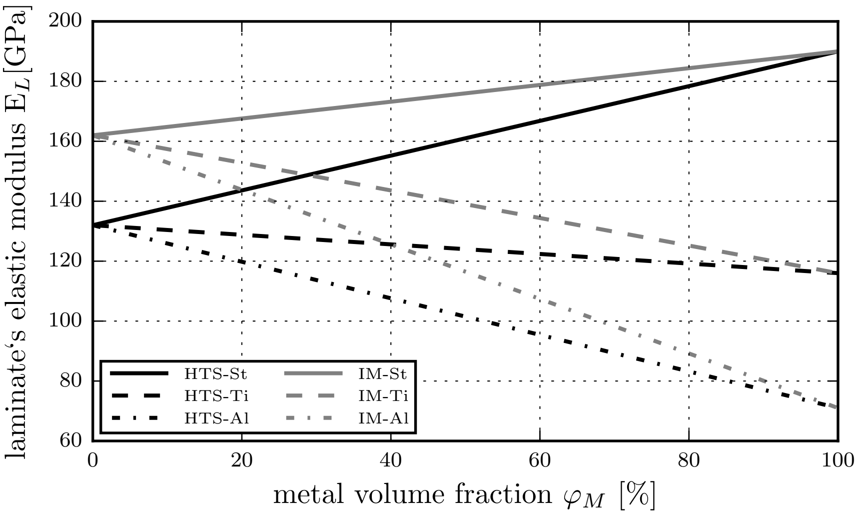

Figure 3.8: Elastic modulus dependency on metal volume fraction for St, Ti and Al combined with HTS- and IM-fiber (tensile)

yield strength is forfeit to the residual cure stresses. The yield strength of a UD-CFRP-aluminum laminate with 5% metal volume fraction is reduced by more than 50% mainly as a result of the high CTE of aluminum. Titanium shows the lowest influence of cure stresses as it has a lower CTE than steel and a lower stiffness. The impact of curing stress on the laminate's strength decreases with higher metal volume fractions and the graph lines meet at the point which represents the yield strength of the particular metal.

IM-fibers have a higher ultimate tensile strength and a higher stiffness. This leads to higher laminate strength at lower metal volume fractions as depicted in Figure 3.11. However, due to the higher stiffness and lower CTE of IM-fibers compared to HTS-fibers, the influence of residual cure stresses on the laminate strength increases as well. Due to load equilibrium in the laminate, the residual curing stresses in the metallic layers are accompanied by compressive stresses in the CFRP layer. This leads to a completely different relationship between laminate strength and residual curing stresses. Additionally,

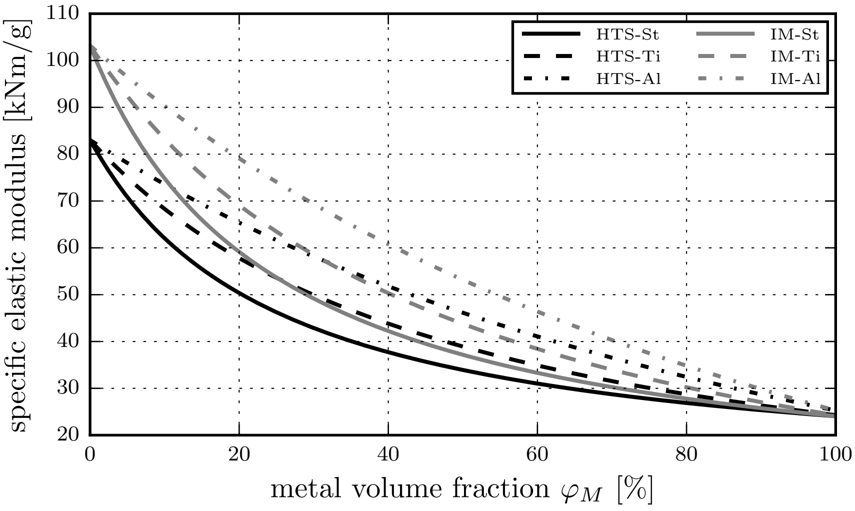

Figure 3.9: Weight-specific elastic modulus dependency on metal volume fraction for St, Ti and Al combined with HTS- and IM-fiber (tensile)

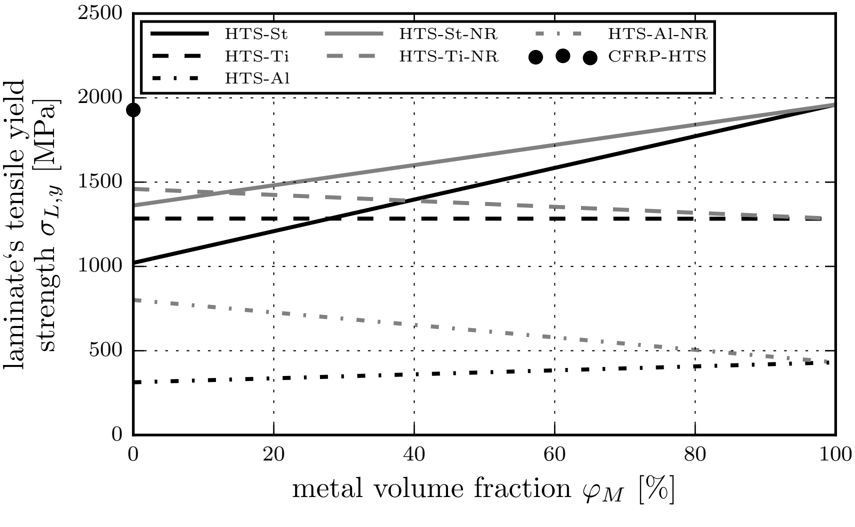

Figure 3.10: Tensile yield strength $\sigma_{L,y}$ dependency on metal volume fraction with and without (NR) consideration of residual cure stresses ($\Delta T = 160K$) for HTS-fiber and ultimate tensile strength of pure HTS-fiber CFRP

the compressive properties of CFRP are significantly lower, see Table 3.2. The ultimate compressive strength values for both fiber types can also be found in Figure 3.12. When residual stresses are not considered, the laminate's yield strength for low metal volume fraction is also decreased, as the effective elongation at the technical elastic limit $\epsilon_{M,0.2}$ of steel is lower than the ultimate elongation of CFRP-HTS and CFRP-IM. When considering the residual tensile stress of the steel layer within the laminate, part of the elongation is compensated and failure of the CFRP determines the crucial limit. The kink in the graph marks the transition from ultimate CFRP failure to metallic yield failure. For

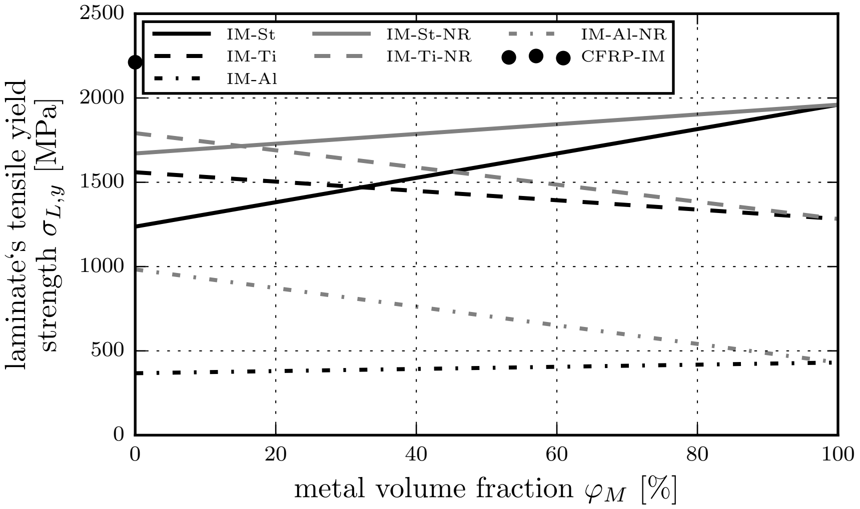

Figure 3.11: Tensile yield strength $\sigma_{L,y}$ dependency on metal volume fraction with and without (NR) consideration of residual cure stresses ($\Delta T = 160K$) for IM-fiber and ultimate tensile strength of pure IM-fiber CFRP

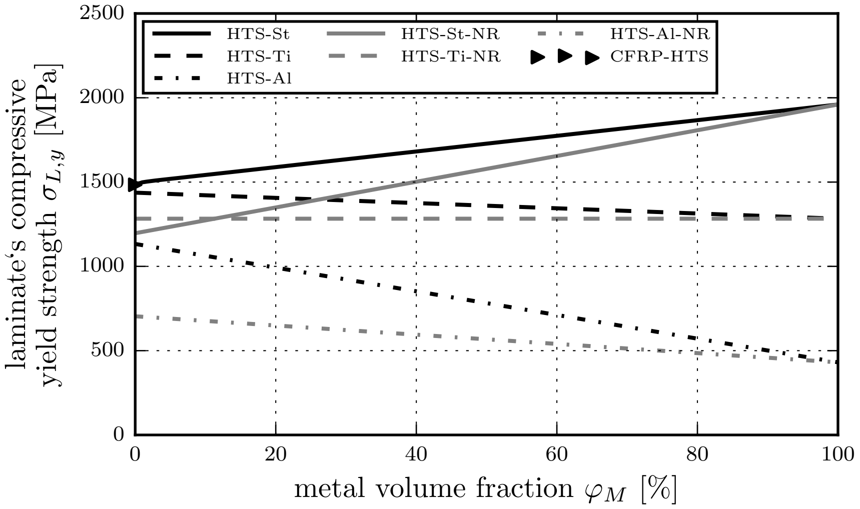

Figure 3.12: Compressive yield strength $\sigma_{L,y}$ dependency on metal volume fraction with and without (NR) consideration of residual cure stresses ($\Delta T = 160K$) for HTS-fiber and ultimate compressive strength of pure HTS-fiber CFRP

the IM fiber the kink is more obvious as the compensation is increased due to increased residual stress as shown in Figure 3.13.

Metal volume fraction and the laminate's weight specific stiffness

The next step is to evaluate the weight-specific requirements compared to pure CFRP laminates. Stacking rules for pure CFRP laminates are discussed in chapter 3.3 in more

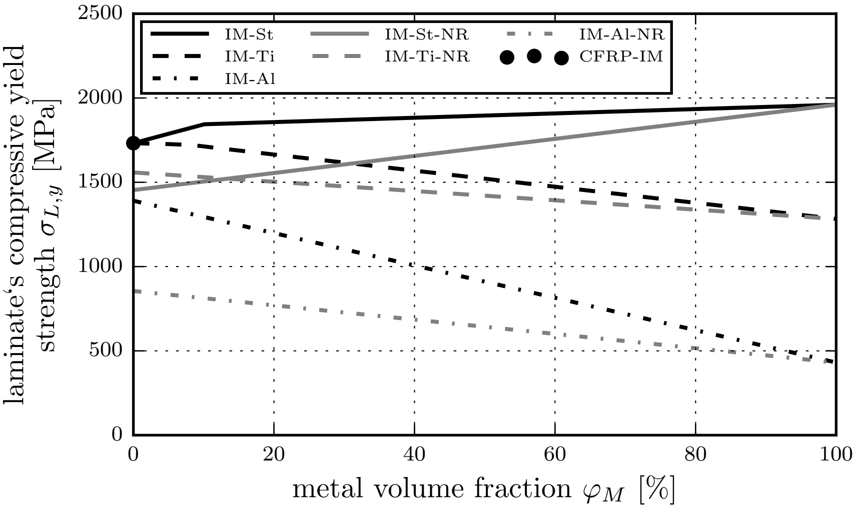

Figure 3.13: Compressive yield strength $\sigma_{L,y}$ dependency on metal volume fraction with and without (NR) consideration of residual cure stresses ($\Delta T = 160K$) for IM-fiber and ultimate compressive strength of pure IM-fiber CFRP

Table 3.2: CFRP material data for compressive loading at RT

material	longitudinal compressive strength σ_{c11}	longitudinal compressive modulus E_{c11}	transverse compressive strength σ_{c22}	transverse compressive modulus E_{c22}	compressive Poisson's ratio ν_{12}
	[MPa]	[GPa]	[MPa]	[GPa]	[-]
CFRP 8552/AS4	1484 [33]	116 [33]	268 [33]	10 [33]	0.335 [33]
CFRP 8552/IM7	1732 [34]	141 [34]	286 [34]	10 [34]	0.356 [34]

detail. However, two common rules are anticipated here. When creating the laminate lay-up for uniaxially loaded parts, designed with a maximum of 0°-layers, the following stacking rules are essential:

- Maximum number of similarly orientated plies $n = 4$ or maximum thickness $t =$ 1 mm.
- Minimum 8% of fibers in each of the four basic orientations.

Most of the applied experiments in this work use specimens with a thickness of $t_{lam} =$ 4 mm. Applying these two rules and taking this laminate thickness as a basis, the resulting lay-up for a common prepreg layer thickness of $t_{lay} = 0.13$ mm is: (62.5/25/12.5). The on-axis stiffness E_R of this pure multiaxial CFRP reference can be analytically calculated following CLT [39]. In order to ensure an advantage in the weight specific stiffness properties of the UD-CFRP-steel laminates compared to the CFRP reference, the selection of the metal volume fraction φ_M must fulfill the following condition (ρ_L and ρ_R are the density of the CFRP-UD-steel laminate and multiaxial CFRP reference stacking, respectively):

$$\frac{E_L}{\rho_L} > \frac{E_R}{\rho_R} \tag{3.14}$$

For the particular reference laminate, the metal volume fraction φ_M must be less than 12.3% to fulfill the above condition (3.14).

Consideration of steel layer's thickness

The previous section describes the relationship between metal volume fraction and stiffness as well as the strength of the laminate. However, the lay-up has not been considered yet. Based on the description of the UD-CFRP-steel approach, see chapter 2, it is assumed that the quantity of interfaces and their position within the laminate affect the residual strength after impact. Although these relationships are investigated in chapter 6, one goal in the design process of the specimens must be the maximization of the interface quantity. The quantity is restricted by the prepreg and steel layer thickness. Based on the previously selected laminate thickness of $t_{lam} = 4$ mm and prepreg thickness of $t_{lay} = 0.13$ mm, only certain lay-ups are possible, as depicted in Figure 3.14.

The figure shows the quantity of metal-CFRP interfaces n for nine different metal layer thicknesses depending on the metal volume fraction φ_M. It is obvious that for a metal foil thickness of 0.01 mm a volume fraction above 8% is not achievable for the present material combination. At the same time, for lower metal volume fractions the thicker metal foils only provide a few layers and interfaces. This relationship indicates that common laminate and prepreg thickness ratios require preferably thin metal foils in order to allow a certain number of plies whilst maintaining the metal volume fraction below 12%.

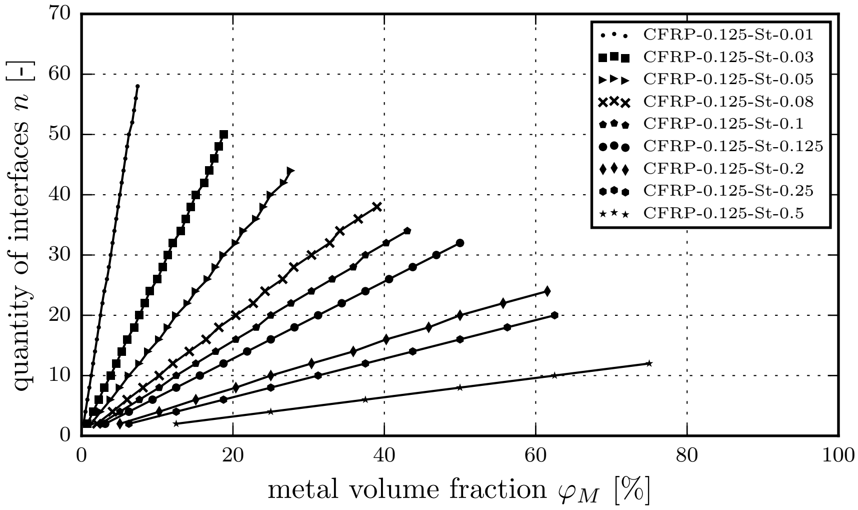

Figure 3.14: Influence of steel-layer thickness on quantity of interfaces depending on metal volume fraction for 0.125 mm prepreg thickness in a 4 mm laminate

3.5 Consideration of bidirectional properties - method

The above mentioned boundary conditions of stacking rules and prepreg to metal layer thickness ratio hinder a closed form solution for assessing the material's suitability irrespective of its application. Instead, a specific application is used to compare the suitability of different materials in comparison to the UD-CFRP-steel laminate. As the UD-CFRP-steel material is intended for use in parts with uniaxial loading, an iterative assessment method is used to compare the suitability of different materials for a typical application of a strut. A case involving separate struts is clearer than a stiffened skin for the following analysis, therefore a single strut as part of a framework design serves as the assessment case.
Two crucial **requirements** influence the design of a strut:

- load
- distance between the two end-restraints.

A strut from an alternative payload adapter design for the ARIANE 5 shall serve as use-case [15], where a parametric study has been performed on the adapter's geometry. The suggested design leads approximately to the following requirements:

- 1000 kN compression load per strut
- strut length/distance between the two end-restraints: 1 m.

For reasons of comprehension, the parameter study is also conducted with 100 kN and 10.000 kN at 1 and 2 m strut length. Within the design space of a strut, the radius of a circular r_s and accordingly the width w_s of a rectangular strut as well as the wall thickness t_{lam} are adjustable, see Figure 3.15. Therefore, these two parameters serve as **working parameters** when performing a parameter study:

- radius r_s / width w_s
- wall thickness t_{lam}

For a compressive loading scenario, the following **criteria** are considered for the parameter study:

- compressive strength
- local buckling
- global buckling.

Again, as the interaction of longitudinal and transverse material properties is of primary interest, it is important to consider the different safety factors on the various **criteria**. Retaining the aeronautical use case, the following safety factors for the given **criteria** are customary within space applications [40]:

• yield safety factor:	$j_y = 1.10$	(applicable on mechanical loads)
• ultimate safety factor:	$j_u = 1.25$	(applicable on mechanical loads)
• global buckling safety factor:	$j_{gb} = 1.25$	(applicable on global buckling).
• local buckling safety factor:	$j_{lb} = 1.25$	(applicable on local buckling).

However, depending on the residual stress and the fiber used, a fiber fracture cannot be ruled out for low metal volume fraction. Therefore, the ultimate safety factor needs to be applied for FML in any case and the yield safety factor can be ignored. As the ultimate safety factor and buckling safety factor are identical, the consideration of safety factors is not necessary for a comparative parameter study. Finally, when different solutions fulfill the requirements under consideration of the given criteria, a decisive parameter is required. Maintaining the aeronautical application, two parameters are typically of major interest and, therefore, serve as **decisive parameters** for the following parameter study:

- weight (primary parameter)
- axial stiffness (secondary parameter)

Estimation of global buckling loads for struts with square cross sections

Local and global buckling is considered for the compressive load case in which a pinned-pinned end-restraint is considered as the most common joining scenario for highly loaded struts.

The global buckling load $P_{buckl,glob,sq}$ of a slender thin walled column is estimated as follows [16]:

$$P_{buckl,glob,sq} = \frac{\pi^2 E_{long} I}{L_e^2} \tag{3.15}$$

where L_e is the effective length defined in terms of the length L_s and the coefficient of restraint K, E_{long} is the longitudinal stiffness and I is the moment of inertia. For further calculation the end-restraint coefficient is selected as $K = 1$, representing a simply supported end-restraint with rotations free and all translations besides the longitudinal, fixed [41].

Estimation of local buckling loads for struts with square cross sections

Thin-walled columns usually display buckling of the walls without the overall deflection of Euler buckling [16]. In this case, the shape of the cross section changes while the longitudinal axis of the column remains straight. For this local buckling, a rectangular plate, simply supported (ss) around the boundary and subjected to one edge load, can be assumed. This case is depicted in 3.16 and represents the minimum buckling load.

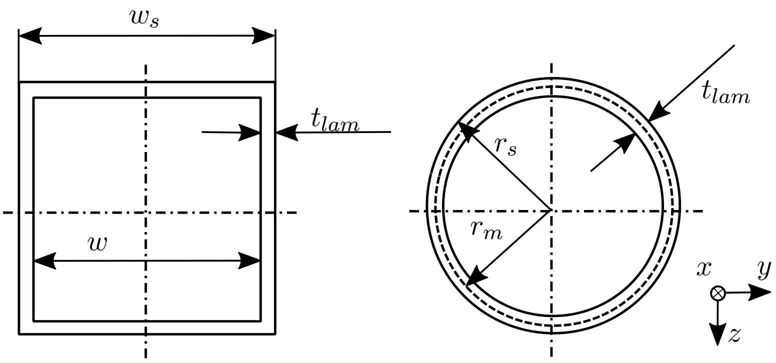

Figure 3.15: Dimensions of rectangular and circular struts

Following the *Navier* solution with $k_l = \widehat{N_{yy}}/\widehat{N_{xx}} = 0$ for a uniaxial loaded $\widehat{N_{xx}} = 0$ rectangular laminate, the critical buckling load is the smallest of $N_0(m,n)$ [26]:

$$N_0(m,n) = \frac{\pi^2}{m^2b^2}\left(D_{11}m^4\left(\frac{b}{a}\right)^2 + 2(D_{12}+2D_{66})m^2n^2 + D_{22}n^4\left(\frac{a}{b}\right)^2\right) \tag{3.16}$$

where a and b describe the plate length and width and D_{ij} the coefficients of the bending matrix. The smallest value of N_0 for any m, is found for $n = 1$. For this case, (3.16) is given as [26]:

$$N_0(m,1) = \frac{\pi^2 D_{22}}{b^2}\left(m^2\frac{D_{11}}{D_{22}}\left(\frac{b}{a}\right)^2 + 2\frac{D_{12}+2D_{66}}{D_{22}} + \frac{1}{m^2}\left(\frac{a}{b}\right)^2\right) \tag{3.17}$$

In the next step, the minimum for equation (3.17):

$$\frac{dN_0}{dm} = 0 \tag{3.18}$$

is given by:

$$m^4 = \frac{D_{22}}{D_{11}}\left(\frac{a}{b}\right)^4 \tag{3.19}$$

If the plate is very long ($a \gg b$) the plate buckles into more and more half-waves and by substituting (3.18) for m^2 it approaches the value:

$$N^{ss}_{buckl,loc,sq} = 2\left(\frac{\pi^2 D_{22}}{b^2}\right)\left(\sqrt{\frac{D_{11}}{D_{22}}}+\frac{D_{12}+2D_{66}}{D_{22}}\right) = \frac{2\pi^2}{b^2}\left(\sqrt{D_{11}D_{22}}+D_{12}+2D_{66}\right) \tag{3.20}$$

As increased plate width results in lower buckling load, the widest face of the strut under consideration is crucial. Following *Kollár* [41], the width b is used for the calculation of the rectangular plate (see Figure 3.15), which yields to a more conservative approach:

$$b = w + 2t_{lam} \tag{3.21}$$

Estimation of global buckling loads for struts with circular cross sections

The global buckling stress of a slender thin-walled strut is given by formula 3.15, where I for the circular cross section is calculated by:

$$I_{circ} = \pi r_m^3 t_{lam} \tag{3.22}$$

and where r_m is the mid-surface radius $r_m = r_s - t_{lam}/2$ (see Figure 3.15).

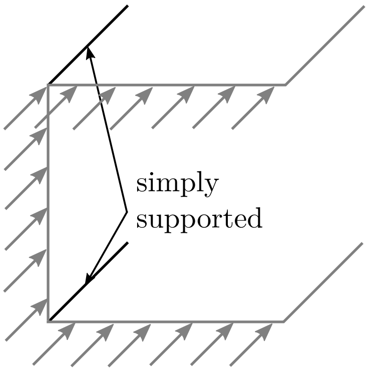

Figure 3.16: Local buckling of an axially loaded box beam (according to *Kollár* [41])

Estimation of local buckling loads for struts with circular cross sections

The buckling of a cylinder can be calculated based on a single-curved shell. The critical load parameter λ_{cr} must be calculated for different values of α and β. When the wall's lay-up is orthotropic, λ_{cr} is given by [42]:

$$\begin{aligned}\lambda_{cr} = \frac{1}{N_x\alpha^2 + N_y\beta^2}\Bigg(\Bigg(&\frac{\frac{\alpha^4}{R^2}(1 - \frac{A_{12}^2}{A_{11}A_{22}})}{\frac{\alpha^4}{A_{22}} + \alpha^2\beta^2(\frac{1}{A_{66}} - \frac{A_{12}(A_{12}+2A_{66})}{A_{11}A_{22}A_{66}}) + \frac{\beta^4}{A_{11}}}\Bigg) \\ &+D_{11}\alpha^4 + 2(D_{12} + 2D_{66})\beta^2\alpha^2 + D_{22}\beta^4\Bigg)\end{aligned} \tag{3.23}$$

where N_x and N_y are the buckling loads in the respective direction, A_{ij} are the coefficients of the stiffness matrix A and R is the radius. The lowest value of λ_{cr} is of interest. For local buckling of only axially loaded parts ($N_y = 0$), the buckling stress is given by

$$\sigma_{buckl,local,circ} = \frac{\lambda_{cr}N_x}{t_{lam}} \tag{3.24}$$

3.6 Consideration of bidirectional properties - parameter study

The parameter study is performed in a Python environment, following the programming logic depicted in the flowchart in Figure 3.17.
The material database contains the properties for the metals steel, titanium and aluminum and the two different CFRP materials 8552/AS4 and 8552/IM7 under consideration, as shown in Table 3.1 and 3.2.
The parameter study is based on different scenarios, as illustrated in Figure 3.17. These scenarios are identified by a certain combination of load, material, stress state and thickness steps.
As depicted in Table 3.3, three different material groups are distinguished: metal, CFRP and FML. These groups are defined by their repetitive stacks, the three metal types, three different pure CFRP lay-ups and six different values for the metal volume fraction (MVF) of the FML. IM and HTS fibers are considered within the CFRP and the FML material groups. Additionally, within the FML group, the metal type is varied and two different thickness values are used, as explained later. As residual curing stresses need to be considered in the FML group, two cases are distinguished: no curing stress (0 K differential temperature) and cured at 180°C with a considered cooling to RT of 23°C (-157K differential temperature). For all material groups, three different loads F, two different strut lengths L_s and two different cross section geometries are analyzed.
Following the approaches described, laminate stackings are created for each material group and listed in Table 3.4. These lay-ups describe a repetitive stacking with the thickness t_r. For the three metals, the repetitive thickness is defined as 0.05 mm. Three repetitive stacks are also created for the pure CFRP group. The QI-stack represents the standard whereas the orthotropic lay-up is created with the highest possible strength and stiffness properties in one main direction following the described stacking rules. Note that the created laminate itself is not symmetrical but the resulting strut creates symmetry along its midplane. As prepreg is available with a certain minimum thickness, the repetitive thickness of theses stacks is 0.524 and 1.048 mm, respectively. For the hybrid laminates,

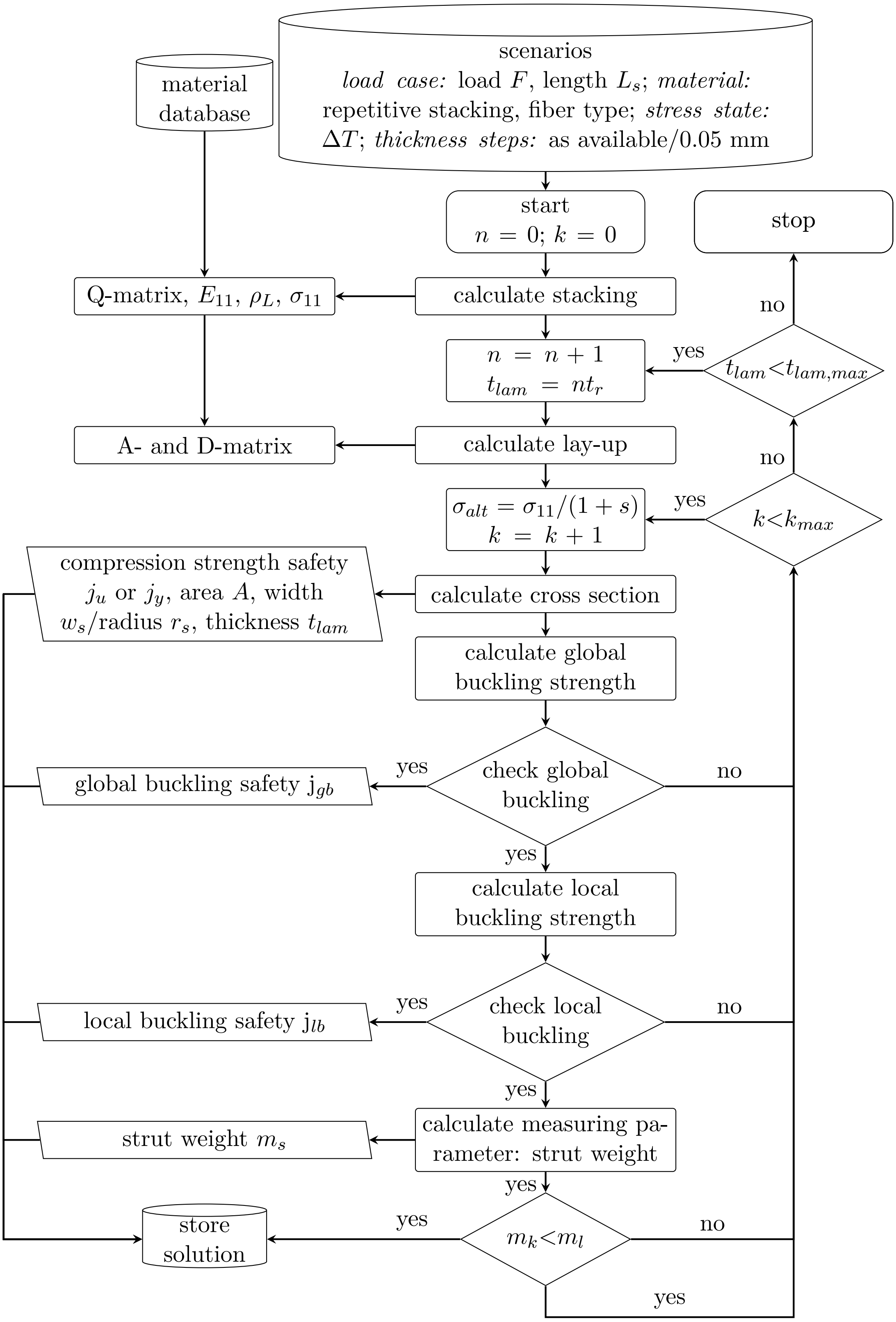

Figure 3.17: Parameter study's programming flowchart for circular and rectangular struts

Table 3.3: Table of parameters

material group	metal	CFRP	FML
repetitive stack	**St** **Ti** **Al**	**QI** **HO** **UD**	13% 10% 7% 5% 4% 3%
fiber type	-	IM HTS	IM HTS
metal type	St Ti Al	-	**St** **Ti** **Al**
thickness	-	given normalized	given normalized
differential temperature	-	-	0 K 157 K
strut length	1 m 2 m		
load	100 kN 1000 kN 10.000 kN		
cross section	circular square		
number of cases	36	144	1728

six stacks using different MVF between 3 and 13% are considered. Their repetitive thickness is between 0.131 and 0.231 mm.

To overcome the restriction that the CFRP prepregs are only available with certain layer thicknesses, an additional approach is pursued, whereby each material is reduced in thickness so that the thickness of the repetitive laminate equals 0.05 mm. This approach means that thicker repetitive stackings are not disadvantageous compared to the thinner ones in scenarios with low wall thickness. These two cases are marked as 'given' and 'normalized' in Table 3.3.

When running the algorithm, these stacks are assembled on top of each other up to a maximum laminate thickness $t_{lam,max}$. Based on this database, the flowchart in Figure 3.17 is launched 954 times for the circular and 954 times for the square cross section.

The in-plane laminate properties as Q-matrix, longitudinal compressive stiffness E_{11}, density ρ_L and longitudinal compressive strength σ_{11} are calculated based on the given repetitive stack. The rest of the program flow consists of two loops.

The outer loop runs the number of stacks up to a predefined maximum laminate thickness $t_{lam,max}$ and is controlled by the variable n. Based on the new lay-up, the A- and D-matrices are calculated using subroutines following CLT.

The inner loop controls an alternative stress level σ_{alt} which is reduced in each loop cycle k depending on a step size s. The step size s is defined here in such a way that the compression stress is lowered up to a safety factor $f_s = 15$ in $k_{max} = 1000$ steps:

$$s = k\frac{f_s}{k_{max}} \tag{3.25}$$

The values are chosen based on a previously undertaken less detailed parameter study. Starting with $k = 0$, the alternative stress level σ_{alt} equals the compression strength and the required cross section area is calculated. As t_{lam} is defined by the outer loop, the radius

Table 3.4: Regarded repetitive laminate stackings

material group	description	stacking	repetitive thickness	MVF	metal layer thickness
[-]	[-]	[-]	[mm]	[%]	[mm]
metal	steel	St	0.05	100	0.05
metal	titanium	Ti	0.05	100	0.05
metal	aluminum	Al	0.05	100	0.05
CFRP	quasi-isotropic	(+45/-45/0/90)	0.524	0	-
CFRP	orthotropic	(+45/-45/0_4/90/0)	1.048	0	-
CFRP	unidirectional	(0)	0.131	0	-
FML	UD-metal	(0/M)	0.151	13	0.02
FML	UD-metal	(0/0/M)	0.161	10	0.03
FML	UD-metal	(0/0/M)	0.171	7	0.02
FML	UD-metal	(0/0/0/M)	0.191	5	0.02
FML	UD-metal	(0/0/0/0/M)	0.211	4	0.02
FML	UD-metal	(0/0/0/0/0/M)	0.231	3	0.02

r_s of the circular strut - or the width of the square strut, as appropriate - is adjusted. Following this procedure, the compression strength requirement is fulfilled in all cases and and the safety factor for compression strength increases with increasing k.

In the following, global buckling and local buckling are calculated for the given geometry following the approaches as described in the previous subchapter. If both requirements are fulfilled, the strut weight is calculated and compared with the previous solution l of lowest weight. If the solution k is of less weight, than the solution is stored. The best solution for each repetitive stack type is stored in a database which covers all scenarios considered. A database of certain stored solutions is provided by the parameter study performed. One way to analyze the results is to compare the performance of the materials in different scenarios described by load case, strut length, cross section and differential temperature.

Examination method

Nine different materials are then compared one against another for each single scenario. These nine materials are shown in bold type in Table 3.3.

Following Table 3.3, one example scenario is defined by the following characteristics (where the additional number at the end marks the total number of possibilities):

- fiber type: HTS fibers are considered for CFRP and FML material (2)
- thickness steps: not normalized (as available on the market) (2)
- differential temperature: 0 K (2)
- strut length: 1 m (2)
- load: 1000 kN (3)
- cross section considered: circular (2).

This leads to 96 different scenarios.
The analyzed results for this example scenario consist of one solution for each of the nine materials with the lowest weight satisfying all the given requirements. The solution is clearly described by the wall thickness and the radius of the strut (or width in the case of a square cross section) for the three metals and the three pure CFRP stackings. In the case of the FML materials, the best solution additionally depends on MVF, therefore, this information is added to the results table. The resulting output including diagram and table for this solution is given in Figure 3.20. The table in each result shows the solution's label number, its individual lay-up, its weight, MVF, radius, wall thickness and cross section area.
When regarding circular struts, the geometry of each material is represented within a sector of the circular diagram, where an excerpt of the struts cross section is shown. Therefore, the inner and outer radii - as well as the wall thickness t_{lam} - are specified, as depicted in Figure 3.18.

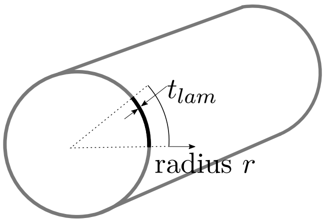

Figure 3.18: Dimensions of circular struts as depicted in diagrams

In the case of square cross sections, the results table is identical but the diagram shows the half width of the strut and its wall thickness t_{lam} instead. This relation is shown in Figure 3.19.

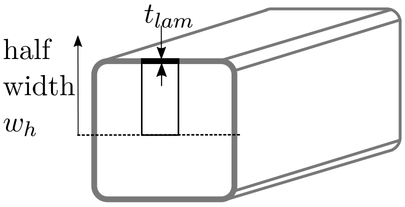

Figure 3.19: Dimensions of rectangular struts as depicted in diagrams

Examination of the results for circular cross sections

The results for the 96 different scenarios have been observed in detail and the most interesting relationships are presented in the following based on seven example scenarios with circular cross section.
The first example with HTS fiber, not normalized thickness (as available on the market) and without consideration of residual stresses is based on a 1 m long strut under 1000 kN axial loading and serves as a pivot example, to which all the following results are compared, see Figure 3.20.
The solutions with the lowest weight are achieved by a UD-CFRP-titanium laminate and the pure UD-CFRP laminate followed by the CFRP-HO and UD-CFRP-steel laminate. The pure steel strut fulfilling the requirements is nearly five times heavier. The CFRP-UD solution shows the lowest radius as it has the highest ratio between longitudinal and

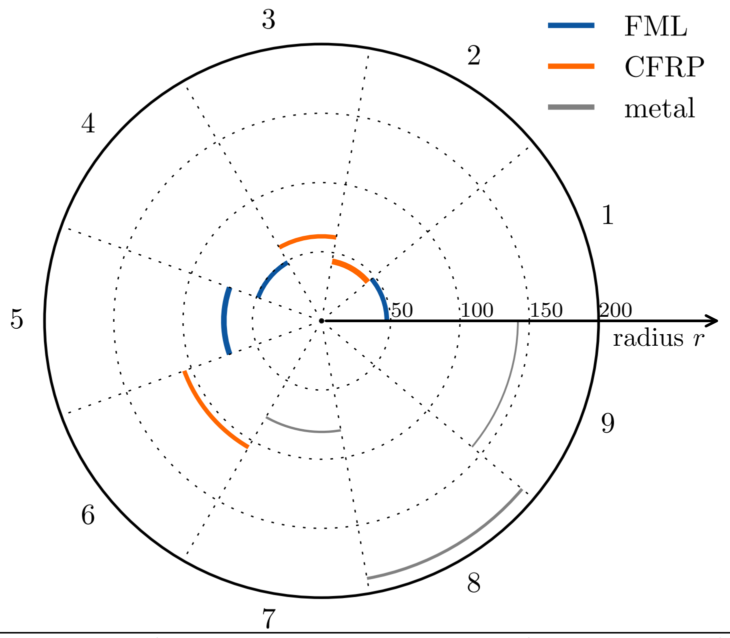

label	layup	weight [g]	MVF [%]	radius [mm]	thickness [mm]	area [mm^2]
1	0/0/Ti	1819.5	7.1	48.8	3.38	1001.8
2	0	1826.8	0.0	45.7	4.19	1148.9
3	45/-45/0/0/0/0/90/0	1919.8	0.0	62.7	3.14	1207.4
4	0/0/0/St	1920.6	4.8	50.5	3.30	1013.2
5	0/0/0/0/0/Al	2921.3	3.0	72.6	4.05	1796.5
6	45/-45/0/90	3313.4	0.0	107.1	3.14	2083.9
7	Ti	4099.1	100.0	81.1	1.70	857.5
8	Al	7174.5	100.0	190.1	2.15	2553.2
9	St	9031.6	100.0	142.4	1.30	1157.9

Figure 3.20: Results chart for HTS fiber, not normalized thickness of 1 m long circular strut under 1000 kN load without residual stress consideration

transverse stiffness of all the materials considered. Due to the low transverse stiffness, a relatively small radius is required to fulfill the local buckling requirement. With regard to global buckling, the high longitudinal stiffness enables the relatively small radius. The aluminum strut represents the solution with the largest radius. It has the lowest longitudinal stiffness in comparison and, therefore, requires a large radius. Local buckling is prevented by a comparatively large wall thickness. Comparing CFRP-QI and CFRP-HO, the QI-laminate shows a larger radius than the HO-laminate at identical wall thickness. This is a consequence of the lower ratio between longitudinal and transverse stiffness. The thickness of UD-CFRP-steel and CFRP-HO is in the same range but, due to the higher longitudinal stiffness and strength of the UD-CFRP-steel, a smaller radius and cross section area is achievable. However, its higher density compensates this relationship and the weight of both solutions is nearly equal.

The second figure shows the results for 100 kN loading instead of the 1000 kN, as depicted in Figure 3.21. First of all, it is noticeable that the weight of the aluminum and the steel strut is exactly one tenth the weight of the pivot example. The reason for this linear relationship is that the compression strength is the crucial parameter in both load cases.

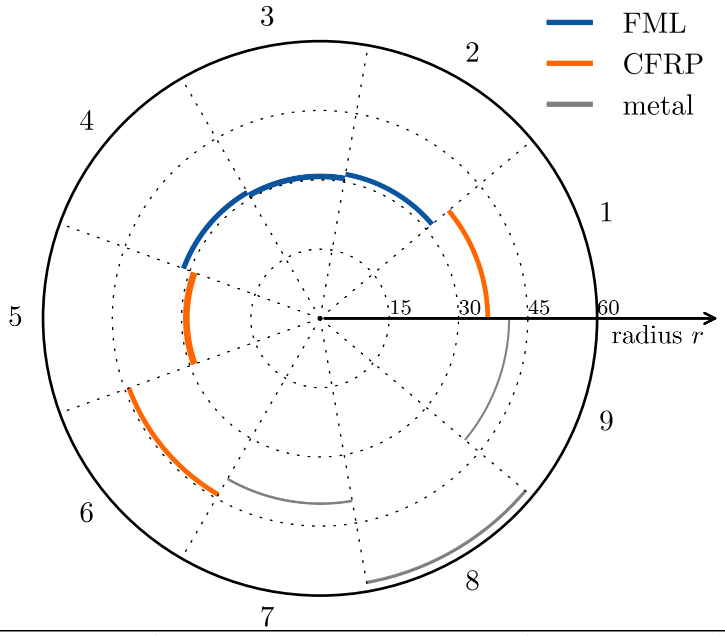

label	layup	weight [g]	MVF [%]	radius [mm]	thickness [mm]	area [mm^2]
1	45/-45/0/0/0/0/90/0	380.3	0.0	36.8	1.05	239.2
2	0/0/0/0/St	394.4	3.7	32.2	1.09	216.5
3	0/0/0/Al	394.7	4.8	31.4	1.24	239.3
4	0/0/Ti	405.2	7.1	32.0	1.13	223.1
5	0	417.2	0.0	29.7	1.44	262.4
6	45/-45/0/90	461.4	0.0	44.6	1.05	290.2
7	Ti	662.7	100.0	40.4	0.55	138.6
8	Al	717.4	100.0	58.4	0.70	255.3
9	St	903.2	100.0	41.2	0.45	115.8

Figure 3.21: Results chart for HTS fiber, not normalized thickness of 1 m long circular strut under 100 kN load without residual stress consideration. Please note the scale change compared to Figure 3.20

Buckling is at least one crucial parameter for all the other materials in the 100 kN example and, therefore, the weight saving is not as high for these materials compared to the pivot example.

Considering the suitability of the different materials for this load case it can be seen that the CFRP-HO solution reaches the lowest weight followed by the UD-CFRP metal solutions. Again the CFRP-UD material shows the lowest radius due to its stiffness ratio. However, it does not show any weight advantage when compared to CFRP-HO. Although the CFRP-HO lay-up is restricted by a comparatively large minimum lay-up thickness, it achieves the lowest weight, showing a slight advantage over UD-CFRP-steel and a 17% weight advantage over the quasi-isotropic CFRP laminate.

Figure 3.22 shows the results chart for a 2 m long strut under 1000 kN load. When comparing to the pivot example (Figure 3.20), the first conspicuous result is that the pure aluminum solution, the pure steel solution, the CFRP-QI and the UD-CFRP-Al solution all show exactly twice the weight for the longer strut. Again, the reason is that compression strength is at least one crucial parameter for both materials in both load

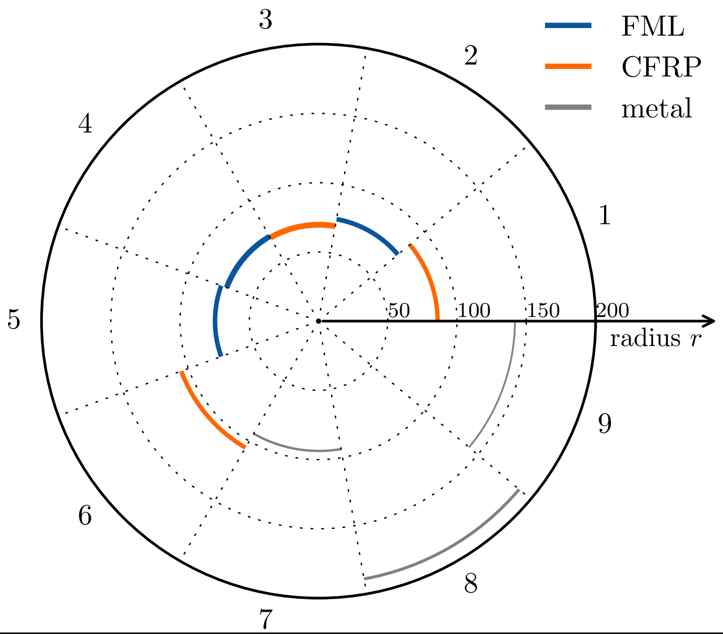

label	layup	weight [g]	MVF [%]	radius [mm]	thickness [mm]	area [mm^2]
1	45/-45/0/0/0/0/90/0	5400.1	0.0	87.5	3.14	1698.1
2	0/0/Ti	5772.1	7.1	76.4	3.38	1589.0
3	0	5830.2	0.0	71.7	4.19	1833.4
4	0/0/0/0/0/Al	5842.7	3.0	72.6	4.05	1796.5
5	0/0/0/St	5886.8	4.8	76.5	3.30	1552.8
6	45/-45/0/90	6626.8	0.0	107.1	3.14	2083.9
7	Ti	9576.8	100.0	94.6	1.70	1001.8
8	Al	14348.9	100.0	190.1	2.15	2553.2
9	St	18063.2	100.0	142.4	1.30	1157.9

Figure 3.22: Results chart for HTS fiber, not normalized thickness of 2 m long circular strut under 1000 kN load without residual stress consideration

cases. This means that the strut length is doubled whereas the area of the cross section is identical. The weight for all other material is more than doubled as the buckling load is one crucial parameter and it does not show a linear relationship. Again, the UD solution shows the smallest radius and the pure steel solution the smallest wall thickness. Compared to the shorter strut length, the advantage of CFRP-HO over CFRP-UD is smaller as global buckling is more crucial for the more slender struts. In this case the higher ratio of longitudinal to transverse stiffness is beneficial for the unidirectional material.

The next chart, Figure 3.23, shows the different solutions for a 1 m long strut under 1000 kN load when the layer thickness is normalized. This means that the materials with a higher repetitive thickness are not disadvantaged compared to the ones with a lower thickness. This comparison is based on a very ideal assumption as the repetitive thickness of a layered material will always be more restricted in reality. However, when comparing with the pivot example (Figure 3.20), it can be seen that the cross sections and the geometry of the pure metal solutions do not change as their thickness was not restricted before. The solutions based on pure CFRP and UD-CFRP-Al show the same weight as in the pivot example as the cross section area is identical. However, as other thickness

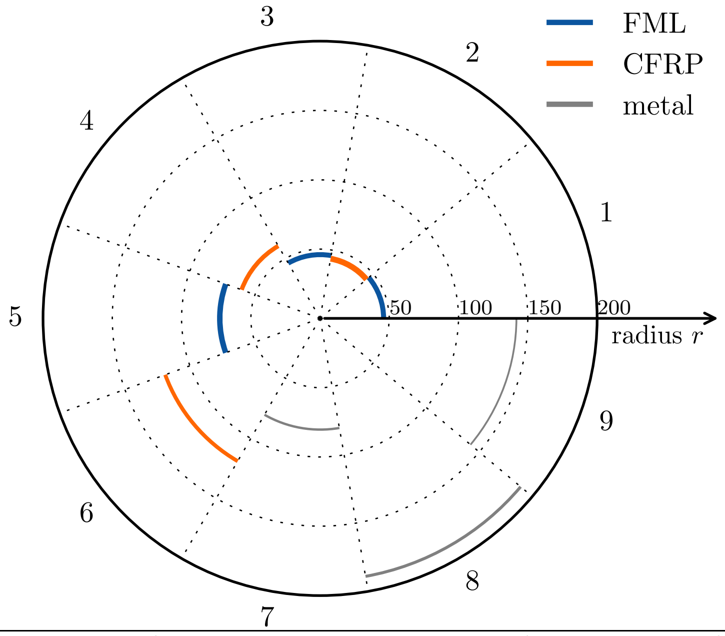

label	layup	weight [g]	MVF [%]	radius [mm]	thickness [mm]	area [mm^2]
1	0/0/0/Ti	1819.1	4.8	47.7	3.62	1042.8
2	0	1826.8	0.0	45.8	4.18	1148.9
3	0/0/0/0/0/St	1847.2	3.0	47.8	3.60	1039.5
4	45/-45/0/0/0/0/90/0	1919.8	0.0	61.9	3.19	1207.4
5	0/0/0/0/0/Al	2921.3	3.0	74.4	3.95	1796.5
6	45/-45/0/90	3313.4	0.0	120.4	2.79	2083.9
7	Ti	4099.1	100.0	81.1	1.70	857.5
8	Al	7174.5	100.0	190.1	2.15	2553.2
9	St	9031.6	100.0	142.4	1.30	1157.9

Figure 3.23: Results chart for HTS fiber, normalized thickness of 1 m long circular strut under 1000 kN load without residual stress consideration

values are possible, the radius and thickness values do change. For UD-CFRP-Ti and UD-CFRP-St, the lay-ups change as solutions with lower MVFs become more attractive. Their repetitive thickness is higher when not normalized, but in the normalized case their lower density compensates their lower strength and solutions with larger cross sections are preferred. The UD-CFRP-Ti solution shows a slight weight benefit compared to CFRP-UD and UD-CFRP-St. The latter still shows a weight benefit of around 4% against the CFRP-HO material.

The changed parameter for the chart in Figure 3.24 compared to the pivot chart in Figure 3.20 is the fiber type. IM fibers with higher stiffness and strength compared to the HTS fibers are investigated. A comparison of these properties can be found in Table 3.2. As a consequence, the pure metal solutions are not affected. When comparing the pure CFRP lay-ups, a weight saving of 7% and 9% can be achieved for QI and UD lay-ups respectively when utilizing IM fibers. The reduction of the cross section area is achieved by lower radii. Additionally, the CFRP-HO solution achieves a lower weight than its UD counterpart. By changing the fiber type, their order changes. The stiffer fiber leads to a weight benefit of 15% for the CFRP-HO laminate and even 10% for the UD-CFRP-St laminate.

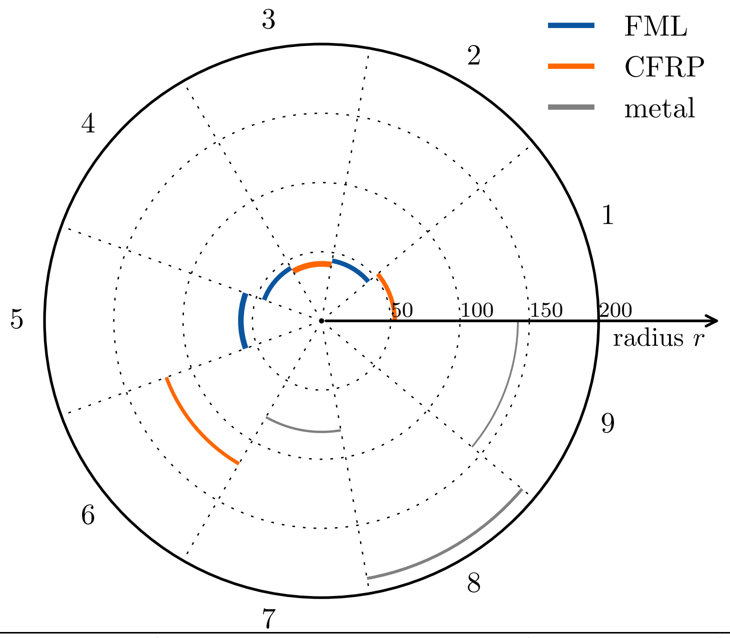

label	layup	weight [g]	MVF [%]	radius [mm]	thickness [mm]	area [mm^2]
1	45/-45/0/0/0/0/90/0	1638.7	0.0	54.4	3.14	1043.8
2	0/0/Ti	1685.4	7.1	45.8	3.38	937.6
3	0	1704.2	0.0	43.3	4.19	1085.5
4	0/0/0/St	1720.0	4.8	45.8	3.30	916.6
5	0/0/0/0/0/Al	2383.7	3.0	60.3	4.05	1483.6
6	45/-45/0/90	3082.3	0.0	120.6	2.62	1963.2
7	Ti	4099.1	100.0	81.1	1.70	857.5
8	Al	7174.5	100.0	190.1	2.15	2553.2
9	St	9031.6	100.0	142.4	1.30	1157.9

Figure 3.24: Results chart for IM fiber, not normalized thickness of 1 m long circular strut under 1000 kN load without residual stress consideration

In the next example the load is increased to 10.000 kN for the solutions in the chart in Figure 3.25 compared to 1000 kN in the pivot example. The cross section area and the weight, respectively, are linearly increased along with the load for the five heaviest solutions: pure steel, aluminum, titanium, CFRP-QI and UD-CFRP-Al. Again, the reason is that compression strength is one of the crucial parameters for both load cases for these materials. For the other materials, the wall thickness has increased by a higher factor than the radius of the strut. In the case of these more thicker-walled struts, the CFRP-UD material shows a comparatively large weight benefit of 18% compared to the UD-CFRP-titanium solution. The weight benefit of UD-CFRP-steel material compared to CFRP-HO is comparatively small with 5%. And again, UD-CFRP shows the smallest radius but - in this case - with a comparatively high wall thickness. The high ratio between longitudinal and transverse stiffness of the UD-material suits this load case the best.

The last example for the circular struts in Figure 3.26 additionally considers the residual stresses between the laminate's constituents acting in the longitudinal direction and influencing the compressive strength. Accordingly, pure CFRP and pure metal solutions are not affected. As the residual stresses induce a higher compression strength in the FML,

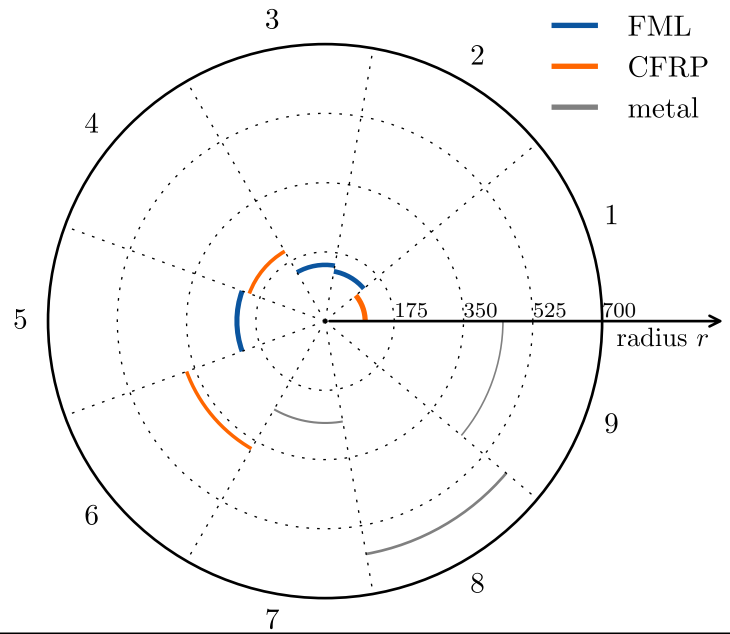

label	layup	weight [g]	MVF [%]	radius [mm]	thickness [mm]	area [mm^2]
1	0	13389.3	0.0	107.9	13.23	8421.0
2	0/0/0/0/0/Ti	16415.4	3.0	133.7	12.15	9744.9
3	0/0/0/0/0/St	18216.6	3.0	147.9	11.47	10251.5
4	45/-45/0/0/0/0/90/0	19198.1	0.0	208.5	9.43	12074.3
5	0/0/0/0/0/Al	29213.4	3.0	229.4	12.82	17964.8
6	45/-45/0/90	33133.8	0.0	376.8	8.91	20838.9
7	Ti	40990.8	100.0	260.2	5.30	8575.5
8	Al	71744.7	100.0	601.0	6.80	25531.9
9	St	90315.8	100.0	451.5	4.10	11578.9

Figure 3.25: Results chart for HTS fiber, not normalized thickness of 1 m long circular strut under 10.000 kN load without residual stress consideration. Please note the scale change compared to Figure 3.20

see section 3.4, a weight benefit can be achieved for the compressive load case considered. The weight benefit increases with increasing residual stress: UD-CFRP-Ti (0.2% weight benefit), UD-CFRP-St (4% weight benefit), UD-CFRP-Al (37% weight benefit). However, it must be considered that this relationship leads to a weight penalty for any tension load case. The benefit of UD-CFRP-St against UD-CFRP-Al is negligible in this case. Accordingly, there is a weight benefit of UD-CFRP-St over CFRP-HO of 4% when considering the residual stresses acting in the FML.

Examination of the results for square cross sections

The results of 96 different scenarios have also been observed for the square struts. As the findings for variation of fiber type and residual stress are comparable to the findings described for the circular struts, they are not discussed again. Hence, four different scenarios are discussed in the following.

In accord with the examination carried out on the circular struts, the pivot example for

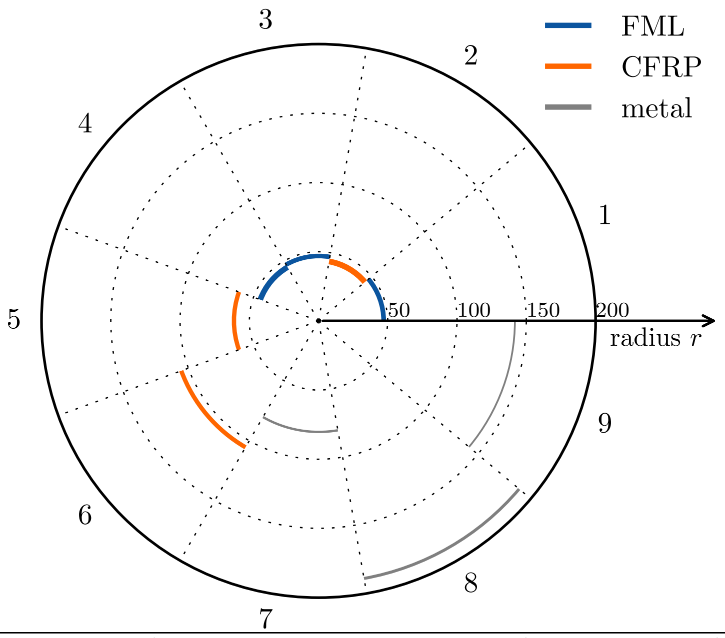

label	layup	weight [g]	MVF [%]	radius [mm]	thickness [mm]	area [mm^2]
1	0/0/Ti	1815.3	7.1	48.7	3.38	999.5
2	0	1826.8	0.0	45.7	4.19	1148.9
3	0/0/0/St	1845.5	4.8	48.5	3.30	973.6
4	0/0/0/0/0/Al	1853.5	3.0	46.8	4.05	1139.8
5	45/-45/0/0/0/0/90/0	1919.8	0.0	62.7	3.14	1207.4
6	45/-45/0/90	3313.4	0.0	107.1	3.14	2083.9
7	Ti	4099.1	100.0	81.1	1.70	857.5
8	Al	7174.5	100.0	190.1	2.15	2553.2
9	St	9031.6	100.0	142.4	1.30	1157.9

Figure 3.26: Results chart for HTS fiber, not normalized thickness of 1 m long circular strut under 1000 kN load with residual stress consideration

the square struts is a 1 m long strut with HTS fiber as reinforcement under a load of 1000 kN, see Figure 3.27. First of all, when compared to the circular strut (Figure 3.20), it is obvious that the weight of the UD-CFRP-Al, the CFRP-QI, pure aluminum and pure steel solutions are identical for square and circular cross sections. Again, the reason is compression strength being one crucial parameter. All other materials show a weight increase of 29 to 34%. The increase is lowest for CFRP-UD material (29%), the material with the highest ratio between longitudinal and transverse stiffness and highest for the pure titanium (34%), the material with the lowest ratio. Regardless, the fundamental relationships are comparable. The CFRP-HO solution shows a crucial weight benefit compared to CFRP-QI and the UD-CFRP-St and UD-CFRP-Ti solutions show a benefit against CFRP-HO. The lowest weight is achieved by the CFRP-UD solution although its width is comparable to the FML solutions. Again, aluminum shows the largest width and steel the smallest wall thickness. The weight benefit of UD-CFRP-St against the CFRP-HO solution is 4%.

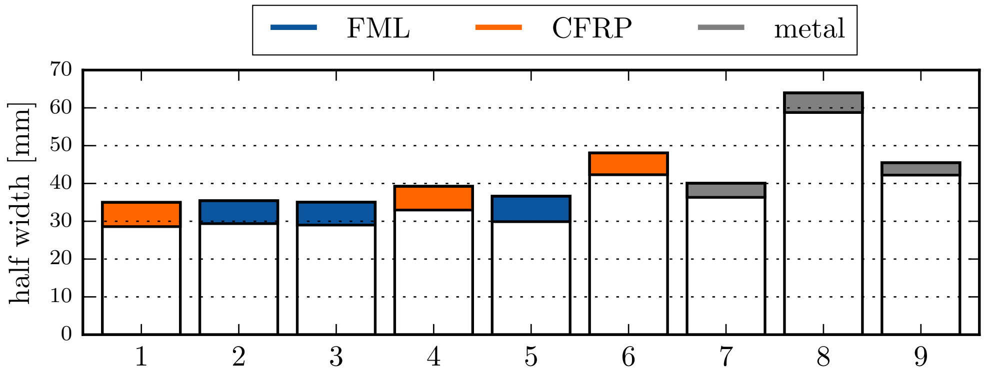

label	layup	weight [g]	MVF [%]	width [mm]	thickness [mm]	area [mm^2]
1	0	2596.1	0.0	70.0	6.42	1632.8
2	0/0/0/0/0/Ti	2653.7	3.0	70.9	6.08	1575.4
3	0/0/0/0/0/St	2766.2	3.0	70.1	6.08	1556.7
4	45/-45/0/0/0/0/90/0	2888.4	0.0	78.5	6.29	1816.6
5	0/0/0/0/0/Al	2921.3	3.0	73.3	6.75	1796.5
6	45/-45/0/90	3313.4	0.0	96.1	5.76	2083.9
7	Ti	5477.7	100.0	80.1	3.75	1146.0
8	Al	7174.5	100.0	127.9	5.20	2553.2
9	St	9031.6	100.0	91.0	3.30	1157.9

Figure 3.27: Results chart for HTS fiber, not normalized thickness of 1 m long square strut under 1000 kN load

The results of the second example, representing a 2 m long strut, are depicted in the results chart in Figure 3.28. As buckling is crucial for all materials, the weight increase is more than doubled for all materials. It is the first example where pure aluminum achieves a weight benefit against titanium. In a departure from the previous examples, CFRP-HO shows a weight benefit compared to CFRP-St (3%) and CFRP-Ti (0.5%). CFRP-UD represents the solution with the lowest weight and the lowest width. The thickness values of the materials with the high ratios between longitudinal and transverse stiffness are comparatively high, as local buckling prohibits thinner walls when transverse stiffness is low.

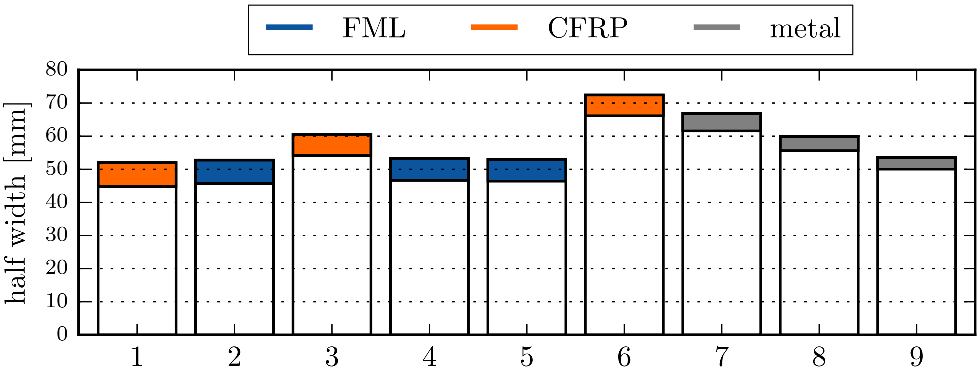

label	layup	weight [g]	MVF [%]	width [mm]	thickness [mm]	area [mm^2]
1	0	8869.9	0.0	104.0	7.21	2789.3
2	0/0/0/0/Al	9109.8	3.7	105.6	7.07	2786.1
3	45/-45/0/0/0/0/90/0	9166.6	0.0	120.9	6.29	2882.6
4	0/0/0/Ti	9212.8	4.8	106.5	6.61	2640.6
5	0/0/0/0/St	9452.0	3.7	105.9	6.53	2593.9
6	45/-45/0/90	11084.4	0.0	144.9	6.29	3485.7
7	Al	15153.3	100.0	133.6	5.25	2696.3
8	Ti	18997.7	100.0	119.8	4.30	1987.2
9	St	22619.6	100.0	107.1	3.50	1450.0

Figure 3.28: Results chart for HTS fiber, not normalized thickness of 2 m long square strut under 1000 kN load. Please note the scale change compared to Figure 3.27

The third chart shows the results for a lower load of 100 kN, as shown in Figure 3.29. When comparing with the pivot example, Figure 3.27, it can be seen that the weight is not reduced to a tenth for any of the materials. For this load case, local buckling is one crucial parameter for all the materials. Again, pure aluminum shows a weight benefit compared to titanium and CFRP-UD represents the solution with the lowest weight. The lowest width is achieved for UD-CFRP-St, which also achieves a benefit against CFRP-HO of 11%.

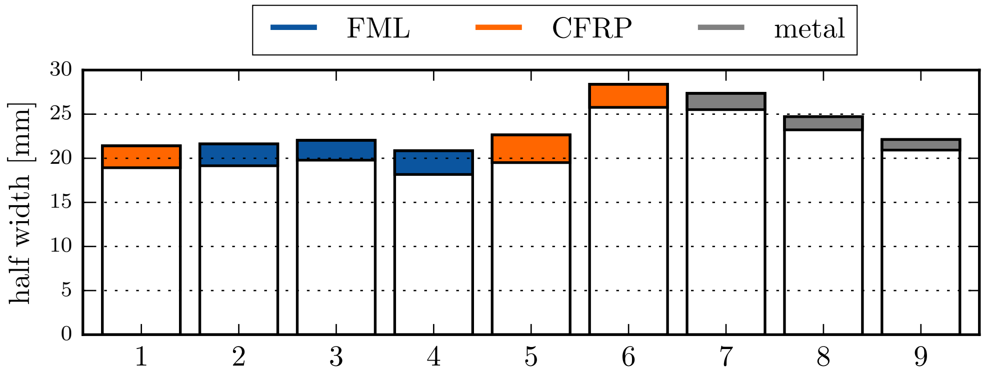

label	layup	weight [g]	MVF [%]	width [mm]	thickness [mm]	area [mm^2]
1	0	638.6	0.0	42.8	2.49	401.7
2	0/0/0/Al	666.5	4.8	43.3	2.48	404.2
3	0/0/Ti	685.5	7.1	44.1	2.26	377.4
4	0/0/0/0/0/St	748.9	3.0	41.7	2.70	421.5
5	45/-45/0/0/0/0/90/0	843.1	0.0	45.3	3.14	530.2
6	45/-45/0/90	902.5	0.0	56.8	2.62	567.6
7	Al	1099.5	100.0	54.7	1.85	391.3
8	Ti	1375.0	100.0	49.4	1.50	287.7
9	St	1611.9	100.0	44.3	1.20	206.7

Figure 3.29: Results chart for HTS fiber, not normalized thickness of 1 m long square strut under 100 kN load. Please note the scale change compared to Figure 3.27

In the last example, Figure 3.30, the load is increased to 10,000 kN compared to the pivot example. In this case, compression strength is one crucial parameter for steel, aluminum, titanium, CFRP-QI and UD-CFRP-Al. And again, CFRP-UD shows the lowest weight with the lowest width. The lowest wall thickness is achieved by the CFRP-HO and UD-CFRP-St material where the latter shows a weight benefit of 5% due to the lower width.

Discussion of results

Basically, the results show that the relative weight difference is low for longer struts and low loads whereas the factor between the results increases with higher loads. When comparing the suitability of the different materials for a certain scenario, this relationship must be kept in mind.

The results clearly demonstrate the weight benefit of all CFRP lay-ups over the three regarded metallic materials considered: titanium, aluminum and steel. For the circular struts, titanium shows an advantage over aluminum which again shows an advantage over steel. As expected, steel leads to slimmer solutions than aluminum. Due to the higher ratio between strength and stiffness of titanium compared to steel, the titanium solutions are even slimmer. The relationship is not that clear for the struts with square cross section. When the load is increased above a certain level, or the strut length is increased above a certain length, then the width of the titanium strut is larger than that of the steel strut.

The results also clearly demonstrate the theoretical weight benefit of CFRP-UD over

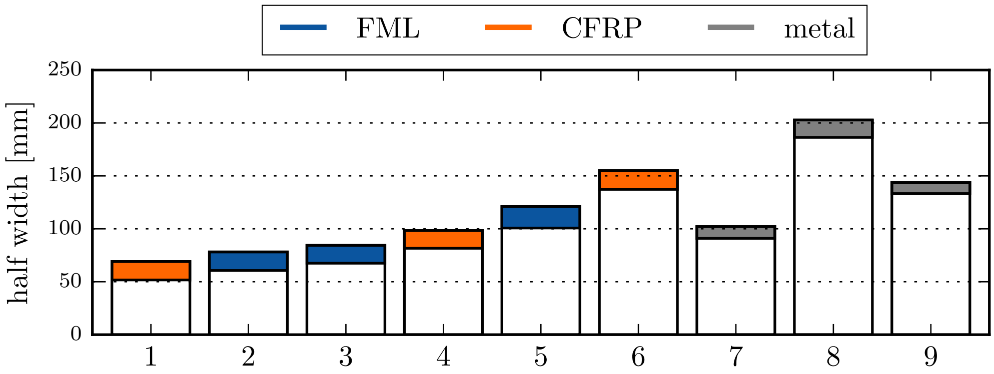

label	layup	weight [g]	MVF [%]	width [mm]	thickness [mm]	area [mm^2]
1	0	13389.3	0.0	138.3	17.42	8421.0
2	0/0/0/0/0/Ti	16415.4	3.0	156.4	17.55	9744.9
3	0/0/0/0/0/St	18216.6	3.0	168.7	16.88	10251.5
4	45/-45/0/0/0/0/90/0	19198.1	0.0	196.8	16.77	12074.3
5	0/0/0/0/0/Al	29213.4	3.0	242.0	20.25	17964.8
6	45/-45/0/90	33133.8	0.0	310.2	17.82	20838.9
7	Ti	40990.8	100.0	204.2	11.10	8575.5
8	Al	71744.7	100.0	405.6	16.40	25531.9
9	St	90315.8	100.0	287.5	10.45	11578.9

Figure 3.30: Results chart for HTS fiber, not normalized thickness of 1 m long square strut under 10.000 kN load. Please note the scale change compared to Figure 3.27

CFRP-HO, which again shows a benefit over CFRP-QI for circular struts as well as for struts with square cross sections. As expected, the solutions utilizing IM fibers achieve a weight benefit over the solutions based on HTS. However, these benefits are small compared to the benefit of fiber orientation.

The influence of the layer thickness restrictions is considered by comparing a solution with a repetitive layer-thickness based on material available on the market and a solution with a repetitive thickness normalized to 0.05 mm. This relationship does not prove that part of the weight benefit of FML against pure CFRP is a consequence of the more restricted lay-up when using pure CFRP. For the case considered, the thickness restriction of pure CFRP was compensated by a different geometry leading to identical weight. Due to the assumptions in the previous chapter, the UD-CFRP-steel laminate is of primary interest. In comparison with the most important reference, the CFRP-HO laminate, the results for FMLs differ from 8% weight increase to 4% weight decrease for the circular strut scenarios considered. The relationship for square struts is also not very clear, as the UD-CFRP-St solutions are up to 5% lighter than CFRP-HO in some scenarios and up to 4% heavier in other scenarios.

The advantages of FML compared to CFRP-UD would diminish for a tensile load case. However, when transverse stiffness is not relevant, the advantages of FML compared to CFRP-HO would also increase. The bending load case of a strut could also be an interesting case for the comparison of the materials.

3.7 Discussion of hypotheses addressed

As discussed at the beginning, this chapter aims to refer to the first two hypotheses.

Hypothesis 1:
The relationship between metal volume fraction and weight-specific elastic modulus and strength has been illustrated for different material combinations based on a bilinear one-dimensional model. It was then analytically substantiated that the MVF φ_M needs to be lower than 12.3% to achieve a higher weight-specific modulus than a reference CFRP laminate (62.5/25/12.5) in a single predominant direction. Additionally, a parameter study on strut geometry has been performed, where longitudinal and transverse stiffness of the laminate are relevant, as local buckling is considered. The favourable MVFs for the UD-CFRP-steel material are between 3.0 and 4.8% for the scenarios considered. Hence, it could be proved that low steel fractions are required to increase weight-specific stiffness and strength.

Hypothesis 2:
The consideration of damage tolerance in today's aircraft composites has been discussed and presented on a novel 3-D perspective based on a three-dimensional representation of crucial parameters. However, as damage tolerance is mainly assessed by experiment, an alternative approach was chosen to consider the material's exploitation under damage tolerance requirements. Common stacking rules are applied to generate a reference laminate which represents a reasonable compromise between mechanical performance and damage tolerance requirements and is often utilized in aerospace applications. The exploitation of this reference called CFRP-HO and the unidirectional, as well as the quasi-isotropic alternatives, are then discussed. Additionally, a more realistic application on a circular and a square strut under uniaxial loading in different scenarios is then regarded in a parameter study. The results underline that the material's exploitation is lowered, which means that the weight of a strut made from CFRP-HO, fulfilling the mechanical requirements, is increased in comparison with a solution made of CFRP-UD material in most cases. CFRP-HO shows a weight benefit compared to the quasi-isotropic laminate in all the cases considered.
However, to clearly prove a weight benefit, the damage tolerance of both materials must be compared. Therefore, it is advisable to prove that the CAI-strength of UD-CFRP-steel is relatively, or at least absolutely, higher than the CAI-strength of the CFRP-HO reference. Further discussion on this hypothesis can be found in chapter 6.

4 Constituent interfaces

Link to hypothesis: Hypothesis 3 is addressed in this chapter by measuring the interlaminar shear stress for different surface treatments applied to the metal foil.

Summary: A Fiber-Metal-Laminate consists of multiple alternating layers of metal and fiber reinforced plastic. This results in multiple interfaces between the inorganic and organic materials. Existing studies reveal that debonding of the CFRP from the steel substrate is one of the main failure modes in CFRP-strengthened steel structures [43], which underlines the importance of the bonding between the different constituents. Although very little attention has been paid in the past to the bond and durability behavior between fiber-reinforced composites and steel structures [44], the number of adhesive bonding applications in various industries is steadily growing [45], providing promising improvements for all relevant fields of this technology.

This chapter summarizes the findings in research with regard to surface treatment of steel and the characterization of the surface. Then test methods to evaluate the interphase between both constituents are presented, the most suitable method is selected and discussed in detail. In so doing the method is adapted to the specifics of FMLs. The most convenient geometry and lay-up is then deduced in order to reduce to a minimum any undesired influence of the method itself on the results.

Based on the literature findings, the most promising surface treatment methods are selected, their essential parameters are systematically varied and specimens are manufactured to determine the interlaminar shear strength (ILSS) of the respective interface. Based on results and practicability, one method is selected and its essential parameters are regarded in more detail. Finally, the suitability of the selected test method and treatment method are discussed, as the latter defines the method applied in the manufacturing of the specimens considered in the following chapters.

4.1 Literature review

As defined in the objectives at the beginning of the present work, the main aims are to increase weight-specific stiffness and strength, suspending any additional materials which do not contribute to the overall stiffness and strength of the laminate. Basically, nonlinear elastic adhesives with low elastic modulus and larger strain capacity lead to much higher interfacial fracture energy than linear elastic adhesives with similar or even higher strength [43]. Therefore, the use of an additional adhesive at the interface between composite and metal layer with a lower elastic modulus and larger failure strain than the reinforced epoxy of the composite would be promising. Curing an additional adhesive at a lower temperature, as enabled by the use of a film adhesive, would also lower the residual thermal stresses if the laminate consisted of previously cured plies.

Although epoxies also show relatively low peel strength and their bond strength is sensitive to moisture and surface contamination [45], the composite layer itself is used for adhesive bonding between composite and metal layer resulting in a co-cure fabrication. This constraint is based on the aforementioned objectives as an adhesive on each side would result in a significant increase in weight per metal layer and manufacturing complexity.

As no additional adhesive is used to bond the laminate's constituents, the effective adherents are the fibers and metal layers bonded by the epoxy resin. However, regarding a homogeneous composite layer and the metal sheet, the bond can also be recognized as a bonding between a composite and metal sheet (see Figure 4.1). The resulting bond is a glassy polymer/non-polymer adhesion and therefore, interdigitation of the polymer chains is not possible. As a consequence, the surface of the solid material determines the topology of the interface. The interaction between the interface and the bulk material also affects the bulk material properties. For example, when reactive groups of a polymer bond to the oxides of a metal surface, these groups cannot contribute to the polymer generation and a weak boundary layer is created within the polymer layer [46]. As a consequence, the mechanical performance of the laminated material is essentially influenced not only by this interface but also by the composition of the entire transition zone. Therefore, a wider definition of the interface is used in this work: the interphase.

The interphase is characterized by the near-surface region of both constituents influenced by interaction between bulk material and interface or by determined surface and heat treatments to increase bonding strength, see Figure 4.1. This interphase is not only responsible for the mechanical properties of the laminate, it also accounts for the chemical or galvanic compatibility of the laminate constituents.

Bonding types and bonding strength

When investigating an adhesive and an adherent which have neither chemical nor specific interactions, the necessary energy to break the acting van der Waals bonds can be predicted by thermodynamic equations. It is well known that the measured adhesion energy in tests is usually several orders of magnitude higher. Therefore, additionally to this adhesion theory, there must be other mechanisms present in an adhesively bonded joint. Phenomena associated with adhesive bonding can be divided into the following bonding types. *Physical bonding* describes weak forces like secondary or van der Waals forces, dipolar interactions and hydrogen bonding. It can be further subdivided in the *absorption theory* and the *electrostatic attraction theory*. The *absorption theory* explains that an adhesive must wet the adherent surface to achieve a successful bond. The electrostatic attraction theory covers acid-base interactions and ionic bonds as a result of electrostatic interaction between a surface carrying net positive and a surface carrying net negative charges. A chemical bond is formed between compatible chemical groups of adhesive and adherent surfaces. Solid solutions and compound formation result in a reaction zone at the adherent surface created by atomic or molecular diffusional transport [47]. This encompasses all types of covalent, ionic and metallic bonding. Transferring these bonding energies to adhesion strength, it can be concluded that a chemical bond must be present in a fair adhesive bonding. However, their limited range may induce weak layers in the

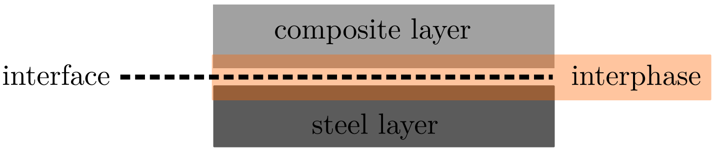

Figure 4.1: Definition of the steel-composite interface and interphase

adhesive and therefore the bonding energy of a chemical bond is not characteristic for the overall bonding strength [48]. Mechanical bonding or mechanical interlocking depends on the ability of the liquid adhesive to penetrate between crevices and pores before it solidifies and the topology of the crevices and pores, meaning the surface roughness. However, for metallic bonds with smooth or only slightly roughened surfaces the contribution of mechanical interlocking to the overall bonding strength is low [48]. Considering the interface between the composite and the metal sheet, only the metal surface is existent as a solid before curing.

Therefore, a surface treatment to increase adhesion between the two constituents is only possible on the metal side of the interphase. As the efficiency of a treatment depends on the original substrate and the depth of the surface treatment, there is often a compromise between the functionalization of the surface and the degradation of the bulk material.

Steel surface characterization

A metal surface is generally characterized by three main properties [49–51]: surface energy, surface chemical composition and surface roughness or topography. All these three properties significantly affect the adhesion strength [52]. Surface energy and adhesion are a complex interaction between surface roughness and chemical composition. However, for a selective adjustment of these properties by a surface pre-treatment, it is essential to know the original surface state of the raw part. The condition of the raw part's surface and the condition of the pre-treated surface vary over time (mainly by oxidation) influenced by the environment. Both mechanisms are dependent on the steel type. The chemical composition of the selected material 1.4310 is given in Table 4.1.

The surface state of the raw part is mainly influenced by its last manufacturing step. The outermost layer (>1 μm) may be contaminated by foreign substances, the next layer (1 nm <t<10 nm) is formed by sorption of carbon and oxygen which influence surface energy. The reaction layer underneath is characterized by the forming of oxides and exhibits a thickness of $1 - 7$ nm [54, 55], altering slowly [56].

The oxidation of metal surfaces is usually broken down into different steps: oxygen adsorption on the surface, initial fast oxidation with oxide nucleation and growth, and finally: oxide film formation and growth [57]. In the presence of oxygen the native protective oxide layer of a few nm on stainless steel forms spontaneously within minutes [56, 58–63]. After storage at room temperature, its thickness typically reaches the aforementioned 1 - 7 nm. The thickness of the layer is independent of temperature for temperatures below 200 °C. Mobility of ions and atoms is insignificant at these temperatures and thus, the growth of the oxide film stops [64]. At higher temperatures, thermal diffusion and therefore oxide layer thickness increase [55]. The oxide layer on the surface of stainless steel exhibits a complex multi-layer structure of hematite Fe_2O_3, magnetite Fe_3O_4, wustite FeO and chromium oxide Cr_2O_3 [65]. All of these oxide layers are able to bind water [59]. Oxide layers formed on stainless steel surfaces at room temperature are chromium-rich on the

Table 4.1: Chemical composition of 1.4310 (X10CrNi18-10 or AISI 301) [53]

C	Cr	Ni	Si	Mn	P	S	Mo	N
0.05 -0.15	16 -19	6.0 -9.5	$\leq$ 2.0	$\leq$ 2.0	$\leq$ 0.045	$\leq$ 0.015	$\leq$ 0.8	$\leq$ 0.11

bulk material/oxide interface and are usually iron-rich in the outermost surface [66]. At temperatures above 700°C, this relationship switches and a chromium-depleted layer is present on the bulk material/oxide interface [54, 60, 67, 68]. The thickness of this layer formed at higher temperatures may also increase to 100 – 1000 nm.

The surface oxides may also be modified by water adsorption as it is always present in an atmospheric environment. This results in hydroxyl species (OH^-) [69, 70]. Regarding the silane post-treatment which is applied in the following experiments, these hydroxyl species are favourable as they ensure good bonding to the metal surface.

The adjacent area is not influenced by any chemical transaction with the environment and may also differ from the bulk material as a consequence of deformation [71, 72]. Forces acting on the surface during manufacturing alter the microstructure of a layer with a thickness exceeding 1 μm. Bonding forces between these layers increase in strength from the surface in the direction of the bulk material and demand higher energy for removal [56].

The aim of the pre-treatment is to allow the adherent to be in contact with the entire surface. This requires a thorough wetting of the surface, for which high surface energy is required for preference [73]. Generally, the surface energy is influenced by its chemical composition and its surface roughness or topography [74, 75]. The wetting test, whereby the contact angle of a given liquid on the surface is measured or where is determined whether it 'wets out', provides a serviceable quality control but does not give any information about the bonding strength. This illustrates that a low contact angle is a necessary but not a sufficient condition for a good bond. The measurement of the surface roughness is another parameter, providing information about the quality or homogeneity of any treatment but not guaranteeing good bonding strength.

In general, an increase in roughness leads to stronger mechanical bonding while an increase in surface energy enhances the wettability and enables a good bond. However, *Hitchcock et al.* showed that an increase in roughness above a certain value may restrict the spreading of adhesive and decrease bonding capability [74].

Treatments

The surface treatment process consists of a surface pre- and post-treatment. There are two common surface treatments for stainless steel in the aerospace industry, the grit-blast and silane process (GBS) and the Boeing sol-gel Process (BSP). The GBS involves surface degreasing, abrasive removal of weakly adhered layers, grit-blasting and application of an epoxy-silane coupling agent [76]. Following the BSP, the material is degreased and then deoxidized using a wet or dry grit-blasting method. Finally, an aqueous sol-gel system, a dilute solution of a stabilized alkoxyzirconium organometallic salt and an organosilane coupling agent, is applied. Typically, an adhesive coating is then applied to the treated surface to generate a durable bond [77].

Both treatment processes utilize a mechanical pre-treatment. However, there are other pre-treatment processes providing deoxidization. The pre-treatments are basically classified into [48]:

- mechanical
- chemical
- physical
- photochemical
- electrochemical

- thermal
- and plasma treatments

The most common methods for steel surface pre-treatment include solvent cleaning and mechanical cleaning using grit blasting or other abrasive tools such as sand paper, wire brushes or abrasive pads [49, 51, 73, 78, 79]. Solvent cleaning does not change the surface properties but removes any contaminants. The mechanical abrasion aims to roughen the surface and remove weak and chemically inactive layers [51, 73]. Among the methods enumerated, grit blasting appears to be the most effective [80] and has a clearly visible measure of effectiveness [81].

Pickling has produced similar results to abrasion and grit blasting for thermoset composites [45]. A number of acid mixtures have been investigated including nitric-hydrofluoric acid and sulphuric acid [47,82,83]. These treatments give adequate dry strength but durability is reported to by quite poor [73, 84].

Plasma treatment uses an electrically conductive low-pressure plasma gas consisting of excited atoms, ions and free radicals. The plasma particles react with each other and with the surface leading to cleaning, removal of material or formation of radicals on the latter [85]. Bond strength equivalent to the best chemical treatments was obtained by plasma treatment on titanium [86].

Laser treatment is mainly used for the treatment of polymer surfaces. However, it has also been utilized successfully on aluminum and titanium surfaces. Durable bonds were achieved with the patented Ciba laser pretreatment (CLP) for aluminum but also for stainless steel [87]. Laser treatment stands out for being environmentally friendly as in the pre-treatment of titanium it replaces chemical and electrochemical processes containing hazardous chemicals such as chromates.

The substitution of chemicals containing chromate was also a major driver in the development of sol-gel coatings, mainly based on silane or zirconium, as well [76, 77, 88–95]. There are two major objectives for the sol-gel treatment of metal surfaces: to provide good adhesion to organic coatings or adhesives and to increase corrosion resistance. The majority of the processes include hydrolysis and condensation reactions of metal alkoxides of zirconium, cerium, tin or aluminum [93]. These metal alkoxides are in solution with water, alcohol or another solvent. The process starts with the mixing of the components and the evolution of a colloidal system through the formation of a sol. The next step is its gelation to form a continuous polymer network the progress of which is affected by the solvent as it evaporates. Therefore, spraying and dipping are used for application of the liquid. In the latter, the solvent evaporates after dipping while the sol is draining off.

Finally, a primer may be applied to the substrate surface to protect the surface until bonding is carried out, to increase surface wettability, as a coupling agent or to prevent corrosion [73]. Epoxy based primers are mainly used to protect the surface prior to bonding and silane coupling agents are utilized to improve durability of adhesive bonds in the presence of water. However, some primers such as BR127 [96] still contain hazardous chromates [73].

Test methods for evaluation of adhesion performance

Mechanical properties of FMLs are governed by the adhesion between composite layer and metal layer. The adhesion can basically be evaluated by determining the interlaminar shear strength or by conducting interfacial fracture tests. Although these methods are suitable for comparison or quality control, they are not appropriate for design specifications [97].

Experiments on interlaminar shear strength can be done by compression loading, three and five-point bending as well as short beam shear loading. By applying a compression load on a double-notch shear (DNS) specimen as set out in ASTM D3846 a shear stress is induced in the bridging area in the center of the specimens [98]. The applied interlaminar shear stress is calculated based on the effective area of the shear plane [99]. *Lawcock et al.* calculated the ILSS of FML based on three and five-point bending tests using the following formula respectively [100–102]:

$$ILSS = (3P_{max}/4Wt) \tag{4.1}$$

$$ILSS = (33P_{max}/64Wt) \tag{4.2}$$

where P_{max} is the initial load for interlaminar failure and W and t are the width and thickness of the specimens. The third type of testing ILSS is the short beam test method as per ASTM D2344 [103] and DIN EN ISO 14130 [104] which is described in more detail in chapter 4.3.

The second approach for the determining adhesion performance is the interfacial fracture. Using single cantilever beam geometry, mixed-mode I/II loading (tension/shear) is introduced at the crack tip [105–107]. The interfacial fracture energy G_c is calculated in the studies using the following formula:

$$G_c = (3P^2ka^2)/2w \tag{4.3}$$

where P is the applied load, k a constant experimentally determined with the compliance calibration method, a is the crack length and w is the specimen width [108].

When the materials permit the setting up of a specimen of a relatively flexible adherent and a rigid adherent then the climbing drum peel test is an alternative to determine the peel resistance of an adhesive bond. The test consists of a thin strip being peeled from the thicker strip by winding it around a drum and is defined in ASTM D1781 [109]. Torque is applied to the drum by pulling down additional straps which are wrapped around the drum on a larger radius.

4.2 Present chapter's structure

The flowchart in Figure 4.2 shows the steps applied in this chapter and their relationship to each other. A suitable test method for determining interlaminar shear strength is selected based on the Literature review in subchapter 4.3. The test method and its stress calculation are then adapted to the special requirements of FML. In the following, the residual stresses induced during manufacturing are regarded concerning their impact on the resulting shear strength of the specimens. Finally, the examination and analysis methods are defined as the basis for the subsequent subchapters. In subchapter 4.7 the different surface treatments are first examined in preliminary investigations whereby parameter combinations for the different treatment methods are selected based on available literature. The selection of vacuum blasting is justified here and the concept of the blasting process developed is introduced. The subchapter ends with a study of the vacuum blasting parameters.

The ILSS results of the different surface treatment methods are then examined and analyzed following the definitions in chapter 4.3. The results are presented and discussed in subchapter 4.6 and finally the relevance to the hypotheses is discussed in subchapter 4.7.

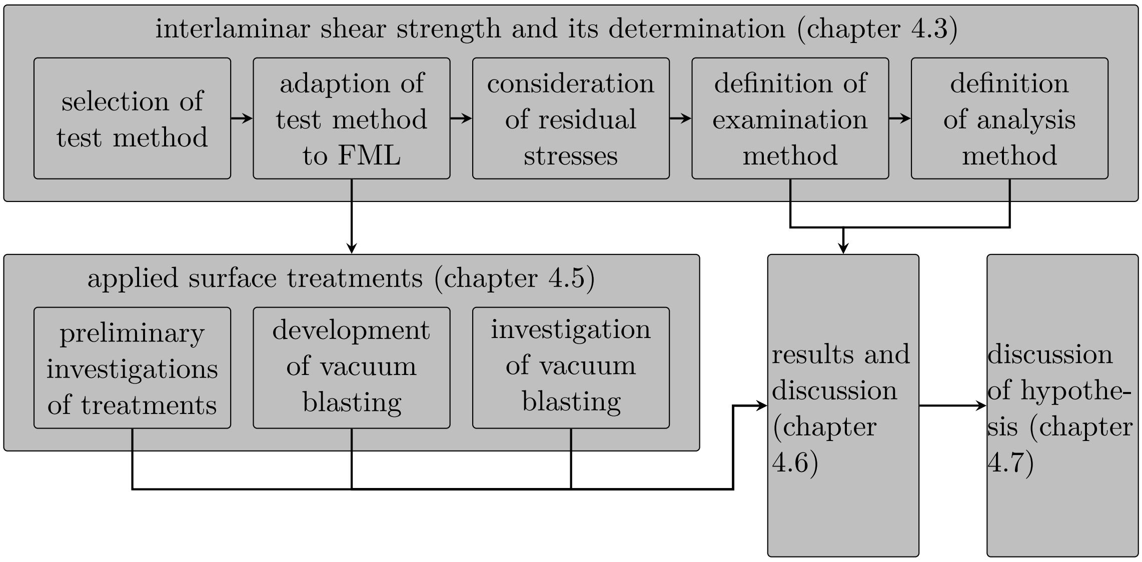

Figure 4.2: Flowchart describing the procedure pursued in chapter 4; individual subchapters marked in gray

4.3 Interlaminar shear strength and its determination

As summarized in chapter 4.1, there are different methods to determine the adhesion between the metal and the composite layer. The short beam test method is selected for the following discussion and mechanical tests, as it seems to be a suitable approach for the FMLs for the following reasons:

- small specimen size
- cut out of a flat laminate
- compared to the specimens to determine the interfacial fracture energy and the peel drum test, the area where the stresses generated by the test load itself and the area where residual stresses induce shear, are separated.

The last of these reasons is discussed in the following in more detail.
Firstly, the standard of the short beam test method is introduced. Then the specific characteristics and requirements which need to be considered when applying the test to non-transversely isotropic laminates are discussed. The specific characteristics which occur when applying this test to non-transversely isotropic laminates with interlaminar curing stresses acting are then also discussed.
Finally, an examination method is developed which considerers the previously discussed specifics. Confirmation of a successful bond is often achieved by a cohesive failure mode. However, as discussed in the 'Literature review' section, the informative value of this result is quite low as a weak layer may be induced in the bulk material.

Short beam test method

The short-beam test method uses very small specimens with an applied three point bending load where the shear strength at the neutral plane - where the shear stress reaches its maximum - is evaluated. This test method is described in ASTM D2344 [103] and DIN EN ISO 14130 [104]. The five-point bending test was first proposed by *Bateman et*

al. for wood composites and is similar to the short-beam test method [110]. Both tests have been compared by means of the finite element method and experiments by *Wang et al.* [111, 112]. They showed that the three point bending test gives lower strength results due to larger deflection. Additionally, in five point bending tests the '*von Mises*' stresses along the midplane have the same order of magnitude as those along interfaces out of midplane. Therefore, the five point bending tests is more suitable for evaluating shear strength out of midplane when accurate values are desired. However, due to its simplicity, the three point bending test is more widespread in quality testing and comparison of different materials and allows better comparison with values in the literature. For these applications the value itself is of less interest then the comparability between the values. *Nishimura* showed that the geometry of the loading nose and supports have a major influence on the results [113], which have carefully to be taken into account when comparing test values.
According to the beam theory, the shear stress can be calculated by:

$$\tau(z) = \frac{QS(z)}{Ib(z)} \tag{4.4}$$

Q defines the transverse load, S the static moment, I the moment of inertia and b the width of the specimen. According to ASTM D2344, the maximum shear stress τ_{max} of a symmetrical laminate with the neutral plane in the center for a rectangular cross section with the laminate thickness t_{lam} under the load F is calculated as follows:

$$\tau_{max} = \frac{3F}{4bt_{lam}} \tag{4.5}$$

whereas the maximum stress at the outer surface σ_{max} caused by bending, with the distance L_{sup} between the supports (see Figure 4.3), is:

$$\sigma_{max} = \frac{3FL_{sup}}{2t_{lam}^2} \tag{4.6}$$

according to the beam theory. The ratio $\varphi_{\tau\sigma}$ between shear stress τ_{max} and normal stress σ_{max} is given by:

$$\varphi_{\tau\sigma} = \frac{\tau_{max}}{\sigma_{max}} = \frac{t_{lam}}{2L_{sup}} = \frac{\tau_{ILSS}}{\sigma_{C,11}} \tag{4.7}$$

where the right term describes the ILS-strength τ_{ILSS} and the compressive strength $\sigma_{C,11}$ of the laminate. This relationship leads to the following expression:

$$\tau_{ILSS} \leq \frac{t_{lam}\sigma_{C,11}}{2L_{sup}} \tag{4.8}$$

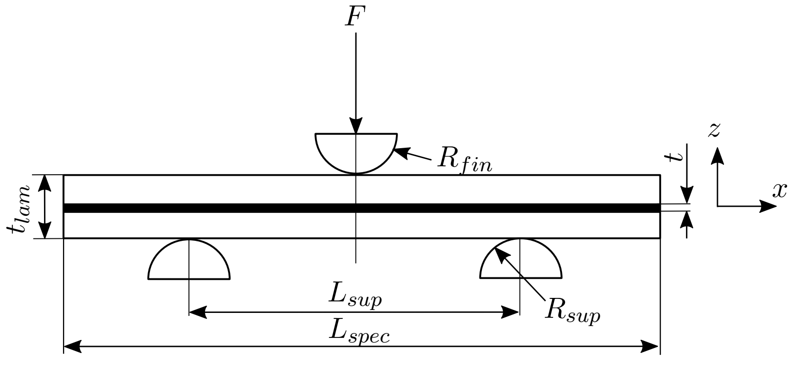

Figure 4.3: Geometries of short beam test setup with multi-material lay-up

Hence, a shear failure can only be achieved if the expression in formula 4.8 is valid. As a pure state of shear can not be achieved and the stress field in the specimen is quite complex, failure occurs due to multiple failure mechanisms [114]. This is the reason why the term 'apparent interlaminar shear strength' - used in both standards [103, 104] - indicates that the value is different from the true shear strength, which is a material property.
Chatterjee reports that for graphite/epoxy laminates with the geometrical ratio $L_{sup}/L = 4.7, 5.7, 6.7$, the following relationship to achieve the true shear strength τ_u fits the test data well [114]:

$$\tau_u = \frac{2\tau_{ILSS}}{3 - \left(\frac{2\tau_{ILSS}}{\sigma_{C,11}} \frac{L_{sup}}{t_{lam}}\right)} \tag{4.9}$$

Short-beam test method on non-transversely isotropic laminates

When applying the short-beam test method on FML, there are three specific characteristics:

1. The shear stress distribution is not parabolic as the laminate consists of single layers with different stiffnesses.

2. The failure does not occur in the midplane, as it is not possible to build a symmetrical laminate out of two different materials with an interface between the two in the midplane. As residual stresses are present as a consequence of the thermo-mechanical mismatch between the constituents, a symmetrical lay-up is required to achieve a flat specimen.

3. The residual stresses induce interlaminar shear stresses which act on the same surface where the shear stress is applied up to failure and induce a multiple stress state.

Consideration of stress distribution along thickness

To fulfill the first requirement, *Kolesnikov* uses the following formula to calculate the shear stress τ of a laminate with the geometry shown in Figure 4.3 [9]:

$$\tau_{ILSS} = 3\frac{F}{b}\frac{t_{lam}^2 - t^2}{(t_{lam} - t)^3 + 3(t_{lam} - t)(t_{lam} + t)^2 + 4t^3\frac{E_M}{E_{C11}}} \tag{4.10}$$

where F is the applied load, b is the specimen width, and E_{C11} and E_M are the stiffness of the composite and the metal layer, respectively. The formula, determined by the methods described by *Darkov* [115], takes into account the different stiffnesses of the constituents and calculates the shear stress for the interface between composite and metal layer, where the failure occurs. As the methods described by *Darkov* [115] are in Russian and are currently unavailable, another simple approach was needed which allows the calculation of the shear stress at an arbitrary position on a laminated beam. *Bednarcyk et al.* of *NASA* propose a simplified shear solution which satisfies these requirements [116]. They show that their approach is in satisfactory agreement with the exact solution of *Williams*' 'Composite Plate Theory with Delamination' [117]. The entire formulation by *Bednarcyk et al.* [116] can be found in appendix 7. The internal shear force can be deduced by:

$$\tau(k, \hat{z}) = -\frac{Q}{I}\, Q'(k, \hat{z}) \tag{4.11}$$

where Q is the applied transverse load, I is the transformed beam-cross section and Q' depends on the layer and the z-position of interest with respect to the neutral axis:

$$\begin{aligned} Q'(k,\hat{z}) = \int_{\hat{z}_N}^{\hat{z}_c} b\ n_k\ \hat{z}\,\mathrm{d}\hat{z} &= \int_{\hat{z}_k}^{\hat{z}_c} b\ n_k\ \hat{z}\,\mathrm{d}\hat{z} + \int_{\hat{z}_{k+1}}^{\hat{z}_c} b\ n_{k+1}\ \hat{z}\,\mathrm{d}\hat{z} + ... + \int_{\hat{z}_N}^{\hat{z}_{N-1}} b\ n_N\ \hat{z}\,\mathrm{d}\hat{z} \\ &= \frac{b\ n_k}{2}(\hat{z}_c^2 - \hat{z}_k^2) + \frac{1}{2}\sum_{m=k+1}^{N} b\ n_m\ (\hat{z}_{m-1}^2 - \hat{z}_m^2) \end{aligned} \tag{4.12}$$

In formula 4.12, b describes the width, k the ply number, c the distance from the neutral plane to the bottom surface of a ply and N the total number of plies. As indicated by the subscript k, n is defined for each ply and describes the ratio of the ply's stiffness and the average laminate's stiffness:

$$n_k = \frac{E_x^k}{\overline{\overline{E_x}}} \tag{4.13}$$

The original width b of each layer is thereby transformed to bn_k, as shown in Figure 4.4. The distance of a point from the neutral plane is denoted by $\hat{z} = z - z^*$ where:

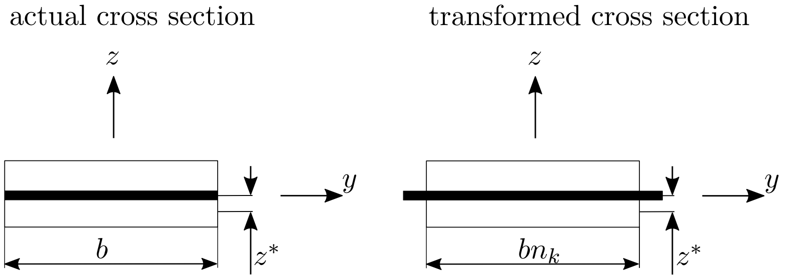

Figure 4.4: Actual and transformed laminate cross sections, based on *Bednarcyk et al.* [116]

$$z^* = \frac{\sum_{k=1}^{N} \frac{1}{2}\ (z_k + z_{k-1})\ A_k}{\sum_{k=1}^{N} A_k} = \frac{\sum_{k=1}^{N} \frac{1}{2}\ (z_k + z_{k-1})\ t_k\ n_k}{\sum_{k=1}^{N} t_k\ n_k} \tag{4.14}$$

A_k and t_k represent the area and the thickness of the layer, respectively. The positions z are denoted in Figure 4.5. Finally, the moment of inertia of the transformed beam cross section is described by:

$$I = \sum_{k=1}^{N}\left[\frac{1}{12} b\ n_k\ t_k^3 + b\ n_k\ t_k\left(\frac{\hat{z}_k + \hat{z}_{k-1}}{2}\right)^2\right] \tag{4.15}$$

When applying this approach to a three layer laminate - as used for the short beam test method - with the thickness t_{lam} and a metal layer in the center with a thickness t, as shown in Figure 4.3, the stiffness ratios for the three plies $N = 3$ are:

$$n_1 = n_3 = n_C = \frac{E_{C11}}{\overline{\overline{E_x}}};\ n_2 = n_M = \frac{E_M}{\overline{\overline{E_x}}} \tag{4.16}$$

where n_C is the transformation factor for the composite layer and n_M the transformation factor for the metal layer. As the neutral axis corresponds to the midplane, $z^* = 0$ and the positions $\hat{z}_k$, see Figure 4.5 are depicted as:

$$\hat{z}_0 = \frac{t_{lam}}{2};\ \hat{z}_1 = \frac{t}{2};\ \hat{z}_2 = -\frac{t}{2};\ \hat{z}_3 = -\frac{t_{lam}}{2} \tag{4.17}$$

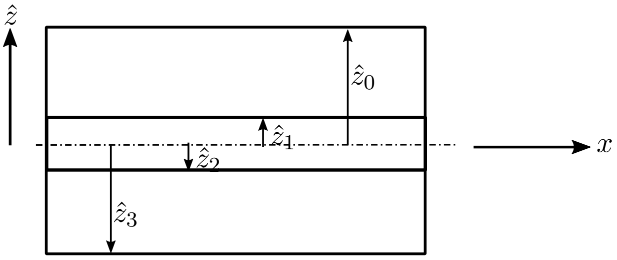

Figure 4.5: Positions z of the layers with reference to the midplane, based on *Bednarcyk et al.* [116]

With the thickness of each layer:

$$t_1 = t_3 = \frac{t_{lam} - t}{2};\ t_2 = t \tag{4.18}$$

the shear stress at the lower interface between CFRP and metal with the distance $\hat{z}_c$ from the neutral axis is given by:

$$\tau(2, -\frac{t}{2}) = 3\frac{F}{b}\frac{t_{lam}^2 - t^2}{(t_{lam} - t)^3 + 3(t_{lam} - t)(t_{lam} + t)^2 + n_M\ 4\ t^3} \tag{4.19}$$

For very low MVFs, when $\overline{E_x}$ is similar to E_{C11}, this formula provides similar results to the one provided by *Kolesnikov et al.* [9] and describes the shear stress at the interface between CFRP and metal layer at any arbitrary position between the supports under the load F.

When the shear stress distribution along the thickness of the specimen is required, the following formula for each of the three plies can be depicted:

$$\tau(1, \hat{z}) = -\frac{F}{b}\ \frac{12\ (\hat{z}^2 - \frac{t_{lam}^2}{4})}{(t_{lam} - t)^3 + 3(t_{lam} - t)(t_{lam} + t)^2 + n_M\ 4\ t^3} \tag{4.20}$$

$$\tau(2, \hat{z}) = \frac{F}{b}\ \frac{3(t_{lam}^2 - t^2) - 12\ n_M \hat{z}^2 - \frac{t^2}{4})}{(t_{lam} - t)^3 + 3(t_{lam} - t)(t_{lam} + t)^2 + n_M\ 4\ t^3} \tag{4.21}$$

$$\tau(3, \hat{z}) = -\frac{F}{b}\ \frac{12\ (\hat{z}^2 - \frac{t_{lam}^2}{4})}{(t_{lam} - t)^3 + 3(t_{lam} - t)(t_{lam} + t)^2 + n_M\ 4\ t^3} \tag{4.22}$$

Applying these formulae to the short beam test method, the thickness of the total specimen is about 2 mm and consists of two composite layers and one metal layer in the center as shown in Figure 4.5. Three different metal layer thicknesses are considered, $t = 0.05$ mm, $t = 0.25$ mm and $t = 1.0$ mm. The remaining thickness consists of composite plies of $t_{lay} = 0.13$ mm which corresponds to the common prepreg thickness chosen for the previous analyses. Figure 4.6 shows the shear stress along the thickness z where the stress values at the corresponding interface are marked with a dot. The stress distribution in a single layer composite beam is represented by a black line as reference and is normalized to one. The increase of the midplane stress value of the multi-layered solutions is thus easily recognized in the diagram.

However, the relationship between maximum shear stress in the midplane and the corresponding stress value at the interface is more crucial as the aim is to achieve a failure at the interface. There are two possible consequences of a high ratio between these values.

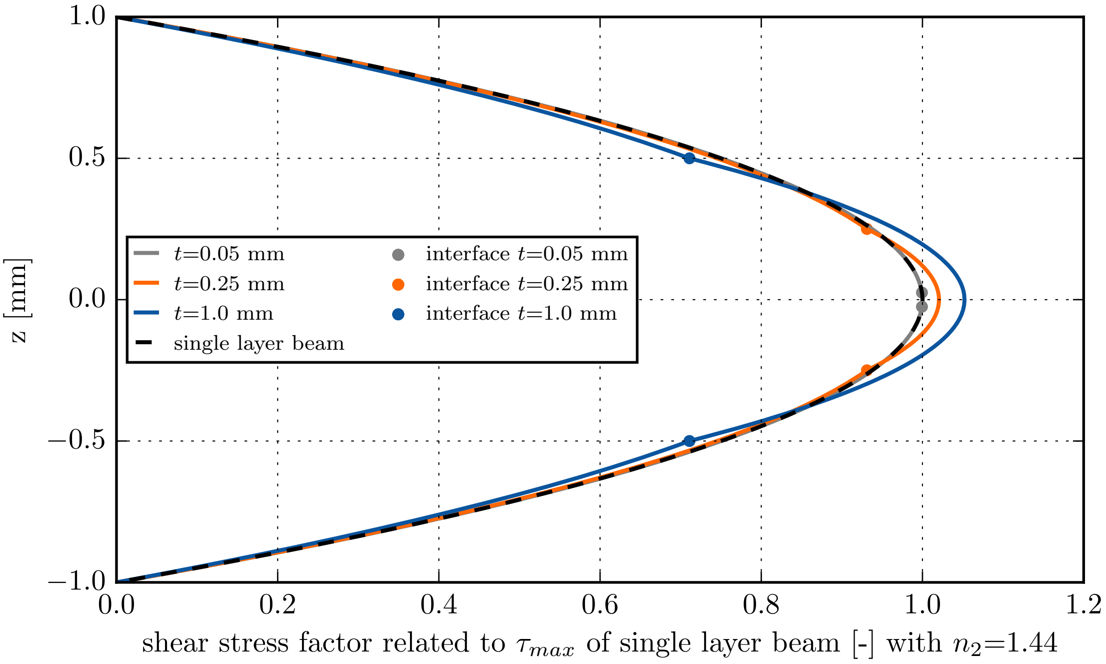

Figure 4.6: Shear stress distribution along the depth of single layered and triple layered specimens with different geometrical fractions

Firstly, the yield under shear load of the metal may be achieved before a failure at the interface is induced. Secondly - and obviously more crucially - with increasing ratio between midplane shear stress and interface shear stress, higher loads are required to provoke failure. As a consequence, bending is increased and the calculated shear stress value is falsified. Based on Figure 4.6 it is obvious that the ratio decreases with smaller metal layer thickness t. Therefore, it seems appropriate to choose a metal layer thickness of 0.05 mm, which represents a lower boundary for the manual handling of the foil.

Consideration of residual curing stresses

A second distinctive feature of the determination of FML's interlaminar shear strength are the residual stresses arising as a consequence of the mismatch in thermal expansion coefficients. These interfacial stresses are also present in the loaded area and hence have an effect on the results. However, these interfacial shear stresses reach their maximum value at the free edges of the specimen. The short beam test method has the advantage that it induces shear stresses only between the supports. Regarding the longitudinal direction of the specimens, the maximum of the thermal interfacial stresses in the fiber direction and the shear stresses induced by the test load are not superimposed. However, the shear stress distribution in the longitudinal as well as the transverse directions must be determined in order to assess its influence on the experimental results of the short beam test method.

Timoshenko introduced an analytical model in 1925 to calculate the maximum values of these interfacial stresses at the freed edges [118]. *Suhir* developed an extension which allows the calculation of their distribution [119]. Investigations by *Eischen et al.* compared this solution to another by Hess [120, 121] and to an FEM-solution and proved it to be useful for preliminary designs and estimations [122]. The aforementioned publications are

recommended for the full discussion on the formula and its derivation. In the following, the formula utilized for the longitudinal residual stresses is presented and adapted to the variable declaration used in the present work:
The shear stress at an arbitrary position x along the specimen length is calculated with

$$\tau(x) = \tau_{max} e^{-k(l-x)} \tag{4.23}$$

where

$$\tau_{max} = \frac{\Delta\alpha\Delta T}{k\kappa} \tag{4.24}$$

The values for $\Delta\alpha$ represent the difference between the two constituents CTE, and ΔT represents the difference between curing temperature and test temperature. The missing variables κ and k are calculated by:

$$k^2 = \frac{\lambda}{\kappa} \tag{4.25}$$

and

$$\lambda = \frac{1}{12}(\frac{t_C^2}{D_{C,11}} + \frac{t_M^2}{D_M} + \frac{h^2}{D}) \tag{4.26}$$

as well as

$$\kappa = \frac{2(1+\nu_{C12})}{3E_{C11}} t_C + \frac{2(1+\nu_M)}{3E_M} t_M \tag{4.27}$$

The variables t_C and t_M describe the thickness of each constituent and h the sum of both. The missing variables D_{C11}, D_{M11} and D are given by

$$D_{C,11} = \frac{E_{C11} t_C^3}{12(1-\nu_{C12}^2)} \tag{4.28}$$

$$D_M = \frac{E_M t_M^3}{12(1-\nu_M^2)} \tag{4.29}$$

$$D = D_{C,11} + D_M \tag{4.30}$$

where ν_{C12} and ν_M are the *Poisson's* ratios ν_{12} of composite and metal, respectively. Applying these formulae to the short beam test method based on a three layer specimen with a metal layer in the midplane, a length L_{spec} of 20 mm, a width b of 10 mm and $\Delta T = -157K$, generates diagrams in Figure 4.7 and Figure 4.8. They show the shear stress τ_{xz} generated by the residual stress acting in the longitudinal direction in black and the shear stress τ_{yz} generated by the residual stress acting in the transverse direction in gray. For the longitudinal case the values on the abscissa represent the longitudinal position whereas for the transverse case the transverse position is represented. The orange lines mark the area in which the shear stress generated by the test itself is acting.
Figure 4.7 shows the stress distribution when the metal layer is 0.05 mm and Figure 4.8 shows the same for a metal layer thickness of 1 mm. Even when using the thicker layer, the longitudinal stress drops to zero within less than two millimeters.
The maximum shear stress τ_{max} at RT for the specimen with the thicker metal layer is 119.75 MPa. For a test temperature of -55°C the stress increases to 179.2 MPa. The shear strength of the pure CFRP specimen is 127.6 MPa for RT and 164.1 MPa at -55°C, which means that this lay-up is not suitable for the short beam test as it is possible that failure occurs due to the residual stress in the longitudinal direction and not as a consequence of the test load.

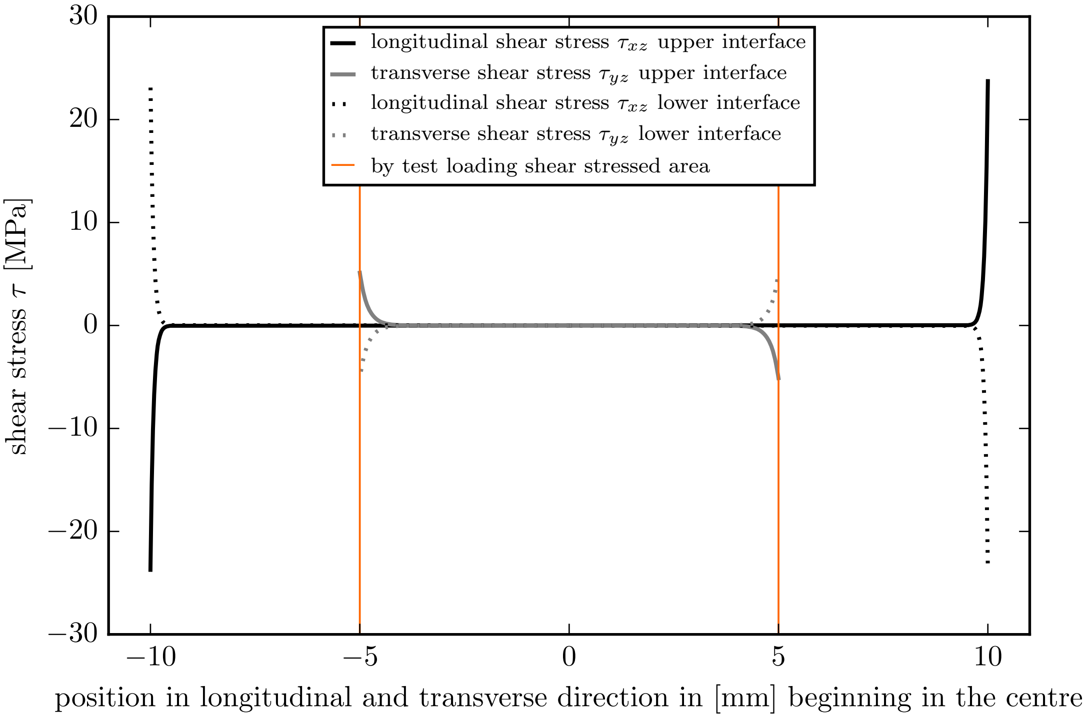

Figure 4.7: Interfacial residual shear stress distribution for ΔT=-157 K and metal layer thickness t_M=0.05 mm

It is obvious that the shear stress drops exponentially and there is no shear stress τ_{xz} present in the loaded area. The shear stress τ_{yz} is smaller, as the composites stiffness is much lower, but it is present in the mechanically stressed area. For the specimen with metal thickness $t = 0.05$ mm the maximum shear stress generated by transverse residual stresses is 5.29 MPa. However, the thermally generated stresses act in a different plane than the stresses introduced by the mechanical test. Regarding the 'equivalent stress' σ_v, the following relationship is given for the general case:

$$\sigma_v = \sqrt{\sigma_x^2 + \sigma_y^2 + \sigma_z^2 - \sigma_x\sigma_y - \sigma_x\sigma_z - \sigma_y\sigma_z + 3(\tau_{xy}^2 + \tau_{xz}^2 + \tau_{yz}^2)} \tag{4.31}$$

which can, for the interface considered, be reduced to:

$$\sigma_{vI} = \sqrt{3((\tau_{xz,test} + \tau_{xz,res})^2 + \tau_{yz,res}^2)} \tag{4.32}$$

where the subscripts '*test*' and '*res*' mark the stresses generated by the test load and the residual thermal stresses, respectively. Superposition of the stresses only takes place in the loaded area where $\tau_{xz,res} = 0$. As a consequence equation 4.32 reduces to:

$$\sigma_{vI} = \sqrt{3(\tau_{xz,test}^2 + \tau_{yz,res}^2)} \tag{4.33}$$

Short beam tests on pure CFRP specimens fail at a shear stress $\tau_{xz,test}$ of around 128 MPa which corresponds to an 'equivalent stress' of 221.7 MPa. It is assumed that there are no other interlaminar shear stresses present in this specimen. Considering a maximum transverse residual stress $\tau_{yz,res}$ of 5.29 MPa, the specimen would fail at a shear stress of $\tau_{xz,test}$ of 127.89 MPa. This deviation is negligible as it is below 1%. The transverse

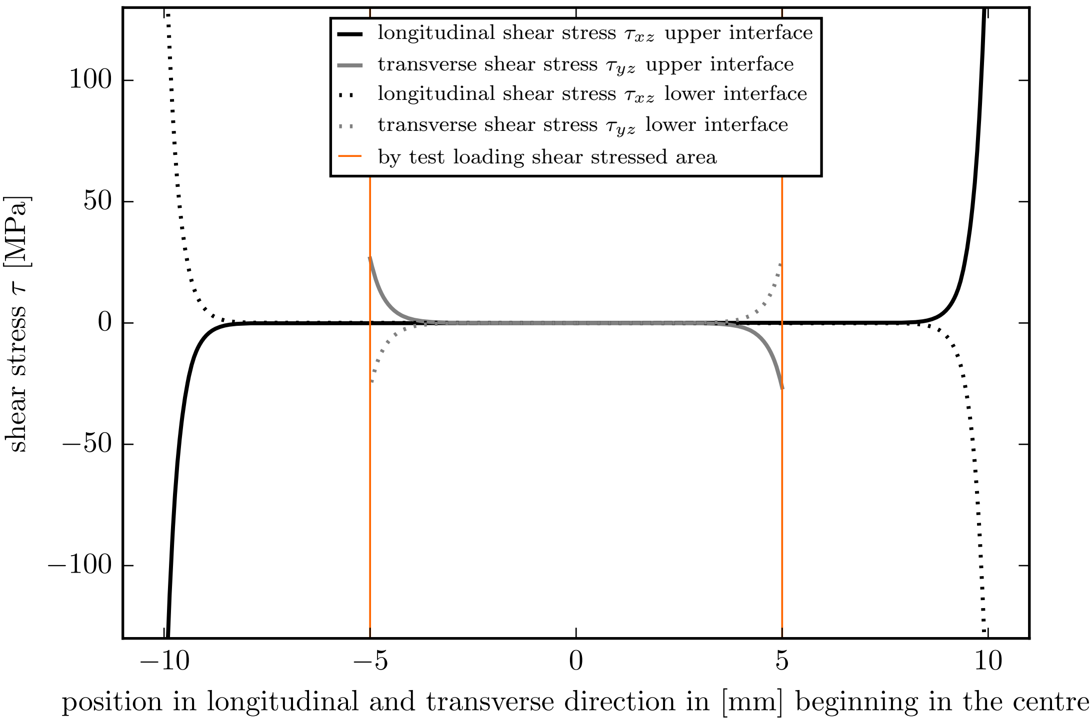

Figure 4.8: Interfacial residual shear stress distribution for ΔT=-157 K and metal layer thickness t_M=1 mm

residual stress $\tau_{yz,res}$ for the specimen with the thicker metal layer, has a maximum value of 30.03 MPa which leads to a deviation of around 3%. Again, the thinner metal sheet is more suitable for the short beam test method.

Applied examination method

The examination method utilized is based on DIN EN ISO 14130 [104] which is comparable with ASTM D2344 [103]. Testing speed is 1 mm/min, the radius of the two support cylinders R_{sup} is 2 mm and the radius of the loading fin R_{fin} is 5 mm. The specimen length L_{spec} is 20 mm. However, due to the hybrid properties of the specimens, some modification is performed. The thickness of the steel foil is t=0.05 mm. The number of prepreg plies is chosen in such a way that the laminate thickness L is close to 2 mm. However, these values vary as a consequence of manufacturing and, therefore, are measured for each specimen separately. The specimen width b is 10 mm but is also measured individually. The support length L_{sup} is intended to be 10 mm but varies within the range of ±0.1 mm when setting up the machine. Therefore, this value is also measured individually. All individually measured values are determined with the help of a micrometer screw.

The validity of the test is assessed for each specimen by investigating the specimen itself after testing. Only pure shear failure in one or multiple layers is valid for this test, as shown in Figure 4.9. Specimens showing shear failure interfering with compression or tension failure, or specimens showing residual bending as a consequence of matrix shear failure, are not valid.

Four different test conditions are chosen. Three of the test conditions are described as dry, as the relative humidity is 50%. The temperature is 23°C for the condition 'RT/dry',

-55°C for the condition ’cold/dry’ and 120°C for the condition marked ’hot/dry’. The fourth test condition is generated by saturated specimens which have been stored in water for 1000 hours and are tested at RT. This test condition is defined as ’RT/wet’. These test conditions are summarized in Table 4.2.

Analysis method

Following the test conditions, only those specimens which show a shear failure as depicted in Figure 4.9 are considered for the results. The measured values for load and deflection of four different example specimens, one under each test condition, are depicted in Figure 4.10. The specimens tested under RT/dry, cold/dry and RT/wet conditions show valid failure modes. The first load drop indicates the first delamination or shear failure and coincides with the maximum load value. Therefore, each measured load value F_n is subtracted from a subsequent load value F_{n+x} to calculate the relative load drop F_{rel}:

$$F_{rel} = \frac{F_{n+x} - F_n}{F_n} \tag{4.34}$$

Table 4.2: Definition of test conditions concerning temperature and humidity.

test temperature	humidity/ specimen state	abbreviation
[°C]	[%]	[-]
23	50	RT/dry
-55	50	cold/dry
120	50	hot/dry
23	100 (saturated)	RT/wet

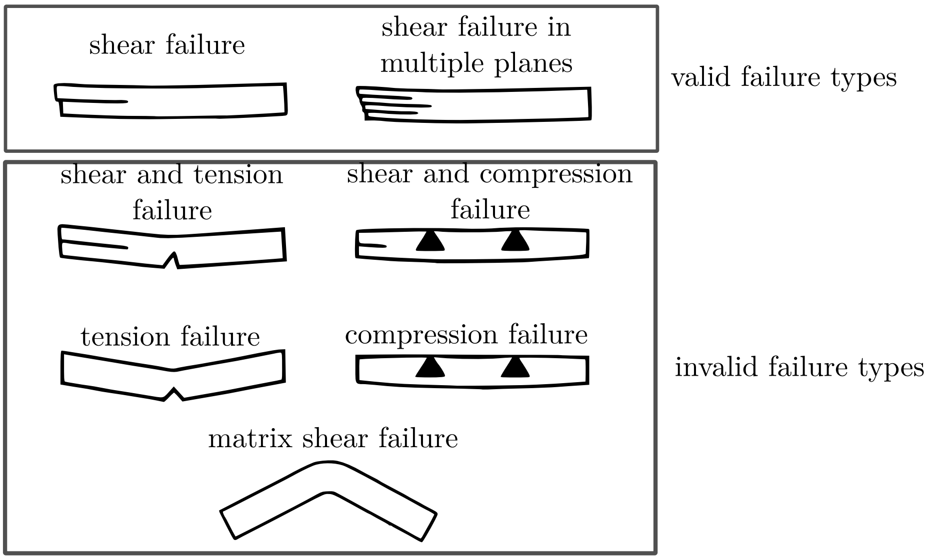

Figure 4.9: Valid and invalid failure modes in ILSS testing [104]

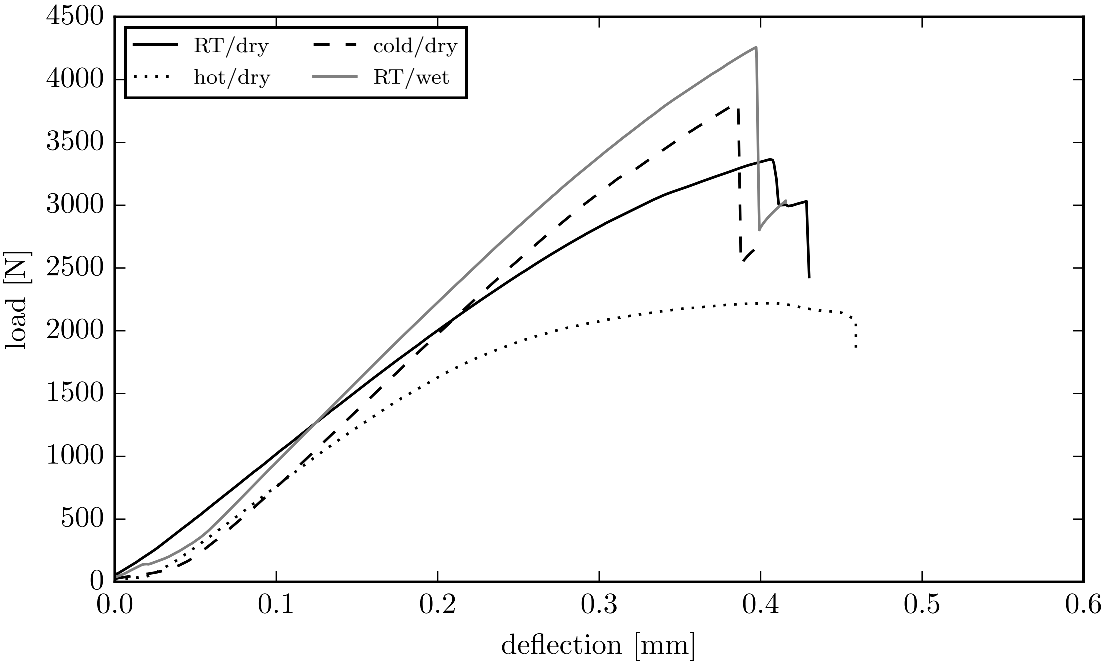

Figure 4.10: Exemplary load-deflection curves at different test conditions.

The results show that a the failure load can be approximated satisfactorily when the threshold value F_{rel} reaches 0.005. As a consequence the shear strength τ_{ILSS} is calculated with this associated load value $F_{0.005}$ following equation 4.10.

The specimens tested under hot/dry conditions show a bending failure and their load-deflection curve shows a smooth decrease in stiffness as shown in Figure 4.10. As the following tests are only used for the relative comparison of different surface treatments, the maximum load values are utilized for the shear strength calculation under hot/dry conditions, although the values must be considered with care. In this case the maximum load F_{max} is used in equation 4.10 to calculate shear strength τ_{ILSS}.

For the thin metal foils with a thickness of t=0.05 mm, the influence of residual stresses is neglected as discussed in the previous chapter.

Ten specimens have been tested for each combination of surface treatment and test condition. However, the amount of valid results varies for each of the cases. Therefore, the box-and-whisker plot is selected for the presentation of the results as it allows the display of different representatives. Following the definitions of *John W. Tukey* [123], the box-and-whisker plot shows the median value, the first and third quartiles ($Q1$, $Q3$), the outliers and the interquartile range IQR. As depicted in Figure 4.11, the median is marked with a red band. The box may vary in color to characterize different parameters (marked in gray in the example) and the bottom and top of the box are the first and third quartiles. This means that 50% of the data is in the box which also describes the interquartile range. The caps at the end of the whiskers mark the lowest and highest value which is still in the range of $Q1-1.5IQR$ or $Q3+1.5IQR$ respectively. Values outside $1.5IQR$ are considered as outliers and marked with a black cross.

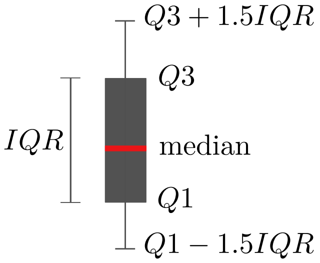

Figure 4.11: Definition of box-and-whisker plot (Tukey boxplot [123])

4.4 Development of a vacuum blasting process for foils

The thin metal foils with a thickness of 0.05 mm were mechanically grit blasted with different grit sizes in previous studies and a homogeneous surface topology could not be achieved without damaging the metal foils with folds and wrinkles on a larger area. The energy input of the particles seems to be too high and the plastically deformed fraction too large. There are two ways to lower the kinetic energy of the individual particles: lower its velocity or lower its mass. The pressure difference in the system, which is related to the velocity of the particles, can not be reduced below a certain value. The lowest particle size of silicon carbide is around 75 μm. Smaller particles require an immense effort in sealing to prohibit contamination and to meet health and safety regulations. Although using fine particles and low pressure, no satisfactory result was achievable.
Figure 4.12 shows part of a foil treated by means of the BSP, as described in the following chapter in more detail. Despite blasting from both sides simultaneously on a special machinery, the foil shows folds and wrinkles. As a consequence, neither the sol-gel nor the primer show a homogeneous dispersal.

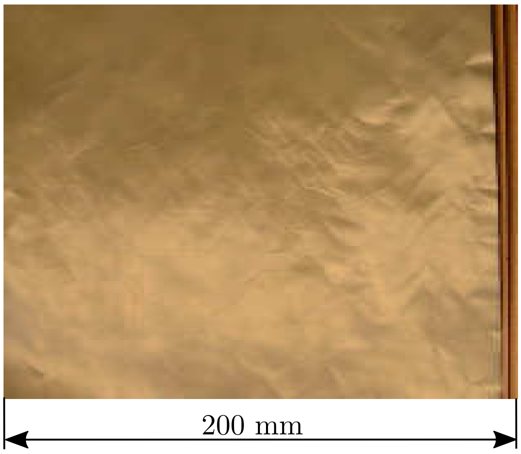

Figure 4.12: 'Boeing sol-gel'-processed 0.05 mm thick steel foil with clearly visible folds and wrinkles

Hence, in collaboration with a company specializing in the vacuum blasting of bulk material, a novel machine was developed. Vacuum blasting of bulk material is characterized by a nozzle, a tube in the simplest setup, entering a chamber where the pressure is lowered with the help of an exhauster. The chamber is open on its bottom and placed on the workpiece. The nozzle is movable and guided above the workpiece. Due to the pressure difference, the grit enters the chamber through the nozzle and strikes the workpiece as a consequence of its inertia, before leaving the chamber in the direction of the exhauster. Normally, the chamber is relatively small and the particles strike the workpiece at a steep angle.

The vacuum blasting unit for foils is designed in such a way that the chamber, or rather the nozzle, is relatively long. It spans the whole width of the foil to be treated. The particles enter this area parallel to the foil surface and pass it in a turbulent flow. As a consequence they strike the surface multiple times at a flat angle. This generates a more gentle abrasion and the foil does not develop any wrinkles.

Figure 4.13 shows the vacuum blasting unit with peripherals. The two nozzles are in the center of the picture. The grit passes through one nozzle from left to right and through the other from right to left. The chamber is divided by the foil into an upper and lower half where the grit is evenly spread. A driving roll feeds the foil, unrolling it from its coil. A brake regulates the tension on the foil and two additional spreader rolls, rubber-covered rolls which can be wrapped into a curve, guarantee continuous tension along its width; also it may have the tendency to wrinkle when laid on a flat surface. There are two clamps to hold the foil down for easy cutting.

Between nozzles and exhauster unit there is a separator to separate the grit from the air. On the bottom there is an automatic abrasive adding system, dosing the required amount of grit into the airstream with the help of an oscillating channel.

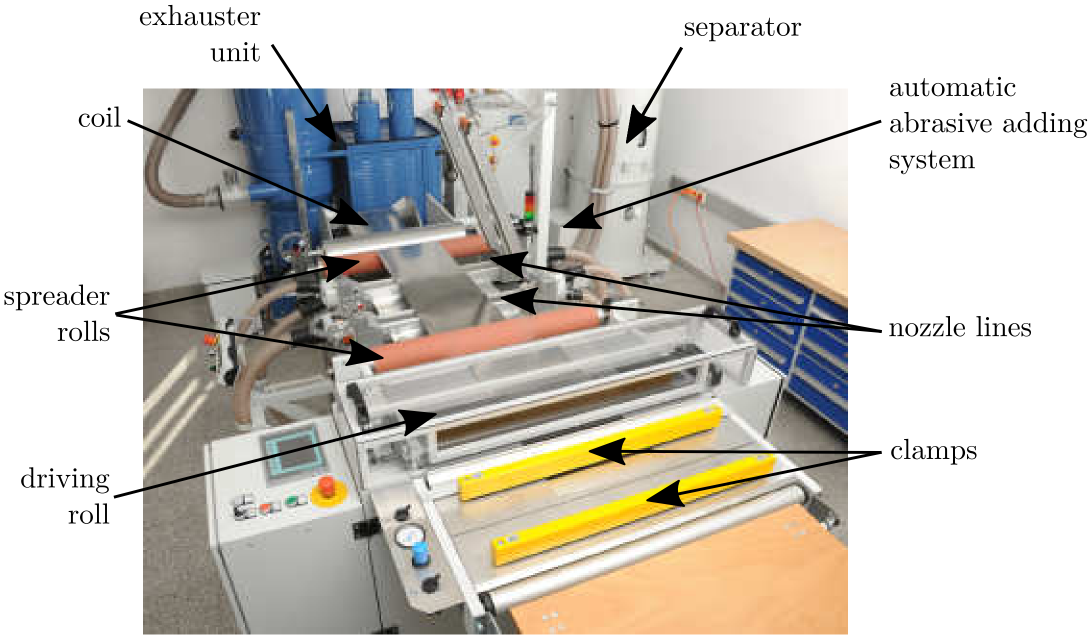

Figure 4.13: Vacuum blasting unit with peripherals

4.5 Applied surface treatments

As indicated in the 'Literature review' subchapter at the beginning of this chapter, the surface treatments of the metal are subdivided in pre- and post-treatment. It is not clearly defined where intermediate cleaning processes relate to, but Figure 4.14 shows the definition applied in the following. As the primary metal surface is contaminated with oleaginous residues as a consequence of the cold-rolling process, the pre-treatment starts with a swipe cleaning with acetone or heptane. Subsequently to the actual surface modification process, a second cleaning process is intended. Heptane, acetone and 'none' define the variation parameters considered in the second cleaning step. Grit-blasting, different pickling processes and vacuum-blasting are investigated as actual surface modification process.

Physical pre-treatment by plasma is not considered in the following due to their economic inefficiency for large surfaces. Additionally, electrochemical treatments are not considered because the possibility of pitting is increased for austenitic chromium-nickel steels [124]. Abrading alternatives like the nylon pad process are also not regarded, as investigations by *Blohowiak et al.* [77] and *Mazza* [91] showed the poorest crack test performance for these surfaces. As a consequence, only mechanical and chemical pre-treatments are considered in the present investigations.

Additionally, tests are performed without any post-treatment, with the application of sol-gel only and with the combination of sol-gel and an additional epoxy primer.

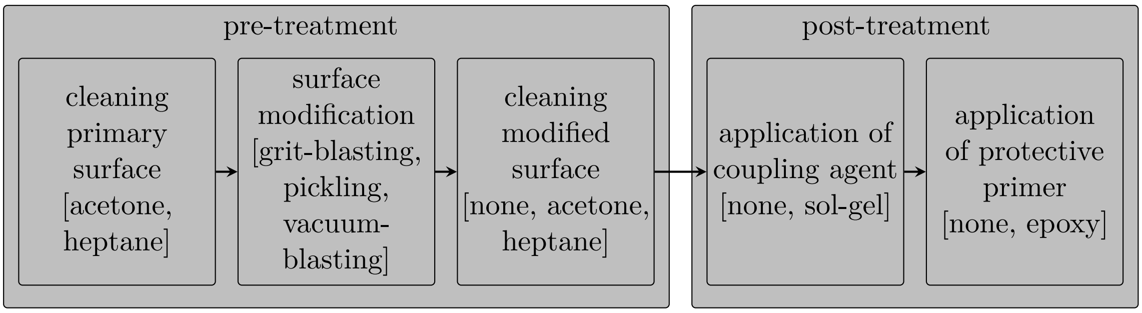

Figure 4.14: Surface treatment process and investigated methods

Specimens manufacturing, materials and lay-ups

All specimens consist of a 1.4310 steel layer with 0.05 mm thickness in the center and two UD-stacks of prepreg on both sides of the center layer. Hexcel 8552/AS4 prepreg and Cytec 977-2/IM7 prepreg are used. The properties of the first can be found in Table 3.1. The second material comes with stiffer fibers and a toughened resin, see [125]. Double the amount of layers is used for Hexcel prepreg as its layer thickness is half of the Cytec prepreg as the first is used as 134 g/m^2 and the second as 268 g/m^2 grade. The lay-up of the specimens are $(0_8/St/0_8)$ and $(0_4/St/0_4)$ for 8552/AS4 and 977-2/IM7, respectively. Both materials are cured following the manufacturer's recommended cure cycle [28, 125] without using peel-ply directly on the specimens surface. The specimens are cut to size with a diamond saw and then measured with a micrometer gauge.

Sol-gel post treatment

The two-part aqueous sol-gel AC-130 by 3M is the only coupling agent in the tests [126]. It is applied by dipping the foil in a shallow bath of the solution. Dipping time is varied as specified in the results, 100 and 150 seconds dipping time are used and the foil is regularly moved in the bath during this period. The foils are then drained and dried under ambient conditions for a minimum of 60 minutes. Any contamination to the foils before adding them to the lay-up is avoided by transportation between clean paper towels.

Boeing-sol-gel reference process

Following Boeing specifications, the pre-treatment of the steel foil was made at Triumph Group Inc., where the grit-blasting was performed from both sides simultaneously in a continuous process. The AC-130 sol-gel was sprayed on the two surfaces in the simultaneous process as well. Finally, BR6747-1 water-based adhesive bonding primer was applied by spraying as well and oven cured following the manufacturer's instructions [127]. The regarded tests encompass 10 ILSS specimens, which are all tested at RT/dry.

Grit-blasting pre-treatment

The grit-blasting parameters are chosen based on previous tests and experience. A grit-size of 180 μm of glass-grit is selected. The foil blanks with a size of 150 x 100 mm are blasted for 1 min per side in one setup and 3 min per side in another setup at 1.5 bar pressure. The tests considered encompass 70 ILSS specimens.

Pickling pre-treatment

Investigation with 304 stainless steel bulk material showed that the dissolution rate of hydrochloric acid HCl is comparable with nitric acid HNO_3 whereas it is lower for sulphuric acid H_2SO_4. The same comparison for oxide covered 304 stainless steel illustrates that sulphuric and nitric acids lead to comparable intermediate dissolution rates and hydrochloric acid to a high rate [124].

However, HCl is not considered for the tests because the $FeCl_3$ formed promotes pitting [124]. Mixing the remaining two acids with hydrofluoric acid HF significantly increases the dissolution rate [128, 129]. Two different pickling systems are investigated for the surface modification process step. The first solution is based on nitric acid and the second is based on sulfuric acid and hydrofluoric acid.

The nitric acid mixture is the most widely used solution for stainless steel but also involves problems such as emission of NO_x-fumes [130]. These gases create an air pollution problem requiring scrubbing towers and a great deal of effort to ensure operational safety. The procedure is depicted in Figure 4.15 and starts with a cleaning step in a bath of Turco6849 (an aqueous alkaline degreaser manufactured by Henkel [131, 132]) at temperatures of 50-70°C. After thoroughly rinsing under demineralized water, the pickling process is conducted with a sulfuric acid. Turco4104, an acidic activator to enhance descaling and pickling, is added to the sulfuric acid. Three different solutions (A, B and E) are created by diluting with water following the manufacturer's recommendations as given in Table 4.3 [133, 134]. Phosphoric acid is given additionally to solution E. Table 4.3 also shows the pickling duration and bath temperature for each solution. A special device is manufactured out of polyethylene for the dipping of the thin metal foils to ensure that up to 10 foils (150x100 mm) can be dipped simultaneously without touching and masking each other. After a second rinsing step, the foils are oven dried at 50°C for 30 minutes.

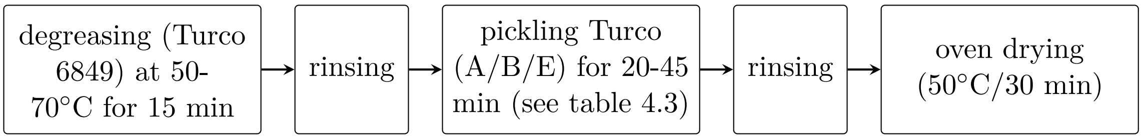

Figure 4.15: Flowchart describing the procedure pursued when pickling with nitric solution

Table 4.3: Content, temperature and duration for nitric pickling solutions

			A	B	E
content	HNO_3 70%	[vol%]	34	40	15
	H_3PO_4 85%	[vol%]	-	-	10
	Turco4104	[vol%]	14	7	5
	duration	[min]	15	15	25
	temperature	[°C]	21-31	22-32	43-49

The second pickling system is characterized by its nitrate-free nature as NO_x emission is not present. The main disadvantage of this nitrate-free $H_2SO_4{-}HF{-}H_2O_2$ bath are dark and adhesive deposits which can appear on the steel's surface [130]. Essential constituents of these nitrate-free alternatives are hydrofluoric acid and an oxidizing agent. When hydrogen peroxide is used, it is common to utilize a secondary acid to account for the low stability of hydrogen peroxide in the presence of iron (ferric) ions [130, 135]. Usually, the initial ferrous ions are added to the idle bath as Iron-(III)-sulphate. The ferric ion Fe^{3+} participates in the pickling process and is converted to ferrous ion Fe^{2+}. This reaction takes place at a specific potential that is obtained by the presence of hydrogen peroxide [135]:

$$2\,Fe^{3+} + 1\,Fe \rightleftharpoons 3\,Fe^{2+} \tag{4.35}$$

Another function of the hydrogen peroxide is the conversion of the ferrous iron to ferric iron [135]:

$$4\,Fe^{2+} + 2\,H_2O_2 \rightleftharpoons 4\,Fe^{3+} + H_2O + O_2 \tag{4.36}$$

This second acid utilized in the tests, containing sulfuric acid H_2SO_4, hydrofluoric acid HF and hydrogen peroxide H_2O_2 is referred to in the following as sulfuric solution and more detailed information can be found in the manufacturer's specifications [136, 137]. When referring to the sulfuric solution, the entire process shown in Figure 4.16 is meant, which starts with degreasing in a solution consisting of SurTec089 and SurTec138 for 15 minutes [138–141]. Both process steps end with thoroughly rinsing in demineralized water. Before applying sol-gel, the metal foils are dried in an oven. Pickling time as well as drying time and temperature are varied as indicated in Figure 4.16.

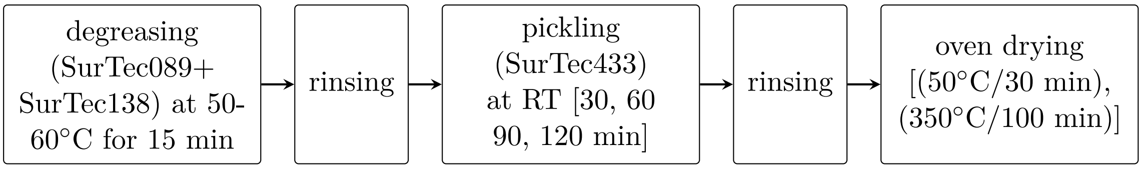

Figure 4.16: Flowchart describing the procedure pursued when pickling with sulfuric solution

All pickling processes are combined with sol-gel and are also tested without the addition of sol-gel. This results in 20 different processes and 230 ILSS specimens.

Vacuum blasting pre-treatment and primer post-treatment

Basically, the vacuum blasting machine permits the variation of the foil's feeding speed and the grit size, as indicated in the previous section. An appropriate feeding speed has already been selected in the development phase of the machine based on rapid electrochemical passivity test desicribed by *Dröschel et al.* [58].

Three different sizes of corundum grit are considered: 75, 105 and 300 μm. After surface pre-treatment the metal foil is cleaned and transported to the post-treatment. The impact of storage conditions on the shear strength is, therefore, of fundamental interest. The different conditions and the related abbreviations used here are specified in Table 4.4. Acetone or no cleaning agent is used in the first testing series concerning storage and cleaning conditions. Sol-gel is applied immediately after treatment or immediately after cleaning. For comparison, specimens are also considered where sol-gel is only applied after a period of 20 hours. The foils are put in aluminum bagging or vacuum bagging for this period.

Acetone is replaced by heptane as the cleaning agent for the second series, see Table 4.5, due to health and safety regulations. As the long time period before sol-gel application is not suitable for the manufacturing process at hand, shorter periods of between 5 and 120 minutes are compared. Additionally, two dipping durations, 100 and 150 seconds, are considered. Finally, two foils are stored in an aluminum bag and evacuated for 133 days before laminating. These different variations and their related abbreviations are specified in Table 4.5.

For a flexible and efficient manufacturing process it is of huge benefit when the individual process steps can be separated from each other in place and time. This means that the metal foil has to be treated and ready-to-use for a certain storage life. Therefore, an additional primer is investigated. The corrosion-inhibiting primer *BR127* [96] from *Cytec Engineering Materials* is a modified epoxy primer which is used in the production of GLARE and is suitable for the temperature range under consideration. The primer is applied by spraying and is tested for 8552/AS4 specimens as well as for 977-2/IM7 specimens. The coat thickness applied is around 5 μm and it is air dried for 30 minutes before being oven cured for 30 minutes at 120°C.

The variations applied result in 380 ILSS specimens.

Table 4.4: Storage and cleaning conditions - series 1

cleaning agent	time before sol-gel application	storage type	abbreviation
[-]	[h]	[-]	[-]
-	0	-	(-/0h/-)
acetone	0	-	(a/0h/-)
-	20	aluminum	(-/20h/Al)
acetone	20	aluminum	(a/20h/Al)
-	20	polyamide bagging	(-/20h/PA)
acetone	20	polyamide bagging	(a/20h/PA)

Table 4.5: Storage and cleaning conditions - series 2

cleaning agent	time before sol-gel application	time in sol-gel bath	time before curing laminate	abbreviation
[-]	[min]	[sec]	[days]	[-]
heptane	5	100	-	(h/5min/100)
heptane	30	100	-	(h/30min/100)
heptane	60	100	-	(h/60min/100)
heptane	90	100	-	(h/90min/100)
heptane	120	100	-	(h/120min/100)
heptane	5	150	-	(h/5min/150)
heptane	30	150	-	(h/30min/150)
heptane	60	150	-	(h/60min/150)
heptane	90	150	-	(h/90min/150)
heptane	120	150	-	(h/120min/150)
heptane	60	150	133	(h/60min/150/133)
heptane	120	150	133	(h/120min/150/133)

4.6 Results and discussion

Basically, a miscellaneous (adhesive–cohesive) failure mode is present at the interface and none of the specimens shows pure adhesive failure. As very different strength values are measured, this proves the achievement of a cohesive failure does not on its own guarantee a good bond.

The specimens manufactured with 8552/AS4 material predominantly show acceptable failure concerning the test standard DIN EN ISO 14130 [104] when testing at RT or -55°C. When using 977-2/IM7 material, only the pure CFRP specimens show acceptable failure modes. At 120°C the predominant failure mode is matrix shear failure as indicated in Figure 4.9. Therefore, an exception is made for the tests at elevated temperatures. Results are included in the analysis at 120°C test temperature when the failure mode is valid or a matrix shear failure is present. The same exception is applied to the 977-2/IM7 hybrid specimens.

In the following, only the results of specimens where the manufacturing includes the application of sol-gel are presented. The specimens without sol-gel are not tested as they show comprehensive delamination as a consequence of the cutting process. As the specimen size is comparatively small, delamination introduced at the edges has a great impact on the remaining undamaged area. When comparing different pre-treatment methods, only the best parameter combination for each method is presented in order to improve clarity.

Pre-treatment methods

The box-and-whisker plot in Figure 4.17 shows a comparison of the different pre-treatment methods under different test conditions in comparison to a pure CFRP laminate. A clear

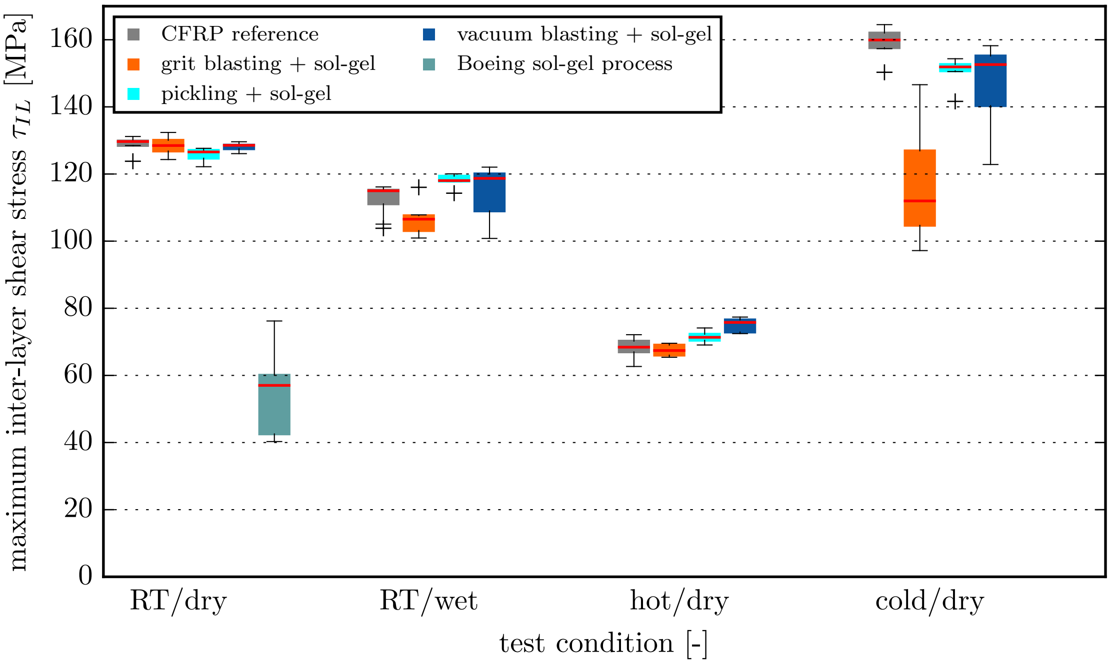

Figure 4.17: Box-and-whisker plot for ILSS comparing different treatment methods under different test conditions

comparison of the pre-treatment is possible as all processes include the application of the same sol-gel. The only exception is the BSP which includes the application of an additional primer as a final process step. Apart from this process, all methods show comparable ILSS at RT. Comparing median, boxes and whiskers, the three other methods show very similar results comparable with the pure CFRP reference. The median ILSS value for the BSP is around 55% lower than for the other three methods.

The ILSS is basically lower for the wet condition. All methods and the pure CFRP reference show a wider variation of the results except pickling. Pickling and vacuum blasting show higher ILSS then the reference pure CFRP and grit blasting. The strength is evenly reduced for all methods when tested at 120°C. Again pickling and vacuum blasting show higher strength than grit blasting and pure CFRP. There is fundamentally little variation of the results at elevated temperatures.

When compared to RT, ILSS is increased under the cold/dry test condition. For grit blasting results, only the strength is decreased and the variation of the results is increased drastically. Vacuum blasting results also show a comparably large variation. The median values of vacuum blasting and pickling are comparable, whereas the median of pure CFRP is slightly higher. Pickling shows the smallest deviations and comparably good results. The results under wet and cold conditions are particularly prominent. This is a contradiction to the findings of *Park et al.* which were mentioned earlier [84]. The reason could be the additional sol-gel which compensates the probable underlying poor durability. However, in a laboratory environment with recurrent small amounts of treatment being required at once, the effort in safety, preparation and cleaning is incomparably high. The grit blasting results under wet and cold conditions prove it to be less suitable than the vacuum blasting process. Additionally, it is not possible to grit blast larger surfaces without damaging the foil. Based on the results presented, vacuum blasting is selected for the following investigations.

Grit size for vacuum blasting

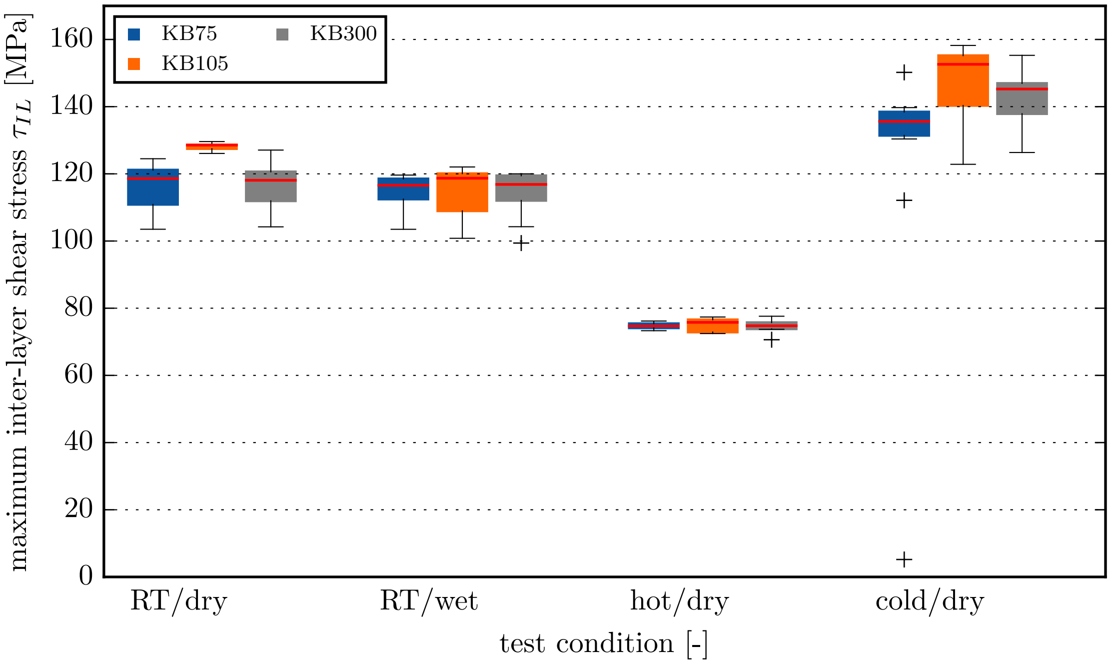

Figure 4.18: Box-and-whisker plot for ILSS comparing different grit size

The diagram in Figure 4.18 shows the ILSS under different test conditions for three grit sizes: 75, 105 and 300 μm. Regarding box size, whiskers and outliers, the variation in results is quite similar for all three processes. In contrast, the results for KB105 show very low variation at RT. Additionally, the KB105 grit results show the highest mean value under each test condition. The impact of the test conditions on the results is comparable with the previous investigations into the different methods. The related surface texture values R_a and R_z are specified in Table 4.6. When looking at the R_z results, the roughness increases with increasing grit size. The roughness is higher in the longitudinal than in the transverse directions for KB105 whereas the relationship is reversed for the other two grit sizes. Based on the R_a results, KB105 shows the highest values in the longitudinal and transverse directions compared to KB75 and KB300 but the relationship between the longitudinal and transverse directions is reversed in comparison to the R_z values. DIN EN ISO 4288:1998-04 [142] provides a relationship between the values R_a and R_z in terms of a scatter band. Most of the relationships measured are within the scatter band but some are slightly outside the range which is based upon chipping processes. However, the surface texture values do not provide a clear indication for the ILSS. Therefore, the selection is based on the ILSS results only and a grit size of 105 μm is selected for all subsequent experiments.

Table 4.6: Steel surface roughness depending on grit size

grit size	R_a long.	R_a trans.	R_z long.	R_z trans.
[μm]	[μm]	[μm]	[μm]	[μm]
75	0.7	0.33	1.5	1.6
105	1.28	1.55	3.7	2.11
300	1.01	0.86	3.91	5.7

Cleaning and storage conditions

Test series 1 aims to investigate the impact of storing time and bagging material before the application of sol-gel. ILSS is compared with the reference group values where sol-gel is applied immediately. ILSS results are depicted in the box-and-whisker plot in Figure 4.19. The group consists of two results, the first without any cleaning after vacuum blasting and the second with acetone swiping. The next two groups consider a storage duration of 20 hours in an aluminum bag and a polyamide vacuum bag, respectively. This corresponds to storing the specimens over night and applying sol-gel the next day. Both groups consist of values without cleaning and with acetone swiping. It emerged from these tests that the cleaning process is required to prevent contamination of the sol-gel bath. Therefore, considering the cleaned groups only storage in an aluminum bag increases ILSS whereas polyamide decreases it.

The second option to increase flexibility in the manufacturing process is to apply sol-gel immediately after pre-treatment and then store the sol-gel coated foil. Tests showed no considerable influence on ILSS when laminating the specimens within 24 hours. This confirms the specifications provided by the manufacturer [126]. Therefore, test series 2 also aims to investigate the impact of storage time before sol-gel application, but with storage durations of 5, 30, 60, 90 and 120 minutes. Additionally, two dipping durations are considered: 100 and 150 seconds. The ILSS results are shown in Figure 4.19. Comparing mean values as well as box size and whiskers, there is no clear indication of any benefit resulting from increasing storage time or dipping time within the range considered All results show relatively low variation and comparable median values. An additional comparison with specimens being stored for 133 days after sol-gel treatment before lay-up and curing, however, shows a considerable decrease in ILSS and increase in variation. This result clearly shows that for the aim of separating the process steps from each other in place and time, a protective layer is required in addition to the sol-gel.

Following the specifications of *BR127* 'primed assemblies which have been cured and wrapped with a protective covering such as Kraft paper may be stored at 24°C for six months or longer without fear of degradation of the final bond' [96]. Test series 3 does not consider the storage time after application of the primer. Instead, a comparison is performed to specimens without primer. Therefore, 977-2/IM7 prepreg is used in addition to 8552/AS4, see ILSS results in Figure 4.20. As discussed at the beginning of this chapter, these results must be regarded warily as the hybrid specimens with 977-2/IM7 show matrix shear failure. Therefore, the following comparisons are performed within one material group. Comparison of the 8552/AS4 (orange) with its primered counterpart (blue) shows clearly that ILSS is increased by 5% (RT/wet) to 22% (RT/dry) and only

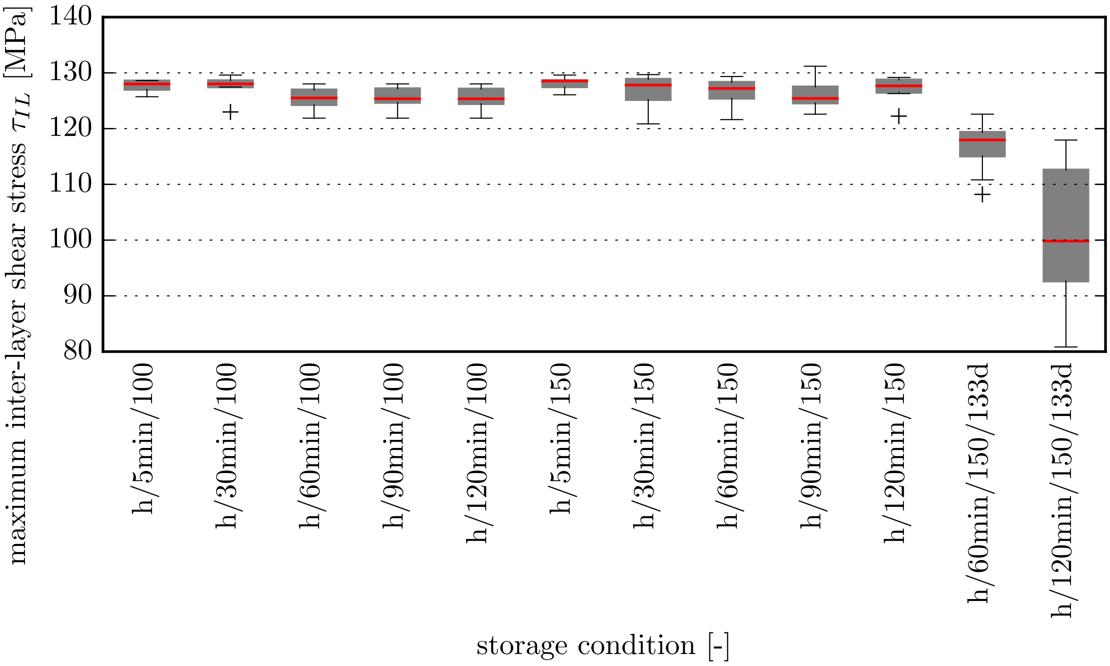

Figure 4.19: Box-and-whisker plot for ILSS comparing different storage conditions (cleaner h: heptane/time spent before sol-gel application [minutes]/time in sol-gel bath [seconds]/time before curing laminate [days])

slightly decreased (3%) under the hot/dry condition. Comparing box size and whiskers, variations are considerably reduced by the primer.

Regarding 977-2/IM7 (cyan) and its primered counterpart (green), strength is only increased for the primered version at RT whereas the values are comparable under the other test conditions. For this material group variations of the results are slightly increased when the primer is used.

However, the results also indicate that the use of a primer is an option without considerable penalty on ILSS. This requires further investigations into ILSS depending on the storage time of the primered metal foil. When undertaking further investigations into the ILSS of toughened prepreg systems such as 977-2 it is advisable to include previous tests on the testing geometry, especially on the distance L_{sup} between the supports and the laminate thickness L to achieve a shear failure in one or multiple planes.

4.7 Discussion of hypothesis addressed

As different treatments for the steel surface were considered and other parameters were kept constant, the differing results can be attributed to the surface treatment itself.

However, the interlaminar shear strength is not measured directly, but the relationship between the results of the ILSS-test and the interlaminar shear strength is linear, as shown by *Chatterjee* [114].

The proof of hypothesis 3 is therefore obvious when considering the results and their variation. Based on the variations, a clear advantage of certain treatments over others is shown, which at the same time proves that the surface treatment exerts an essential

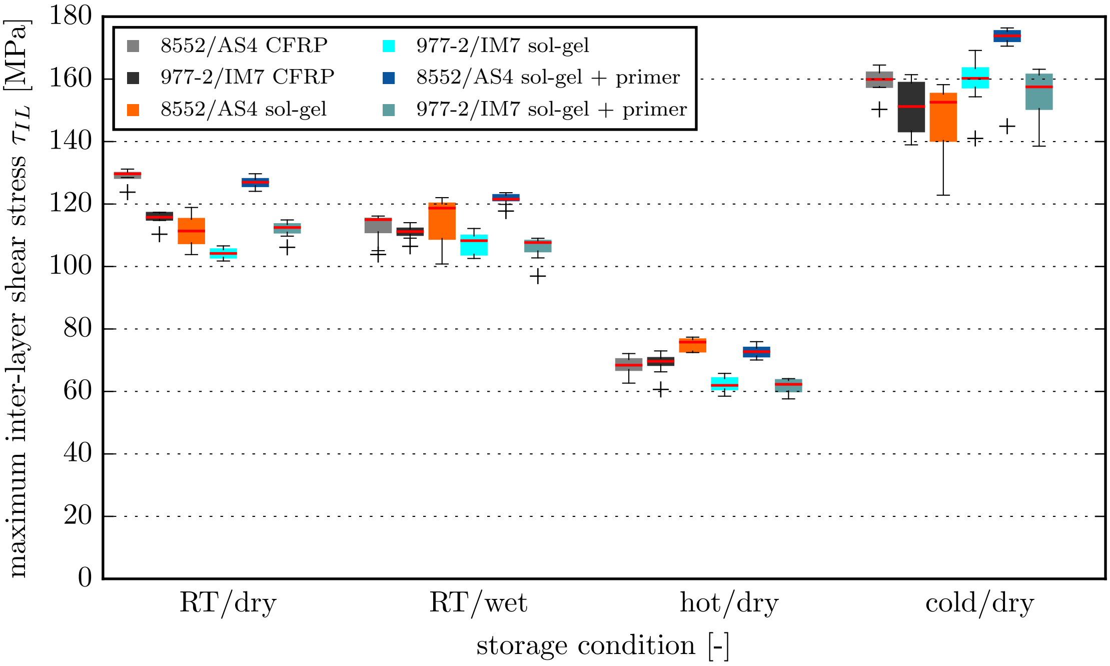

Figure 4.20: Box-and-whisker plot for ILSS comparing primered and non-primered specimens under different test conditions

influence on interlaminar shear strength.

Based on the information available in the literature, it is assumed that the chemical composition of the surface is very time sensitive and changes quickly after each treatment. Therefore, the chemical composition of the surface is not determined to assess its impact on shear strength as many tests would be required. An empirical approach is selected instead, and the time passing after treatment and before the application of sol-gel is varied. In addition, the material in which the treated foils are stored is varied. It is assumed that the material and the time both have an impact on the chemical composition of the surface but do not influence any other relevant parameter. As both variations have a significant influence on the shear strength, it may be deduced that only the change in the chemical composition accounts for this shear strength change.

5 Process-induced residual stress

Link to hypothesis: The assumption that the residual thermal stresses directly depend on the difference between cure temperature and operational temperature is investigated in this chapter and thereby addressing hypothesis 4.

Summary: The discussions in chapter 3 showed that the thermal residual stresses reduce the materials exploitation drastically, in particular for low metal volume fractions. However, these calculations are based on the assumption that the stress level depends on the difference between cure and operational temperature.

Investigations with respect to process-induced deformations, which are presented here in excerpt, indicate that a shear interaction between the plies may be present. This interaction may reduce the residual stresses and lead to a stress-free temperature below cure temperature.

Residual thermal stresses for the material combination at hand are regarded with respect to the steel volume fraction and the restriction of different models is considered.

Different methods for the evaluation of the residual stresses are discussed and three approaches are selected. Finally, specimens are manufactured and the pressure is modified to consider the influence of the ply interaction discussed. Additionally, the temperature process is modified and an expansion clamp is applied in order also to evaluate other methods for stress reduction.

5.1 Literature review

The residual stress state within an FML does not depend only on the material constituents. It is true that the materials define stiffness and CTE, but the volume fraction, curing temperature and operational temperature are also major parameters. Therefore, concerning residual stresses, a classification with regard to the application seems to be more constructive.

The most prominent FML is the glass fiber reinforced laminate GLARE as it is used in the upper panels of the A380 to extend fatigue life. The aluminum used has a Coefficient of Thermal Expansion (CTE) 3.8 times higher than the GFRP which shows a slightly lower stiffness [143]. In the transverse direction the CTE of both constituents is nearly equal. Thermal residual curing stresses are therefore comparatively low in contrast to any combination with CFRP [97, 144, 145].

However, some combinations with CFRP are quite promising, hence the increasing interest in research to counter this difficulty in recent years. For example, TiGr (Titanium Graphite) and HTCL (Hybrid Titanium Composite Laminate) have been investigated by Boeing and NASA to provide high specific stiffness and strength at environments with high temperatures [146].

In another application, local steel or titanium reinforcements increase the bearing strength [4–6]. Fundamentally, the thermal compatibility of titanium and CFRP is advantageous when compared to steel and CFRP. Metallic sheets replace single CFRP layers in the joining area allowing an increased joining capacity when compared to pure CFRP laminates.

The stress state at the free edges is different to the stress state on the global part. Therefore, the load introduction at open edges, or bolts in particular, is of particular interest as bearing loads and thermal shear and peel stresses superimpose in these areas.

However, thermal residual stresses are also of interest in pure composite parts, particularly at very low operational temperature [36, 147, 148].

Effects of residual stresses

Depending on the application under consideration, the residual stresses demonstrate different effects. In most material combinations the composite shows lower CTE in fiber, and therefore in the main load direction, than the metallic constituent. As operational temperature is generally lower than cure temperature, a tensile stress state is present in the metallic part which may increase fatigue.

The thermal edge effect basically lowers strength and enhances delamination or crack growth in pure composite, as well as in FML. Over the last thirty years, many investigations have been carried out on predicting stresses and ply delamination in the region of free edges of laminated plates subjected to axial strain [149]. For instance, *Herkovich* used the finite element method (FEM) to investigate the thermal edge effect of boron/epoxy in combination with aluminum and titanium [150].

However, most of the investigations focus on pure composite parts as matrix failure [151], delamination [152] and fatigue crack propagation [153] are enhanced as a consequence of thermal residual stresses. A further FEM based investigation on 0°/90° laminates showed that the theoretical uniaxial tensile strain to failure is reduced by 45% as a consequence of thermal stresses.

Another field of major interest is the distortion of parts as a consequence of induced stresses [154–165]. Some of the distortion phenomena depend on temperature and some are irreversible. However, they are all driven by a stress gradient within the part.

Measuring residual thermal stresses

A relatively simple method to evaluate the stress in a laminate is by manufacturing an asymmetrical specimen and measuring its curvature at a reference temperature. This method is applied for FML [166–168] as well as for pure composite laminates [35, 158, 169]. Another method is the incremental hole drilling technique [170], which uses the deformations accompanying the stress relief induced by the hole to conclude the original residual stress.

However, these methods offer the possibility of drawing conclusions from the stress state after cure, but do not give the opportunity to observe the stress formation itself.

Alternatively, fiber bragg gratings (FBGs) sensors are embedded in the composite to measure the strain at one or multiple points along the fiber [171, 172] or discrete spots of the prepreg are pre-cured and strain gauges are bonded [173], allowing strains to be measured throughout the cure cycle.

With the help of the Cure Reference method [174], the residual strain in composites can be determined. A laser-based optical method of Moiré Interferometry captures strains on the laminate's surface. The method requires a high frequency diffraction grating on the specimen while in the autoclave. The grating cures with the composite and carries the same thermal strain and chemical shrinkage as the specimen. On a metal surface, x-ray diffraction and neutron diffraction provide similar possibilities [175].

Reducing residual stresses

Different investigations have been performed in order to reduce residual stresses in pure composite as well as in fiber metal laminates. Some approaches utilize modifications of the temperature process known as 'smart cure cycles' [163, 168, 176–178] for which a detailed investigation into the curing kinetics of the resin system is required [179, 180]. Another approach pursued by *J. Xue et al.* [181] is clamping the laminate to compensate the lower thermal strain of the composite layer by elastic strain that is induced by a massive steel tool which has a higher CTE or a similar tool to induce compression during co-curing of aluminum hybrid shafts [182]. A further approach is called 'post-stretching' and was investigated for GLARE-laminates [29]. The cured laminate is stretched above its yield point to lower residual stresses and fatigue progression of the metallic constituent. However, this approach was never used industrially due to the obvious difficulties in load introduction and necking of the metallic sheets. As reported earlier, residual stress reduction is of interest in pure composite as well, where cure cycles are modified with the same aim [178].

5.2 Present chapter's structure

The further procedure pursued in the present chapter is subdivided into five following subchapters, as shown in Figure 5.1.

Different models to describe the intra- and interlaminar stress state and related assumptions are considered in the first of the subsequent subchapters. The plane stress assumption is applied to the FMLs and compared with the simple ROM considered in chapter 3.4.

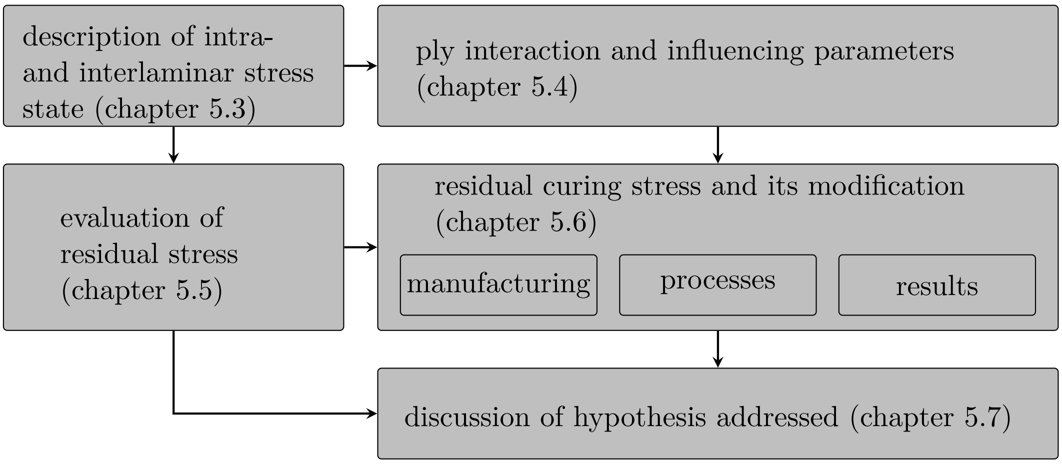

Figure 5.1: Flowchart describing the procedure pursued in chapter 5; single subchapters marked in gray

Ply-interaction, a topic known from investigations on process-induced deformations, is subsequently discussed. Some former findings of the author are presented and their impact on FMLs is considered. The interaction process provides the fundamentals for some modifications tested later.

Firstly, different approaches for the evaluation of residual stresses are discussed and the required equations are derived. Some analytical models are compared with respect to their applicability and a procedure for the evaluation is selected for the assessment of the modifications performed in the subsequent subchapter.

Different procedures are tested there to clarify whether any enable reduction of the stress level. Pressure and temperature processes are varied and steel clamping is considered. The results are compared and the potential for further investigations is identified. Finally, the impact of the findings on hypothesis 4 addressed earlier is discussed.

5.3 Intra- and interlaminar stress state

An estimation of the fiber metal laminate's yield strength under consideration of residual curing stresses was performed in chapter 3.4 using an approach without consideration of restrained transverse contraction. This former method is based on the ROM. However, for a more detailed investigation, the constraining effect of the adjacent layers on the transverse strain of the individual layer is required. Therefore, the plane stress state is considered in the following by using the CLT to investigate the metal volumes impact on the intralaminar stress.

The required formulae are introduced first and then the relationship between fiber type and metal volume fraction is discussed for the longitudinal and transverse directions.

Thereafter, these relationships are investigated for the interlaminar stresses which induce shear and peel stresses at the laminate edges.

Thermal stress formulation in plane stress state

In chapter 3.4 it was sufficient to determine the two different constituents, whereas a layer-wise determination is required for the plane stress state due to the coupling between the single layers. The CLT is based on the assumptions that the strains vary linearly through the thickness of the laminate. According to the CLT, the loads N and moments M are obtained by [16]:

$$\begin{Bmatrix} N_x \\ N_y \\ N_{xy} \\ M_x \\ M_y \\ M_{xy} \end{Bmatrix} = \begin{vmatrix} [A] & [B] \\ [B] & [D] \end{vmatrix} \begin{Bmatrix} \epsilon_x^\circ \\ \epsilon_y^\circ \\ \gamma_{xy}^\circ \\ \kappa_x \\ \kappa_y \\ \kappa_{xy} \end{Bmatrix} - \begin{Bmatrix} N_x^T \\ N_y^T \\ N_{xy}^T \\ M_x^T \\ M_y^T \\ M_{xy}^T \end{Bmatrix} \tag{5.1}$$

where the first part describing the plate stiffness and compliance with the 3 x 3 matrices [A], [B] and [D] is extended by the thermal loads and thermal moments indicated by the superscript 'T'. The thermal loads N^T and thermal moments M^T per unit length are

$$\begin{Bmatrix} N_x^T \\ N_y^T \\ N_{xy}^T \end{Bmatrix} = \Delta T \sum_{k=1}^{N} [\bar{Q}]^k \begin{Bmatrix} \alpha_x \\ \alpha_y \\ \alpha_{xy} \end{Bmatrix} t_k \tag{5.2}$$

$$\begin{Bmatrix} M_x^T \\ M_y^T \\ M_{xy}^T \end{Bmatrix} = \Delta T \sum_{k=1}^{N} [\bar{Q}]^k \begin{Bmatrix} \alpha_x \\ \alpha_y \\ \alpha_{xy} \end{Bmatrix} t_k \hat{z}_k \tag{5.3}$$

where t_k and $\hat{z}_k$ are the thickness and middle surface coordinate of the k-th ply in the laminate respectively. The different α variables describe the CTE in the laminate's global coordinate system. The midsurface strains and curvatures of the laminate are evaluated by adding N^T and M^T to their mechanical counterparts N and M in formula 5.1.

The strains at the midsurface of a laminate free to expand can also be described by the apparent laminate thermal expansion coefficients α_x°, α_y°, α_{xy}° as given in:

$$\{\epsilon^\circ\} = \Delta T \begin{Bmatrix} \alpha_x^\circ \\ \alpha_y^\circ \\ \alpha_{xy}^\circ \end{Bmatrix} \tag{5.4}$$

and for the non-symmetric case with the thermal curvatures:

$$\{\kappa\} = \Delta T \begin{Bmatrix} \alpha_x^* \\ \alpha_y^* \\ \alpha_{xy}^* \end{Bmatrix} \tag{5.5}$$

Substituting formula 5.4 and 5.5 in 5.1 with no mechanical loads and moments present ({N}={M}=0), the apparent thermal laminate expansion coefficients are given by:

$$\begin{Bmatrix} \alpha_x^\circ \\ \alpha_y^\circ \\ \alpha_{xy}^\circ \\ \alpha_x^* \\ \alpha_y^* \\ \alpha_{xy}^* \end{Bmatrix} = \frac{1}{\Delta T} \begin{vmatrix} [A] & [B] \\ [B] & [D] \end{vmatrix}^{-1} \begin{Bmatrix} N_x^T \\ N_y^T \\ N_{xy}^T \\ M_x^T \\ M_y^T \\ M_{xy}^T \end{Bmatrix} \tag{5.6}$$

For the simple case of a symmetric FML with one fiber direction, the residual stress components in the metal layer are obtained by:

$$\sigma_{M,R,long} = [Q_{11,M}(\alpha_x^\circ - \alpha_M) + Q_{21,M}(\alpha_y^\circ - \alpha_M)]\Delta T \tag{5.7}$$

$$\sigma_{M,R,trans} = [Q_{21,M}(\alpha_x^\circ - \alpha_M) + Q_{22,M}(\alpha_y^\circ - \alpha_M)]\Delta T \tag{5.8}$$

for the longitudinal and transverse direction respectively. The residual stresses in longitudinal and transverse direction in the composite layer are given by:

$$\sigma_{C,R,long} = [Q_{11,C}(\alpha_x^\circ - \alpha_{11,C}) + Q_{21,C}(\alpha_y^\circ - \alpha_{22,C})]\Delta T \tag{5.9}$$

$$\sigma_{C,R,trans} = [Q_{21,C}(\alpha_x^\circ - \alpha_{11,C}) + Q_{22,C}(\alpha_y^\circ - \alpha_{22,C})]\Delta T \tag{5.10}$$

For further information see *Cowley and Beaumont* [169], where a similar approach based on apparent thermal expansion coefficients is discussed.
The interlaminar shear stress at an arbitrary position is calculated by equation 4.23. With the equations 4.24-4.30, the thickness of the metal and composite layer t_M, t_C and the *Poisson's* ratio ν_{12} of metal ν_M and composite layer ν_C, the maximum shear stress is given by:

$$\tau_{max} = \frac{\Delta T \Delta\alpha}{\pm\sqrt{\frac{\frac{t_M^2}{12D_M}+\frac{t_C^2}{12D_C}+\frac{(t_C+t_M)^2}{12D}}{\frac{2t_M}{3E_M}(\nu_M+1)+\frac{2t_C}{3E_C}(\nu_C+1)}}\left(\frac{2t_M}{3E_M}(\nu_M+1)+\frac{2t_C}{3E_C}(\nu_C+1)\right)} \tag{5.11}$$

Investigation of intralaminar stress

The residual normal stress in the laminate layer - the intralaminar stress - depends on the metal volume fraction φ_M and in the case of the UD-CFRP-steel laminate, differs in longitudinal and transverse direction, as indicated in Figures 5.2 and 5.5. The first

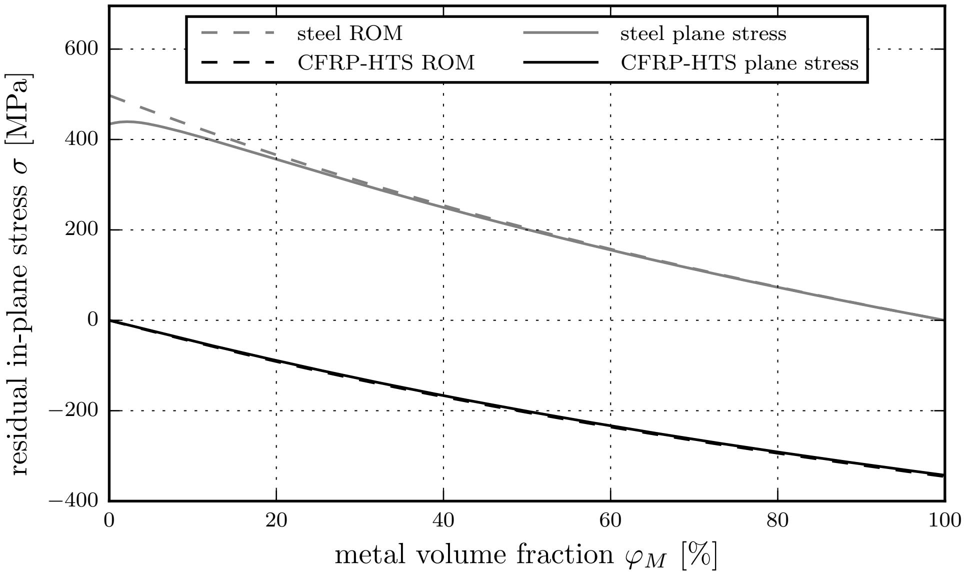

Figure 5.2: Residual stress dependency on metal volume fraction of a UD-CFRP-steel laminate with HTS-fibers for one dimensional ROM and plane stress calculation in longitudinal direction for ΔT=157 K

diagram shows the dependency on φ_M in longitudinal direction at ΔT=157 K which corresponds with a stress free temperature T_{sf}=180°C (the curing temperature of the prepreg systems under consideration) and an operational temperature T_{op}=23°C. The residual stress characteristics are also shown for the ROM-model discussed earlier, without consideration of transverse contraction constraint. The stress in the steel layer converges to zero at high volume fractions and maximum tensile stress is reached at low metal volume fractions. According to this, compressive stress in the composite reaches its maximum value when composite content is low.

The maximum tensile stress in the steel part is higher than the absolute value of the stress in the composite as the stiffness of steel is higher.

The characteristics are identical but the values are increased for an increased absolute value of ΔT. Comparing Figure 5.2 (ΔT=157 K) and Figure 5.3 (ΔT=235 K) the absolute values for tensile and compressive stress are increased proportionally. Comparing the maximum tensile stress in steel, the maximum stress value obtained by the plane stress calculation is increased from 440 MPa to 658 MPa when decreasing operational temperature T_{op} to -55°C.

However, particularly at the low metal volume fractions preferred for UD-CFRP-steel laminates, a deviation between the two models is present. The plane stress model takes into consideration that the compressive transverse strain in the steel part is high at low metal volume fractions and the associated contraction in longitudinal direction reduces the effective thermal elongation. This deviation between the two models can be seen in Figure 5.2 and 5.3.

This is not the case for a UD-CFRP-steel laminate with IM-fibers as shown in Figure 5.4. The transverse CTE of the IM composite layer is much lower and only 15% higher than the steel CTE. There is no contraction in longitudinal direction with its source in transverse strain. Hence, plane stress results are not lower than those calculated by the ROM-

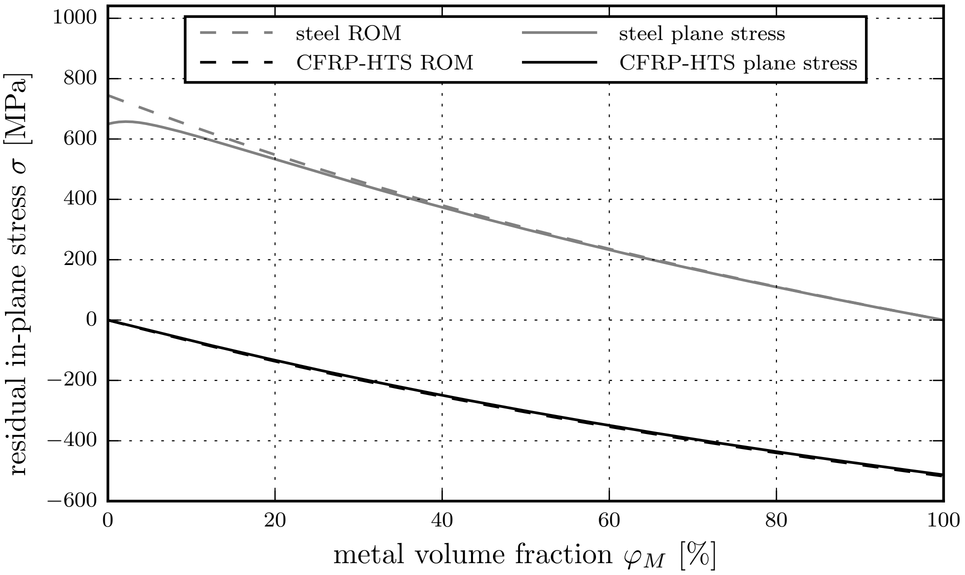

Figure 5.3: Residual stress dependency on metal volume fraction of a UD-CFRP-steel laminate with HTS-fibers for one dimensional ROM and plane stress calculation in longitudinal direction for ΔT=235 K

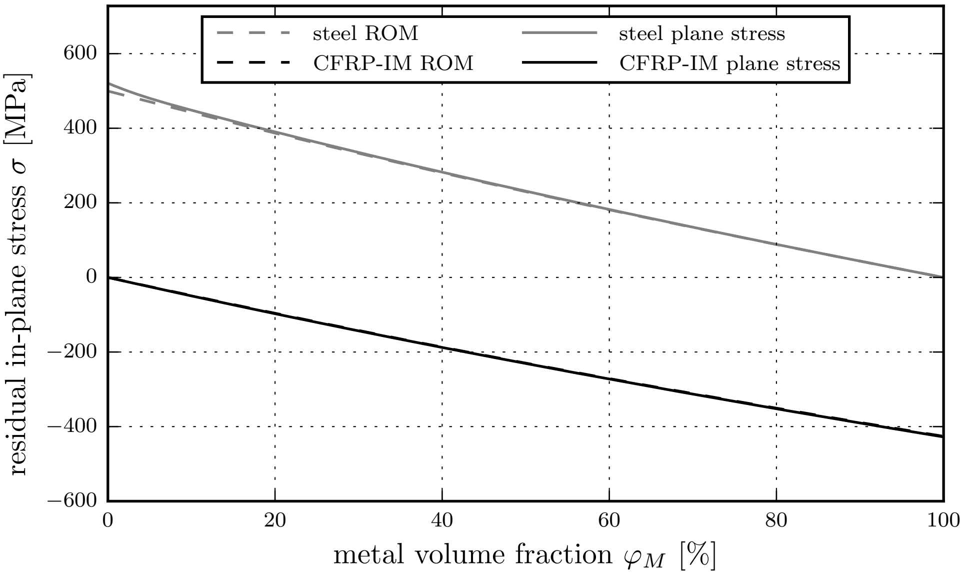

Figure 5.4: Residual stress dependency on metal volume fraction of a UD-CFRP-steel laminate with IM-fibers for one dimensional ROM and plane stress calculation in longitudinal direction for ΔT=157 K

approach. Instead, the stress calculated at low metal volume fractions are even higher compared to the one-dimensional ROM model.

Regarding the transverse direction, the relationships of the thermal expansion coefficients reverse. The CTE of the composite is higher than the CTE of steel. The results of the unidirectional models for HTS-fiber reinforcement in Figure 5.5 and for IM-fiber reinforcement in Figure 5.6 show identical relationships. Although inverted in comparison to the longitudinal direction, again, the stresses in the steel layer reach their maximum for low metal content and stresses in the composite layer achieve their maximum values for low composite content. However, the absolute values of compression stress in steel reach values many times higher than the tensile stress of the composite as the stiffness of the composite in transverse direction is many times lower.

Comparing the two models, the plane stress assumptions leads to lower absolute stress values for the HTS-fiber reinforcement, but shows a similar relationship as the ROM-approach, see Figure 5.5. The metal layers are under tension in longitudinal direction and their transverse contraction reduces the effective elongation, resulting in lower absolute compression stress values when contraction restraining is considered. For IM-fiber reinforcement, the contraction of the metal in transverse direction is larger than the difference of thermal strains between steel (16.4×10^{-6}/K) and composite (19×10^{-6}/K). This leads to tensile stress in the metal part and compression stress in the composite, see Figure 5.6. This is contrary to the stresses obtained by the ROM-model. In this case the error is considerable for low metal volume fractions, as for steel a compression stress of 63 MPa is determined by the ROM-approach at φ_M=1% and a tensile stress of 61 MPa is calculated with the CLT for the identical metal volume fraction.

Investigation of interlaminar stress

The shear stress distributions as well as their maximum values depending on the metal volume fraction φ_M are calculated. For the stress distribution, the metal volume fractions of 10 and 20% are regarded exemplary. In addition 1 and 4 mm laminate thickness are

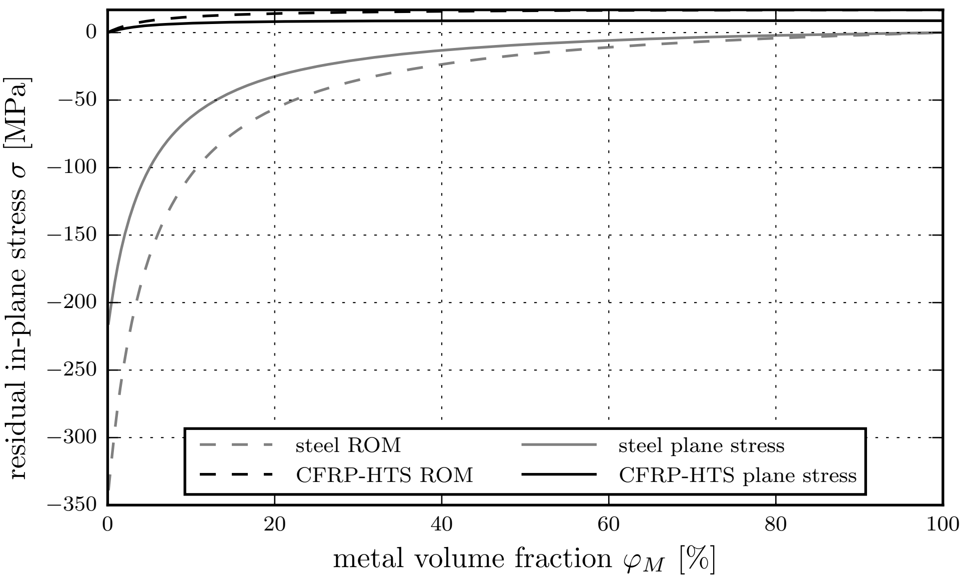

Figure 5.5: Residual stress dependency on metal volume fraction of a UD-CFRP-steel laminate with HTS-fibers for one dimensional ROM and plane stress calculation in transverse direction for ΔT=157 K

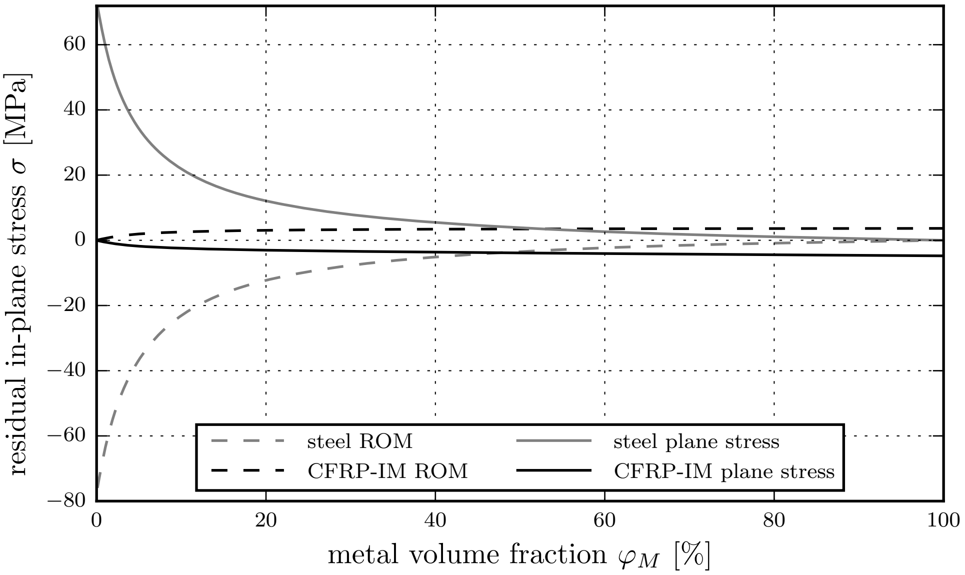

Figure 5.6: Residual stress dependency on metal volume fraction of a UD-CFRP-steel laminate with IM-fibers for one dimensional ROM and plane stress calculation in transverse direction for ΔT=157 K

considered. The regarded laminate consists of two layers only and the curvature is not permitted. This correlates with the consideration of one half of a symmetrical laminate. The values are shown for a stress-free temperature T_{sf}=180°C and an operational temperature T_{op}=23°C.

The shear stress distribution depending on the edge distance x is presented in Figure 5.7 for HTS-fibers and in Figure 5.8 for IM-fibers. The relationship between the two fiber types is identical to the normal stress as the longitudinal shear stresses are higher for IM-fibers than for HTS-fibers, but transverse shear stresses are very small for IM-fibers due to the lower CTE. The maximum shear stress value depends on the metal volume fraction and is higher for φ_M=20%. However, the stress distribution depends on the layer thickness and the shear stress, as expected, drops much more quickly for lower laminate thickness. This means that any shear failure may grow faster as the total shear load at the part's end is larger.

The maximum shear stress values depending on the metal volume fraction are shown in Figure 5.9 for both IM and HTS fiber types, in the longitudinal direction and for two different temperature differences. With increasing content of any of the two constituents, the shear stress in the longitudinal direction increases and it converges to zero for very low content of any of the two. The maximum shear stress values reach their maximum at around 20% and 80% metal volume fraction.

When metal content is low, the metal layer is very thin and the laminate CTE is dominated by the composite. This leads to very high tensile stresses in the metal. However, the shear stress to be transferred between the two constituents is very low as the load in the metal layer is low. Increasing metal volume fraction to around 20%, the CTE is still dominated by the composite but the metal layer is thicker and the loads are higher. This leads to one of the two maximum shear stress values. Increasing the metal volume fraction to around 50%, the difference between the metal's and the laminate's CTE is smaller and

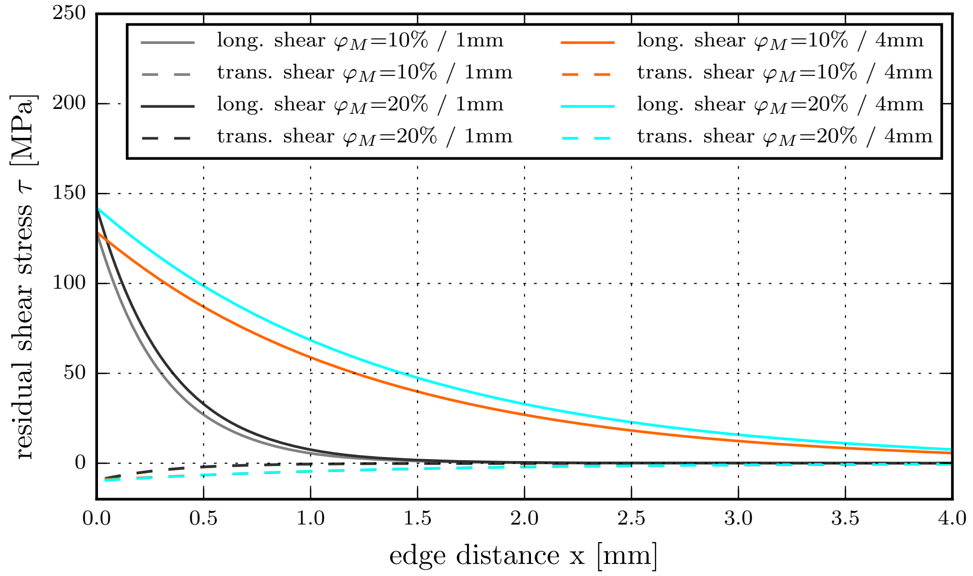

Figure 5.7: Shear stress distribution at the free edge of UD-CFRP-steel laminates with HTS-fibers in longitudinal and transverse direction for ΔT=157 K

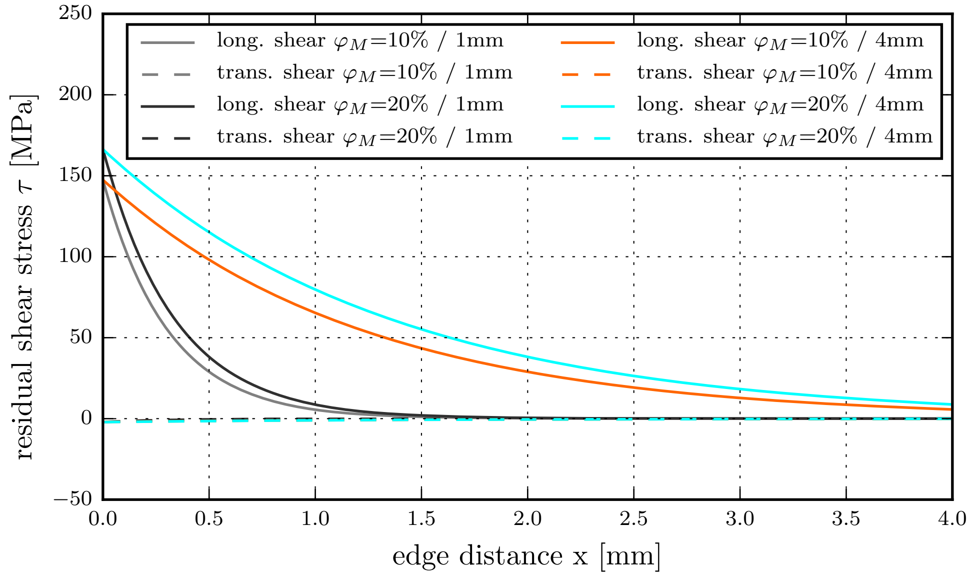

Figure 5.8: Shear stress distribution at the free edge of UD-CFRP-steel laminates with IM-fibers in longitudinal and transverse direction for ΔT=157 K

although the metal layer is thicker, the shear stress is reduced again. The next maximum at around 80% is due to the high difference in CTE between laminate and composite, as the laminates CTE is dominated by the metal.

Due to the higher stiffness of steel, the second local maximum is higher. The position of the two peaks depends on the stiffness relationship of the two materials. When regarding

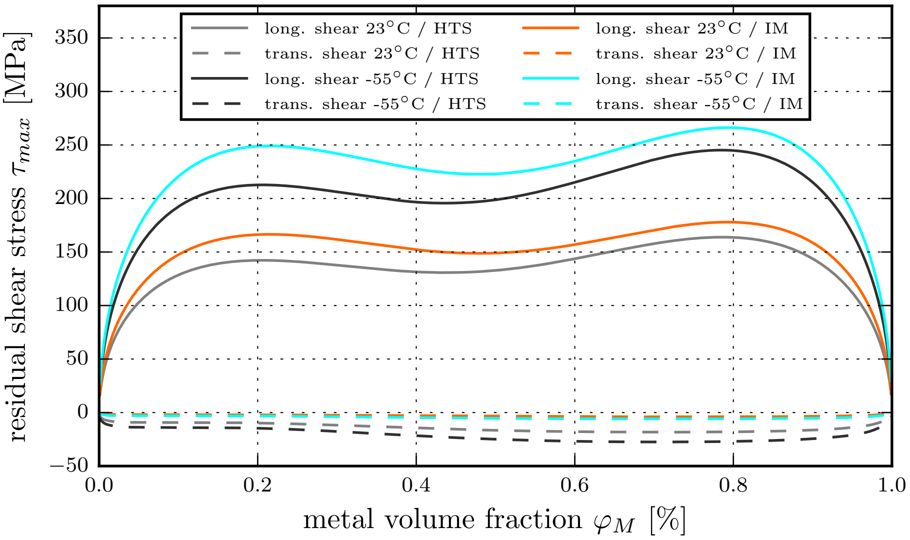

Figure 5.9: Maximum shear stress dependence on metal volume fraction φ_M of UD-CFRP-steel laminates with HTS- and IM-fibers in longitudinal and transverse direction for ΔT=157 K and ΔT=235 K

aluminum with CFRP, the first peak is reached at higher metal volume fraction and is much higher than the second peak.

The calculated shear stress is very high. At 20% metal volume fraction the maximum shear stress in longitudinal direction reaches around 140 MPa for HTS and around 165 MPa for IM fibers at RT. For the cold operational temperatures the values are even higher.

The maximum shear stress is higher than the measured shear strength. As this peak is reached at the very end of the specimen or part, different phenomena may reduce the peak stress. Any inter-fiber fraction reduces the maximum value and very local relaxation may also be present.

However, the results clearly indicate that the shear strength of the laminate is locally exceeded although no stresses other than the residual thermal stresses are present. The shear stress distribution of thinner laminates with a smaller area of the part where it is actually present, represents a more favourable stress state, as this distribution is more beneficial for the local reduction of the stress peak by local inter-fiber fracture or relaxation.

5.4 Ply interaction and influencing parameters

As discussed in the 'Literature revue' chapter, different mechanisms to reduce residual stresses in fiber metal laminates have been investigated and published in the literature.

However, one mechanism has not been considered before: the mechanical interaction between the metallic and composite layers on the inter-ply level during the curing process, particularly during heating.

Investigations performed by *Twigg et al.* [31,183] showed that there is even a stress transfer between tool and part, despite the use of release agents, which induces a stress gradient in a flat laminate resulting in curved parts when laminate thickness is low. *Kappel et al.* and *Stefaniak et al.* identified that these curvatures and, therefore, the induced shear stress depends on the surface roughness and the prepreg type, in particular the prepreg architecture [30, 32].

The metal surface in an FML is prepared in a manner intended to increase adhesion. Hence, a comparably high interaction can be expected. Two models for tool-part interaction which can be applied to the interaction within an FML are discussed in the literature.

In an open mould process the autoclave pressure is applied to the flexible membrane, compensating the change in laminate thickness and continuously generating a normal force [184]. Even at low degrees of cure, prior to resin gelation, considerable stress interaction between tool and part is observed [31, 180, 185–187]. This interaction is believed to be a consequence of fiber friction at the interfaces due to the normal force being shared by the fibers and the resin [188].

A common model, used to describe this mechanism [173, 183, 186] is based on inter-ply slippage. Tows close to the metallic tool surface are in tension and a gradient of tensile stress, due to inter-ply slippage is locked in during vitrification. For FML this is shown in Figure 5.10 on the left, where the adjacent metal layers in gray introduce tensile stress to the black colored CFRP layers. Due to equilibrium of forces, this induces a compression stress in the metal layers. The original length of the plies at RT is identical for both constituents. The white areas show the free thermal elongation and the blue areas mark the mechanical elongation of both materials. The free thermal strain of CFRP is very low or even negative for some laminates depending on the fiber type which is indicated by a negative elongation. This is marked by a white area reducing the length of the CFRP layers compared to RT. The higher CTE of the metal layer is indicated by a positive elongation at curing temperature. Any interaction between the single plies induces a tensile mechanical strain in the CFRP plies and a compressive mechanical strain in the metals layers, both indicated by a blue coloring. In the compression case it is subtracted from the thermal elongation and in the tension case it is added.

However, by direct measurement of the interfacial shear stress transfer, *Martin and Seferis* [189] as well as *Larberg and Akermo* [190] showed that the inter-ply friction depends on the prepreg generation and *Ersoy et al.* [186] showed that prepreg/prepreg interfaces have a better stress transfer compared to prepreg/tool interfaces for the material system at hand. Due to this conclusion, inter-ply slippage caused by tool-part interaction is unfeasible. Hence, another model was proposed by *Stefaniak et al.* based on frozen deformations in the matrix [30]. *Svanberg and Holmberg* [191] discussed frozen deformations in connection with the 'spring-in'-phenomenon. The extended relaxation times in the transition state

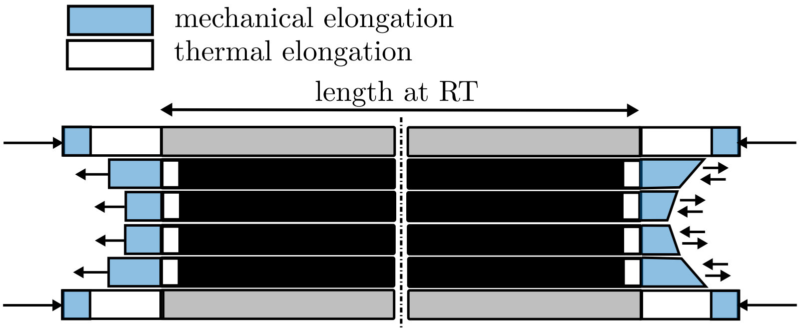

Figure 5.10: Inter-ply slippage left and frozen shear strain right for a symmetrical laminate with metal (gray) and CFRP (black)

from glassy to rubbery, explain the ability of polymers to freeze deformations obtained in the rubbery state [159]. When vitrification takes place during heat-up and a tensile stress σ_{vit} is present, the resin transforms at point 3 in Figure 5.11 at the current strain ϵ_{rub}. At glassy state the molecular mobility is limited and large molecular elements, aligned under external load in rubbery state, cannot return to their equilibrium position [159]. After unloading in glassy state with a higher stiffness, a frozen strain ϵ_{froz} results at point 2, due to the difference between rubbery and glassy strain $\epsilon_{froz} = \epsilon_{rub} - \epsilon_{glass}$. A similar relationship is assumed for shear γ when a shear stress τ is present. This relationship is shown in Figure 5.11 on the right. Regarding the FML, only the CFRP layers are sheared or a combination of shear and tensile loading is applied by the adjacent metal layers, as indicated in Figure 5.10 on the right. A stress gradient is locked in after curing which reduces the stress level when the part is cooled down.

The mechanism described in 5.10, is significant on the macro and micro levels as long as there are layers with approximately constant moduli and layers with cure dependent moduli. Therefore, the cure-dependent layers may represent the matrix in-between individual fibers or neat resin areas in-between prepreg layers, whereas the latter exhibit a higher Young's modulus on average compared to the neat resin areas. This mechanism leads to the assumption that the effect of tool-part interaction on distortion is higher for laminates with thicker interleaved resin layers but the effect on residual stress reduction is higher for laminates with thinner or no interleaved resin layers.

Regardless of which model may be more appropriate or which combination of both reflects the process best, any mechanical interaction must reduce the stress level at RT. Hence, it can be assumed that as a consequence of the interaction generated by the autoclave pressure, the stress-free temperature T_{sf} is lower than curing temperature $T_{cure,max}$, although no further modifications are performed. Besides prepreg architecture and surface roughness other influential parameters on the stress interaction can be deduced.

Intrinsic parameters are stiffness ratio of composite and metal as shown in the previous chapter, composite lay-up, the resin's gel temperature and glass transition temperature as well as the resin's CTE in glassy and rubbery state. Extrinsic parameters may be further classified in process and tooling related parameters. Process-related parameters are temperature and pressure characteristics. The tooling-related parameters describe

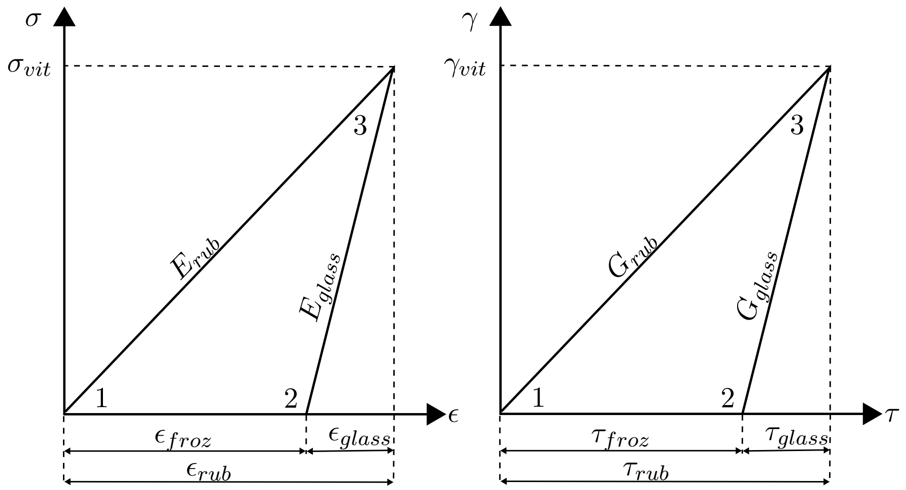

Figure 5.11: Frozen tensile and shear strain in resin layer or inter-fiber area at cure temperature

each influence on the interaction between the laminate and its environment, also increasing and decreasing the influence of process-related parameters: tool CTE and stiffness, tool surface roughness, geometrical locking between tool and laminate as well as any operating consumable such as fluorinated ethylene propylene (FEP)-release foil, bleeder sheets or release agents. However, not all of the mentioned parameters can be modified selectively on purpose.

5.5 Evaluation of residual stress

The required time and effort for measurements with FBG sensors discussed above are very high. Therefore, three other methods for the evaluation of the residual stress level are discussed in the following, being more suitable for a first investigation on influential parameters.

The basic aim of the measurements is to calculate the effective residual stress in the metallic part $\sigma_{M,R}$ and the composite part $\sigma_{C,R}$ in order to enable the assessment of each approach applied in this work. However, as these stress levels depend on the ambient temperature during measurement or the operating temperature of the part, it seems to be more appropriate to compare the stress free temperature T_{sf}. As operation temperature is much lower than cure temperature and T_{sf} is expected to be slightly below the cure temperature, the stress level at any operational temperature is lowered proportional with T_{sf}. Three different approaches are used, two for asymmetrical specimens and one for symmetrical specimens.

Asymmetrical specimens

With the help of the deformed asymmetrical specimens, two approaches are employed: the curvature measurement of the specimens at room temperature and the measurement of the specimens during reheating in an oven.

For the first approach, the geometrical values a and S (see Figure 5.12) are measured by placing the specimens on scale paper at room temperature T_{RT}=23°C allowing the calculation of the radius R of the curved specimens.

For the second approach, six specimens at a time are clamped at one end and placed in an oven. The oven door is replaced by a heat resistant glass panel to allow the taking of pictures during heat-up. The specimens are then reheated with a heat rate of 2 K/min and a picture is taken every 30 sec. Regression analysis of the variable provides the stress-free temperature T_{sf}.

The dependent value of interest is thereby directly obtained by the regression analysis in the second approach, whereas the relationship between curvature and T_{sf} is required for the first approach.

Simple beam theory can be applied to calculate this relationship. The width of the strip is taken to be one and it is assumed that the cross sections originally being plane and perpendicular to the longitudinal axis remain plane and become perpendicular to the curved longitudinal axis. The forces acting on the composite layer are a longitudinal compressive load P_C and bending moment M_C, as depicted in Figure 5.12. The load represents the mechanical load being necessary to achieve the thermal elongation difference between the two layers when lying flat. The forces in the metal are a tensile load P_M and a bending moment M_M. There are no external forces acting on the strip which means that the forces over the cross sections need to be in equilibrium:

$$P_C = P_M = P \tag{5.12}$$

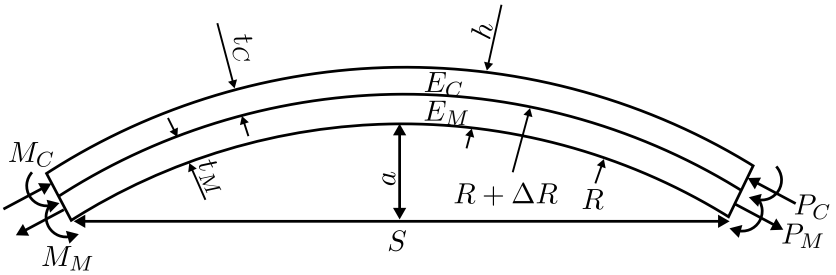

Figure 5.12: Deflection of bi-material strip cured at elevated temperature

$$P\frac{h}{2} = M_1 + M_2 \tag{5.13}$$

From beam theory

$$M_i = \frac{E_i I_i}{R} \tag{5.14}$$

with the flexural rigidity of each material $E_i I_i$. Substitution leads to:

$$P\frac{h}{2} = \frac{E_C I_C + E_M I_M}{R} \tag{5.15}$$

According to Figure 5.12, the strain due to bending can be written as:

$$\epsilon_b = \frac{\Delta l}{l} = \frac{l + \Delta l - l}{l} = \frac{2\pi(R + \Delta R) - 2\pi R}{2\pi R} = \frac{\Delta R}{R} = \frac{t_k}{2R} \tag{5.16}$$

with the thickness t_k of the respective layer. This equation simply proves that ϵ can equally be written as $\Delta R/R$. The elongation on the interface between the two constituents must be identical and consists of thermal strain, strain due to mechanical loads and strain due to bending (width unified to 1):

$$\alpha_C \Delta T + \frac{P_C}{E_C t_C} + \frac{t_C}{2R} = \alpha_M \Delta T - \frac{P_M}{E_M t_M} - \frac{t_M}{2R} \tag{5.17}$$

Together with 5.12 and 5.15, the last expression can be written as:

$$\frac{h}{2R} + \frac{2(E_C I_C + E_M I_M)}{hR}\left(\frac{1}{E_C t_C} + \frac{1}{E_M t_M}\right) = \Delta T(\alpha_M - \alpha_C) \tag{5.18}$$

which leads to

$$R = \frac{\frac{h}{2} + \frac{2(E_C I_C + E_M I_M)}{h}\left(\frac{1}{E_C t_C} + \frac{1}{E_M t_M}\right)}{\Delta T(\alpha_M - \alpha_C)} \tag{5.19}$$

Timoshenko simplifies formulas of this type with the help of the thickness ratio $m = t_C/t_M$ and stiffness ratio $n = E_C/E_M$:

$$R_{beam} = \frac{h\left[3(1+m)^2 + (1+mn)\left(m^2 + \frac{1}{mn}\right)\right]}{6\Delta T(\alpha_M - \alpha_C)(1+m)^2} \tag{5.20}$$

Considering transverse contractions ν_{12} of composite and metal in a plate geometry, the equation extends to [192]:

$$R_{plate} = \frac{\frac{h}{2} + \frac{2\left(\frac{E_C}{(1-\nu_C)}I_C + \frac{E_M}{1-\nu_M}I_M\right)}{h}\left(\frac{1}{\frac{E_C}{(1-\nu_C)}t_C} + \frac{1}{\frac{E_M}{1-\nu_M}t_M}\right)}{\Delta T(\alpha_M - \alpha_C)} \tag{5.21}$$

A third approach to determine stress in strips with planar interfaces which includes *Poisson's* ratio effects was introduced by *Oel and Frechette* [193]. According to their work, the thermal strain at a point with the distance y from the interface between the two constituents is given by [166, 167]:

$$\epsilon_k = \frac{n_k - y}{R_{OF}} \tag{5.22}$$

where n_k describes the distance between the neutral axis in layer k from the materials interface. Thereby the equation 5.22 is equal to 5.16. The terms n_k for the composite and the metal layer are derived by consideration of strain energy, see Oel and Frechette [193]:

$$n_C = \frac{S_M t_M^2 + 4 S_C t_C^2 + 3 S_C t_C t_M}{-6 S_C (t_C + t_M)} \tag{5.23}$$

$$n_M = \frac{S_C t_C^2 + 4 S_M t_M^2 + 3 S_M t_M t_C}{-6 S_C (t_C + t_M)} \tag{5.24}$$

with the stiffnesses S_C and S_M determined by:

$$S_k = \frac{E_k t_k}{1 - \nu_{k12}} \tag{5.25}$$

where E_k is the *Young's* modulus of the k-th layer, t the thickness of the k-th layer and ν_{k12} the *Poison's* ratio of the k-the layer. At the interface between the two materials:

$$\epsilon_C - \epsilon_M = \frac{n_C - n_M}{R_{OF}} = (\alpha_C - \alpha_M)\Delta T \tag{5.26}$$

All three theories are applied to specimens with three different thicknesses, t=0.25, t=1.0 and t=2.0 mm consisting of equal number of 0.13 mm prepreg layers 8552-AS4 and 0.12 mm steel where the curvature measurement is expected at RT. The stress-free temperature T_{sf} is varied between 40 and 180°C and the results of all three theories show less then 1% deviation, as depicted in Figure 5.13.

However, the assumptions with planar and rectangular cross sections are more accurate for thinner specimens. For this reason, 0.25 mm specimens are manufactured. The plate formula is selected for the calculation of T_{sf} in the following. With $\Delta T = T_{sf} - T_{op}$, the required equation can be written as:

$$T_{sf} = \frac{\frac{h}{2} + \frac{2\left(Q_{C,11} I_C + Q_{M,11} I_M\right)}{h} \left(\frac{1}{Q_{C,11} t_C} + \frac{1}{Q_{M,11} t_M} \right)}{R_{plate} (\alpha_M - \alpha_C)} + T_{op} \tag{5.27}$$

Symmetrical specimens

The symmetrical specimens are tested on a Zwick 1476 testing machine. $\sigma_{L,y}$ and E_L - when adding strain gauges - can be calculated as a result of tensile testing. According to equation 3.10 in chapter 3.4 and with the residual strain in the metal layer

$$\epsilon_{M,R} = \frac{\sigma_{M,R}}{E_M} \tag{5.28}$$

the residual stress in the metal layer is also given by

$$\sigma_{M,R} = \sigma_{M,y} - \frac{\sigma_{L,y} E_M}{E_L} \tag{5.29}$$

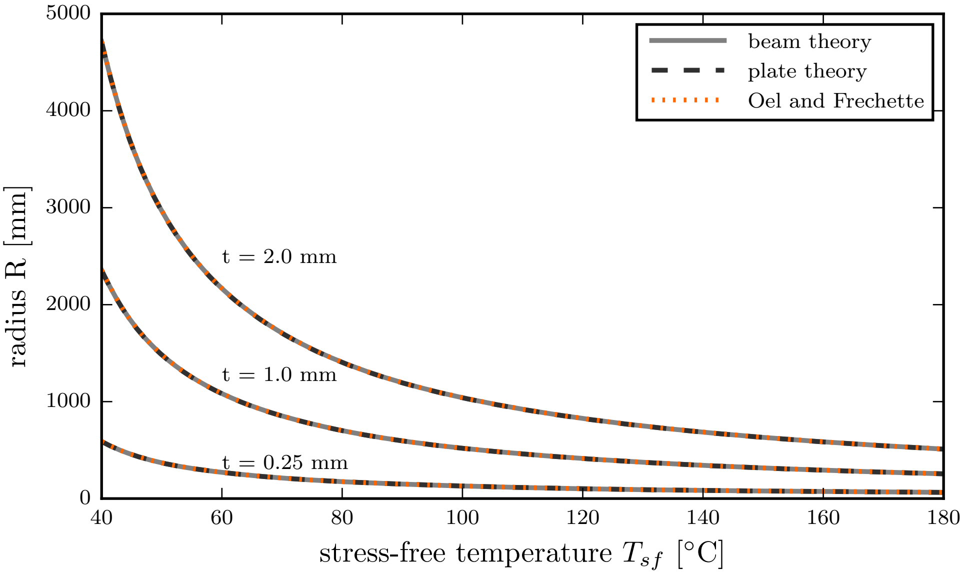

Figure 5.13: Calculation of the radius R of the curvature of bi-material strips cooled to RT depending on the stress-free temperature T_{sf}, where beam theory is based on ROM and plate theory on plane stress assumptions

Substituting the residual stress $\sigma_{M,R}$ with the equation 5.7, the following relation is given:

$$[Q_{11,M}(\alpha_x^\circ - \alpha_M) + Q_{21,M}(\alpha_y^\circ - \alpha_M)]\Delta T = \sigma_{M,y} - \frac{\sigma_{L,y}E_M}{E_L} \tag{5.30}$$

where α_i° is the laminates plate CTE in the respective direction. With $\Delta T = T_{sf} - T_{op}$, the stress-free temperature T_{sf} is given by:

$$T_{sf} = \frac{\sigma_{M,y} - \sigma_{L,y}\frac{E_M}{E_L}}{Q_{11,M}(\alpha_x^\circ - \alpha_M) + Q_{21,M}(\alpha_y^\circ - \alpha_M)} + T_{op} \tag{5.31}$$

5.6 Residual curing stress and its modification

Manufacturing

As manufacturing is part of the investigation, specimens are not cut out of a plate but directly manufactured individually to the final geometry. As discussed earlier, the specimen thickness is selected to be as thin as possible and so that the curvature due to the specimen's net weight can be neglected in comparison to the curvature investigated.
Three specimens are manufactured for each configuration and two basic specimen geometries are used; symmetrical and asymmetrical specimens allow two different measurement methods.
All specimens are 20 mm in width and, except for the clamped specimens, have a length of 200 mm with all fibers oriented in the longitudinal direction. The clamped specimens are extended by the clamping area and cut to 200 mm length after cure. Two different lay-ups are used, one symmetric and one asymmetric, as shown in Figure 5.14. The symmetrical

specimens consist of two stainless steel 1.4310 outer sheets with a thickness of 0.12 mm and a HexPly-8552/134/AS4 center layer, in order to eliminate any interaction between tool surface and specimens.
However, as there is interaction expected between the outer and center layers, this may also result in interaction between the metallic outer layer and the tool. For the same reason, the asymmetric specimens are manufactured in a double configuration as shown in Figure 5.14 and the two specimens are separated by an FEP-sheet *Nowofol-NowoflonET*. All metallic sheet surfaces were treated with an AC-130 sol-gel post-treatment after corundum-blasting with 105 μm particles and then added to the laminate stacking within one hour. Manufacturer's recommended cure cycle (MRCC) is used if not indicated otherwise.

Processes

In the following, the manufacturing or rather testing is described in which three variations are considered:

- Variation of effective pressure
- Variation of temperature process
- Application of thermal expansion clamp

The effective process pressure was varied in two ways. As the normal force acting on the laminate is varied, the size of the cover plate is changed. By choosing a larger cover plate, whose bending stiffness is sufficient to prevent unwanted bending between the specimens, the effective pressure on a specimen can be increased. In combination with two different autoclave pressures, five effective pressure levels are reached: 6, 8, 12, 16 and 24 bar.
A modification of the temperature process influences the resin's behavior as well as the inter-ply interaction. Utilizing 'smart cure cycles' with cooling and re-heating, influences the resin's gel and glass transition temperatures as well as its exothermic reaction [176,177]. MRCC for the HexPly-8552 prepreg recommends two heat-up ramps and two dwell stages. The autoclave is heated up to 110°C at 1-3 K/min. After the 60 minute dwell it is heated up again at 1-3 K/min to 180°C. After a hold of 120 minutes the autoclave is cooled down at 2-5 K/min. This MRCC cycle is used as reference with heat-up ramps at 2-3 K/min and cool down at 3 K/min and marked as M0. All the other three cycles are interrupted

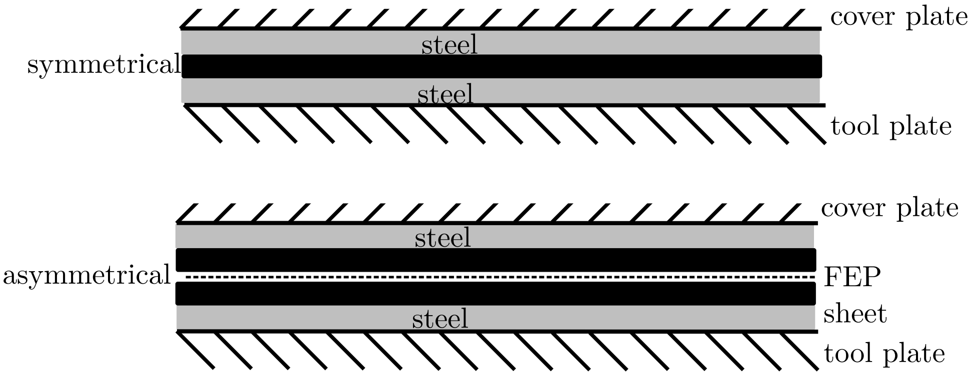

Figure 5.14: Lay-up of symmetrical and asymmetrical lay-up

after the first holding phase. Modification M1 is reheated after reaching RT at 2-3 K/min and the cure cycle is finalized as the MRCC. Modifications M2 and M3 do not use pressure at reheating and therefore an oven is used. Heating rates are identical to M1, but before reheating M3 a period of five days at RT is introduced.

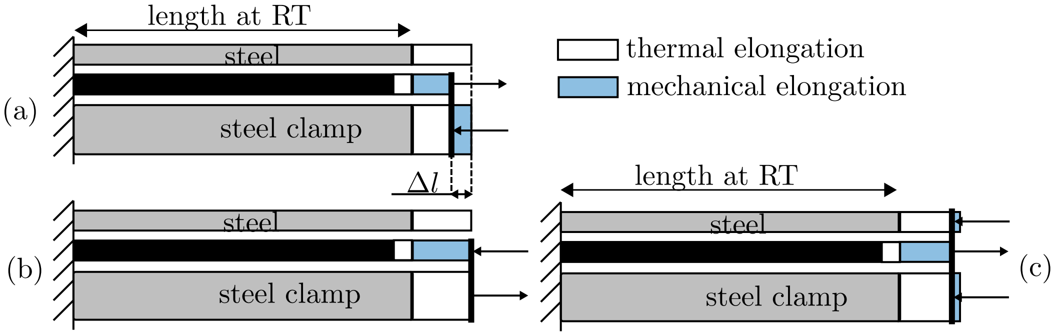

Figure 5.15: Force equilibrium for different clamping scenarios

Constructive modifications are conceivable for a predominant direction only. However, for profiles of unidirectional fiber metal laminates with constant cross section, clamping similar to that proposed by *Xue et al.* [181] may be serviceable. The idea is to connect the two constituents at RT or operational temperature. When heating to cure temperature, the difference in thermal elongation is compensated by mechanical strain. The resulting laminate is stress-free at the temperature at which the constituents have been connected to each other when any relative movement is prohibited.

The principle of the thermal expansion clamp is shown in Figure 5.15. Bending moments are neglected in the schematic illustration. Firstly, it seems to be obvious to only clamp the composite or CFRP layers, case (a) in the figure, and thereby evoke a mechanical strain identical to the thermal strain of the steel. However, a steel clamping with infinite stiffness is required for this, case (b), otherwise a mismatch between the strain or elongation of the composite and the steel constituent will remain, as indicated in Figure 5.15 (a).

In contrast, thermo-mechanical equilibrium is achieved when both constituents are clamped only to each other. However, as the thin steel layers would wrinkle under the compression load due to their low bending stiffness, an additional clamp is used to fix both constituents, Figure 5.15 (c). This leads to a decreased compressive strain in the steel constituent and an increased tensile strain in the CFRP layer compared to the constituents clamped only to each other and reduces the stress-free temperature T_{sf} of the laminate.

Tensile force is applied to the laminate during the cure process by using the thermal expansion clamp, shown in 5.16. In the clamping area, the laminate is wrapped around a wedge and the cover plate is then fixed by seven M16 steel bolts. Additionally, conical spring washers are used to maintain the applied clamping force.

Results

Two different methods are applied for the estimation of the residual stresses, in particular of the stress free temperature. When comparing the two methods on asymmetrical specimens by looking at the two diagrams in Figure 5.17 and Figure 5.18 it is obvious that the temperature measurement results indicate higher stress-free temperatures T_{sf} than the curvature measurement at RT. One possible source for the difference could be the burrs which formed at the specimens edges increasing their bending stiffness. Smaller curvatures at RT correspond to lower T_{sf}. The difference between the two measurement methods

Figure 5.16: Thermal expansion clamp without specimens

decreases with higher effective pressure where no burr is detected at the edges. However, both methods show similar relationships between the single results and their variation is also comparable.

The stress-strain curves for the tensile tests are shown in Figure 5.19. It is obvious that the 7 pure steel specimens show a higher elastic stiffness compared to the 9 CFRP-UD-steel specimens. When increasing the stress above the laminates yield strength, the curve flattens for both materials and steel shows a typical yield behavior. Unfortunately, the determination of the yield strength or yield point is not distinct and variation is large. Table 5.1 shows the single results for 0.2%, 0.1% and 0.01% yield strength for pure steel. The resulting variations in these result may generate a variation in the T_{sf} calculation of around 200 K when using equation 5.31. As the material stiffness after passing steel's yield point is higher for CFRP-UD-steel than for pure steel, the 2%-yield strength of CFRP-UD-steel is higher while the 0.01%-yield strength of CFRP-UD-steel and pure steel are comparable, see Table 5.1 and 5.2.

However, due to the inaccurate determination of the yield point, this method is not feasible

Table 5.1: Yield strength thresholds for pure 1.4310 steel specimens

yield criterion	unit	1	2	3	4	5	6	7
0.2%	[MPa]	1267	1295	1241	1261	1217	1309	1251
0.1%	[MPa]	1166	1194	1123	1140	1081	1227	1124
0.01%	[MPa]	1020	1062	939	932	880	1039	913

Table 5.2: Yield strength thresholds for 9 variations of CFRP-UD-steel specimens

yield criterion	unit	6 bar	8 bar	12 bar	16 bar	24 bar	M1	M2	M3	clamping
0.2%	[MPa]	1343	1513	1519	1435	1509	1441	1309	1281	1359
0.1%	[MPa]	1159	1353	1364	1270	1345	1272	1126	1109	1175
0.01%	[MPa]	838	985	1013	915	969	905	808	809	853

for the calculation of T_{sf}. Applying equation 5.31 leads to the results in Table 5.3 which do not correlate with the results of the other methods or with any expectations.

Therefore, only the asymmetrical specimens are utilized for the further discussion. These results show a clear dependency on the effective pressure during cure as depicted in Figure 5.17. This correlates with the assumptions that interaction during heat-up is increased by increasing the normal load. By increasing the effective pressure from 6 to 24 bar, the residual stresses at RT are reduced by 50%. The second diagram, Figure 5.18, shows the measured and calculated stress-free temperatures for the different temperature processes used and for the clamping scenario. The processes M1 and M2 do not show any benefits compared to the MRCC process M0. However, the results of the M3 process indicate a stress-free temperature below 70°C, what correlates with a stress reduction at RT of nearly 60%. Comparable results are achieved by the clamping. This means that slippage is not fully prevented in the clamping. However, the clamping can only be utilized when the part is not curved along the direction the clamp is applied.

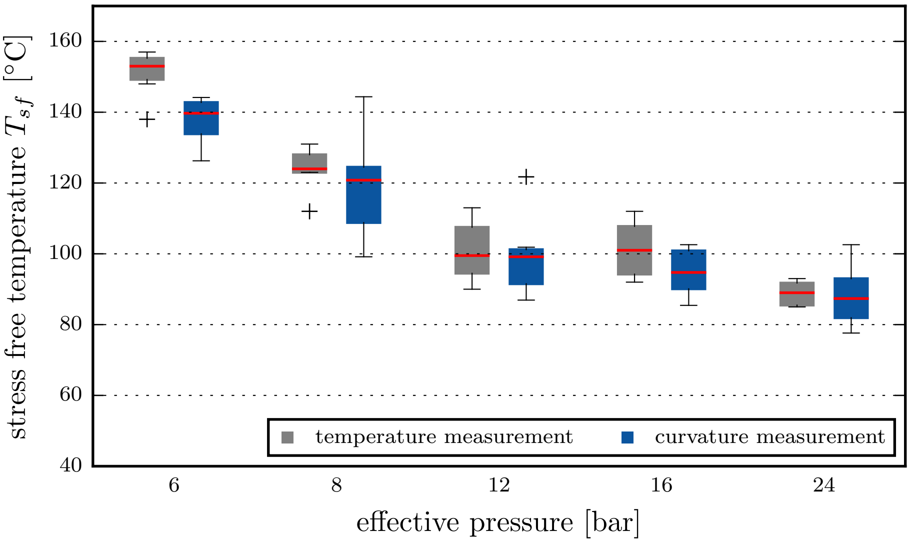

Figure 5.17: Stress-free temperature T_{sf} depending on effective pressure determined by temperature and curvature measurement

Altogether, the results clearly indicate that there are different promising approaches to reduce the residual stresses in the laminate which are worth further investigations. Although exploratory, the results also indicate that an interaction between the two constituents is present even at MRCC which has not been considered before. This interaction lowers the

Table 5.3: Unsatisfactory calculation of stress-free temperature T_{sf} based on tensile testing

	unit	6 bar	8 bar	12 bar	16 bar	24 bar	M1	M2	M3	clamping
T_{sf}	[$°C$]	62	265	304	167	243	154	21	23	83

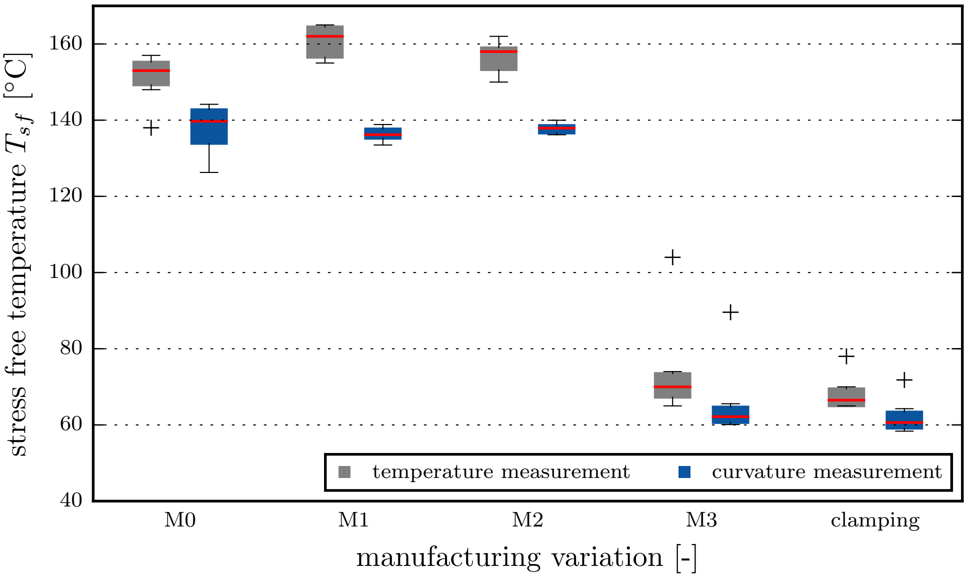

Figure 5.18: Stress-free temperature T_{sf} depending on chosen process and clamping determined by measurement and curvature measurement

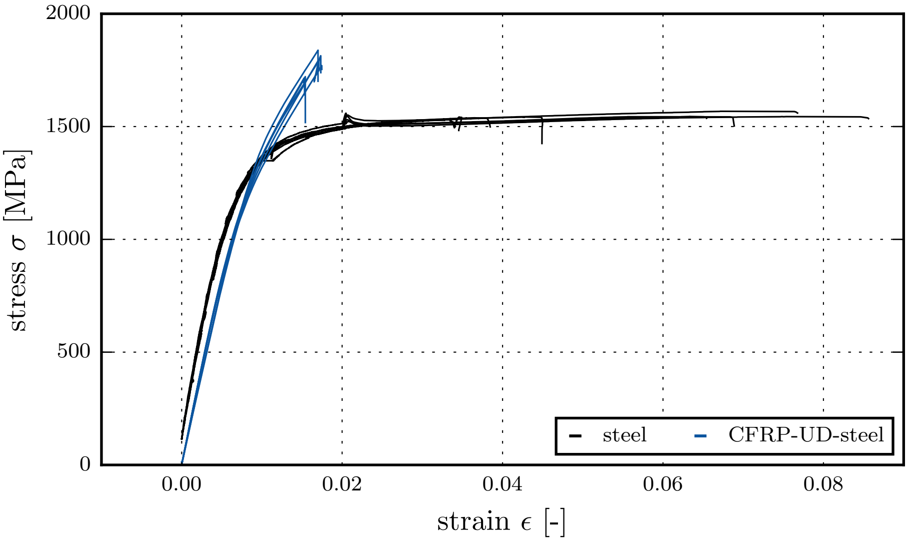

Figure 5.19: Stress-strain curves for tensile testing of pure steel and CFRP-UD-steel specimens

residual stress in a way that thermo-mechanical calculation assuming that the laminate is stress-free at cure temperature, provide incorrect results. Although a measuring technique based on fiber-Bragg or spot curing would be beneficial as they provide the opportunity to measure during the curing process, the asymmetrical specimens provide a simple and convenient method to estimate the stress level in a comparable symmetrical part. In contrast, the tensile tests do not provide any exploitable results for this goal.

5.7 Discussion of hypothesis addressed

As formulated in hypothesis 4, it is a current approach that the difference between cure and operational temperature is used to calculate the residual thermal stress.

It has already been shown in literature that a reduction of this stress level can be achieved by a modification of the temperature cycle. However, this finding implies a 'worst case' temperature cycle which is than improved. Assuming that the temperature cycle modification is the only way to reduce the stresses, there must be a cycle which leads to the 'worst case' scenario where the stress-free temperature equals the cure temperature.

In contrast, the present findings show that the stresses can be lowered without changing the temperature cycle but by increasing effective pressure. This means that a mechanism must be present depending on the pressure level. Although it is not a final proof, the results meet the assumptions concerning the interaction between the plies.

All composite manufacturing processes using prepreg include a normal force generated by a pressure difference. Therefore, the stress-free temperature must always be lower than the cure temperature as a consequence of the interaction.

6 Experimental evaluation of residual strength

Link to hypotheses: Hypothesis 5 and hypothesis 6 are analyzed in this chapter to obtain clarity of the relationship between the arrangement of steel layers, failure geometry and compression strength after impact.

Summary: This chapter first provides an overview of the different experimental procedures to determine damage resistance and residual strength with respect to impact damage.
The manufacturing of samples and the test procedure used for the determination of compression strength and stiffness are then discussed in more detail. Before conducting impact testing on the specimens, two specific requirements are regarded in more detail. First: the failure evaluation on UD-CFRP-steel specimens is different to CFRP as no depth information is achievable by ultrasonic (US) inspection. Alternatively, some of the specimens are analyzed by computer tomography (CT).
Second: the test procedure is adapted to the needs of the UD-CFRP-steel specimens to obtain meaningful results. Then specimens with different lay-ups are subjected to impact damage for the evaluation of the generated damage and for the determination of their residual compression strength. Finally, theses results are compared with the pristine compression strength of the different lay-ups.

6.1 Literature review

The term 'residual strength' is traditionally used to define the strength of a metal structure after the formation of cracks caused by fatigue or corrosion.
As composites show reasonable good fatigue properties, the term residual strength represents static strength when damage due to low-energy-level impact is present [194]. There can be mentioned for it. First: composites are very brittle and sensitive to even slight damage. Second: low energy impact causes damage in form of fiber fracture, delamination, disbonding or matrix cracking whereas high energy may lead to penetration with little or no local delamination of the laminate [12, 194].

Experimental determination of residual strength

Hence, impact damage appears to be the most critical of all defects. Consequently, most residual strength testing is carried out on coupons or structures containing impact damage. In addition, it is assumed that this encompasses the effect of the other defects [194]. The CAI-test is the most widespread test for its evaluation and is described in *DIN EN 6038* [195], *AITM1-0010* [196] and *D7137/D7137M* [197]. Especially for pure composites, the influence of a variety of parameters on the materials residual compression strength after impact have been studied. For example, different resin and fibre properties are regarded by *Cartié and Irvin* [198].

Sanchez, Saez et al. [199] as well as *Tanaka and Kageyama* [200] show that the variation of the test results is mainly induced by the impact procedure and not by the compression test itself, as buckling is prevented by the test fixture [201]. Therefore, most of the investigations focus on the impact process.

Generally, the strength reduction or the residual strength is determined empirically. Thus, many CAI-tests are performed to describe the relationship between strength, damage size and damage type.

Impact on composites

The low-energy or low-velocity impact primarily creates a 'pine-tree' distribution of damage, which can also be found in FML [39]. This means that the detectable damage on the impacted surface is small, but the damage size expands to the backside of the laminate. These delaminations are often not detectable with the bare eyes, but reduce the strength of the laminate by up to 60% [199]. Most of the studies in literature focus on impact on pure CFRP [202–204], GFRP [205] or GLARE [206–208].

Besides material modification, research also focusses on the arrangement of the layers to achieve the best results for the materials used.

Hitchen and Kemp [209] illustrate a direct dependence of the residual strength on the delamination in the laminate, which again depends on the dispersion of the differently orientated layers in a pure CFRP laminate [210–212], the ply thickness of the single layers [203] and the laminate thickness [213]. In a similar way, it is also shown for FMLs that the stacking sequence, constituents [214, 215] and the temperature [216] have a large influence on the damage geometry.

However, there are still many investigations performed on the testing methodology itself, as the influence of the clamping is substantial. For example, different clamping situations and specimens geometries are investigated by *Ghelli and Minak* [217, 218] for pure CFRP laminates.

Non destructive inspection

The inspection is also an essential part of residual strength testing, as it allows the assessment of the damage after impacting and before residual strength testing without affecting the specimens functionality. This enables a better understanding of the relationship between damage geometry and residual strength and allows a more goal-oriented research on the materials and lay-ups to alter the obtained damage geometry on purpose.

Certainly, visual inspection is the simplest and most economical inspection method. As it is used routinely for final inspection and during service life of a part, it is also an important indicator in testing. In determination of the damage in a specimen, accurate thickness measurement is also an important non destructive inspection method.

However, for a more detailed detection of internal flaws, US inspection has become the most widely used method. The involved restrictions when FMLs are inspected, are discussed in further detail in chapter 6.5.

Therefore, CT is regarded as an alternative method and allows to retrieve data by X-ray imaging and producing a 3D-image of the part. The benefits as well as the limitations of CT are discussed in chapter 6.5.

6.2 Present chapter's structure

The structure of this chapter is presented in Figure 6.1. All of the required specimens are cut out of flat plates. Hence, the manufacturing process can be regarded irrespective of the testing and analysis. Surface treatment of the metal layers, the lay-up process, curing and cutting of the specimens are discussed in this section.

In the subsequent subchapter 6.4, a test approach to determine compression strength and modulus, is selected. As high moduli and strength values are expected for the UD-CFRP-St laminates, different available test standards are discussed with regard to their suitability and a test procedure is derived afterwards.

The evaluation of the generated impact failure before compression testing is an essential part of CAI testing and is mainly undertaken by means of dent depth measurement and US inspection. The use of the latter is restricted for the UD-CFRP-St specimens considered as described later. Thus, CT inspection is discussed in addition. The essential information about these three applied methods for failure evaluation, are provided in subchapter 6.5 and the approach to generate the results in form of damage images and values is discussed. CAI testing consists of two mechanical test steps, the impacting procedure and the compression testing. Specifications for both operations are provided by different test standards and are discussed in subchapter 6.6. Although compression testing of a previously impacted specimen deviates from testing of pristine specimens, the application

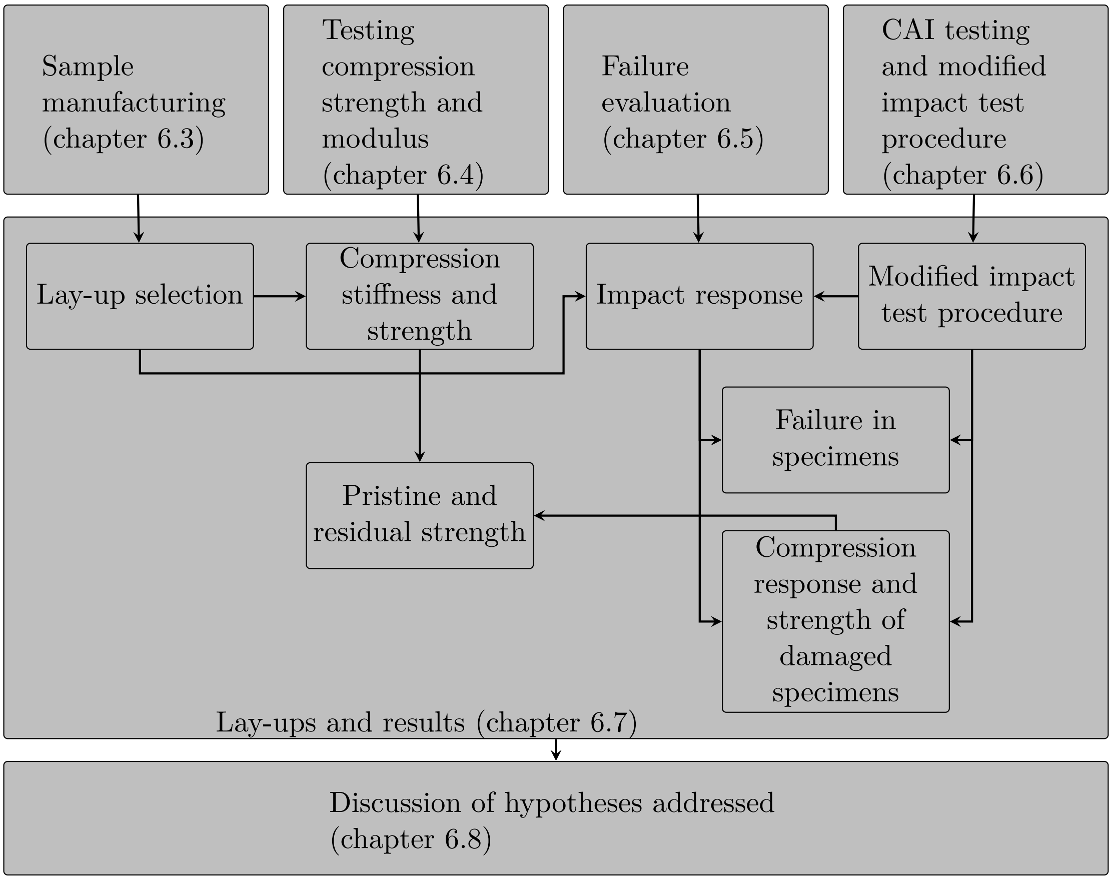

Figure 6.1: Flowchart describing the procedure pursued in chapter 6; individual subchapters marked in gray

of the provided specifications lead to meaningful results. This is not a matter of course since the laminate properties, especially the stiffness ratio between the longitudinal and the transverse direction, are deviant from most CFRP test specimens. As discussed in this subchapter in more detail, some of the test standards are explicitly intended for QI laminates only. A modified impact test fixture is discussed and developed in this section to overcome these restrictions.

Chapter 6.7 contains all the testing and analysis conducted in accordance with the methodologies discussed in subchapter 6.3 to 6.6. Firstly, the relevant parameters of the lay-ups selected for the tests are provided. Then the validation of the modified impact test fixture is performed using pure CFRP laminates with QI and HO lay-ups. The outcome of this is the selection of the cut-out window dimensions for further testing. Compression testing of pristine specimens to evaluate stiffness and strength is undertaken with a variety of lay-ups to investigate the influence of ply arrangement, MVF and metal ply thickness. The impact response of some of the lay-ups, tested on the modified test fixture, is then regarded in more detail. The generated failure is considered by means of dent depth and damage area obtained by US inspection. Some of the specimens are additionally analyzed by CT and allow the comparison of the two methods. The compression strength results achieved by the different lay-ups are than discussed with regard to their lay-up and impact failure. Finally, the pristine compression strength and residual compression strength after impact results are discussed by comparison.

The subsequent chapter 6.8 induced the link to the hypotheses addressed in chapter 6.

6.3 Sample manufacturing

The required specimens are 32x162, 100x150 and 150x150 mm at a thickness around 4 mm. There is a minimum of one plate manufactured per lay-up. The lay-ups are introduced in section 6.7. All specimens consist of Hexcel 8552/AS4 with the properties provided in Table 3.1. All UD-CFRP-steel specimens additionally consist of 1.4310 steel layers with a thickness of 0.03, 0.05 or 0.08 mm.

Two different approaches are utilized for the surface treatment of the metal. Although vacuum blasting was selected - based on the results in chapter 4 - some preliminary tests concerning compression strength have been performed in parallel. Therefore, pickling was utilized.

Both surface treatments follow a similar procedure (as presented in Figure 6.2) and only the pre-treatment process of the two is different. After solvent swiping with acetone or heptane, the pickling process (a) is applied onto the steel foils used for the preliminary compression tests. After degreasing with SurTec089+SurTec138 at 50-60°C for 15 minutes and rinsing with demineralized water, the foils are pickled in SurTec433 for 120 minutes. After a second rinsing process the foils are dried in an oven at 50°C for 30 minutes as shown in Figure 4.16 and described in chapter 4. The alternative (b) in Figure 6.2 represents a vacuum blasting step with 105 μm sized corundum grit and is applied to all remaining specimens.

Subsequent to a second solvent swiping, the sol-gel AC-130 is applied for 150 seconds. After drying for 1 hour, the foils are immediately placed in the laminate lay-up.

The lay-up is done manually and the laminates are cured following the manufacturer's recommended cure cycle [28]. The specimens are cut to size and then measured with a micrometer gauge.

Pure CFRP specimens are successfully and effectively cut by a diamond saw. The geometrical precision meets the test standards and the cut itself does not show any damage.

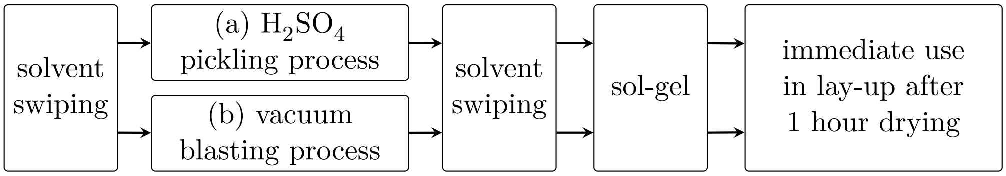

Figure 6.2: Flowchart describing the surface treatment procedures applied

However, when cutting UD-CFRP-steel with a blade saw, one has to agree a compromise. Whereas the diamond blade is ideal to cut the CFRP, a hardened steel specimens provides better results for steel. Basically, the diamond saw generates better results for the UD-CFRP-steel material. Although detailed parameter studies have been performed on cutting speed and feed rate to identify the ideal settings, there is still some damage present that can only be identified by ultrasonic inspection. Therefore, the diamond saw is used for the cutting of the preliminary tests on compression specimens only and waterjet cutting is used for the remaining specimens.

An automatic tilting head that tilts the nozzle during machining is required to achieve straight edges and meet the demands of the test standards with regard to the geometry. For waterjet cutting, the edge delamination is not detectable whereas the edges of a diamond cut specimen clearly show delaminations, as indicated in Figure 6.3. A comparison between compression strength values obtained by the preliminary tests and the additional tests with waterjet cut specimens is hence reduced in explanatory power.

6.4 Testing compression strength and modulus

The determination of in plane compression strength of fiber reinforced plastics is described in *AITM1-0008* [219], *ASTM D6641/D6641M* [220], *ASTM D3410/D3410M* [221], *DIN EN ISO14126* [222], *DIN EN 2850* [223] and *DIN 65380* [224], where the last two are withdrawn. *AITM1-0008* differentiates between specimens for shear loading and specimens for combined loading, which is a combination of shear and end loading. The pure end loading is explicitly prohibited. *ASTM D3410/D3410M* describes the shear loading case and is extended by *ASTM D6641/D6641M* for the combined loading compression (CLC) case. *DIN EN ISO14126* is in accordance with the shear load case only.

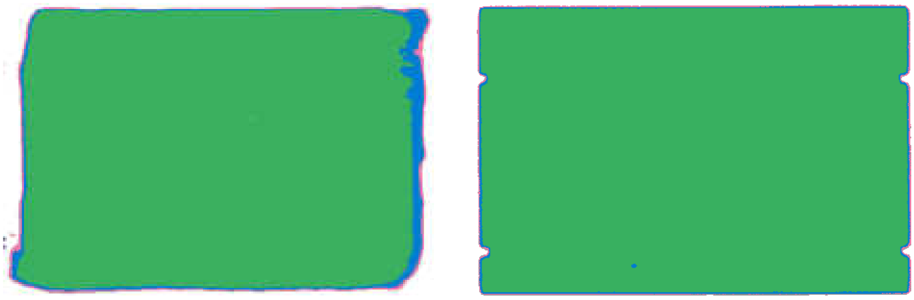

(diamond saw cutting) (waterjet cutting)

Figure 6.3: Comparison of edge delamination obtained by ultrasonic inspection on specimens cut by diamond saw and cut by waterjet

The geometries required in the standards vary in length, width and thickness of the specimen. *AITM1-0008* distinguishes between thick lay-up with approximately 4.0 mm thickness and thin lay-up with approximately 2.0 mm thickness. The width of the specimens is 32±0.2 and 22±0.2 mm respectively with an associated gauge length (free length between tabs) of 32±0.5 and 22±0.5 mm. The length of the specimens depends on the tab length which is derived from the requirement that the allowed tab shear is less than 35 MPa. Recommended tab length is 80 mm for shear loading and 65 mm for combined loading. The specimen geometries specified in *ASTM D3410/D3410M*, *ASTM D6641/D6641M* and *DIN EN ISO14126* vary between 110 to 155 mm in length, 6 to 25 mm in width and 2 to 10 mm in thickness. ASTM D3410/D3410M provides a scheme to determine the minimum required stiffness depending on specimen modulus and expected strength. The variation of the thickness for any laminate shall be within ±2% of the measured mean thickness [219]. No constrictions concerning lay-up are mentioned in *ASTM D3410/D3410M*, *ASTM D6641 /D6641M* and *DIN EN ISO14126* but *AITM1-0008* says that the laminate shall be QI. The determination of the stiffness is also performed differently in the standards. Following *AITM1-0008*, the stiffness is determined between 10 and 50% of the average failure load, whereas it is identified between 25 and 50% of failure strain in *ASTM D6641/D6641M* and *DIN EN ISO14126.* In *ASTM D3410/D3410M* stiffness is calculated between 1000 and 3000 $\mu\epsilon$.

As high compression loads are expected for the UD-CFRP-steel specimens, a combined loading is more suitable. The selection of a preferably wide specimen reduces the relative influence of delaminations induced by the cutting process on the results. Therefore, the compression tests are performed following the *AITM1-0008* test standard although the lay-up is not QI.

The plain compression strength is calculated with the failure load P_u, the laminate thickness t_{lam} and the specimen width w as follows:

$$\sigma_{cu} = \frac{P_u}{t_{lam} w} \tag{6.1}$$

According to *AITM1-0008* the compressive stiffness E_c is given by [219]:

$$E_c = \frac{\Delta P}{t_{lam} w \Delta \epsilon_x} \tag{6.2}$$

where the load increase ΔP is given by:

$$\Delta P = \frac{Av(P_u)}{2} - \frac{Av(P_u)}{10} \tag{6.3}$$

and $\Delta\epsilon_x$ is the difference between the related strains at 10 and 50% of the average failure load $Av(P_u)$.

Failure is considered as valid when it occurs in the gauge length [221]. However, an *Euler* buckling failure cannot be determined by visual inspection of the specimen after testing, hence it is inspected through comparison of the strain on the front and back face of the specimen. Therefore, *AITM1-0008* introduces the percent bending strain (PBS) parameter. The failure is only considered as valid if the difference between strains measured on each face of the test specimen in the load range 0.1P$_u$ to 0.9P$_u$ remains such that PBS is less than 10%:

$$PBS = \left| \frac{\epsilon_{faceA} - \epsilon_{faceB}}{\epsilon_{faceA} + \epsilon_{faceB}} \right| \leq 0.10 \tag{6.4}$$

where ϵ_{faceA} is the measured strain on specimen face A and ϵ_{faceB} is the measured strain on specimen face B.

Figure 6.4 (a) shows a fully equipped compression specimen with tabbing at the ends and strain gauges glued to both faces. For installation in the test rig (see 6.4 (b)), the specimen is placed between the lower clamping jaws and is fixed. The strain recording is reset and the upper jaws are fixed. Neither information is provided about a pre-load which is necessary to clamp the specimens free of clearance in longitudinal direction, nor information is given in the standards concerning required or recommended clamping force. The pre-load is therefore adjusted manually to 50 N and the necessary clamping force is determined by preliminary test.

6.5 Failure evaluation

The evaluation of failure is an important intermediate step in the determination of the residual strength after impact. The assessment of the damage size, geometry and detectability is part of the damage tolerance approach and their influence on the residual strength is of major interest in the present work. Therefore, the applied inspection methods US, CT and dent measurement are discussed in detail and their presentation procedures in form of diagrams and images are introduced.

Ultrasonic inspection

The US inspection is based on the measurement of the propagation of a sound pulse through the laminate. The pulse is emitted from a transducer on top of the specimen and recorded by a receiver located with the transducer and/or on the opposite surface. The US wave is reflected or scattered by any defect or foreign material which acoustic impedance differs from that of the composite. Planar defects like delaminations, voids and cracks that are normal to the propagated pulse, cause a loss or attenuation in the transmitted sound and display a defect by means of comparison. The 'pulse-echo' or reflection mode, where the transducers work in a 'pitch-catch'-configuration, is used for examining the pure CFRP specimens. Due to the high number of layers with different acoustic impedance


(a) (b)

Figure 6.4: Compression specimen with tabs and strain gauge (a) and hydraulic composite compression fixture (HCCF) test fixture (b)

properties, this method is not applicable for the UD-CFRP-steel specimens. The through transmission technique with a separate receiver is used for the inspection of the hybrid material specimens. All inspections are performed in water and a C-scan presentation is obtained. The C-scan is an image slice showing the plan view of the tested area.

Figure 6.5 (a) shows an exemplary C-scan obtained by the 'pulse-echo' technique where each color represents the amplitude of a certain indication. With the help of the traveling time, the back wall echo of the specimens and its thickness this information can be converted into chart (b) where each color represents a certain depths. The bottom echo of the water tank is used for the third C-scan result depicted in Figure 6.5 (c). Each color in the C-scan image represents a certain reduction of the signals amplitude. This method is suitable to obtain the damage size and represents the projected damage area. Therefore, the result is comparable with C-scan representation (d) obtained in 'through transmission' mode with a separate receiver. This approach is used for the UD-CFRP-steel and is hence, illustrated on a different specimen.

In the last case only the projected area is available in form of a C-scan image which is then analyzed with the help of a Python script and an associated intensity threshold of the gray scale image. In this way, the area of the damage projection in the xy-plane, the maximum length and maximum width of the damage are analyzed within the image - similar to the approach shown in Figure 6.7.

The analysis by the 'pulse-echo' technique case starts with a C-scan image as depicted in Figure 6.5 (b). Each color represents a certain depths of the damage. This approach is based on the assumption that the damage propagation through the thickness is conical. By placing the transducer and receiver on the impacted top-surface of the specimen, the geometry of the damage can be captured, but the height of the damage below the first inspected flaw remains ambiguous. However, the comparison of the C-scan image with the

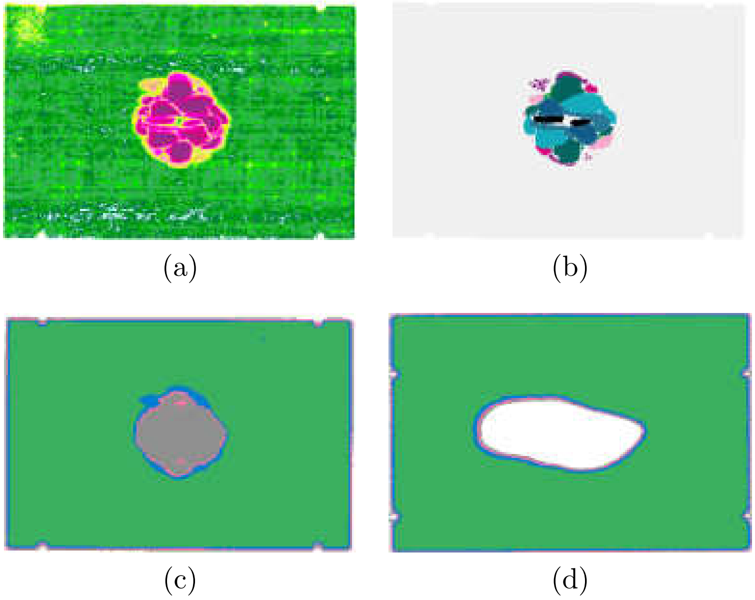
(a) (b)
(c) (d)

Figure 6.5: Example C-scans: Flaw echo (a), flaw depths (b), water tank bottom echo (c) on pure CFRP specimen and through transmission (d) on UD-CFRP-steel specimen

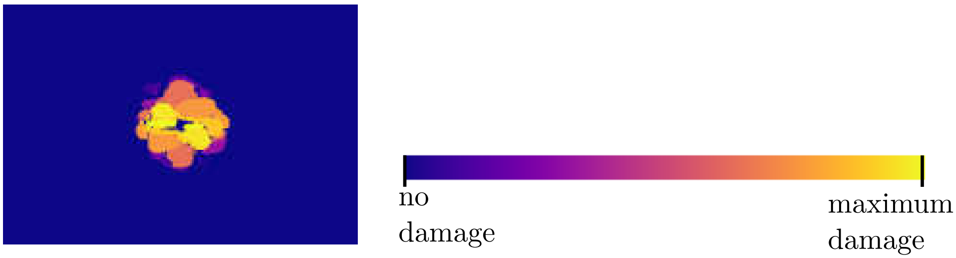

(intensity plot xy-plane) (applied colormap)

Figure 6.6: Example intensity plot and applied colormap created of a C-scan image

specimens shows that the visible damage on the back surface equals the size of the projected damage area. Therefore, it can be assumed for the present impact energies that the damage top equals the depth obtained by the 'pulse-echo' technique and the bottom equals the back surface of the specimen. Additionally, it can be suspected that this assumption is not valid below a certain energy threshold. Based on the C-scan image and the colored depth information, the two dimensional image is transformed into a three dimensional information with volume elements (voxels). By means of the discussed assumptions, each voxel below the damage top is defined as damage. In this way, the C-scan image is translated into an intensity plot as depicted in Figure 6.6. The aim of the intensity plot is to typify the geometry of the damage. Therefore, the maximum damage height in z-direction is normalized to the maximum damage color in the applied colormap in Figure 6.6. This means that the brighter colors represent a larger damage height or damage intensity in z-direction.

Applying this approach in all three dimensions leads to the images in Figure 6.7. The corresponding maximum length, maximum width and maximum height of the damage are depicted in additional diagrams. The intensity plot of each plane represents the failure expansion perpendicular to each plane. In addition to the intensity plot and the failure geometry diagrams, such a plot also includes information about the damaged volume fraction of the specimen, the total damaged area in the xy-plane and the maximum failure height, width and length. This information is calculated with the damaged voxels, their position and volume. The image of the xz-plane is oriented in the plot in a such a way that the impacted surface is located at the upper end of the image. The image of the yz-plane is orientated with the impacted surface facing to the right.

Computer Tomography

To overcome the restrictions of the US through transmission technique, where no information about the damage depth is available, CT is applied to some of the UD-CFRP-steel specimens. The level of absorption of the ionizing radiation depends on the physical density of the material. Defects, which include foreign objects or cracks that lead to different physical densities of certain areas, can be detected by radiography when oriented in the same plane as the transmitted beam. Planar cracks and planar delaminations are difficult to detect by using radiography [194].

Combining many different radiographs taken from different angles, overcomes this restriction and allows the production of cross-sectional (tomographic) images from the scanned object.

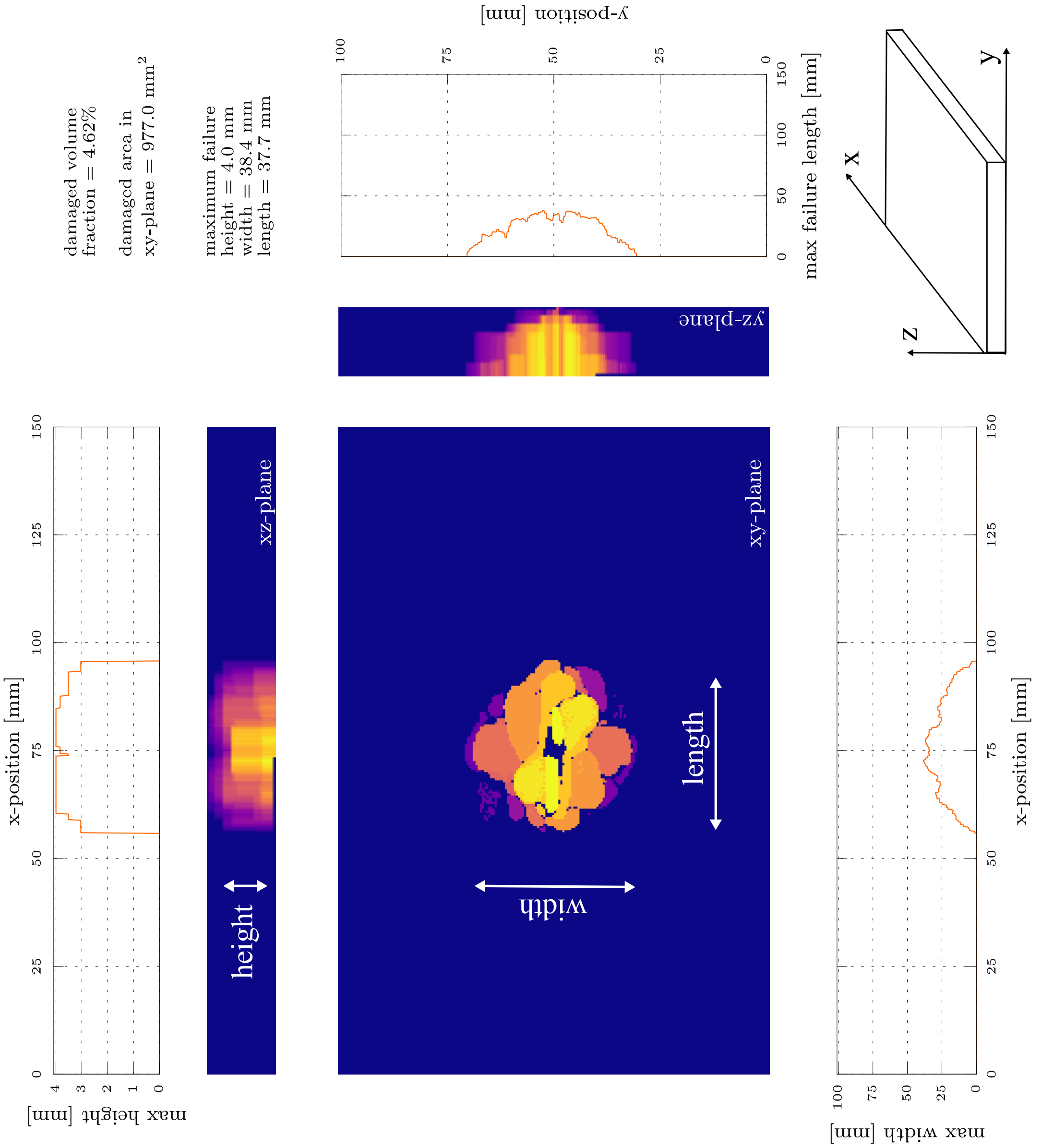

Figure 6.7: Example damage size and damage intensity plot calculated on basis of an ultrasonic C-scan

2430 radiographs are taken per UD-CFRP-steel specimen, which corresponds to an image every 0.148°, as the specimens is turned along its longitudinal axis. The general arrangement is depicted in Figure 6.8. The X-ray tube is operated with 160 kV and 0.4 mA. A flat panel X-ray detector XRD 1620 xN CS from *PerkinElmer Techologies GmbH & Co. KG* with a pixel matrix of 2048 x 2048 and 200 μm pixel pitch is used, which allows the recording of 65.536 gray levels [225]. The pixel size is 0.05851 mm x 0.05851 mm with a magnification of 3.42 in the center of the specimen. The magnification is a consequence of the distances between the x-ray tube focus and the rotation axis of the specimen (234.09 mm) as well as the distance between the rotation axis of the specimen and the detector (800.13 mm).

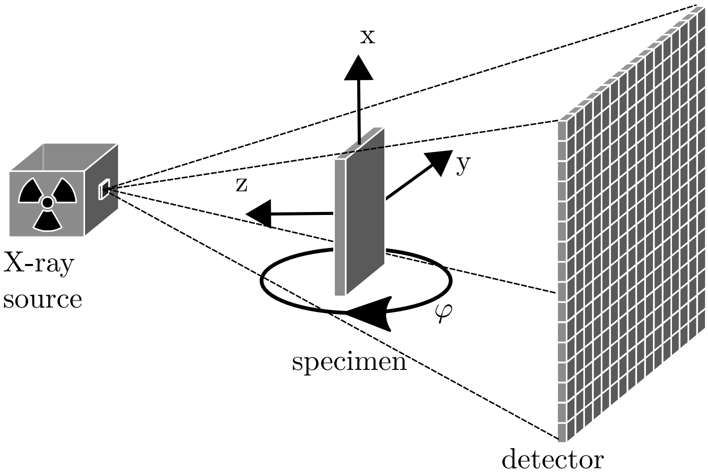

Figure 6.8: CT arrangement with specimen coordinates

The image reconstruction is performed by using discrete filtered back-projection. For further details see 'Digital Image Processing' by *Jähne* [226]. The result of the back-projection are 2048 square images of single cross sections. Figure 6.9 shows one cut-out of such a reconstructed image in the yz-plane. The fractures in the centre of the specimen are darker than the rest of the specimens and can be detected with the help of a gray scale threshold. However, the surrounding of the specimens is dark as well. As the fracture and the surrounding of the specimen may be connected, the combination of a gray scale threshold and an object size threshold does not lead to a robust process. Edge detection does also not work as the right and left edge of the surface are not recognized also different approaches have been tested.

Instead, the mainly intact specimen is identified with the help of a gray scale threshold and a morphological closing algorithm [227] is applied to this single large object. With the help of the closing algorithm, the connection between any fracture and the surrounding is eliminated. Applying this new object as a mask to the original image allows the isolation of the specimen. When the sample is isolated, the damage can be identified with the help of a gray scale threshold.

The gray scale threshold is determined as follows. The left 1/5-th and the right 1/5-th of the specimen are assumed to be undamaged. Therefore, the gray scale of the darkest pixel within these two areas serves as damage threshold value for every single image. The position of each damaged pixel is stored in a damage matrix. As the pitch of the single reconstructed images is known, a three dimensional damage matrix with the position of each damage voxel can be created.

The very different density of the materials in the specimens may lead to severe streaking artifacts, that occur due to the fact that the high density of the metal results in incomplete attenuation profiles [228]. This overranging can be reduced by means of special software corrections, but there remains a loss of detail around the metal interface. Therefore, a

Figure 6.9: Cut-out of reconstructed image of yz-plane (100 mm specimen width)

physical filter is used instead. There is a standard filter of 1 mm aluminum built in, which is extended by an additional copper filter of 0.5 mm thickness. The use of an additional filter enhances the achieved contrast. Different filter materials such as aluminum, copper, zinc and lead have been tested with different material thickness where the best results were achieved with 0.5 mm copper. However, despite the filters, there are still some artifacts present as illustrated in Figure 6.10. The diagonal lines on the left of the image are artifacts with unknown source. The artifacts near the right edge are a consequence of incomplete projections. The intensity plot is created with the same approach as described for the US images. The damage size and damage intensity plots are also drawn in a similar way as the damaged voxels, and their positions are known.

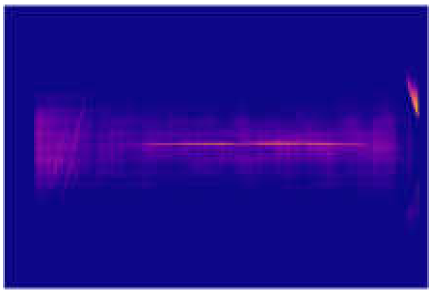

Figure 6.10: CT damage intensity plot in xy-plane with artifacts

The main difference between the plots created based on the US C-scan images and the plots created based on the yz-cross sections is in the damage progression in the thickness direction. Basically, the damage in the US-plots is extended up to the bottom of the specimens, whereas the CT reconstruction allows the identification of a lower end or bottom of the damage. Therefore, comparing the damage volume obtained by the US-scans with the volume obtained by the CT-scans is not valid.

Dent measurement

In *AITM D7136/D7136M* the dent depth is described as the residual depth of the depression formed by an impact after the impact. It is defined as the maximum distance normal to the face of the specimen from the lowest point in the dent area to the plane of the undisturbed surface [229]. As the dent depth may decrease over time due to relaxation of the composite material, in accordance with *AITM D7136/D7136M*, it is desired to record its depth and duration after impacting as well as the environmental conditions prior to measurement. There is no information about relaxation and time provided in *DIN EN 6038* [195], but *AITM1-0010* [196] requests the measurement within 30 minutes after impacting. Therefore, the dent depth is measured within this time.
Although the dent depth is defined precisely in *AITM D7136/D7136M*, the necessary positions for the reference measurement of the undisturbed surface are not defined clearly [229]. In contrast, *DIN EN 6038* [195] and *AITM1-0010* [196] define four measurement coordinates to measure the indentation 20 mm from the main indentation, as depicted in Figure 6.11. The depth t is measured with a flush pin gauge at the deepest point and the depths t_1 to t_4 at the four surrounding coordinates are measured as set out in the given pattern. The depth of indentation e is defined as [195, 196]:

$$e = t - \frac{t_1 + t_2 + t_3 + t_4}{4} \tag{6.5}$$

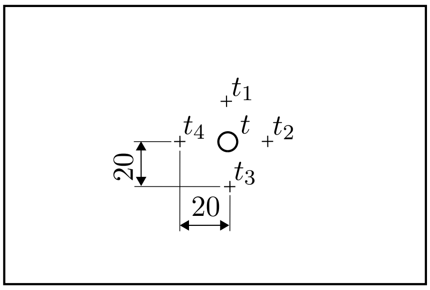

Figure 6.11: Measurement coordinates for t_1 - t_4 with the maximum dent depth t in the indented area at the impact location in the center of the specimen

6.6 CAI testing and modified impact test procedure

CAI testing consists of impacting the specimen at a certain energy level and then testing the residual compressive strength properties, as described in *DIN EN 6038* [195] and *AITM1-0010* [196]. In addition, the *American Society for Testing and Materials (ASTM)* provides the *D7137/D7137M* [197] test method for compressive residual strength testing of specimens which have previously been subjected to drop-weight impact test per method *D7136/D7136M* [229]. As described in more detail in the following subchapter, the test methods are developed for balanced and symmetrical specimens with three fiber directions. Other lay-ups lead to specimens with substantially divergent longitudinal and transverse bending stiffness. Based on the given geometry of the impact test fixture, it is assumed that testing these specimens by means of the standards leads to an anomalous influence of the fixture on the damage. This would prohibit a clear conclusion. Therefore, a modified test fixture is presented in the following after the current test standards are introduced.

Impact testing

All three mentioned test standards utilize a specimen with 150 x 100 mm size and a clear window of 125±0.2 x 75±0.2 mm, see Figure 6.12 (a) [195, 196, 229]. The specimen is clamped down to the steel base and its position is ensured by guide pins.
The specimen is then impacted with the desired energy E, which is calculated by the impactor mass m, the drop height h and the gravitational acceleration g:

$$E_{imp} = mgh \tag{6.6}$$

AITM1-0010 [196] additionally defines a minimum drop height of h_{min}=0.5 m and a maximum impact velocity of v_{max}=15 m/s. *ASTM D7137/D7137M* [197] requires an impactor mass of 5.5±0.25 kg. In terms of mass and velocity, *AITM1-0010* is applied for the present investigations. The demanded impactor geometry is identical for all three standards with a diameter D=16±0.1 mm and a smooth hemispherical striker top with a radius r=8±0.25 mm, as shown in Figure 6.12 (b).
An additional mechanism is required to ensure that the striker hits the specimen only once, which is provided by the used *CEAST drop tower impact system* by default. The contact force at the striker is measured by a piezo-electric load cell and is recorded. The velocity right before the impact is measured with the help of a photoelectric cell. After impacting each dent depth is measured as described in chapter 6.5 page 105. Before the compression strength is measured, impact damage is monitored and details - such as

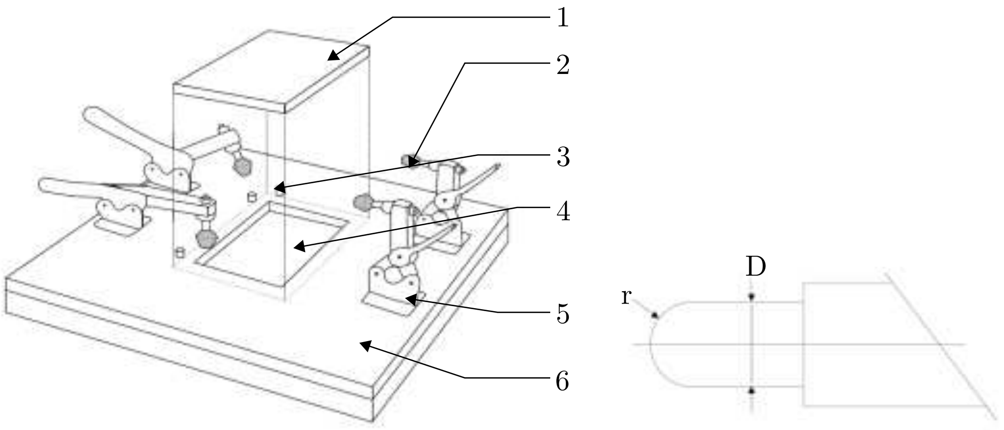

(a) (b)

Figure 6.12: Illustrative example of impact test equipment with fixture (a) and impactor geometry (b) with specimen (1), rubber cup (2), guide pin (3), clear window (4), clamping system (5) and steel base (6); based on *AITM1-0010* [196]

the extent of visible fiber breakage, delamination and indentation on both faces of the specimen - are recorded. A full scale nondestructive inspection (NDI), illustrating the extent of delamination, is prepared as described in chapter 6.5.

All three standards restrict valid lay-ups in a certain way. *AITM1-0010* [196] requires a QI-laminate approximately 4.0 mm thick. The variation of the thickness for any of the manufactured laminates shall be within ±2% of mean thickness. *DIN EN 6038* [195] prescribes the following lay-up:

$$((45/0/-45/90)_n)_s \tag{6.7}$$

where the number n of QI-sublaminates is to be determined in order to obtain a thickness as close as possible to 4 mm. This leads to identical requirements regarding the lay-up in both standards. Divergent from this, *ASTM D7136/D7136M* [229] demands for a 5 mm laminate consisting of the same sublaminates. A 4 mm laminate is selected for the present work.

Residual compression strength testing

The damaged and inspected specimen is loaded with a compressive load along its longitudinal axis while positioned in a fixture. It is designed to support the specimen and to prevent buckling as shown in Figure 6.13. The side supports are snug fit and allow the specimen to slide vertically. Some clearance prohibits any additional transverse load due to *Poisson's* effect. Crosshead speed defined to 0.5 mm/min and the load versus time curve is recorded. A typical and valid failure mode is obtained when the failure occurs through the impact damage whereas failure within 10 mm from the loaded top or bottom is invalid [196]. Strain measurement is only required for test fixture validation concerning *AITM1-0010,* but recommended in *ASTM D7137/D7137M* [197].

The compression strength after impact σ_{CAI} at a specific impact energy E_{imp} is calculated with the break failure load P_u , the specimen thickness t_{lam} and the specimen width w:

$$\sigma_r(E_{imp}) = \frac{P_r}{wt_{lam}} \tag{6.8}$$

Modified test fixture

The residual compression strength shall serve as essential parameter for comparison of UD-CFRP-steel and CFRP-HO. The change to a QI-laminate for the FML and the pure CFRP to enable a comparison in compliance with the current test standards is not convenient as the residual strength of orthotropic laminates may show a different behavior.

It is assumed that a comparison of CFRP-HO with UD-CFRP-steel or the consideration of different lay-ups of UD-CFRP-steel is currently influenced by test fixture's clear window with a predominant direction. This geometry interacts with the flexural bending stiffness ratio between longitudinal and transverse direction. The aim is to eliminate this influence by using a circular cut-out window in the impact test fixture. Figure 6.14 shows the novel test fixture with a circular window.

Due to the limited size of the specimen, the damaged area could reach or extend past the edges of the window in the supporting frame and be influenced by the supporting structure.

Figure 6.13: Compression test tool for damaged specimen with installed specimen

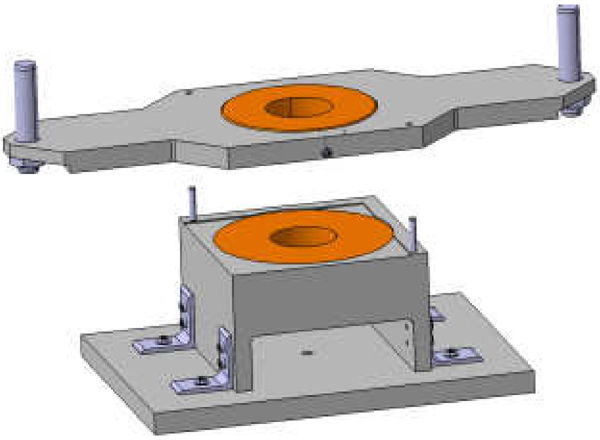

Figure 6.14: Modified impact test fixture without specimen

Therefore, it is convenient to create similar damage size on both test fixtures when using QI-laminates. In this way, the damage sizes are in the same order of magnitude.

In order to investigate different window sizes or window diameters, an interchangeable concept is chosen. The orange ring in Figure 6.14 is demountable and in this way exchangeable to different sizes. Four different steel rings are manufactured for the steel fixture with the following window diameters: 60, 80, 100 and 120 mm. The adapter rings and the fixture are designed in a way to create a H7/h6 clearance fit. They are inserted in a cool state and fastened with radially oriented set screws.

Figure 6.14 also shows the holding-down clamp, which takes adapter rings with identical diameter. The clamp is mounted to the drop tower impact system and is moved up and down automatically. The specimens are placed in the corner, created in the fixture.

6.7 Lay-ups and results

The present subchapter gives the results, which are introduced with means of the methods described above.

Firstly, the lay-ups selected for the different test methods are introduced. After that the modified test fixture is discussed and the diameter of the adapter ring is selected for the following investigations. The compression testing results of pristine pure CFRP and pristine UD-CFRP steel specimens are described before impacting is regarded. Initially, the difference in impact response between the CFRP reference and the FML lay-ups is considered and then the damage geometry and size is compared. Finally, the residual compression test is analyzed with regard to the load-displacement behavior and to the obtained compression strength values.

In the last subsection the residual compression strength properties are discussed in relation to the pristine strength properties.

Lay-up selection

The selected lay-ups can be described by the number of layers, steel thickness, theoretical and measured laminate thickness as well as metal volume fraction. This information is provided in Table 6.1 based on the laminate's notation. Three different steel layer thicknesses are used: 0.03, 0.05 and 0.08 mm. The metal volume fraction varies from 2.87 to 12%.

Besides the variation of the metal layer thickness and the volume fraction, the distribution of the metal layers may have an influence on compression strength, impact response, failure geometry and residual compression strength. Therefore, the distribution is varied as well. The lay-up notations indicate whether the metal layers are spread more to the *outer* or *inner* of the laminate or are distributed more *equaly*. In addition, the metal volume fraction in percentage is provided at the end of the notation.

Although the lay-up codification is given in the table, the relative distribution and fraction of the metal layer is not comprehensible. Hence, the lay-ups are additionally depicted in Figure 6.15, 6.16 and 6.17, where a true-to-scale representation of the thickness ratios is provided to enhance traceability.

Modified impact test procedure

The following tests are based on the test methods discussed in the previous subchapter. After impacting with different energy levels, the failure evaluation is performed by dent

Table 6.1: Specimen lay-ups with notation, number of layers, steel thickness, theoretical and measured laminate thickness as well as metal volume fraction

notation	lay-up	no. C-layers	no. St-layers	steel thickness	theor. laminate thickness	meas. laminate thickness	MVF
[-]	[-]	[-]	[-]	[mm]	[mm]	[mm]	[%]
CFRP-QI/0	$((45/0/\text{-}45/90)_4)_s$	32	0	-	4.19	4.02	-
CFRP-HO-1/0	$(45/90/\text{-}45/0_3/45/0_3/\text{-}45/0_3/90/0)_s$	32	0	-	4.19	4.02	-
CFRP-HO-2/0	$((0_3/45/\text{-}45)_2/0_3/90/0/90/_s$	32	0	-	4.19	4.02	-
CFRP-HO-3/0	$(0/45/0/90/0/\text{-}45/0_2/45/0_2/90/0_2/\text{-}45/0)_s$	32	0	-	4.19	4.01	-
CFRP-UD/0	0_{31}	32	0	-	4.19	4.00	-
UD-St-P-0.03-low/3	$((0_5/St)_2/0_5/\overline{0})_s$	31	4	0.03	4.18	4.00	2.87
UD-St-P-0.05-low/5	$((0_5/St)_2/0_5/\overline{0})_s$	31	4	0.05	4.26	4.08	4.69
UD-St-P-0.03-equal/6	$((0_3/St)_4/0_3)_s$	30	8	0.03	4.17	3.99	5.76
UD-St-P-0.05/6.25	$(0_6/St/0_4/St/0_5/\overline{St})_s$	30	5	0.05	4.18	4.00	5.98
UD-St-P-0.05/7.5	$((0_4/St)_2/0_5/St/0_2)_s$	30	6	0.05	4.23	4.05	7.09
UD-St-0.05-outer/12	$((0/St)_2/0_2/(St/0_4)_2/St/0_2)_s$	28	10	0.05	4.17	3.97	12.00
UD-St-0.05-inner/12	$((0_4/St)_2/(0_2/St)_2/0/St/0)_s$	28	10	0.05	4.17	4.02	12.00
UD-St-0.08-equal/12	$((0_4/St)_3/0_2)_s$	28	6	0.08	4.15	3.05	11.57
UD-St-0.03-low/4	$((0_4/St)_3/0_3/\overline{0})_s$	31	6	0.03	4.24	4.11	4.24
UD-St-0.05-low/7	$((0_4/St)_3/0_3)_s$	30	6	0.05	4.23	4.11	7.09
UD-St-0.03-inner/11	$((0_2/St)_6/0/St/0/\overline{St})_s$	28	15	0.03	4.12	4.0	10.93
UD-St-0.05-equal/11	$((0_3/St)_4/0_2/\overline{St})_s$	28	9	0.05	4.12	3.98	10.93

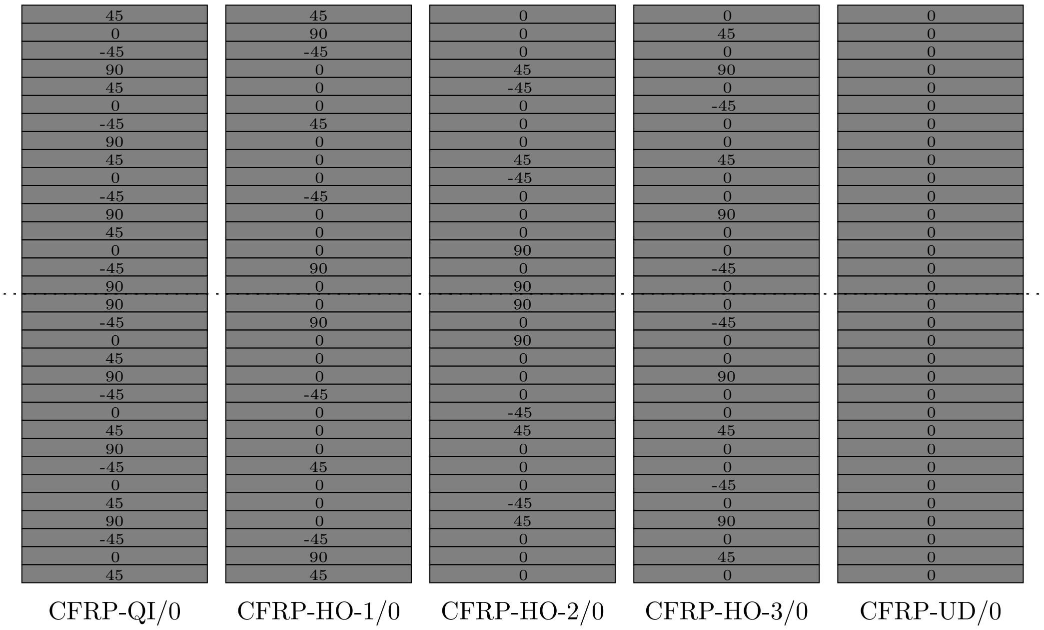

Figure 6.15: Pure CFRP reference laminate lay-ups with true-to-scale representation of the thickness ratios

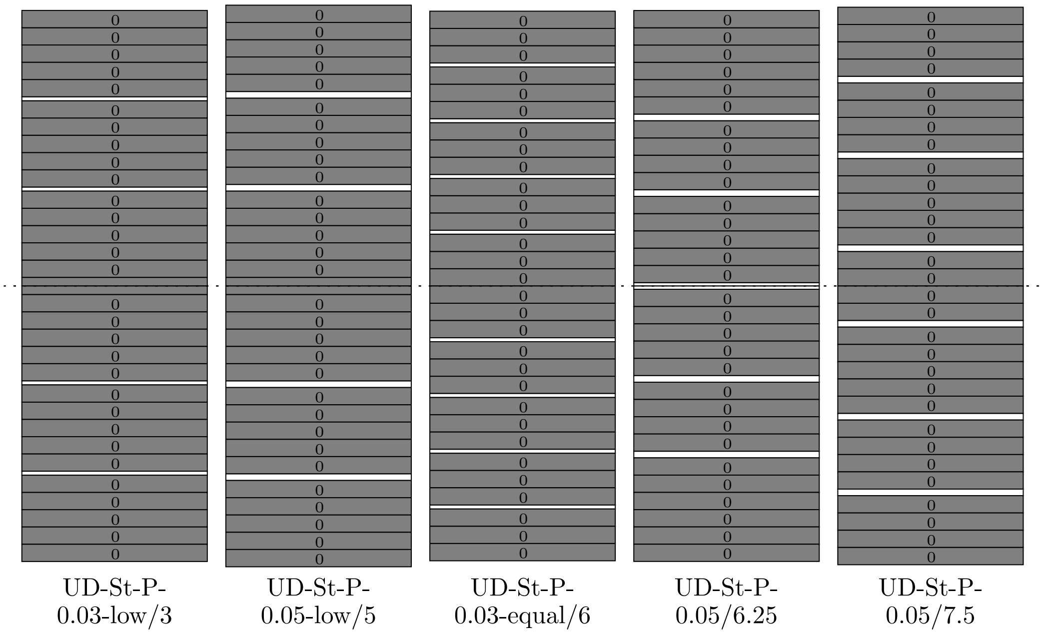

Figure 6.16: Lay-ups selected for compression testing with true-to-scale representation of the thickness ratios; steel layers in white

depth, damage area and damage geometry.

At first, QI laminates are tested on the standard impact test fixture with a cut-out of

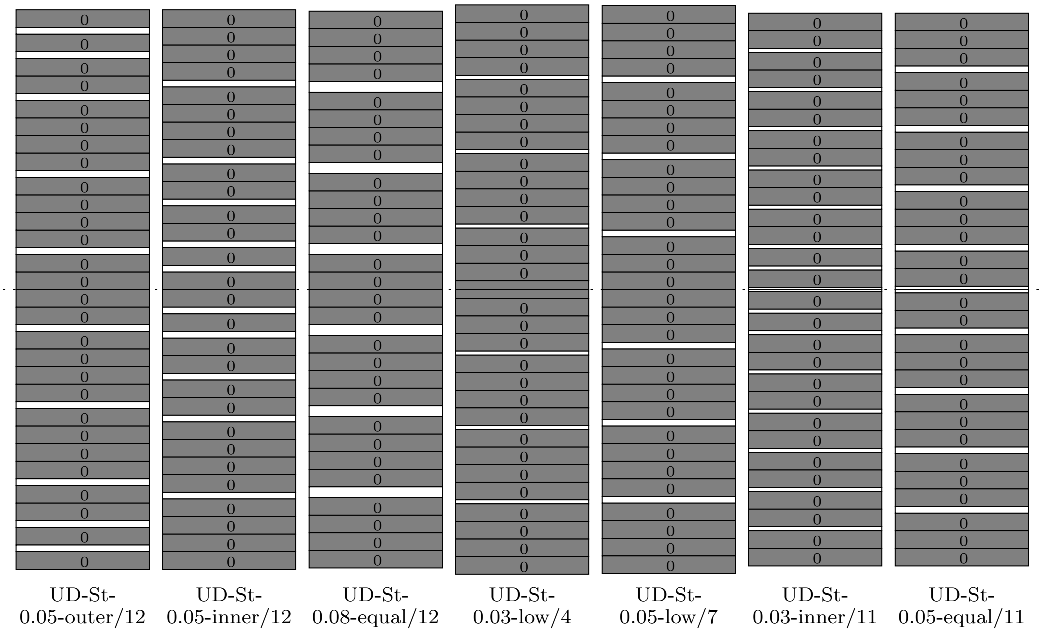

Figure 6.17: Lay-ups selected for CAI and compression testing with true-to-scale representation of the thickness ratios; first three lay-ups used for impact response comparison and last four lay-ups used for CT inspection; steel layers in white

75x100 mm and on the modified test fixture with circular cut-out of 60, 80, 100 and 120 mm in diameter. The induced damage is evaluated and an adapter size for the further tests is selected.

The further testing is performed with the CFRP-HO-1/0 lay-up and the CFRP-QI/0 lay-up. By rotating the specimens by 90°, the stiffness ratios change. Rotated specimens as well as the non-rotated specimens are tested on the standard tool and the modified tool to compare the tools' influence on the damage geometry.

Thereby, the relationship between the laminate stiffness and the cut-out geometry can be represented by the deflection of a plate under a point load. The bending of a simply supported rectangular plate under point loading is discussed by *Reddy* [26]. Unfortunately, as shown in Figure 6.12, the bearing conditions are not distinct. The plate is partly clamped and the remaining part of the edges is simply supported.

However, it is assumed that the damage is guided in the direction of the higher structural stiffness and a determination of the accountable parameter is required for the analysis of the damage results.

Thus, the spring stiffness in longitudinal and transverse direction of each specimens for the simply supported case is calculated. The longitudinal direction is identical to the 0°-direction in the lay-up's coordinate system of each specimen if not stated otherwise. In the determination of the spring stiffness of a beam, the width of the beam is required. As the relevant width depends on the cut-out dimension rectangular to the beam's longitudinal direction, it is normalized to one. Although this alternative spring stiffness does not represent the actual plate under point loading, it represents the influence of cut-out size and flexural stiffness.

Firstly, the longitudinal and transverse flexural stiffness of each considered lay-up is required. As explained by *Schürmann*, the flexural bending stiffness under consideration of the transverse contraction can be determined as follows [230]:

$$\hat{E}_{long,b} = D_{11}\frac{12}{t_{lam}^3}; \qquad \hat{E}_{trans,b} = D_{22}\frac{12}{t_{lam}^3} \tag{6.9}$$

where D_{11} and D_{22} are the respective values of the laminate's bending stiffness matrix, t_{lam} the laminate's stiffness and $\hat{E}_{long,b}$ as well as $\hat{E}_{trans,b}$ are the flexural stiffness moduli in longitudinal and transverse direction respectively. The particular values for the two regarded laminates are provided in Table 6.2.

In the second step, spring stiffness is separately calculated in the longitudinal and the transverse direction. The specimen is therefore represented by a beam, which length L_{sup} is equal to the cut-out dimension in this direction, as shown in Figure 4.3. The deflection of the center of the beam w_c subject to a point loading P in its center with both ends simply supported, is given by [231]:

$$w_c = \frac{FL_{sup}^3}{48\hat{E}_b I} \tag{6.10}$$

where I is the moment of inertia and $\hat{E}_b$ represents the flexural stiffness in the given direction.

The spring stiffness c represents the constant relationship between load and deflection:

$$F = cw \tag{6.11}$$

With the laminate's moment of inertia $I = bt_{lam}^3$, where b is the beam width, inserting equation 6.10 in equation 6.11 and solving for c leads to:

$$c = \frac{4\hat{E}_b t_{lam}^3}{L_{sup}^3} \tag{6.12}$$

Inserting the two equations under 6.9 in 6.12, leads to the following two relationships between laminate bending stiffness matrix values D_{11}, D_{22} and spring stiffness c:

$$c_{long} = \frac{48D_{11}b}{L_{sup}^3}; \qquad c_{trans} = \frac{48D_{22}b}{L_{sup}^3} \tag{6.13}$$

The results for both considered laminates and their rotated counterparts for each of the cut-out geometries are given in Table 6.2. As discussed above, the width b is normalized to one. The maximum factor between the obtained flexural stiffness values is 1.9, whereas the maximum factor for the obtained spring stiffness is 2.9.

The energy levels for this test need to be selected high enough to induce delamination but not that high that too many fibre breaks occur as they absorb energy and distort the results [217]. However, at a cut-out diameter with 120 mm, delamination needs to be obtained. According to *Caprino*, this threshold is 4.37 J [213]. Though, at 60 mm, the damage must not reach the supported area of the specimens. Based on literature results and for comparison reasons, two levels are chosen for these tests: 9 and 16 J.

The first damage evaluation parameter observed is the dent depth. The dent depth e is determined as defined in the previous subchapter and depicted in Figure 6.18. It can be observed that the dent depth created by the 16 J impact is around 43 to 51% higher with decreasing trend. It is also clearly influenced by the cut-out size and is decreased by 30%

Table 6.2: Flexural stiffness of the lay-ups considered and their alternative spring stiffness c on the different fixture cut-out geometries

notation	direction	$\hat{E}_{long,b}$	$\hat{E}_{trans,b}$	cut-out length L_{sup}				
				60 mm	75 mm	80 mm	100 mm	120 mm
				c	c	c	c	c
[-]	[-]	[GPa]	[GPa]	$[\frac{kN}{mm}]$	$[\frac{kN}{mm}]$	$[\frac{kN}{mm}]$	$[\frac{kN}{mm}]$	$[\frac{kN}{mm}]$
CFRP-QI/0	long	68.76	56.43	297.8	238.2	223.3	178.7	148.9
CFRP-QI/0	trans	56.43	68.76	244.4	195.5	183.3	146.6	122.2
CFRP-HO-1/0	long	87.91	47.14	380.7	304.6	285.5	228.4	190.4
CFRP-HO-1/0	trans	47.14	87.91	204.2	163.3	153.1	122.5	102.1

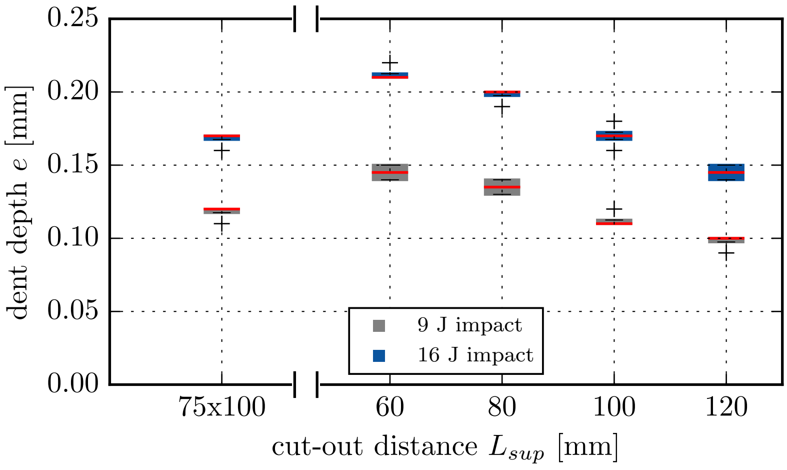

Figure 6.18: Dent depth e dependence on cut-out distance L_{sup} for 9 and 16 J impact; rectangular cut-out 75x100 mm and circular cut-outs

when increasing L_{sup} from 60 to 120 mm. It is also obvious that the dent depth obtained on the 100 mm diameter cut-out matches the dent depth of the standard fixture with 75x100 mm cut-out best.

In contrast, the damage area A_d observed by US is more sensitive to the cut-out geometry, as demonstrated in Figure 6.19. The relative difference between the largest and smallest mean damage area for 16 J impact is 137%. The difference in damage size between the two impact energies reduces with increasing cut-out size. This relationship is comparable with the dent depth. It is clearly visible that the damage size varies, although the relation is regressive.

Again, the damage obtained on the 100 mm diameter fixture is most similar in size to the damage created by the standard fixture.

Observing the damage geometries given in Figure 6.20, it shows that the projection in the xy-plane (larger figures) are all circular when using a QI-laminate. Even on the standard

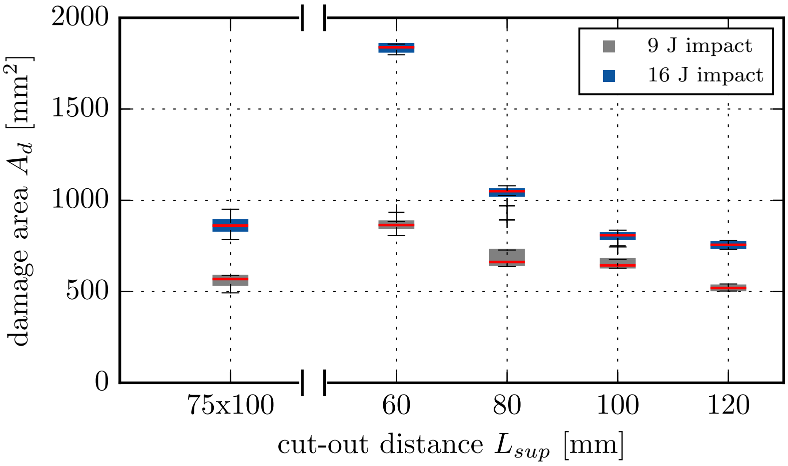

Figure 6.19: Damage area A_d obtained by US related to cut-out distance L_{sup} for 9 and 16 J impact; rectangular cut-out 75x100 mm and circular cut-out windows

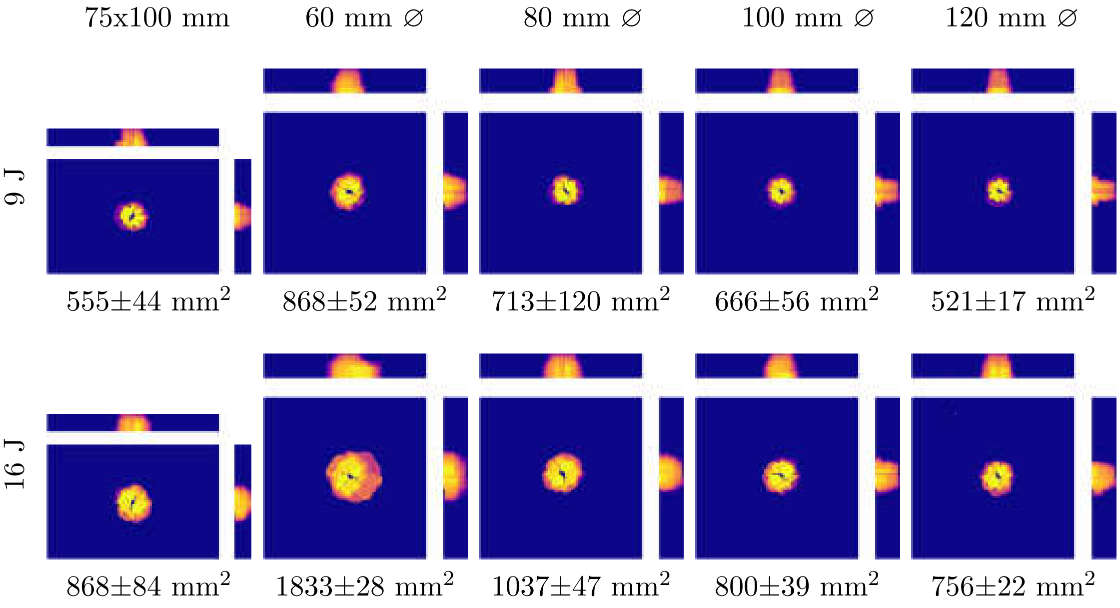

Figure 6.20: US reflection C-scan intensity plot of QI-specimens impacted with 9 and 16 J on different fixture cut-out geometries and mean damaged area plus/minus one standard deviation ($\mu \pm \sigma$)

fixture with rectangular cut-out, the damages are quite circular. Comparing the two remaining projections of each specimen with each other shows that the failure geometry in both planes is equal. Therefore, the length to width ratio of the damages is not considered in more detail for the QI-laminates.

The alternative spring stiffness on the standard fixture for the QI lay-up is 178.7 kN/mm in longitudinal direction and 195.5 kN/mm in transverse direction, which is a relative difference of 10%. The relative difference for the circular cut-outs for QI lay-up is 22%. It seems that this difference is too low to generate a distinct deviation from circular shape.

For the utilized energy levels, the distance between damage and edge is sufficient to fulfill the requirements, defined in the standard and to ensure that the failure does not reach the cut-out edge.

Based on these results, the 100 mm cut-out is selected for further examinations with the CFRP-HO-laminates in order to validate the novel fixture.

Figure 6.21 shows the US C-scans obtained by reflection of specimens impacted with 16 J as an intensity plot. The larger images show the xy-plane and the smaller images the xz- and yz-planes. The figure also shows the calculated damage area and the damage length l_d to damage width w_d ratio l_d/w_d or respectively the ratio w_d/l_d. The pictograms on top indicate that the specimens presented in the first two columns are tested on the standard fixture with a cut-out of 75x100 mm. The specimens depicted in the third and fourth column are tested on the modified fixture geometry with a cut-out diameter of 100 mm. The pictograms indicate that the lay-up in the second and fourth row is rotated by 90°. In these cases, the ratio w_d/l_d is provided to allow an easier comparison of the lay-ups. The first row shows specimens with CFRP-QI/0 lay-up and the second column specimens with CFRP-HO-1/ lay-up. The ratio in longitudinal to transverse flexural

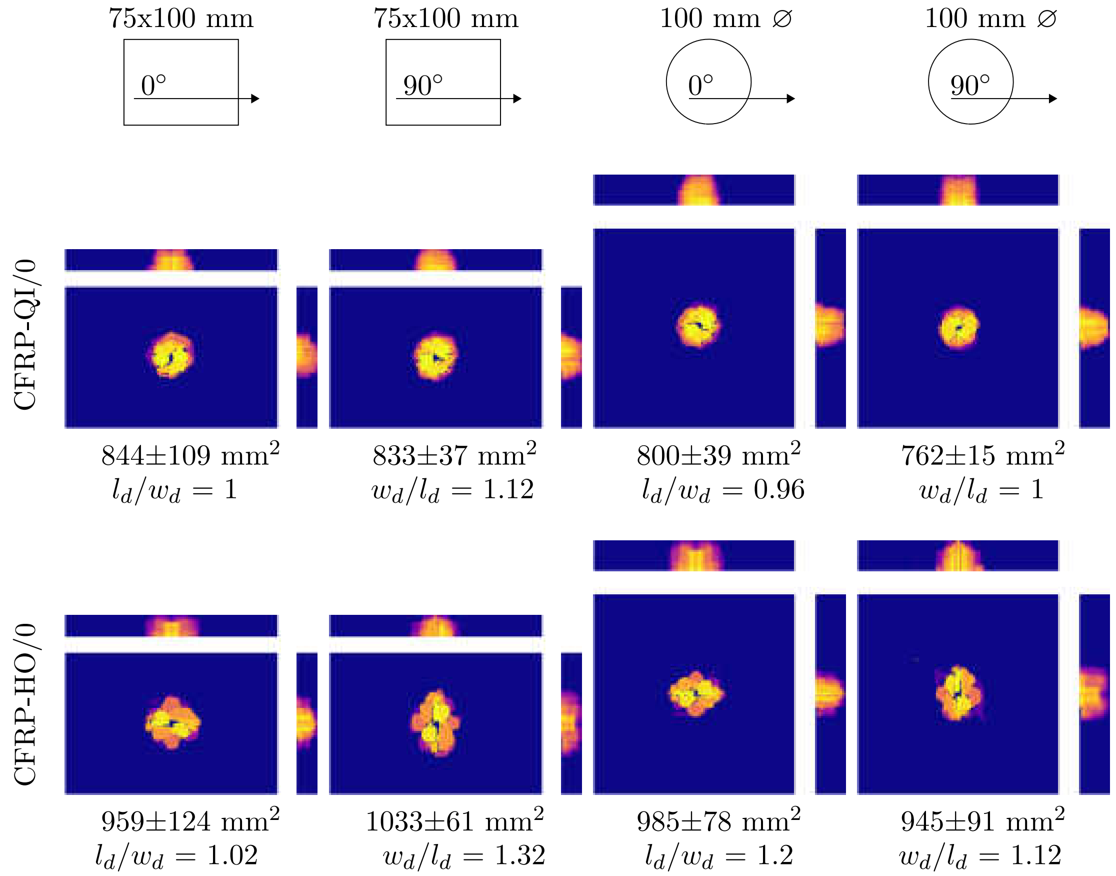

Figure 6.21: US reflection C-scan intensity plot of QI and HO-specimens impacted with 16 J on different fixture cut-out geometries, mean damaged area plus/minus one standard deviation (μ±σ) and damage length to damage width ratio l_d/w_d and its reciprocal value respectively

stiffness $\hat{E}_{long,b}/\hat{E}_{trans,b}$ is 1.22 for the QI laminate and 1.87 for the CFRP-HO-1/0 lay-up.

On the circular cut-out, the ratio between the flexural stiffness in longitudinal and transverse stiffness is identical to the flexural stiffness ratio. As a consequence, it is assumed that the obtained damage ratios given in Figure 6.21 are equal for both QI laminates irrespective of their rotational angle and that they are equal for both HO laminates irrespective of their rotational angle. Although not identical, deviation obtained between the QI laminates is 4% and the deviation between the HO-laminates is 7%.

Regarding the damage results obtained by impacting on the standard fixture, different cases need to be distinguished. The flexural stiffness ratio of the QI laminate interacts with the two different cut-out dimensions. For the non-rotated case, the spring stiffness ratio between longitudinal and transverse direction is 0.91. In this case, the spring stiffness ratio is closer to one than the flexural stiffness ratio and the obtained damage ratio is $l_d/w_d = 1$. The alternative spring stiffness values are given in Table 6.2.

When the QI-laminate is rotated by 90°, the spring stiffness ratio is 1.62 and, therefore, larger than the flexural stiffness ratio. In this case, the damage ratio is $w_d/l_d = 1.12$.

For the HO laminate, the flexural stiffness ratio is already higher. For the non-rotated case, this leads to a spring stiffness ratio of 1.39 and the generated ratio of the damage geometry is 1.02. When rotating the HO laminate on the fixture by 90°, the spring stiffness ratio increases to 2.49 and the obtained ratio in damage is 1.32.

Result plots for two example specimens representing the cases with a CFRP-HO/0 laminate impacted with 16 J on the standard test fixture are depicted in Figure 6.22 for the non-rotated case and in Figure 6.23 for 90°rotation. The difference in damage ratio between the two cases is obvious when comparing the damage in xy-plane. However, these two figures show that besides the change of the projected area, the shape changes as well. In case one, the damage shows a conical cross section in the yz-plane and a more cylindrical form when the xz-plane is regarded. In contrast to that, the damage shows a cylindrical cross section in the yz-plane and a conical cross section in the xz-plane for case two. This means that on a face perpendicular to the main fiber direction (in case one: yz-plane; in case two: xz-plane), the projection of the damage shows a triangular shape whereas on a face parallel to the main fibre direction it shows a rectangular shape. One possible explanation for the damage being transferred differently is the shear stiffness in these two planes. The low shear stiffness in the plane perpendicular to the main fiber direction may prohibit that larger delaminations are transferred up to the bottom of the specimen.

In addition, the damage volume in case two is increased as the spring stiffness of the plate is also increased as a consequence of the alignment of the higher flexural stiffness in the direction of the shorter cut-out distance.

A similar behavior with varied damage cross-section geometry can be observed for the HO laminates on the circular cut-out as well, although the damage volume does not change as the overall spring stiffness does not change.

The results clearly show a relationship between the spring stiffness ratio and the obtained damage ratio l_d/w_d. In order to achieve a simplification when regarding the ratio, the spring stiffness ratio and the damage ratio are transferred to the lay-ups coordinate system. Hence, the ratio for spring stiffness is c_{long}/c_{trans} describing the stiffness in 0°and 90°-direction of the laminate's lay-up. Likewise, the damage dimension ratio d_{long}/d_{trans} is consisting of the damage dimension in 0°and 90°-direction, respectively.

This relation is depicted in Figure 6.24, where an increasing trend between damage ratio and alternative spring stiffness can be noticed. This means that the damage is conducted in the direction of higher spring stiffness, which leads to an increased damage ratio.

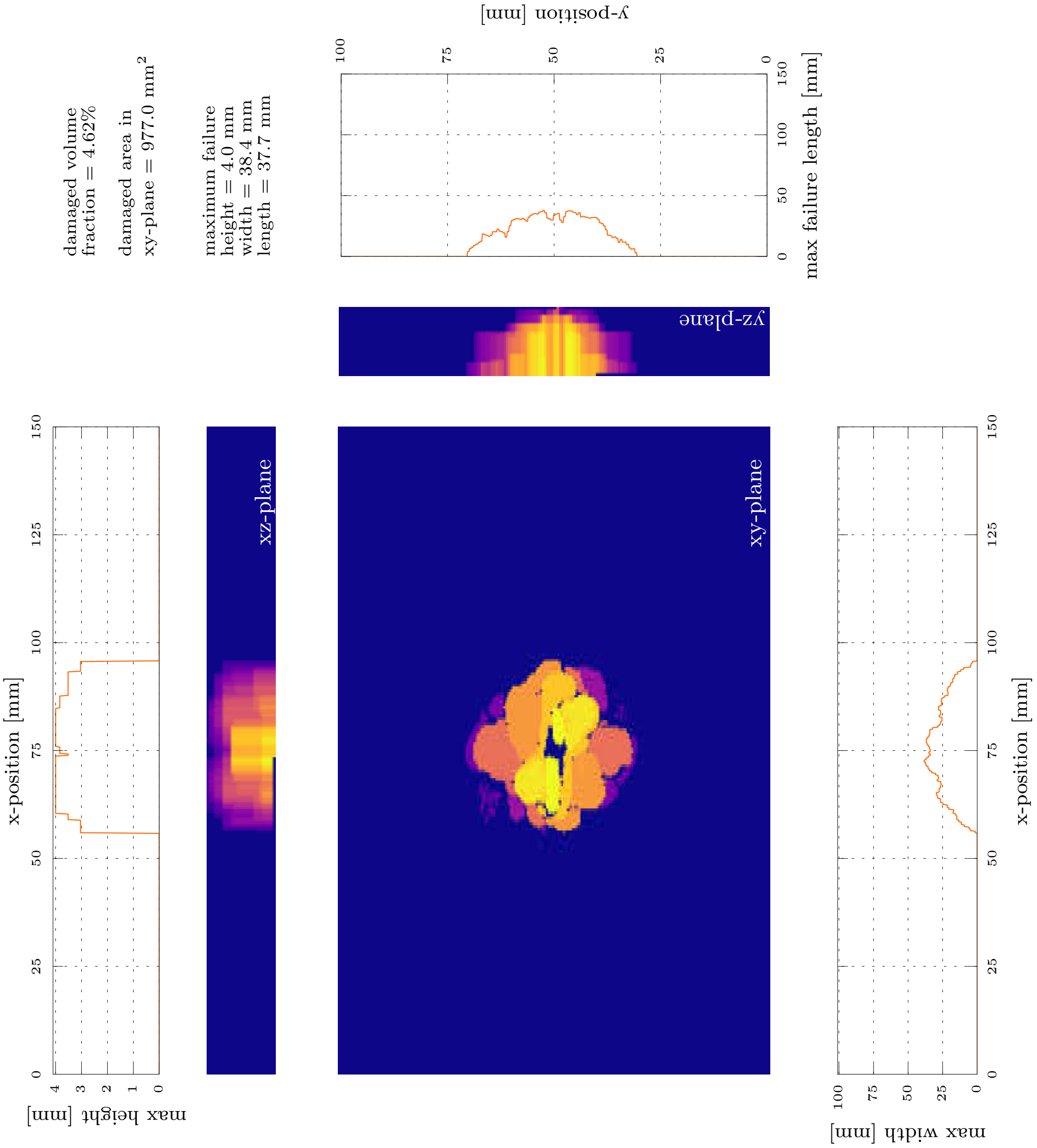

Figure 6.22: Damage intensity plot of a CFRP-HO/0 lay-up impacted with 16 J on the standard test fixture with 0°-direction aligned with longitudinal direction of cut-out

However, more data are required to describe this relationship in more detail.

As shown by the results in Figure 6.21, this effect is a combination of test fixture geometry and flexural stiffness. Though, in material development in general, the interaction of both effects may be cumbersome. By using the circular cut-out geometry, the interaction can be prevented. Hence, the modified test fixture geometry is used for subsequent testing of the orthotropic UD-CFRP-St lay-ups.

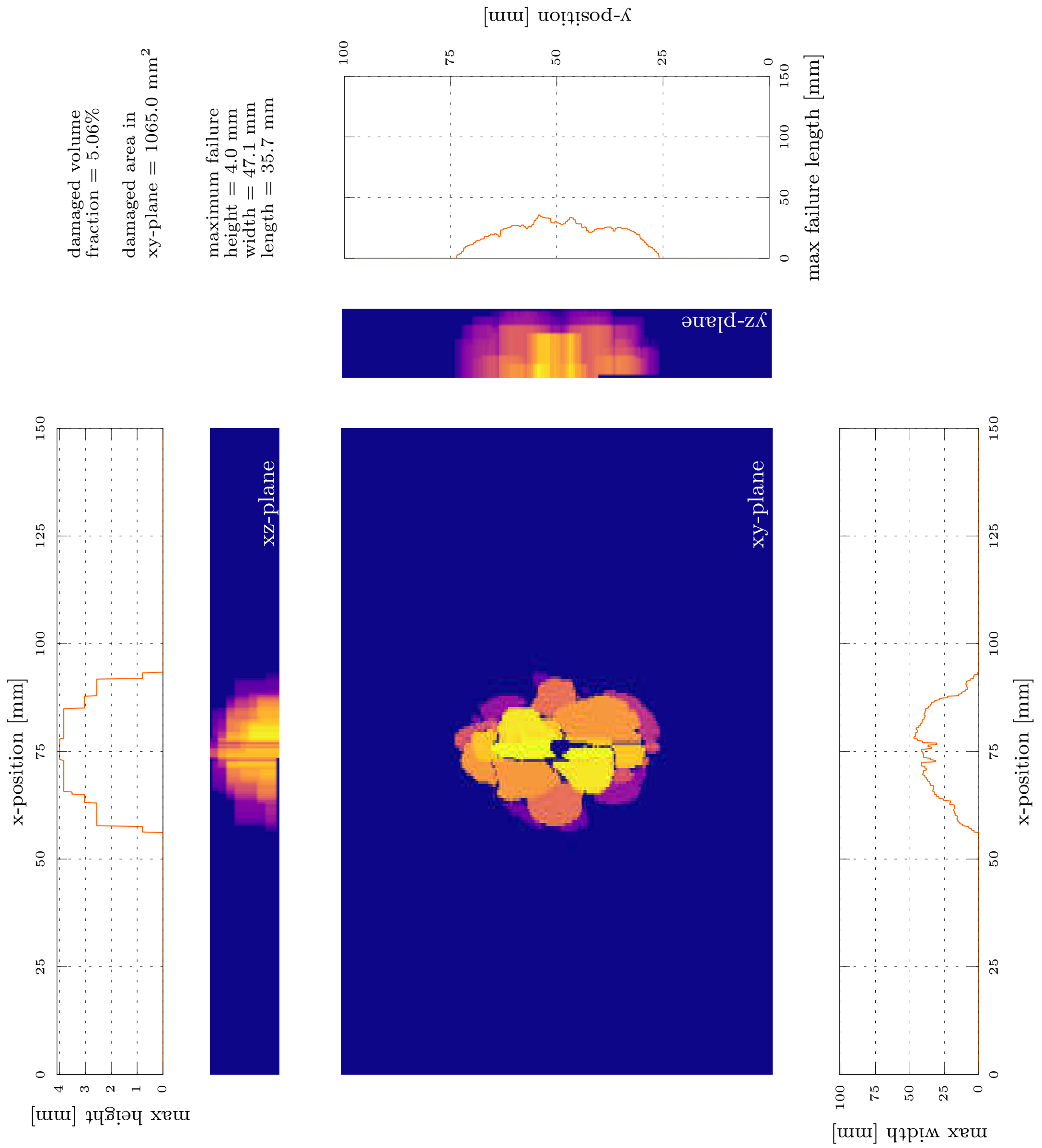

Figure 6.23: Damage intensity plot of a CFRP-HO/0 lay-up impacted with 16 J on the standard test fixture with 0°-direction aligned with transverse direction of cut-out

Compression stiffness and strength of UD-CFRP-steel and pure CFRP

The testing for the determination of the compression stiffness and strength is conducted along *AITM1-0008* [219], as presented in subchapter 6.4 with a specimen width of 25 and 32 mm.

All lay-ups introduced in the previous chapter, are tested in compression aside from the CFRP-QI/0 lay-up. Three specimens are used per lay-up for the majority except the lay-ups UD-St-0.03-low/4, UD-St-0.05-low/7, UD-St-0.03-inner/11 and UD-St-.05-equal/11, where four specimens are tested. The stress-strain curve of all specimens is linear up to their abrupt failure and there is no evidence for any yield behavior. Therefore, stiffness and

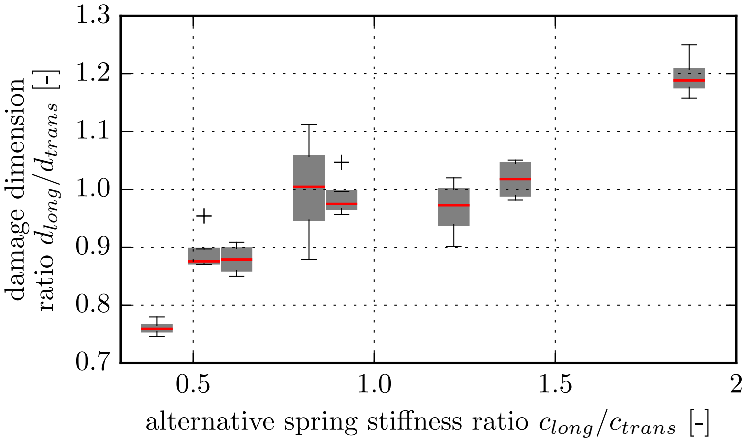

Figure 6.24: Ratio between longitudinal damage d_{long} and transverse damage d_{trans} dimension depending on alternative spring stiffness ratio c_{long}/c_{trans}

strength are regarded only in the following and the stress-strain behavior is not discussed any further.

The PBS threshold of 10% is exceeded by some specimens at the beginning of the test, indicating unacceptable bending. However, above 40% of their failure load, all specimens achieve a PBS value below 10%. The comparison of stiffness and strength between these basically invalid specimens with valid the specimens of the same lay-up does not show any trend. Therefore, contrast to the definition in the test standard, all specimens are included for the following evaluation.

The compression moduli E_c of the different lay-ups are depicted in Figure 6.25. As expected, the stiffness of all three CFRP-HO lay-ups is considerably lower than the stiffness of all other lay-ups. The sensitivity with regard to the lay-up is quite small as the total deviation is less than 5%.

In comparison to HO, the CFRP-UD/0 lay-up shows an increase in stiffness of nearly 50%. The moduli of the lay-ups with 0.03 mm steel layers do not show any significant increase. The median of the UD-St-0.03-inner/11 is slightly increased compared to the UD laminate by 2% even though 11% steel is used. In contrast, the specimens with metal volume fraction φ_M above 12% and steel layer thickness above 5 mm, show a clear stiffness gain of 8 to 12% compared to the UD lay-up.

Regarding the compression strength of the different lay-ups investigated, as shown in Figure 6.26, the advantage of the UD-laminate over the HO lay-ups is smaller than with regard to stiffness. Basically, the relative variation of the compression strength is larger than the variation of the stiffness results. All UD-CFRP lay-ups, except UD-St-0.05-outer/12, show a benefit in strength over the UD-lay-up. The highest increase of strength is achieved by the UD-St-0.03-low/4 and the UD-St-0.03-inner/11 laminates.

Conspicuously, the highest strength is obtained in particular by the lay-ups containing 0.03 mm steel layers albeit the use of low metal fraction. Exactly these lay-ups exhibit the lowest stiffness. In contrast, the two lay-ups with the highest stiffness UD-St-0.05-outer/12 and UD-St-0.05-inner/12 reveal the lowest compression strength. However, this rule is not applicable on the UD-St-0.08-equal/12 laminate, which shows comparably high stiffness and strength.

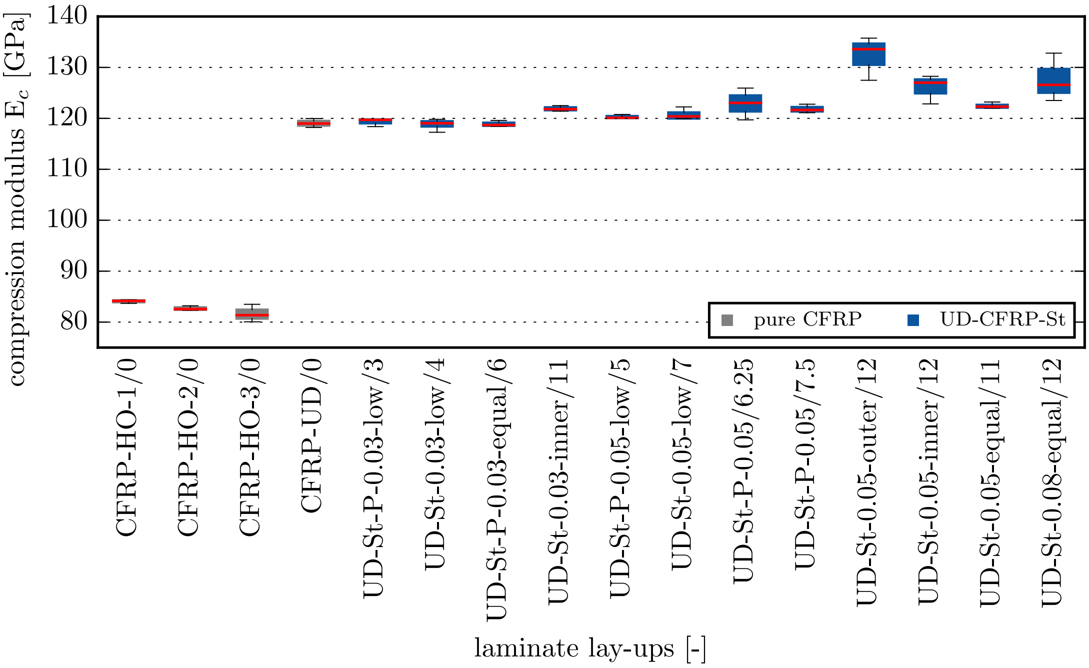

Figure 6.25: Compression stiffness modulus of different lay-ups with increasing metal ply thickness from left to right

There is no clear indication, neither in stiffness nor in strength results that the arrangement of the metal layers with cumulation to the inner or outer layer is of any influence. The more equally distributed arrangement of the metal layers does also not show any advantage or disadvantage for the pure compression loading scenario.

As the density of the lay-up increases with metal volume fraction, the consideration of the weight-specific stiffness and strength results is essential as well. Figure 6.27 shows the specific compression moduli of the different lay-ups. The lay-up itself is not indicated for sake of clarity but the results are arranged with regard to φ_M. The calculated relationship based on ROM, as discussed in chapter 3, is also indicated by a black line in the diagram. The HO results in blue are given for comparison only as they do not meet the assumptions for the ROM calculation. The measured stiffness of the UD lay-up is slightly higher than the calculation, which is based on the manufacturer information [33]. The majority of the compression moduli meet the calculation quite well. Therefore, any deviation from the calculation indicates an advantaged or disadvantaged lay-up. UD-St-P-0.05/6.25, UD-St-0.08-equal/12, UD-St-0.05-inner/12 and UD-St-0.05-outer/12 are lay-ups, that show a certain advantage whereas UD-St-P-0.03-equal/6, UD-St-0.03-inner/11 and UD-St-0.05-equal/11 show a certain disadvantage.

Again, no clear trend for any of the lay-ups can be derived, except that some of the lay-ups containing 0.03 mm metal foil are disadvantageous.

Recalling formula 3.14 on page 24, which describes the relationship between stiffness and density to achieve a weight-specific stiffness benefit over the HO-reference laminate, leads to the assumption that metal volume fraction must be less than 12.3% for the CFRP-HTS and steel material used. As the stiffness, achieved by the HO-laminates, is lower than estimated and the stiffness of the lay-ups with 12% are higher than expected, there is a

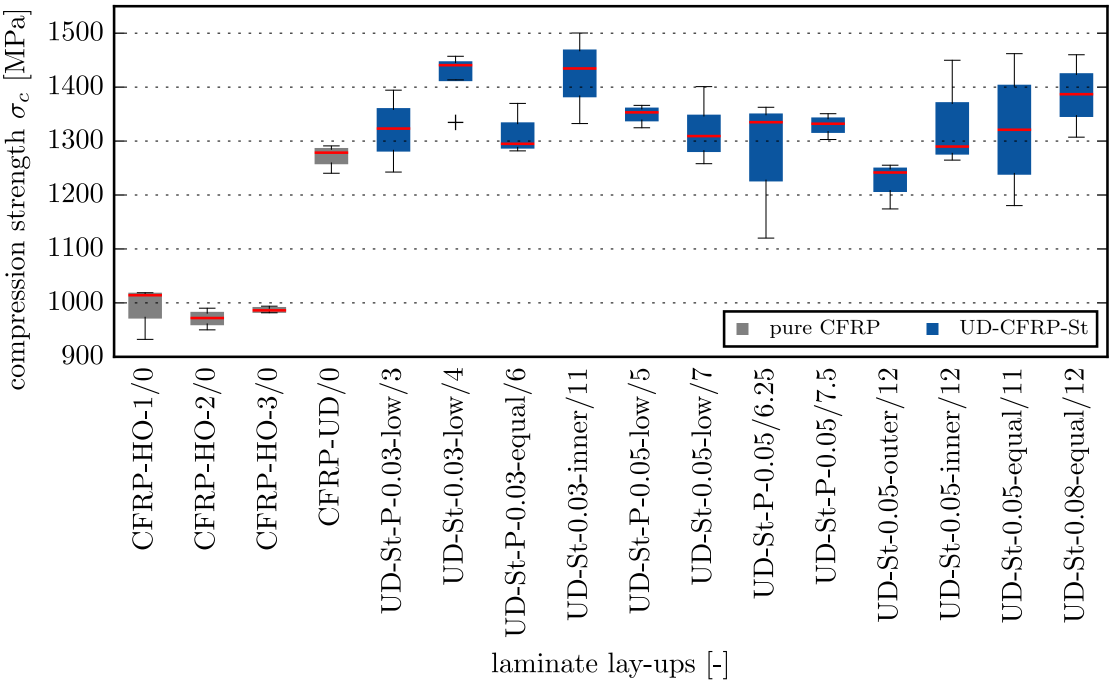

Figure 6.26: Compression strength of different lay-ups with increasing metal ply thickness, from left to right

clear advantage of the FML even though an equal weight-specific stiffness is estimated. The weight-specific stiffness of UD-St-0.05-outer/12 is 10% higher than the weight-specific stiffness of the HO laminates.

On the other hand, the compression strength results do not meet the estimations, neither by the pure CFRP specimens, nor by the UD-CFRP-steel laminates (as shown in Figure 6.28). As emphasized in chapter 3, the residual stress induced by the manufacturing is advantageous for the compression load case. Based on the investigations in chapter 5, a stress free temperature T_{sf} of 150°C can be assumed when applying the manufacturer's recommended cure cycle. The graphs indicate the calculated compression strength for 180°C, when no interaction is present as well as for 140°C and 160°C. The results are therefore expected in the range between the latter two. However, none of the results achieves this range. Although UD-St-0.03-low/4 lay-up is close to meet this range, there is one lower outlier present, which derogates the explanatory power of this result.

As discussed earlier, the lay-ups containing 0.03 mm steel layers show comparatively high compression strength values. However, there is only one 0.03 mm steel layer lay-up tested with φ_M above 6%, what impedes the identification of a trend. Instead, the orange trend line obtained by simple linear regression analysis, shows a slightly decreasing trend.

The different densities of the lay-ups are considered in Figure 6.29, where the weight-specific compression strength $\sigma_{c,spec}$ is shown. The decrease of specific compression strength is clearly recognizable. The UD-St-0.03-inner/11 lay-up exhibits a comparable strength to HO lay-ups. All remaining UD-CFRP-St lay-ups with $\varphi_M \geq 11\%$ show a lower specific strength whereas the lay-ups with $\varphi_M \leq$ 7-5% show higher specific values. The CFRP-UD/0 lay-up clearly exhibits the highest weight-specific compression strength.

Although all specimens fail abruptly and the load drop is similar, the test specimens exhibit

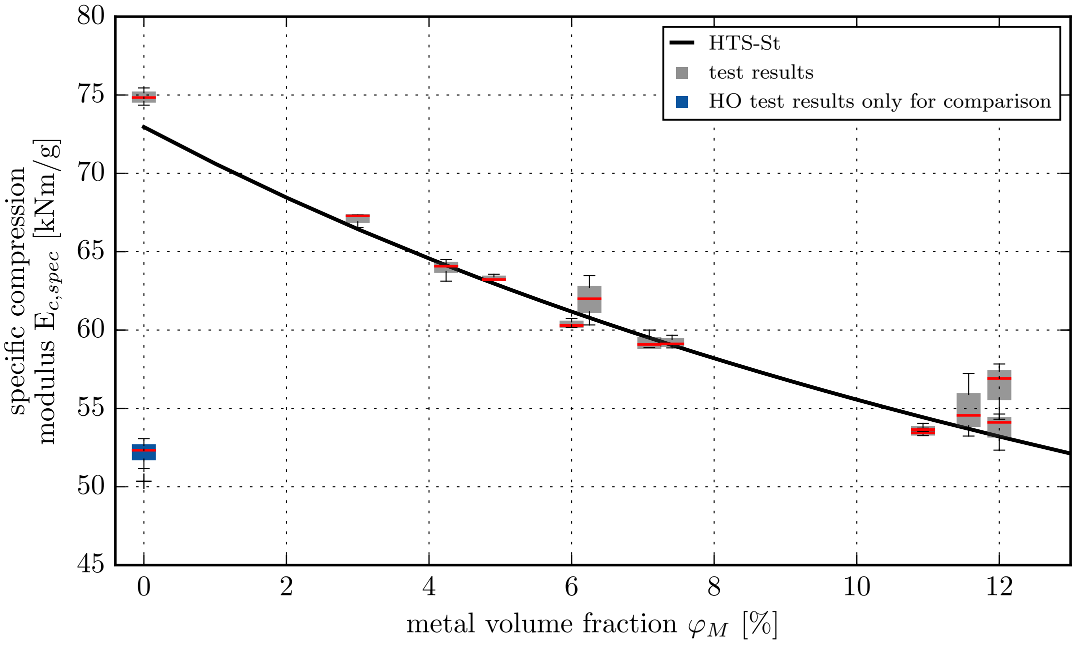

Figure 6.27: Weight-specific compression stiffness modulus of different lay-ups related to metal volume fraction φ_M in comparison to HTS-St modulus calculated with ROM

a different appearance. Figure 6.30 shows a pure CFRP specimen and a UD-CFRP-steel specimen tested for compression. It is clearly visible that the pure CFRP specimen exhibits a splintered and spiky geometry. Contrary, the failure in the UD-CFRP-steel specimen seems more even with only a few open fibers. When dangling the CFRP specimens and moving the two ends relative to each other manually, the two pieces fall apart. The UD-CFRP steel specimens can not be separated by hand and are still able to transfer shear and tensile loads.

Impact response of UD-CFRP-steel and pure CFRP

In this subchapter, the impact response is inspected with focus on the material and lay-up specific characteristics. Four different lay-ups are used for the subsequent analysis: CFRP-HO2/0 as reference, UD-St-0.05-outer/12 and UD-St-0.05-inner/12 to consider stacking sequence influences and UD-St-0.08-equal/12 to include another metal layer thickness. All specimens are impacted with 9, 12 and 16 J on the 80 mmØ modified test fixture. However, for the analysis of the impact response, only the 9 J impact is regarded. Different parameters are considered thereby: the threshold force F_t, the maximum contact force F_{max} and the contact time t_c. The threshold force F_t is defined as the force peak at which first damage occurs in the laminate. The failure leads to a decrease of the measured contact force and creates a characteristic first peak [213, 232] in the time-force curve. The maximum contact force F_{max} is the maximum force measured, irrespective of F_t. In general, the force increases after reduction is generated by the failure while bending of the specimen is obtained. The contact time t_c aims to describe the duration whereas impactor and specimens are in contact. However, as this is not measured directly, the measurement

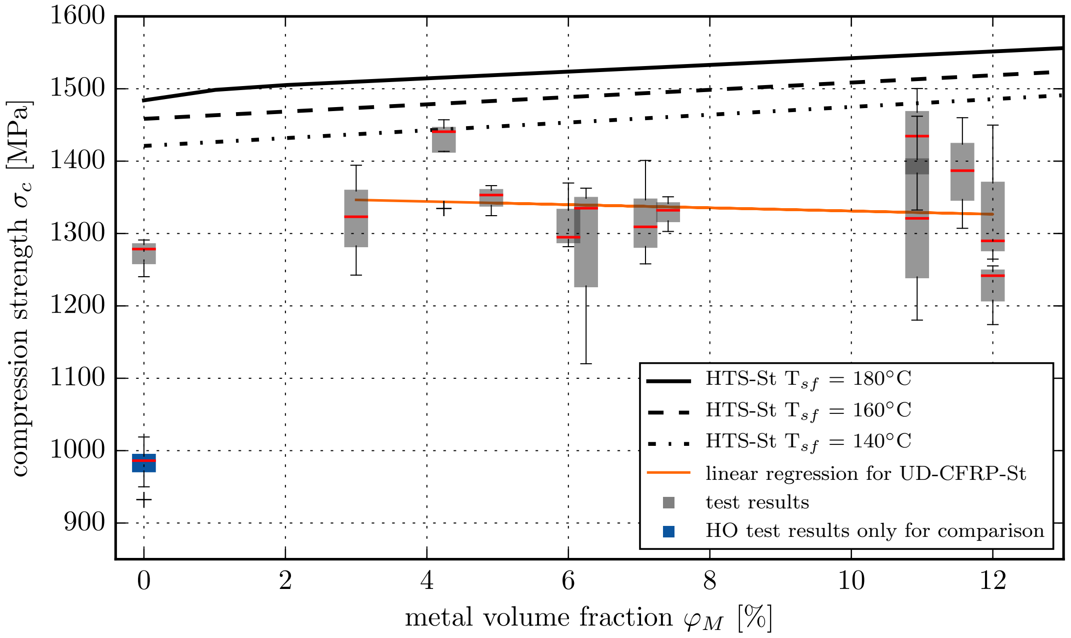

Figure 6.28: Compression strength of different lay-ups related to metal volume fraction φ_M in comparison to HTS-St compression strength calculated with ROM

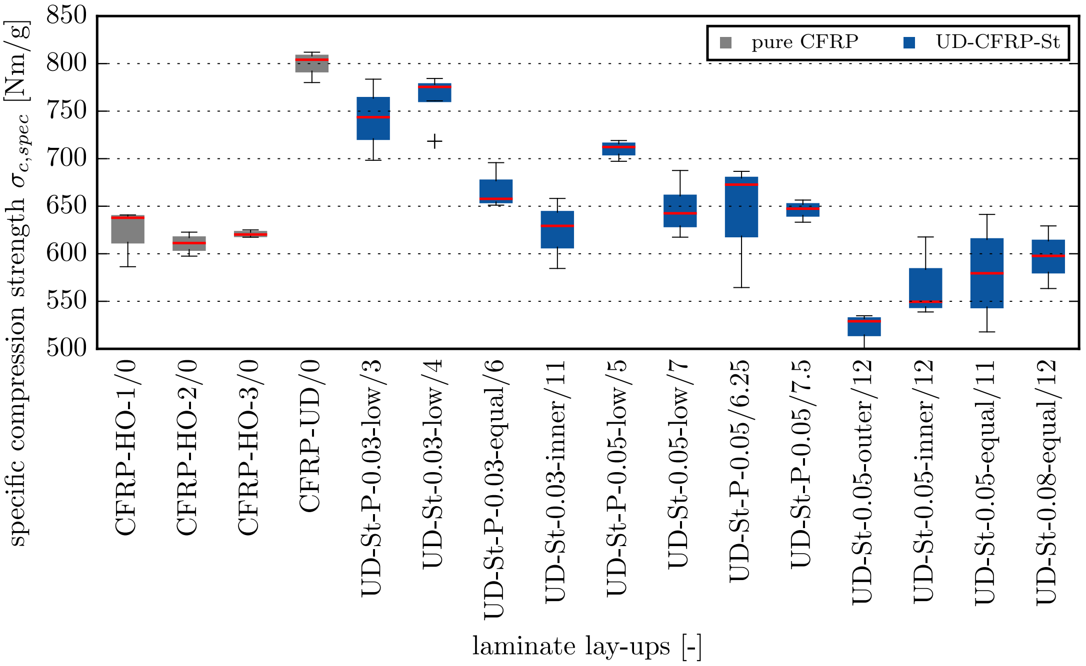

Figure 6.29: Weight-specific compression strength of different lay-ups with increasing metal ply thickness, from left to right

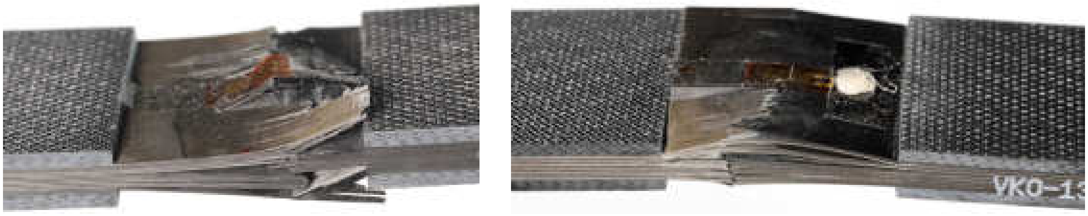

pure CFRP UD-CFRP steel

Figure 6.30: Material dependent compression failure of test specimens

of the contact time t_c equals the time span in which a contact force is observed.
Based on the impactor velocity, measured with the help of the photoelectric cell, the deformation or displacement over time is obtained and allows the calculation of the kinetic impactor energy over time. In Figure 6.31 one representative time-force curve is given whereas Figure 6.32 shows one representative time-kinetic energy curve per specimen.
All the force-time curves show a pronounced threshold force, enabling the identification of the threshold, the maximum force and the contact time in the diagram. All energy-time curves show comparable characteristics. The reduction of the impactor's kinetic energy starts with its contact to the specimen surface and reaches zero when its movement is stopped completely. Then, the strain energy stored in the specimens starts to accelerate the striker in the opposite direction and its kinetic energy increases again. As the process is not reversible, the residual energy is not equal to the starting value. Instead, a 'plateau' is reached, which corresponds with kinetic energy reclaimed by the striker. The difference

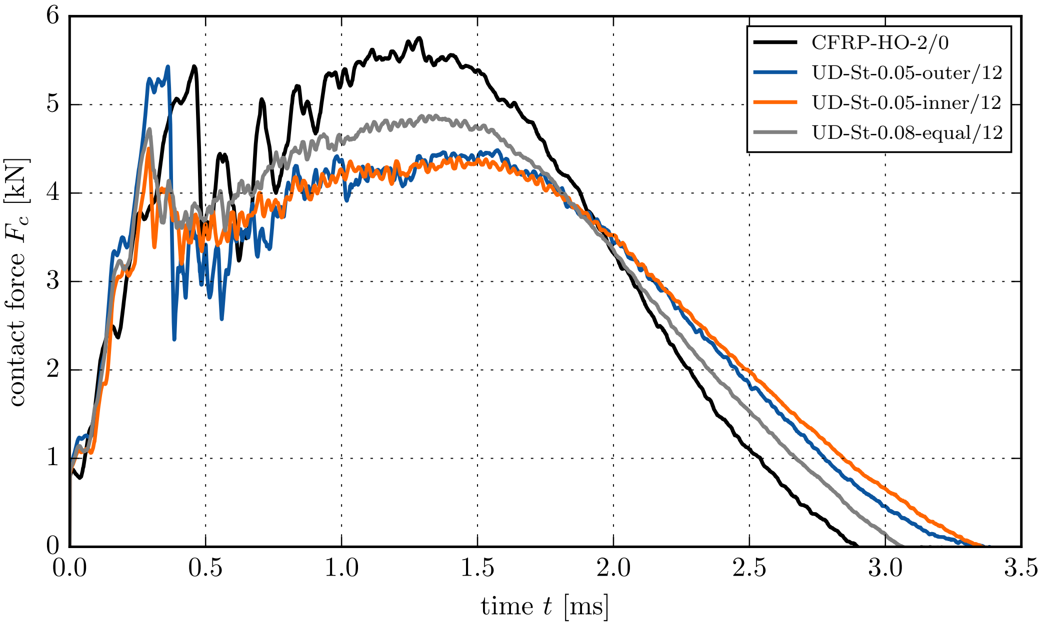

Figure 6.31: Force-time diagram representing the impact response of four example specimens with different lay-ups at 9 J

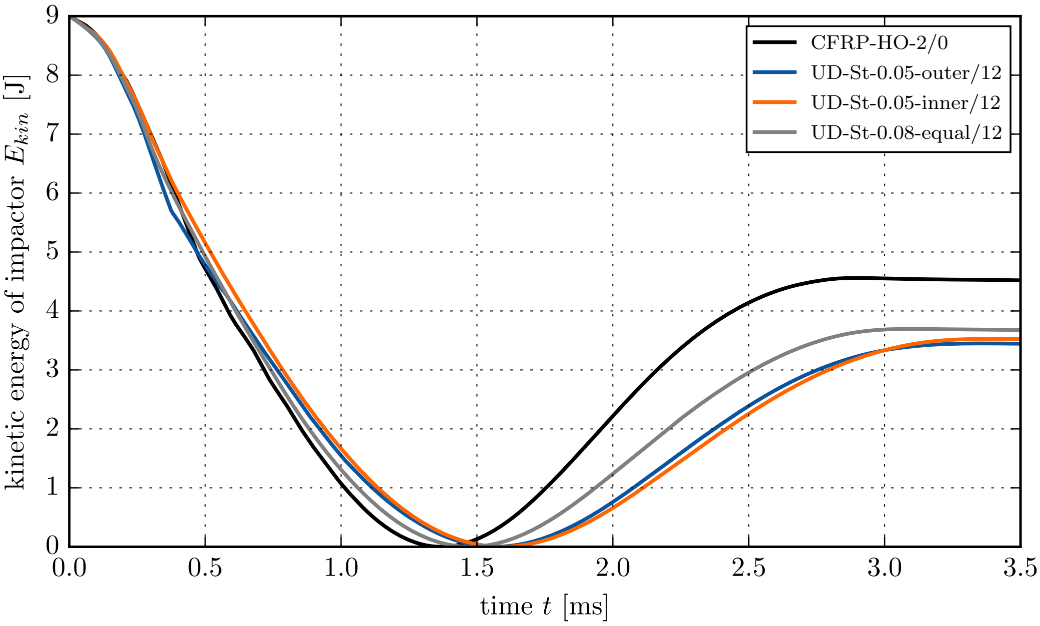

Figure 6.32: Energy-time diagram showing the kinetic energy of the impactor during 9 J impact on four example specimens with different lay-ups

between the initial kinetic energy of the striker and the 'plateau' contains the energy absorbed due to failure, delamination, heat and vibration.

Basically, a higher bending stiffness leads to a shorter contact time and higher forces. Table 6.3 points out the flexural stiffness values of the four lay-ups considered. The CFRP-HO-2/0 lay-up shows the lowest flexural stiffness values and UD-St-0.05-outer/12 lay-up shows the highest flexural stiffness values. The lay-ups UD-St-0.05-inner/12 and UD-St-0.08-equal/12 are quite similar with respect to their flexural stiffness. The graph lines in Figure 6.31 do not describe the expected relationship as the highest value of maximum contact force F_{max} is achieved by the laminate with the least flexural stiffness, the HO laminate, which also shows the shortest contact time. Comparing only the UD-CFRP-St lay-ups to each other also demonstrates that it is not the stiffest laminate, which achieves the highest contact force and the shortest contact time. Rather, it is the laminate with the higher metal layer thickness of 0.08 mm, that reaches these parameters. Regarding the maximum contact force and the contact duration leads to the assumption that more energy must be absorbed in damage by the UD-CFRP-St lay-ups than by the CFRP-HO lay-up. Within the UD-CFRP-St lay-ups, the UD-St-0.08-equal/12 seems to exceed less damage as it shows the shortest contact time despite its comparatively lower flexural stiffness.

All laminates show a threshold force F_t comparable to their maximum contact force F_{max} apart from the UD-St-0.05-outer/12. With more metal layers positioned to the outside, the damage initiates at a higher force. However, based on the force-time curve the maximum contact force and the contact time are comparable to the UD-St-0.05-inner/12 lay-up although the pristine flexural stiffness is higher. One possible explanation could be the larger drop in force right after the initial threshold force peak, which could be an indication for a more distinct damage initiation.

Table 6.3: Flexural stiffnesses of the lay-ups utilized for impact response consideration

	unit	CFRP-HO-2/0	UD-St-0.05-outer/12	UD-St-0.05-inner/12	UD-St-0.08-equal/12
$\hat{E}_{long,b}$	[GPa]	106.6	144.9	137.8	138.8
$\hat{E}_{trans,b}$	[GPa]	19.17	41.00	21.91	24.54

Regarding the kinetic energy of the impactor in Figure 6.32, it can be observed that contact time differences between the lay-ups are mostly generated during the downwards movement of the impactor. The UD-St-0.05-outer/12 lay-up in particular, shows a large decrease in steepness at around 0.4 ms after damage initiation leading to a longer contact time. The HO lay-up achieves the highest plateau value at the end of the impact process, which proves that less energy is absorbed by damage in these specimens than by the other laminates. Despite their difference in stiffness, the two lay-ups with 0.05 mm steel-layer thickness show equal kinetic energy values after impact.

Failure in UD-CFRP-steel and pure CFRP specimens

The failure evaluation in the following is undertaken by dent depth measurement, regarding the damage area achieved by US inspection and consideration of the results obtained by CT. Dent measurement and US inspection are applied to all specimens but only a few specimens are scanned by CT. Three specimens per each of the following lay-ups are impacted at 9, 12 and 16 J and inspected by US and the dent depth is determined:

- CFRP-HO-2/0
- UD-St-0.05-outer/12
- UD-St-0.05-inner/12
- UD-St-0.08-equal/12

As CT analysis is very time-consuming and cost-intensive, only the following laminates are scanned by CT. Four specimens per lay-up are manufactured and impacted at 9 J. These specimens are compared with the aforementioned group in terms of damage size inspected by US inspection:

- UD-St-0.03-low/4
- UD-St-0.05-low/7
- UD-St-0.03-inner/11
- UD-St-0.05-equal/11

The first group includes some essential lay-up variations and its impact response has been discussed before. Therefore, this group is regarded first to analyze the lay-ups influence on dent depth and damage area at three different impact energy levels. Then, the damage area of all lay-ups at 16 J is compared and finally the findings by CT analysis are observed. Firstly, the dent depth e, measured and calculated by the aforementioned methodology is regarded for the first group, as depicted in Figure 6.33 for 9, 12 and 16 J impact levels.

The dent depth as well as its difference in results obtained by the different lay-up increases with increasing impact energy. However, lay-up UD-St-0.05-inner/12 is one exception from this rule as the dent depth obtained on the surface of these specimens is not increasing with higher impact energy for the energy levels considered.
Basically, the largest dent depth is generated in the CFRP-HO lay-up. At 16 J impact the median dent depth in CFRP-HO is 0.26 mm which is more than 2.5 times the median dent depth generated in the UD-St.0.05-inner/12 laminate. The UD-CFRP-St laminate with 0.08 mm metal layer thickness obtains the largest dent depth for impact energy above 12 J within the CFRP-St specimens. The comparison of the two lay-ups with 0.05 mm metal layer thickness shows that the one with the metal layers positioned more to the outside generates a larger dent depth, although MVF and metal layer thickness are identical.
This may be an indication for less fiber breakage being created in the UD-CFRP-St lay-ups than in the CFRP-HO lay-up and a larger delamination being generated instead. In this case, the dent formed in the UD-CFRP-St laminates is rather obtained by plastic deformation of the metal than by fiber breakage. Hence, a laminate with its metal layers further away from the surface shows less dent depth.
Figure 6.34 pictures a dent on a UD-CFRP-St specimen impacted with 30 J. Despite the fracture, which forms in longitudinal direction, the dent itself does not show any fiber breakage. The geometry of the mark makes it relatively easy to detect, although its dent depth is lower than the one of a pure CFRP specimen impacted with the same energy.
The subsequent Figure 6.35 shows the damage area obtained by US inspection in through transmission for the same specimens as considered for the dent depth measurement. The damage area increases with higher impact energies E_{imp} for all lay-ups considered. The relationship between the single lay-ups is contrary to the dent depth. The damage area obtained in the CFRP-HO lay-up is in average around 50% smaller than in the CFRP-steel laminates. The relationship between the single UD-CFRP-St lay-ups is also contrary to dent depth as a smaller damage area is generated in the UD-St-0.08-equal/12 lay-up, which showed the highest dent depth. The UD-St.0.05-inner/12 lay-up obtains a damage area comparable to the area generated in the other CFRP-steel lay-ups, although its dent depth is much smaller. This leads to the question of energy absorption. With regard to the kinetic energy of the impactor, energy absorption is also comparable to the others. As

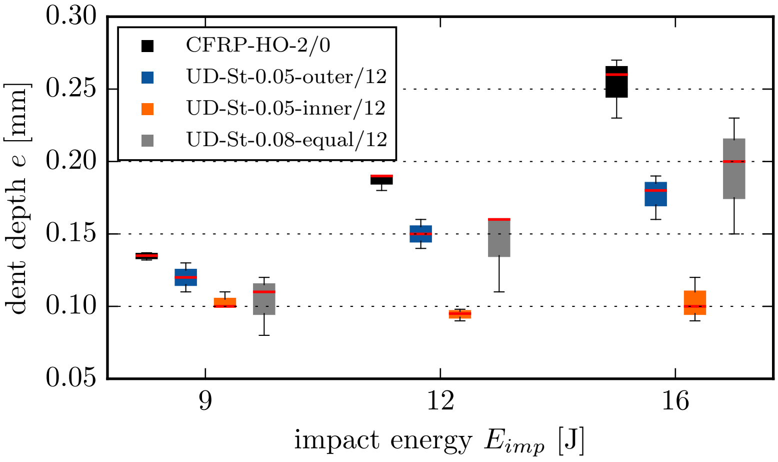

Figure 6.33: Dent depth e of different lay-ups impacted at 9, 12 and 16 J

Figure 6.34: Dent on impacted UD-CFRP-St specimen

dent depth is the only parameter substantially deviating from the others, another failure may have remained undetected.

The damage area after an impact with E_{imp}=16 J is present in Figure 6.36 for all lay-ups considered. Each CFRP-steel lay-ups show 50% to 220% larger damage areas than the CFRP-HO lay-up. However, the results do not show any clear indication for the influence of the metal-layer positioning, MVF or metal layer thickness.

As the maximum load of an elastic impact occurrence depends on the laminate's flexural stiffness, the damage results are referred to their flexural stiffness. Figure 6.37 indicates the results of the division of the damage area A_d by the flexural stiffness $\hat{E}_{long,b}$ of the respective specimen. Compared to the results without consideration of the flexural stiffness, the results show less dependency on the lay-up as relative differences are smaller. In this consideration, the UD-St-0.05/11-equal lay-up is nearly equal to the CFRP-HO lay-up in damage size. However, there is also no indication for one of the varied parameters being of crucial influence on the damage area.

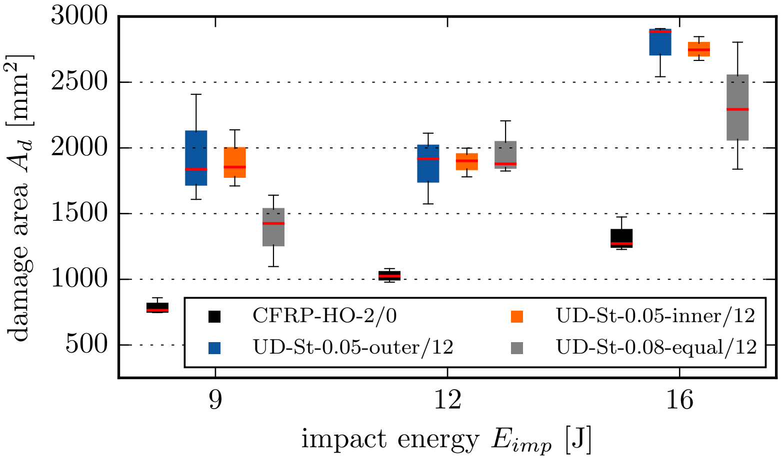

Figure 6.35: Damaged area A_d obtained by US inspection of different lay-ups impacted at 9, 12 and 16 J

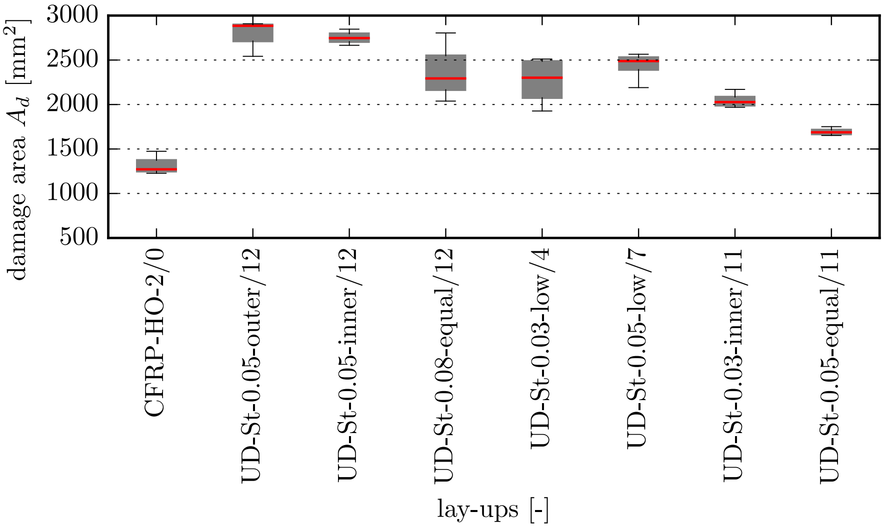

Figure 6.36: Damage area A_d obtained by US inspection of all lay-ups considered at 16 J

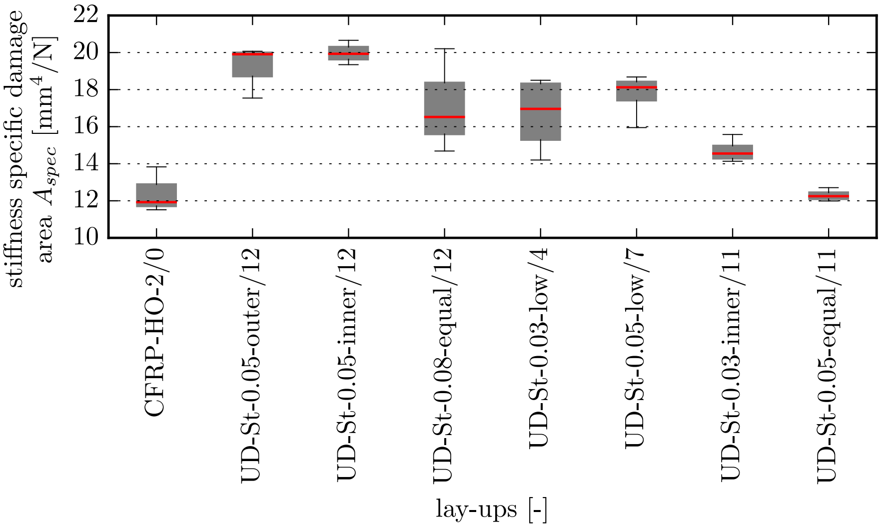

Figure 6.37: Damage area obtained by US inspection at 16 J of all lay-ups considered divided by their flexural stiffness

Unfortunately, by means of through transmission ultrasonic inspection, only the projected area of the damage is obtained. The depth and the total volume of the damage remains undefined. However, another failure form or the total damaged volume could explain the aforementioned relationship of the lay-ups with very similar damage size and energy absorption, but large difference in dent depth.

Therefore, some of the specimens have been analyzed by CT. By mischance, the two lay-ups mentioned are not included. The approach taken for the CT and its analysis are presented in the preceding subchapter.

Figure 6.38 gives images of cross sections in the yz-plane obtained by CT image reconstruction with the fiber direction perpendicular to the image plane. Hence, these cross sections show the center of the specimen right below the impact centre, despite one specimen that has not been positioned properly in the fixture. The images of this specimen are also presented as it shows a similar failure, but its results are not considered in any further analysis.

The figure depicts four specimens per row of four lay-ups analyzed. The first row shows the images of the UD-St-0.03-low/4 lay-up. The typical pine tree pattern of fractures can be observed in each of the specimens, and the specimens also show different numbers of diagonal fractures. However, the fractures vary over the length of the specimen and depend also on the position of the cross section. The main vertical fractures span the whole height of the specimens whereas the smaller ones are detectable up to around half of the laminate thickness. A delamination can clearly be observed right below the top-surface in specimen 2 and 4.

The width of the pine tree pattern is smaller in the second row, that shows specimens of the lay-up UD-St-0.05-low/7. The extent of the diagonal fractures is also less. The main fracture in the centre again spans the whole specimen thickness. The increased metal layer thickness prohibits the formation of smaller cracks.

The rows C and D in Figure 6.38 give the cross section images of lay-up UD-St-0.03-inner/11 and lay-up UD-St-0.05-equal/11. With 11%, both have a higher MVF in comparison to the other two lay-ups. There is no typical pine tree pattern observable as the diagonal fractures are missing. Instead, the main fracture obtains a staggered geometry in most of the specimens.

The images presented are adjusted in contrast to allow a better detectability of the flaws in a printed version. As a consequence, the images receive different brightness.

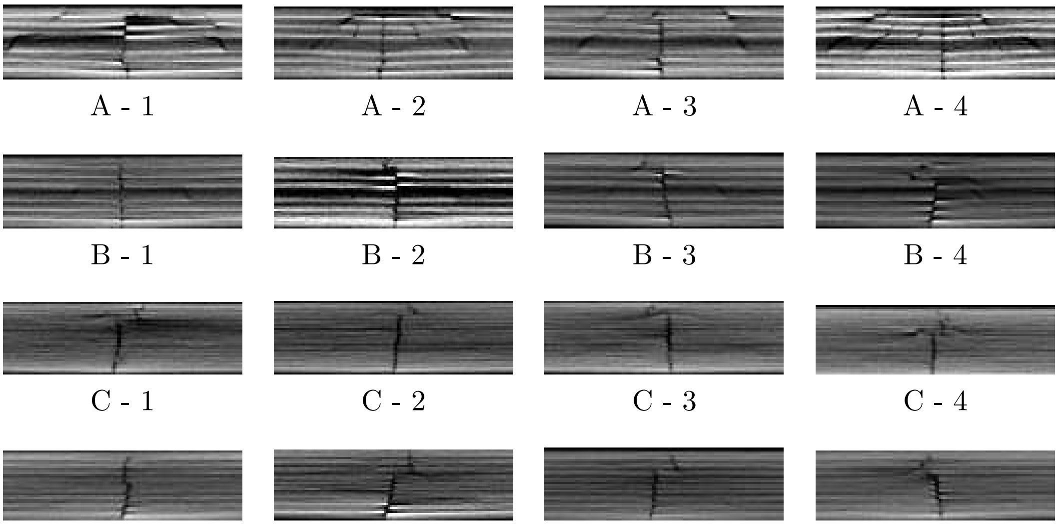

A - 1 A - 2 A - 3 A - 4

B - 1 B - 2 B - 3 B - 4

C - 1 C - 2 C - 3 C - 4

D - 1 D - 2 D - 3 D - 4

Figure 6.38: CT cross sections in the center of the failure in yz-plane with A: UD-St-0.03- low/4; B: UD-St-0.05-low/7; C: UD-St-0.03-inner/11 and D: UD-St-0.05- equal/11

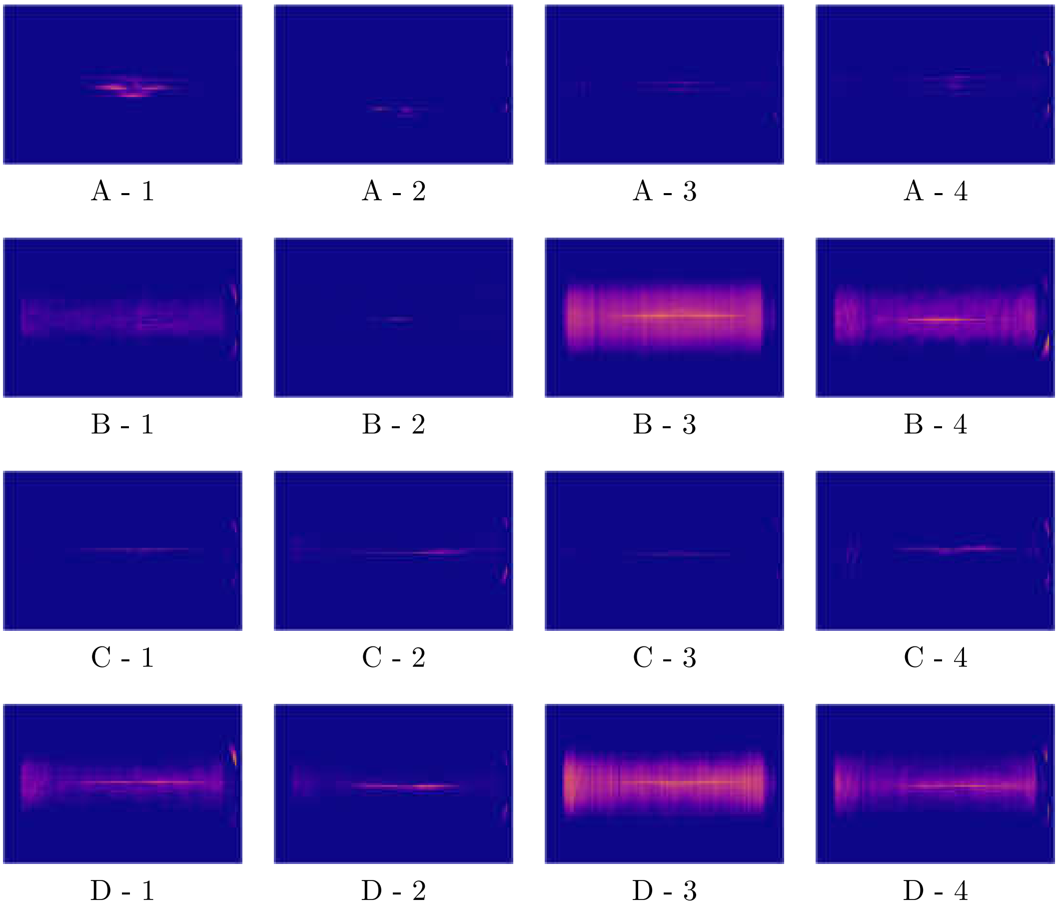
A - 1 A - 2 A - 3 A - 4
B - 1 B - 2 B - 3 B - 4
C - 1 C - 2 C - 3 C - 4
D - 1 D - 2 D - 3 D - 4

Figure 6.39: CT intensity plots in xy-plane with A: UD-St-0.03- low/4; B: UD-St-0.05-low/7; C: UD-St-0.03-inner/11 and D: UD-St-0.05- equal/11

Despite the fact that the original images do not vary in brightness, the approach presented in the previous subchapter does not allow a robust analysis of the delaminations. The obtained damage intensity plots are depicted in Figure 6.39. In some cases larger areas are detected as a damage, whereas only the longitudinal fractures are detected in other cases. In this way it is not possible to use the CT results for determination of delaminations, but for the analysis of the thin longitudinal fractures. Hence, the planar geometries and the artifacts must be ignored.

The damage intensity plots in three planes with the accompanying information as introduced before, are given in Figure 7.1 - Figure 7.16 (in the appendix) to allow a more detailed consideration of the results.

When regarding the plots of the xy-plane in Figure 6.39, the pine tree pattern in the first row for lay-up UD-St-0.03-low/4 can be observed as different fractures in the specimen's longitudinal direction. The length of the fracture, however, is shorter compared to the lay-up UD-St-0.05-low/7 shown in the second row. The fractures of the laminates UD-St-0.03-inner/11 and UD-St-0.05-equal/11 presented in the third and fourth column show a larger width due to their staggered geometry.

For comparison reasons, Figure 6.40 gives the US transmission results of the same specimens in the same plane. The delaminated area, detected by US inspection, is shown

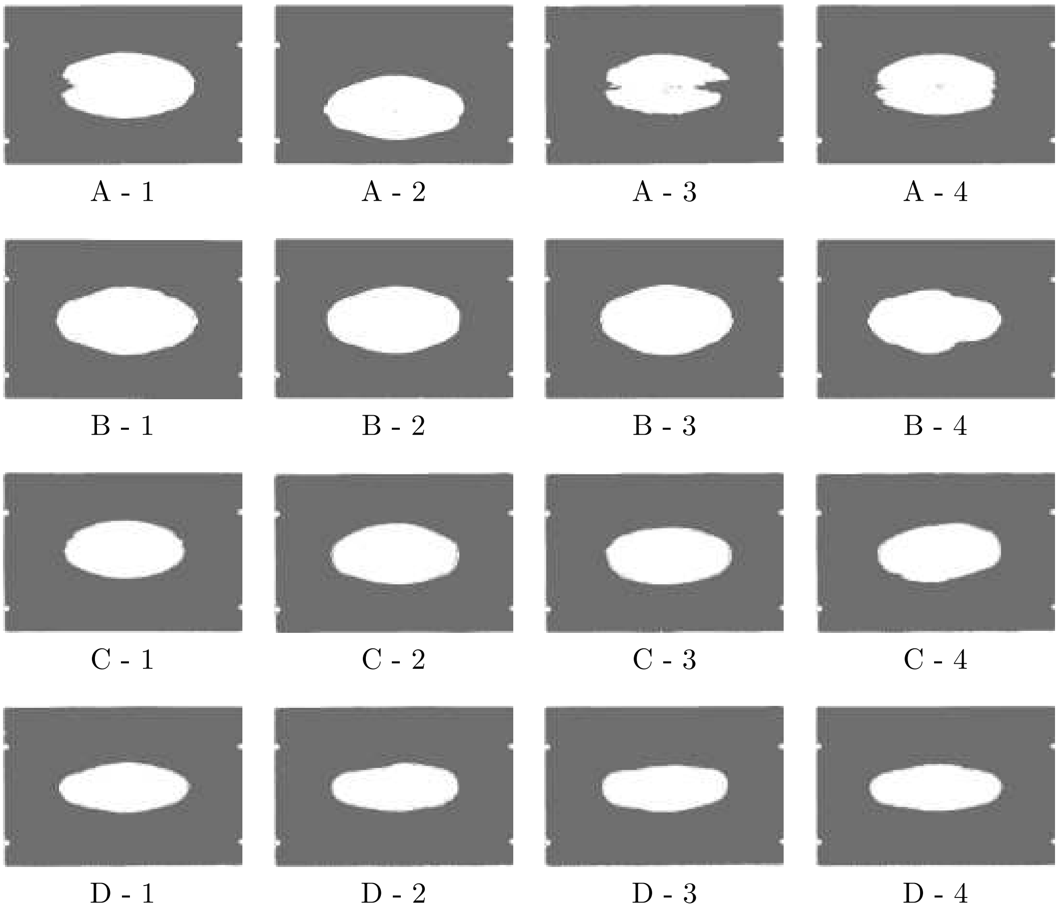

A - 1 A - 2 A - 3 A - 4

B - 1 B - 2 B - 3 B - 4

C - 1 C - 2 C - 3 C - 4

D - 1 D - 2 D - 3 D - 4

Figure 6.40: US transmission C-scan in xy-plane with A: UD-St-0.03-low/4; B: UD-St-0.05-low/7; C: UD-St-0.03-inner/11 and D: UD-St-0.05-equal/11

as white area in the center of the specimens. The length to width ratio correlates with flexural stiffness in longitudinal and transverse direction of the lay-ups. However, the presentation aims on the comparison of CT and US results. Whereas delamination is not reliably detectable by CT analysis, the fractures clearly visible in the CT results are not detected by US inspection. The detailed comparison of single cross section areas prove that the cracks in z-direction are not observed by US inspection.

These fractures are a possible explanation for the preceding discussion on the two lay-ups with identical damage area and energy absorption, but differing dent depth. In this way, a more extensive formation of a crack or fracture in the laminate with the metal-layers positioned more to its center, which showed a lower dent depth, could serve as an explanation and balance the energy consideration.

Compression strength and response of damaged specimens

The compression strength results of the previously impacted specimens are discussed similarly to the damage area. At first, the results for the first group of lay-ups are regarded, which haven been impacted by 9, 12 and 16 J. The residual compression strength σ_{CAI} results are shown in Figure 6.41. As expected, the compression strength is reduced with increasing impact energy. For impacts at 9 J, the median compression strength value of the CFRP-HO lay-up is comparable to the UD-St-0.05-inner/12 lay-up, which is characterized by its low dent depth. The other two UD-CFRP-St lay-ups achieve 8% to 13% higher compression strength values. At 12 J, the UD-St-0.08-equal/12 laminate has a 7% higher median strength value than CFRP-HO. The other two lay-ups have median strength values, in the range of the CFRP-HO results.

At 16 J, the strength of UD-St-0.08-equal/12 lay-up is 6% to 7% increased compared to the other lay-ups. The strength results for the second lay-up group, also impacted at 16 J, are provided in Figure 6.42. The additional last four lay-ups produce mean strength values that are 2% to 11% lower than the mean value of the CFRP-HO-2/0 laminate.

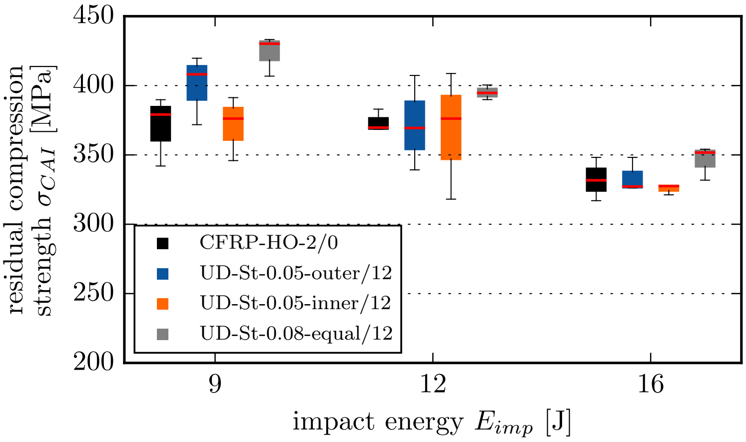

Figure 6.41: Residual compression strength σ_{CAI} of different lay-ups after 9, 12 and 16 J impact

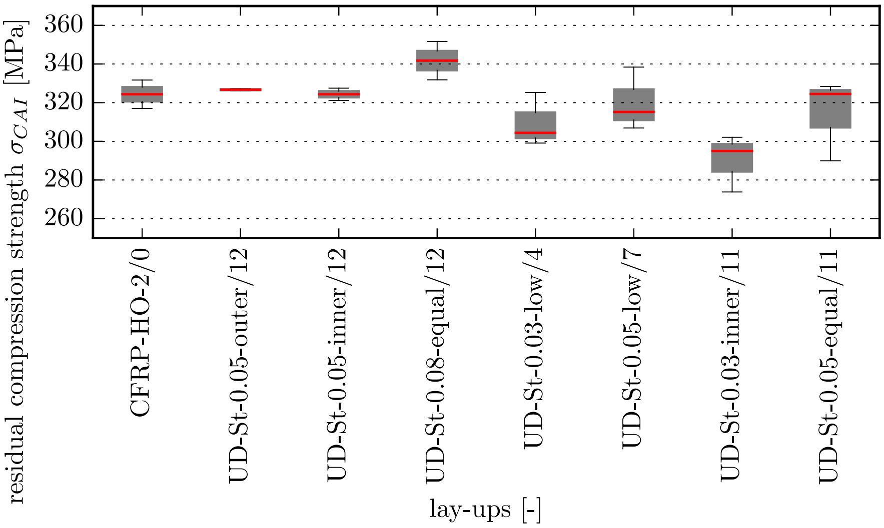

Figure 6.42: Residual compression strength σ_{CAI} after 16 J impact of all lay-ups considered

Comparing the specimens with each other, it is conspicuous that the lay-up UD-St-0.03-low/4 reaches a higher residual compression strength than the UD-St-0.03-inner/11 lay-up, despite its lower metal fraction and larger damage area. The CT inspection of the first shows a relatively intense but very compact damage, whereas the latter is characterized by a comparatively long and thin fracture.

As the specimens have different MFV, the laminate density is also different. Therefore, the weight-specific residual compression results are also considered and provided in Figure 6.43. The relative advantage of the HO-laminate over the UD-CFRP-St lay-up in terms of median specific residual compression strength $\sigma_{CAI,spec}$ is 25% to 60%. The lay-ups with comparatively low MVF, UD-St-0.03-low/4 and UD-St-0.05-low/7, reach the highest specific strength values within the group of UD-CFRP-St lay-ups.

As the absolute strength values do not show a clear dependency on MVF, it can be derived for the lay-ups considered that the specific reinforcement effect of metal layers decreases with increasing MVF.

However, it is conspicuous that the damage area generated in UD-CFRP-St lay-ups at 16 J is in average 80% larger than the area generated in CFRP-HO, whereas the absolute compression strength lies in the same range. Therefore, an additional consideration is undertaken by dividing the damage area A_d of each specimen by its residual compression strength σ_{CAI} values. The results for the fraction area A_d/σ_{CAI} are given in Figure 6.44. As a matter of fact, some of the UD-CFRP-St lay-ups show twice the damage size than the CFRP-HO, when related to the same compression strength.

This means that the UD-CFRP-St material is more tolerant to damage but at the same time less resistant against it. It might be reasonable to assume that the damage tolerance is increased for manufacturing defects also, but this is has not been investigated yet. Again, there is no clear trend for any lay-up or MVF.

Besides the pure residual compression strength value, the load-displacement behavior is also of major interest. For clarification, one representative load-displacement curve is shown per lay-up in Figure 6.45. The four lay-ups of the first group are selected as they

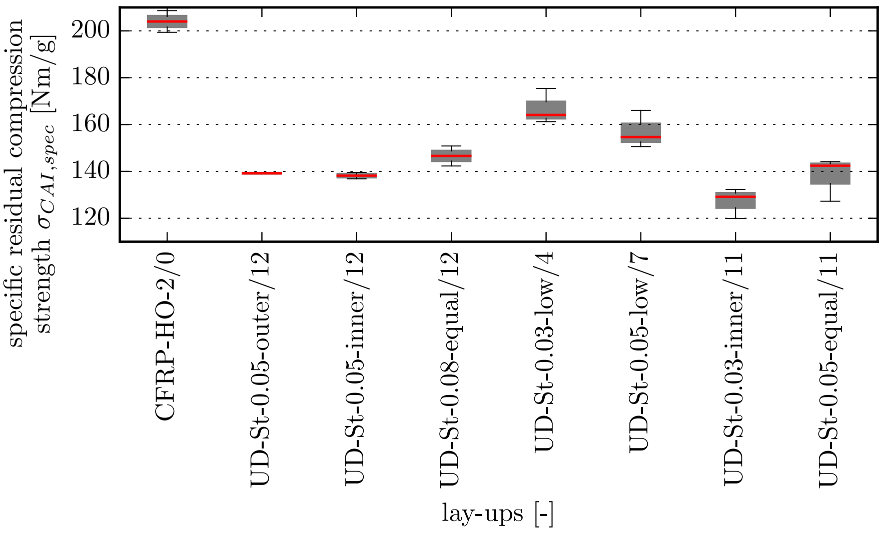

Figure 6.43: Weight-specific residual compression strength σ_{CAI} after 16 J impact of all lay-ups considered

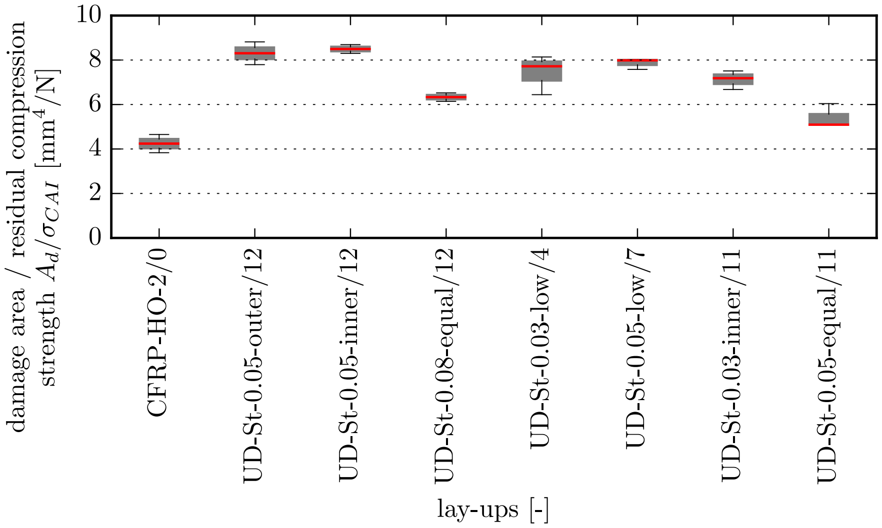

Figure 6.44: Damage area A_d divided by compression strength σ_{CAI} after 16 J impact of all lay-ups considered

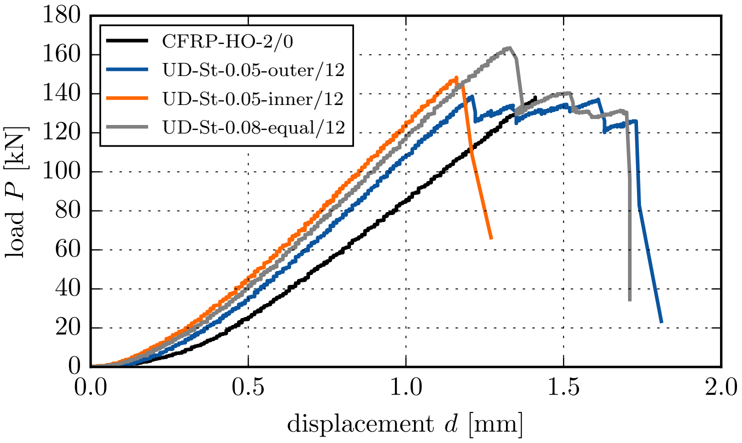

Figure 6.45: Compression load-displacement curves of impacted specimens with different lay-ups

have a similar MVF and have been impacted by 9 J. The CFRP-HO-2/0 laminate, shown as a black line, is characterized by a lower stiffness. The maximum load is 138 kN and identical to the UD-St-0.05-outer/12 lay-up. At the maximum load, the specimen fails abruptly and no further load can be beard by the remaining fragments.

The UD-CFRP-0.05-outer/12 specimen, marked in orange, reaches a higher maximum load and has the highest stiffness. Right after the first failure, there is a second peak present in the load-displacement curve but the displacement between first and second peak is small as the specimen also fails comparatively abrupt.

In contrast, the other two lay-ups with their metal layers dispersed equally (UD-St-0.08-equal/12 - gray line) or more to the outside (UD-St-0.05-outer/12 - blue line) exhibit

a large displacement with a staggered load-displacement curve. The load level of the staggered pattern is lowered by around 20% in comparison to the maximum load for the UD-St-0.08-equal/12. The load level during the staggered pattern exhibited by the UD-St-0.05-outer/12 is nearly equal to the maximum load achieved.
This means that a pseudo-plastic behaviour for compression failure is achievable for a damaged specimen by positioning the layers more to the outside, which at the same time lowers the compression modulus and compression strength of the pristine specimen, as observed before.

Pristine strength and residual strength after impact

As the design process of the applications is based on pristine laminate properties and damage or defects are considered by markdown factors, it is not clear whether the aim is to achieve a high residual strength as absolute value or to achieve a high ratio with respect to the pristine properties. As shown in chapter 3, this depends on the approach selected and is a complex procedure under consideration of a variety of mechanical and economical parameters.

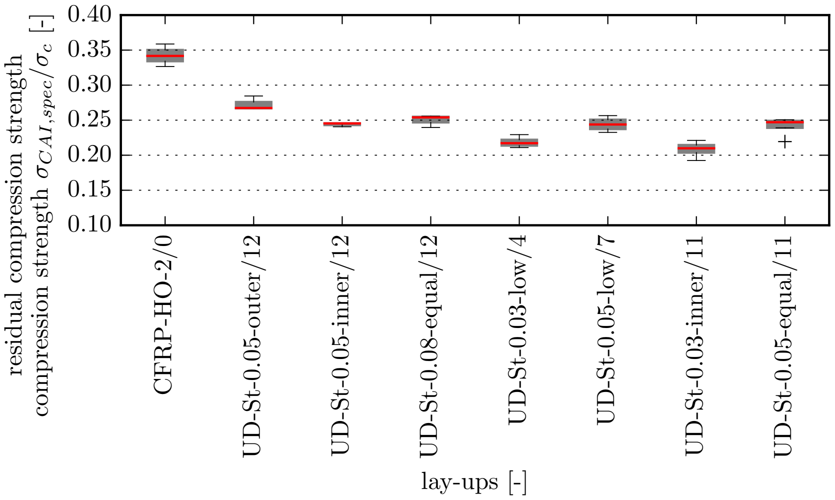

Figure 6.46: Relationship between residual compression strength σ_{CAI} after 16 J impact and compression strength σ_c of all lay-ups considered

However, for a better understanding, the relationship between residual compression strength σ_{CAI} and compression strength σ_c is provided in Figure 6.46 for the 16 J impact case. In accordance with the figure, the CFRP-HO laminate maintains around 35% of its residual strength after being impacted at 16 J.
This conclusion must be regarded with caution, as the residual compression strength σ_{CAI} is not a scalable and inherent material value. To put it more precisely: the residual compression strength σ_{CAI} is a strength value obtained by a certain specimens size, which was damaged by an impactor with a certain energy. In this way the ratio between damage size and specimens cross section has a substantial influence on the residual compression strength σ_{CAI} obtained.
Therefore, also both parameters use the description 'strength', the ratio is only regarded here as the ratio between two test results.

However, when comparing the results achieved by the UD-CFRP-St specimens with the CFRP-HO lay-up, it can be seen that they forfeit more of their pristine strength. The results are in the range between 21% to 27%, which correlates with a loss in strength between 73% to 79%.

6.8 Discussion of hypotheses addressed

This chapter aims to refer to the last two hypotheses.

Hypothesis 5:
For the discussion on this hypothesis it is important to distinguish between dent depth and failure depth, where latter is recognized as a failure inside the laminate. It is observed that the dent depth strongly depends on the arrangement of the plies. With the metal layers arranged more to the center, a comparably low dent depth is achieved whereas dent depth is increased when metal layers are closer to the outer surface. Basically, the CFRP-HO laminates showed larger dent depth than the UD-CFRP-steel lay-ups.
The damage area is measured by means of US inspection, which does not provide information about the damage depth when applied on FML. However, after 16 J impact for example, the damage area in the UD-CFRP-St lay-ups is in average 80% larger than the damage obtained in a CFRP-HO lay-up. At the same time, residual strength is comparable. This means that the damage is not reduced by adding metal layers, rather the residual strength per damage area is increased. At the measured impact energy, all failures span over the total specimen thickness in CFRP-HO as well as in UD-CFRP-St lay-ups.
It could be shown by CT inspection that there are longitudinal fractures present in the laminate which are not detected by US inspection. There is also some indication that theses longitudinal fractures lower residual compression strength.

Hypothesis 6:
The failure geometry in terms of the projected damage area is not influenced crucially by the arrangement of the plies, although the length to width ratio is influenced slightly by the lay-up's flexural bending stiffness ratio. On the other hand, the failure pattern can be observed in more detail by CT-inspection. The detected pine tree pattern of the damage is typical for brittle materials such as composites, especially CFRP. The cross section images obtained by CT show that the failure geometry changes when adding more than 7% MVF from the more compact pine tree pattern to a single thin staggered crack. However, the more compact geometry obtained in the lay-ups with less MVF seems to be more beneficial, when tested for residual compression strength.
The arrangement of the plies, however, also has an influence on pristine compression behavior and on the load-displacement behavior of damaged specimens. With the metal layers arranged more to the center, the compression strength and stiffness is increased. However, the arrangement more to the outside prohibits an abrupt compression failure and introduces a pseudo-plastic behavior.

7 Conclusions and outlook

In this thesis a novel material called 'UD-CFRP-steel' is examined. It consists of unidirectionally orientated CFRP-layers, that are combined with steel layers of a thickness below 0.08 mm. This laminate is taken to test the following principle hypothesis step-by-step:

'Using thin steel layers in carbon-fiber-reinforced epoxy laminates permits an increase in weight-specific stiffness with no reduction of compression strength after impact.'

Conclusions

It is obvious that the reference is not defined clearly by this hypothesis as it may depend on the application. In general, stiffness and strength properties of composite laminates are adjusted by the alignment of the fibers. However, increasing the portion of fibers, that are oriented in a certain direction, is basically accompanied by a reduction of the laminate's resistance to impact.
Therefore, a compromise between the laminate‘s performance - with regard to the intended load case - and the laminate‘s behavior under unexpected loading or impact has to be found. This agreement depends on the laminate‘s service environment and risk of unexpected impact or loads and is often regarded by applying so-called 'stacking rules'. For most of the applications, the consideration of such rules ensures that unexpected impact or loading requirements are inherently fulfilled. But at the same time, the degree of capacity utilization of the CFRP material is essentially limited.
Recognizing these limitations, a new lay-up to increase the degree of capacity utilization of CFRP is analyzed in this thesis. The technology of UD-CFRP-steel laminates uses a lay-up of CFRP and steel layers with a thickness below 0.08 mm to reduce the aforementioned disadvantages. At first, it is shown theoretically that a higher specific stiffness is achievable when using less than 12% steel in the laminate than by taking the CFRP reference. However, this only proves to be beneficial if the residual strength after an impact is comparable to the residual strength achieved by the CFRP reference after an impact of the same energy.
In the majority of applications, the exclusive consideration of uniaxial properties is not sufficient. Hence, circular and rectangular struts under longitudinal compression are regarded. When considering compression strength, local and global buckling, a strut provides a simple example in which not only the laminate's longitudinal strength and stiffness play an important role, but also the laminate's transverse and flexural bending stiffness. Therefore, a parameter study on struts with different lengths and loads is conducted which considers a variety of different arrangements of the metal layers, different metal layer thicknesses and thereby metal volume fractions. In addition, it respects the CFRP reference material. The ideal cross section described by wall thickness and diameter (or width respectively), is calculated for each material system and loading scenario. The results obtain certain scenarios, where UD-CFRP-steel laminates show a beneficial relationship between the aforementioned parameters and offer a weight saving potential compared to the reference laminate. With the help of these findings and with a simple mechanical model -

deduced for the estimation of the laminate properties - the metal volume fraction and different lay-ups are selected for the further investigations.

However, before manufacturing meaningful specimens for compression and compression after impact testing, the interface between the two constituents CFRP and steel must be regarded as well as the thermal stress in the laminate.

Different surface pre- and post-treatment processes are investigated for the treatment of the steel layer in order to enhance adhesion. Pickling in different solutions and grit-blasting under different parameters in combination with a sol-gel post-treatment are examined. In addition, a vacuum-blasting machine is developed to allow a more gentle pre-treatment of the comparatively thin steel foil. The different treatments are assessed by determination of interlaminar shear strength. The results illustrate that the vacuum blasting process combined with the sol-gel treatment provides a reliable method, which achieves a fairly good bonding between the laminate constituents. At the same time, this process proves to be more flexible and economical, especially for manufacturing in a research laboratory environment.

Residual thermal stresses are tested to assess their influence on the mechanical results that are obtained, and to get an estimation of the additional potential when reducing these stress factors. The findings show that the stresses can be lowered without changing the cure cycle, but by increasing the effective pressure during cure, as a consequence of an interaction between the plies. Due to this effect, residual thermal stresses in fiber metal laminates are generally overestimated, when prepreg is used. Although the results are promising and it seems that residual stress may be reduced by an essential portion, it is only beneficial for a certain operation temperature. If this component gets suspended to large temperature changes, the efficacy of adjustments with respect to thermal stresses is limited.

Specimens with different lay-ups for pristine compression testing and residual compression after impact testing, are manufactured based on the methodologies achieved within the scope of the aforementioned investigations. The compression strength of pristine specimens is improved by 25 to 45% compared to the pure CFRP reference. In this way, the specific elastic modulus is also increased by up to 25%. Lay-ups with a metal volume fraction of approximately 12% show a weight-specific compression stiffness comparable to the pure CFRP reference and prove the first estimation, viz. that a consideration of higher metal volume fractions is not reasonable.

Compression after impact testing is conducted to determine residual compression after impact strength. This examination includes impacting and subsequent compression testing. Based on the given geometry of the standard impact test fixture, it was assumed that the testing of these specimens by means of the standards leads to an anomalous influence of the fixture on the damage and hence prohibits a clear conclusion. Therefore, a modified test fixture is developed and analyzed with the help of pure CFRP specimens. These preliminary tests showed that the predominant direction of the standard fixture influences the damage geometry in particular. The results also point out that this directionality is prevented by the use of the modified circular fixture geometry.

All of the UD-CFRP-steel specimens are then tested on the modified fixture and the damage is inspected by dent depth measurement, ultrasonic inspection and some specimens by computer tomography.

A clear dependency of dent depth on the metal layer arrangement is shown, whereas basically, the dent depth obtained on UD-CFRP-steel specimens' surface is lower than on CFRP specimens. The damage area is measured by means of ultrasonic inspection, which does not provide information about the damage depth when applied on FML. However,

after for example 16 J impact, the damage area in the UD-CFRP-steel lay-ups is in average 80% larger than the damage obtained in CFRP.
The failure geometry in terms of the projected damage area is not influenced by the arrangement of the plies essentially, although the length to width ratio is influenced slightly by the lay-up's flexural bending stiffness ratio. Although the specimens indicate larger damage after being impacted at 9, 12 and 16 J, the residual compression strength is comparable to the CFRP reference. Hence, the specific residual compression strength of UD-CFRP-steel is lower. Additionally to dent depth, the compression failure of the previously damaged laminate is also influenced by the arrangement of the metal layers. Specimens with the metal layers positioned more to the outside achieve a more ductile compression failure than CFRP or specimens with the metal layers orientated preferably more to the center of the specimen.
Regarding the aforementioned principle hypothesis, the findings can be summarized as follows:

It can be shown that a metal volume fraction of below 12% is required to achieve a weight-specific benefit in stiffness, whereas residual compression strength of the reference is reached by certain UD-CFRP-steel lay-ups. Thin steel-layers are required to generate a certain amount of layers when - at the same time - using low metal volume fractions. However, it is not yet verified by test results that a certain amount of layers is required, as the minimum number of layers and metal volume fraction, to realize a reinforcing effect is not achieved by the lay-ups tested in this thesis.

Outlook

As the 'novel material' was proven to be beneficial in pristine specific compression strength and load-deflection relation against the CFRP reference, it is worth to continue with research in this field even though the specific residual compression strength after impact values achieved by UD-CFRP-steel are lower than those gained by the reference samples. The maturity of both materials is very different and hence a larger potential in development is conceivable for the UD-CFRP-steel laminates. Lower metal fractions should be considered for the compression load case as the lower limit of the reinforcement effect - in terms of metal volume fraction - is not found with the lay-ups used. Longitudinal fractures in the metal layers are very distinct. This leads to the question whether a more ductile steel alloy could be more advantageous. As an increase in ductility is accompanied by a reduction of tensile strength, the tensile strength properties of the hybrid laminate must be determined to answer this question. Basically, the tensile properties must be regarded as the thermal tensile stresses in the metal layer are critical in this load case.
The achieved bond between the two constituents is exceptionally promising as the interlaminar shear strength values are high compared to values available in literature. This could also be shown by single-lap shear results, which are not part of this thesis. Additionally, most of the obtained failure is cohesive in nature. Hence, a large potential for further improvements in bonding strength is not expected. However, a change in focus from metal surface treatment to a more general development of the interphase between the two constituents may be beneficial. A functionally gradient stiffness could improve the laminate's impact response.
Any further investigations need to be accompanied by experiments on corrosion and development of nondestructive inspection methods to make sure that they do not form a final obstacle.

List of Figures

List of Tables

Bibliography

[1] European Aviation Safety Agency EASA. *CS25.571 Part of CS-25*. EASA, July 2011.

[2] European Aviation Safety Agency (EASA). *CS25.603 Part of CS-25*. EASA, July 2011.

[3] S. Arbrate. *Impact on composite structures*. Cambridge University Press, 1998.

[4] L.J. Hart-Smith. Mechanically Fastened Joints for Advanced Composites - Phenomenological Considerations and Simple Analysis. In *4th Conference on Fibrous Composites in Structures, Plenum Publishing Corp., New York*, pages 543–574, 1978.

[5] S.D. Thoppul, J. Finegan, and R.F. Gibson. Mechanics of mechanically fastened joints in polymer-matrix composite structures - A review. *Composites Science and Technology*, 69(3-4):301–329, 2009.

[6] A. Crosky, D. Kelly, R. Li, X. Legrand, N. Huong, and R. Ujjin. Improvement of bearing strength of laminated composites. *Composite Structures*, 76(3):260–271, 2006.

[7] A. Fink, B. Kolesnikov, and H. Wilmes. CFRP/titanium hybrid material improving composite structure coupling. *JEC Compos*, 7(1):64–67, 2004.

[8] A. Fink, P.P Camanho, J.M. Andrés, E. Pfeiffer, and A. Obst. Hybrid CFRP/titanium bolted joints: Performance assessment and application to a spacecraft payload adaptor. *Composites Science and Technology*, 70(2):305–317, 2010.

[9] B. Kolesnikov, L. Herbeck, and A. Fink. CFRP-titanium hybrid material for improving composite bolted joints. *Composite Structures*, 83(4):368–380, 2008.

[10] A. Vlot and J.W. Gunnink. *Fibre Metal Laminates*. Kluwer Academic Publishers, 2001.

[11] C. Santiuste, S. Sanchez-Saez, and E. Barbero. Residual flexural strength after low-velocity impact in glass/polyester composite beams. *Composite Structures*, 92(1):25–30, 2010.

[12] M.C.Y. Niu. *Composite Airframe Structures - Practical Design Information and Data*. Conmilit Press Limiled, 2008.

[13] M.F.S.F. Moura and A.T. Marques. Prediction of low velocity impact damage in carbon-epoxy laminates. *Composites Part A: Applied Science and Manufacturing*, 33(3):361–368, 2002.

[14] D. Stefaniak, E. Kappel, B. Kolesnikov, and C. Hühne. Improving the mechanical performance of unidirectional CFRP by metal-hybridization. In *ECCM15 - 15th European Conference on Composite Materials, Venice, Italy*, 2012.

[15] D. Stefaniak, B. Kolesnikov, E. Kappel, and C. Hühne. Improving Impact Endangered CFRP Structures by Metal-Hybridisation. In *12th European Conference on Spacecraft Structues, Materials & Environmental Testing, Nordwijk, Netherlands*, page ., 2012.

[16] E.J. Barbero. *Introduction to Composite Materials Design*, volume 2nd ed. CRC Press Taylor & Francis Group, 2011.

[17] P.A. Lagace and E. Wolf. Impact Damage Resistance of Several Laminated Material Systems. *The American Institute of Aeronautics and Astronautics (AIAA)*, 33(6):1106–1113, 1995.

[18] S.M. Lee and P. Zahuta. Instrumented Impact and Static Indentation of Composites. *Journal of Composite Materials*, 25:204–222, 1991.

[19] C.T. Sun and S. Rechak. Effect of Adhesive Layers on Impact Damage in Composite Laminates. In *Composite Materials: Testing and Design (Eighth Conference), ASTM STP 972, American Society for Testing and Materials*, pages 97–123, 1988.

[20] R.L. Sierakowski and G.M. Newaz. *Damage Tolerance in Advanced Composites*. Technomic Publishing Company, Lancaster, Basel, 1995.

[21] Department of Defense - United States of America. *MIL-HDBK-17-1F Composite Materials Handbook - Volume 1. Polymer Matrix Composites - Guidelines for Characterization of Structural Materials*, 2002.

[22] R.C. Alderliesten. Designing for damage tolerance in aerospace: A hybrid material technology. *Materials and Design*, 66:421–428, 2015.

[23] European Aviation Safety Agency (EASA). *AMC 20-29*. European Aviation Safety Agency (EASA), July 2010.

[24] A. T. Nettles. The importance of damage tolerance in aerospace structures. *JEC-Composites*, 72(1):59–61, 2012.

[25] T.C. Anderson. Certification Cost Reduction Usind Compression-After-Impact Testing. *Composite Structures: Theory and Practice ASTM STP1383*, pages 29–46, 2000.

[26] J.N. Reddy. *Mechanics of Laminated Composite Plates - Theory and Analysis*. CRC Press, Boca Raton, FL, 2004.

[27] M. Knops. *Analysis of Failure in Fiber Polymer Laminates*. Springer-Verlag, 2008.

[28] Hexcel. *HexPly 8552 Epoxy Matrix - Product Data*, 2008.

[29] S.U. Khan, R.C. Alderliesten, and R. Benedictus. Post-stretching induced stress redistribution in Fibre Metal Laminates for increased fatigue crack growth resistance. *Composites Science and Technology*, 69(3-4):396–405, 2009.

[30] D. Stefaniak, E. Kappel, T. Spröwitz, and C. Hühne. Experimental identification of process parameters inducing warpage of autoclave-processed CFRP parts. *Composites Part A: Applied Science and Manufacturing*, 43(7):1081 – 1091, 2012.

[31] G. Twigg, A. Poursartip, and G. Fernlund. An experimental method for quantifying tool-part shear interaction during composite processing. *Composites Science and Technology*, 63(13):1985–2002, 2003.

[32] E. Kappel, D. Stefaniak, T. Spröwitz, and C. Hühne. A semi-analytical simulation strategy and its application to warpage of autoclave-processed CFRP parts. *Composites Part A: Applied Science and Manufacturing*, 42(12):1985–1994, 2011.

[33] K. Marlett. *Hexcel 8552 AS4 Unidirectional Prepreg 190 gsm & 35Qualification Material Property Data Report - FAA Special Project Number SP4614WI-Q*. National Instiute for Aviation Research, 2011.

[34] K. Marlett. *Hexcel 8552 IM7 Unidirectional Prepreg 190 gsm & 35Qualification Material Property Data Report - FAA Special Project Number SP4614WI-Q*. National Instiute for Aviation Research, 2011.

[35] S. Wijskamp, R. Akkerman, and E.A.D. Lamers. Residual Stresses in non-symmetrical carbon/epoxy laminates. In *ICCM14 International Conference on Composite Materials San Diego*, 2003.

[36] L. Raffaeilli. *Thermomachanics of Fibre Reinforced Epoxies for Cryogenic Pressurized Containment*. PhD thesis, Technische Universität München, 2006.

[37] A. Fink. *Lokale Metall-Hybridisierung zur Effizienzsteigerung von Hochlastfügestellen in Faserverbundstrukturen*. PhD thesis, Technische Universitaet Braunschweig, 2010.

[38] Alcoa Mill Products. Alloy 7075 Plate and Sheet. Technical report, IOWA, 2010.

[39] N. Tsartsaris, M. Meo, F. Dolce, U. Polimeno, M. Guida, and F. Marulo. Low-velocity impact behaviour of fiber metal laminates. *Journal of Composite Materials*, 45(7):803–814, 2011.

[40] D. Mugnier. Ariane Structure For Auxiliary Payload 5 - User's Manual. Technical Report 1, Arianespace, 2000.

[41] L.P. Kollár and G.S. Springer. *Mechanics of Composite Structures*. Cambridge University Press, 2003.

[42] R.M. Jones. Buckling of Circular Cylindrical Shells with Multiple Orthotropic Layers and Eccentric Stiffeners. *AIAA Journal*, 6:2301–2305, 1968.

[43] T. Yu, D. Fernando, J.G. Teng, and X.L. Zhao. Experimental study on CFRP-to-steel bonded interfaces. *Composites Part B: Engineering*, 43(5):2279–2289, 2012.

[44] A. Al-Shawaf and X.-L. Zhao. Adhesive rheology impact on wet lay-up CFRP/steel joints‘ behaviour under infrastructural subzero exposure. *Composites Part B: Engineering*, 47(1):207–219, 2013.

[45] A. Baldan. Rewiew Adhesively-bonded joints in metallic alloys, polymers and composite materials: Mechanical and environmental durability performance. *Journal of Materials Science*, 39:4729–4797, 2004.

[46] W. Brockmann, O.-D. Hennemann, H. Kollek, and C. Matz. Adhesion in bonded aluminum joints for aircraft construction. *International Journal of Adhesion and Adhesives*, 6(3):115–143, 1986.

[47] P. Molitor and T. Young. Adhesives bonding of a titanium alloy to a glass fibre reinforced composite material. *International Journal of Adhesion and Adhesives*, 22(2):101–107, 2002.

[48] G. Habenicht. *Kleben.* Springer-Verlag, 2006.

[49] S. Amada and T. Hirose. Influence of grit blasting pre-treatment on the adhesion strenght of plasma sprayed coatings: fractal analysis of roughness. *Surface and Coatings Technology*, 102(1-2):132–137, 1998.

[50] A. N. Gent and C.-W. Lin. Model Studies of the Effect of Surface Roughness and Mechanical Interlocking on Adhesion, Technical Report No. 25. Technical report, Office of Naval Research, Institute of Polymer Engineering, The University of Akron, Ohio, 1990.

[51] A.F. Harris and A. Beevers. The effects of grit-blasting on surface properties for adhesion. *International Journal of Adhesion and Adhesives*, 19(6):445–452, 1999.

[52] J.G. Teng, D. Fernando, T. Yu, and X.L. Zhao. Treatment of Steel Surfaces for Effective Adhesive Bonding. In *CICE 2010 - The 5th International Conference on FRP Composites in Civil Engineering, Beijing, China*, page ., 2010.

[53] Lamineries Matthey SA. *Stahl 1.4310*, 2006.

[54] C. Olsson and D. Landoldt. Passive films on stainless steels - chemistry, structure and growth. *Electrochimica Acta*, 48(9):1093–1104, 2003.

[55] A. Vesel, M. Mozetic, and A. Zalar. Oxidation of AISI 304L stainless steel surface with atomic oxygen. *Applied Biochemistry and Biotechnologyed Surface Science*, 200(1-4):94–103, 2002.

[56] B. Haase. Qualitätssicherung in der Oberflächentechnik. In *Fachtagung Qualifizierungsnetze Oberflächentechnik im Norden Deutschlands, Hamburg, Vol. 9*, pages 49–68, 2001.

[57] K. Lawless. The oxidation of metals. *Reports on Progress in Physics*, 37(.):231–316, 1974.

[58] H. Dröschel and P. Volk. Passivieren von nichtrostenden, technischen Stählen - Notwendigkeit der Passivierung, Einfluss des Grundwerkstoffs und seiner Oberfläche, Prüfung der Gütte der Passivität. In *3-Länder-Korrosionstagung - Nichtrostenden Stahl Reinigen, Beizen, Passivieren, Korrosionsschutz optimieren*, page ., 2009.

[59] R.M. Cornell and U. Schwertmann. *The iron oxide: structure, properties, reactions, occurence and uses.* Wiley-VCH, Weinheim, 1996.

[60] A.P. Greff, C.W. Louw, and H.C. Swart. The oxidation of industrial FeCrMo steel. *Corrosion Science*, 42:1725–1740, 2000.

[61] M. Honkanen, M. Hoikkanen, M. Vippola, J. Vuorinen, and T. Lepistö. Metal-Plastic Adhesion in Injection-Molded Hybrids. *Journal of Adhesion Science and Technology*, 23(13-14):1747–1761, 2009.

[62] M. Honkanen, M. Vippola, and T. Lepistö. Characterisation of Stainless Steel Surfaces - Modified in Air at 350°C. *Surface Engineering*, 27(5):325–331, 2011.

[63] M. Honkanen, M. Hoikkanen, M. Vippola, J. Vuorinen, T. Lepistö, P. Jussila, H. Ali-Löytty, M. Lampimäki, and M. Valden. Characterization of Silane Layers on Modified Stainless Steel Surfaces and Related Stainless Steel-Plastic Hybrids. *Applied Surface Science*, 257(22):9335–9346, 2011.

[64] M. Honkanen. *Injection-Molded Hybrids - Characterization of Metal-Plastic Interfacial Features.* PhD thesis, Tampere University of Technology, 2011.

[65] J.E. Tang, M. Halvarsson, H. Asteman, and J.-E-Svensson. The microstructure of the base oxide on 304L steel. *Micron*, 32(8):799–805, 2001.

[66] W. Zielinski and K.J. Kurzydlowski. TEM Studies of the oxide scales formed on type 316 stainless steel during annealing at 600C in a vacuum and air. *Scripta Materialia*, 43(1):33–37, 2000.

[67] K. Nomura and Y. Ujihira. Analysis of oxide layers on stainless steel (304, and 316) by conversion electron Mössbauer spectometry. *Journal of Materials Science*, 25(3):1745–1750, 1990.

[68] N. Padhy, R. Paul, U.K. Mudali, and B. Raj. Morphological and compositional analysis of passive film on austenitic stainless steel in nitric acid medium. *Appiled Surface Science*, 257(11):5088–5097, 2011.

[69] E. Petrie. *Handbook of adhesives and sealants*, chapter Surfaces and surface preparation, pages 227–275. McGraw-Hill, New York, 2007.

[70] P. Jussila. *Advances in nanoscale functionalization of stainless steel surfaces.* PhD thesis, Tampere University of Techology, 2009.

[71] P.M. de O. Silva, H.F.G. de Abreu, V.H.C. de Albuquerque, P. de Lima Neto, and J.M.R.S. Tavares. Cold deformation effect on the microstructures and mechanical properties of AISI 301LN and 316L stainless steels. *Materials and Design*, 32:605–614, 2011.

[72] M. Kciuk and A. Kurc-Lisiecka. The influence of heat treatment on structure, mechanical properties and corrosion resistance of steel X10CrNi18-8. *Archives of Materials Science and Engineering*, 55(2):62–69, 2012.

[73] A. Baldan. Review Adhesively-bonded joints and repairs in metallic alloys, polymers and composite materials: Adhesives, adhesion theories and surface pretreatment. *Journal of Materials Science*, 39:1–49, 2004.

[74] S.J. Hitchcock, N.T. Caroll, and M.G. Nicholas. Some effects of substrate roughness wettability. *Journal of Material Science*, 16:714–732, 1981.

[75] R.D. Adams, J. Comyn, and W.C. Wake. *Structural adhesive joints in engineering.* Chapman and Hall, London UK, 1997.

[76] A. Rider, I.W.E. Shum, and L. Mirabella. *Environmental Durability Trial of Bonded Composite Repairs to Metallic Aircraft Structures*, 2005.

[77] K.Y. Blohowiak, J.H. Osborne, and K.A. Krienke. *US005869140A Surface pretreatment of metals to activate the surface for sol-gel coating*, 1999.

[78] L.C. Hollaway and J. Cadei. Progress in the technique of upgrading metallic structures with advanced polymer composites. *Progress in Structural Engineering and Materials*, 4(2):131–148, 2002.

[79] G.P. McCombe, J.A. Etches, P.H. Mellor, and I.P. Bond. Development of a ferromagnetic fibre metal laminate. *Composite Part A: Science and Manufacturing*, 42(10):1380–1389, 2011.

[80] D. Schnerch, M. Dawood, S. Rizkalla, E. Summer, and K. Stanford. Bond Behaviour of CFRP Strengthened Steel Structures. *Advances in Structural Enigineering*, 9(6):805–817, 2006.

[81] M. Davis and D. Bond. Principles and practices of adhesive bonded structural joints and repairs. *International Journal of Adhesion and Adhesives*, 99(2-3):91–105, 1999.

[82] P. Molitor, V. Barron, and T. Young. Surface treatment of titanium for adhesive bonding to polymer composites: a review. *International Journal of Adhesion and Adhesives*, 21(2):129–136, 2001.

[83] P. Molitor and T. Young. Investigation into the use of excimer laser irradiation as a titanium alloy surface treatment in a metal to composite adhesive bond. *International Journal of Adhesion and Adhesives*, 24(1):127–134, 2004.

[84] S. Y. Park, W. J. Choi, and H. S. Choi. A comparative study on the properties of GLARE laminates cured by autoclave and autoclave consolidation followed by oven postcuring. *The International Journal of Advanced Manufacturing Technolgy*, 49(5-8):605–613, 2010.

[85] A. Kinloch. *Adhesion and adhesives.* Springer-Verlag, 1987.

[86] G. D. Davis, G. B. Groff, and R. A. Zatorski. Plasma Spray Coatings as Treatments for Aluminum, Titanium and Steel Adherends. *Surface and Interface Analysis*, 25(5):366–373, 1997.

[87] R. Broad, J. French, and J. Sauer. CLP new, effective, ecological surface pretreatment for highly durable adhesively bonded metal joints. *International Journal of Adhesion and Adhesives*, 19(2):193–198, 1999.

[88] K.Y. Blohowiak, R.A Anderson, W.B.H. Grace, J.W. Grob, and D.H. Fry. Development of new thin adhesive systems and test methods for TiGr laminates. In *SAMPE 2008 - Long Beach CA*, pages –, 2008.

[89] R.A.U. Carrion. *Investigation of Stabilizing Agents in Thin Sol-Gel Zirconium Oxide Anti-corrosion Coatings on Iron Materials.* PhD thesis, Technischen Universität Darmstadt, 2010.

[90] J. Gallardo and P. Galliano. Bioactive and Protective Sol-Gel Coatings on Metals or Orthopaedic Prostheses. *Journal of Sol-Gel Science and Technology*, 21(1):65–74, 2001.

[91] J.J. Mazza. *Sol-Gel Technology for Low-Voc, Nonchromated Adhesive Bonding Applications SERDP Project PP-1113*, 2004.

[92] M.S. Oliver, K.Y. Blohowiak, and R.H. Dauskardt. Reliability of adhesive interphases for titanium-graphite laminates. In *SAMPE 2008 - Long Beach CA*, page ., 2008.

[93] H.K. Schmidt. Das Sol-Gel Verfahren. *Chemie in unserer Zeit*, 3(3):179–184, 2001.

[94] H. Schmidt, S. Langenfeld, and R. Naß. A new corrosion protection coating system for pressure-cast aluminium automotive parts. *Materials and Design*, 18(4/6):309–313, 1997.

[95] J.T. Wong. Evaluation of Titanium Bonding Surface Preparation Method: Sol-Gel AC-130-2. In *American Helicopter Society 68th Annual Forum, Fort Worth, Texas*, 2012.

[96] Cytec Engineered Materials U.S.A Tempe Arizona. *BR®127 Corrosion Inhibiting Primer - Technical Data Sheet*, August 2010.

[97] T. Sinmazcelik, E. Avcu, M. Özgür Bora, and O. Coban. A review: Fibre metal laminates, background, bonding types and applied test methods. *Materials and Design*, 32(7):3671–3685, 2011.

[98] ASTM. *ASTM D3846 - 08(2015) Standard Test Method for In-Plane Shear Strength of Reinforced Plastics*, 2015.

[99] S. Hinz, T. Omoori, M. Hojo, and K. Schulte. Damage characterisation of fibre metal laminates under interlaminar shear load. *Composites Part A: Applied Science and Manufacturing*, 40(6-7):925–931, 009.

[100] G. Lawcock, L. Ye, Y.-W. Mai, and C.-T. Sun. The effect of adhesive bonding between aluminum and composite prepreg on the mechanical properties of carbon-fiber-reinforced metal lamintes. *Composites Science and Technology*, 57(1):35–45, 1997.

[101] G.D. Lawcock, L. Ye, Y.Q. Mai, and C.T. Sun. Effects of fibre/matrix adhesion on carbon-fibre-reinforced metal laminates I. Residual strength. *Composites Science and Technology*, 57(12):1609–1619, 1997.

[102] G.D. Lawcock, L. Ye, Y.Q. Mai, and C.T. Sun. Effects of fibre/matrix adhesion on carbon-fibre-reinforced metal laminates II. Impact Behaviour. *Composites Science and Technology*, 57(12):1621–1628, 1997.

[103] ASTM. ASTM D2344-84, Standard test method for apparant interlaminar shear strenght of parallel fiber composites by short-beam method, 1984.

[104] DIN Deutsches Institut für Normung e.V. *DIN EN ISO 14130 Fibre-reinforced plastic composites - Determination of apparent interlaminar shear strength by short-beam method*, 1998.

[105] G. Reyes and W.J. Cantwell. The mechanical properties of fibre-metal laminates based on glass fibre reinforced polypropylene. *Composites Science and Technology*, 60:1085–1094, 2000.

[106] P. Cortés and W.J. Cantwell. The fracture properties of a fibre–metal laminate based on magnesium alloy. *Composites Part B: Engineering*, 37:163–170, 2006.

[107] J.G. Carrillo and W.J. Cantwell. Mechanical properties of a novel fiber–metal laminate based on a polypropylene composite. *Mechanics of Materials*, 41:828–838, 2009.

[108] D.F. Adams, L.A. Carlsson, and R.B. Pipes. *Experimental characterization of advanced composite materials.* CRC Press LLC, 2003.

[109] ASTM. *ASTM 98(2012) Standard Test Method for Climbing Drum Peel for Adhesives*, 2012.

[110] H.J. Bateman, M.O. Hunt, and C.T. Sun. New interlaminar shear test for structural wood composites. *Forest Products Journal*, 40:9–14, 1990.

[111] W.-X. Wang, M. Higashijima, Y. Takao, and T. Matsubara. Test methods for evaluating the interlaminar shear strength of CFML. In *ATEM - Proceedings of International Conference on Advanced Technology in Experimental Mechanics; CDROM ID-90286*, pages 1–6, 2007.

[112] W.-X. Wang, Y. Takao, and T. Matsubara. Galvnic Corrosion-Resistant Carbon Fiber Metal-Laminates. In *16th International Conference on Composite Materials, Kyoto, Japan*, pages 1–10, 2007.

[113] A. Nashimura. Effect of radius of loading nose and suports in short beam test fixture on fracture mode and interlaminar shear strength of GFRP at 77K. In *CP986 Advances in Cryogenic Engineering: Transactions of the International Cryogenic Materials Conference . ICMC, Vol 54*, 2008.

[114] S.N. Charrerjee. Analysis of the short-beam shear test for unidirectional composites. *Composite Materials: Testing and Design (Twelfth Volume), ASTM STP 1274*, 12:320–339, 1996.

[115] A.W. Darkov and G.S. Spiro. *Strength of materials.* Wisshaja Shkola, Moscow, 1969.

[116] B.A. Bednarcyk, J. Aboudi, and P.W. Yarrington. Determination of the Shear Stress Distribution in a Laminate From the Applied Shear Resultant - A Simplified Shear Solution. Technical report, NASA/CR-2007-215022, 2007.

[117] T.O. Williams. A Generalized Multilength Scale Nonlinear Composite Plate Theory with Delamination. *International Journal of Solids and Structures*, 36:3015–3050, 1999.

[118] S. Timoshenko. Analysis of Bi-Metal Thermostats. *Journal of the Optical Society of America*, 1925.

[119] E. Suhir. Interfacial Stresses in Bimetal Thermostats. *ASME Journal of Applied Mechanics*, 56(3):595–600, 1989.

[120] M.S. Hess. The End Problem for a Laminated Elastic Strip I. The General Solution. *Journal of Composite Materials*, 3:262–280, 1969.

[121] M.S. Hess. The End Problem for a Laminated Elastic Strip II. Differential Expansion Stresses. *Journal of Composite Materials*, 3:630–647, 1969.

[122] J. W. Eischen, C. Chung, and J. H. Kim. Realistic Modeling of Edge Effect Stresses in Bimaterial Elements. *Journal of Electronic Packaging*, 112(1):16–23, 1990.

[123] J.W. Tukey. *Exploratory data analysis.* Addison-Wesley, 1977.

[124] B.S. Covino. *Information circular 8985*, chapter Pickling of Stainless Steels - A Review. United States Department of Interieur, Bureau of Mines, 1984.

[125] Arizona Cytec Engineered Materials, U.S.A Tempe. *Cycom 977-2 Toughened Epoxy Resin*, 2001.

[126] 3M Aerospace and Aircraft Maintenance Department St.Paul. *3M^{TM} Surface Pre-Treatment AC-130*, February 2012.

[127] Arizona Cytec Engineered Materials, U.S.A Tempe. *BR 6747-1 Water-Based Adhesive Bonding Primer System*, 2005.

[128] A. Schmitz, D. Sen Gupta, and H. Peter. *DE4417284 C2 Verfahren zum Beizen von Werkstücken aus hochlegierten Werkstoffen*, 1999.

[129] B.S. Covino, J.V. Scalera, T.J. Driscoll, and J.P. Carter. Dissolution behaviour of 304 stainles steel in HNO3/HF mixtures. *Metallurgical and Materials Transactions A*, 17(1):137–149, 1986.

[130] L. Narváez, E. Cano, and J.M. Bastidas. Effect of ferric irons in AISI 316L stainless steel pickling using an environmentally-frindly H2SO4-HF-H2O2 mixture. *Materials and Corrosion*, 54(1):84–87, 2003.

[131] Henkel. *Sicherheitsdatenblatt - Turco 6849*, September 2011.

[132] Henkel. *Technical Information Bulletin - Turco 6849 - Aqueous Alkaline Degreaser)*, October 1998.

[133] Henkel. *Sicherheitsdatenblatt Turco 4104*, February 2011.

[134] Henkel. *Technical Information Bulletin - Turco Nitradd (Turco 4104)*, June 1999.

[135] S. Piesslinger-Schweiger and O. Böhme. *DE102009038795 A1 Beizverfahren für Edelstahl*, 2009.

[136] SurTec Deutschland GmbH. *SurTec 433 - Produktinformationsblatt*, November 2010.

[137] SurTec Deutschland GmbH. *SurTec 433 - Sicherheitsdatenblatt*, February 2011.

[138] SurTec Deutschland GmbH. *SurTec 089 - Produktinformationsblatt*, April 2011.

[139] SurTec Deutschland GmbH. *SurTec 089 - Sicherheitsdatenblatt*, April 2011.

[140] SurTec Deutschland GmbH. *SurTec 089 - Produktinformationsblatt*, December 2010.

[141] SurTec Deutschland GmbH. *SurTec 138 - Sicherheitsdatenblatt*, February 2010.

[142] DIN Deutsches Institut für Normung e.V. *DIN EN ISO 4288:1998-04 - Geometrische Produktspezifikation (GPS) - Oberflächenbeschaffenheit: Tastschnittverfahren - Regeln und Verfahren für die Beurteilung der Oberflächenbeschaffenheit*, April 1998.

[143] M. Hagenbeek, C. van Hengel, O.J. Bosker, and C.A.J.R Vermeeren. Static Properties of Fibre Metal Laminates. *Applied Composite Materials*, 10(4-5):207–222, 2003.

[144] C.T. Lin and P.W. Kao. Effect of fiber bridging on the fatigue crack propagation in carbon fiber-reinforced aluminum laminates. *Materials Science and Engineering*, 190(1-2):65–73, 1995.

[145] R. Van Roojnen, J. Sinke, T.J. De Vries, and S. Van Der Zwaag. Property Optimisation in Fibre Metal Laminates. *Applied Composite Materials*, 11(2):63–76, 2004.

[146] D.F. Silva, E.C. Botelho, A.C. Ancelotti, and C.A. Damato. Environmental Conditioning Effects on the Mechanical Properties of Titanium Fiber-Metal-Laminates. In *ICCM19 - The 19th International Conference on Composite Materials*, 2013.

[147] D. Djokic, A. Johnston, A. Rogers, P.Lee-Sullivan, and N. Mrad. Residual stress development during the composite patch bonding process: measurement and modeling. *Composites Part A: Applied Science and Manufacturing*, 33(2):277–288, 2002.

[148] T. Haberle. *Thermomechanik werkstoffhybrider, faserverstärkter Schichtverbunde und Bauteile bei tiefen Temperaturen*. PhD thesis, Technische Universität München, 2001.

[149] J. Díaz, C. Fagiano, M.M. Abdalla, Z. Gürdal, and S. Hernández. A study of interlaminar stresses in variable stiffness plates. *Composite Structures*, 94:1192–1199, 2012.

[150] C.T. Herakovich. On thermal edge effects in composite laminates. *Internation Journal of Mechanical Sciences*, 18:129–134, 1976.

[151] E. Correa, V. Mantic, and F. París. Effect of thermal residual stresses on matrix failure under transverse tension at micromechanical level: A numerical and experimental analysis. *Composite Science and Technology*, 71:622–629, 2011.

[152] S. Laik and A. A. Skordos. Influence of residualstresss on the delamination and shear response of carbon epoxy. In *ECCM15 - 15TH European Conference on Composite Materials, Venice, Italy, 24-28*, 2012.

[153] H. Hosseini-Toudeshky, M. Sadighi, and A. Vojdani. Effects of curing thermal residual stresses on fatigue crack propagation of aluminum plates repaired by FML patches. *Composite Structures*, 100:154–162, 2013.

[154] M.K. Alam and M.S. Anghelescu. Analysis of Deformation and Residual Stresses in Composite Processed on a Carbon Foam Tool. *Journal of Composite Materials*, 43(19):2057–2070, 2009.

[155] G. Fernlund, A. Poursartip, G. Twigg, and C. Albert. Residual stress, spring-in and warpage in autoclaved composite parts. In *14th International Conference on Composite Materials (ICCM-14); San Diego, California, USA, July 14-18*, page ., 2003.

[156] T. Garstka, N. Ersoy, K.D. Potter, and M.R. Wisnom. In situ measurements of through-the-thickness strains during processing AS4/8552 composite. *Composites Part A: Applied Science and Manufacturing*, 38(12):2571–2526, 2007.

[157] M. Gigliotti, M.R. Wisnom, and K.D. Potter. Development of curvature during the cure of AS4/8552 [0/90] unsymmetric composite plates. *Composites Science and Technology*, 63(2):187–197, 2003.

[158] M. Gigliotti, F. Jaquemin, and A. Vautrin. On the maximum curvatures of 0/90 plates under thermal stress. *Composite Structures*, 68(2):177–184, 2005.

[159] V. Kominar. Thermo-mechanical regulation of residual stresses in polymers and polymer composites. *Journal of Composite Materials*, 30(3):406–415, 1996.

[160] D.W. Radford and T.S. Rennick. Seperating Sources of Manufacturing Distortion in Laminated Composites. *Journal of Reinforced Plastics and Composites*, 19(8):621–641, 2000.

[161] D.W. Radford. Balancing Mechanisms of Distortion to Yield Distortion-free/Shape Stable Composites. *Journal of Reinforced Plastics and Composites*, 29(12):1875–1892, 2010.

[162] E. Ruiz and F. Trochu. Numerical analysis of cure temperature and internal stresses in thin and thick RTM parts. *Composites Part A: Applied Science and Manufacturing*, 36(6):806–826, 2005.

[163] S. Yi and H.H. Hilton. Effects of thermo-mechanical properties of composites on viscosity, temperature and degree of cure in thick thermosetting composite laminates during curing process. *Journal of Composite Materials*, 32(7):600–622, 1998.

[164] E. Kappel, D. Stefaniak, and G. Fernlund. Predicting process-induced distortions in composite manufacturing: A pheno-numerical simulation strategy. *Composite Structures*, 120:98–106, 2015.

[165] E. Kappel. Forced-interaction and spring-in – relevant initiators of process-induced distortions in composite manufacturing. *Composite Str*, 140:217–229, 2016.

[166] F.S. Jumbo, I.A. Ashcroft, A.D. Crocombe, and M.M. Abdel Wahab. Thermal residual stress analysis of epoxy bi-material laminates and bonded joints. *International Journal of Adhesion and Adhesives*, 30(7):523–538, 2010.

[167] Y. Yu, I.A. Ashcroft, and G. Swallow. An experimental investigation of residual stresses in an epoxy-steel laminate. *International Journal of Adhesion and Adhesives*, 26:511–519, 2006.

[168] H.S. Kim and D.G. Lee. Avoidance of fabricational thermal residual stresses in co-cure bonded metal-composite hybrid structures. *Journal of Adhesion Science and Technology*, 20(9):959–979, 2006.

[169] K.D. Cowley and P.W.R. Beaumont. The measurement and prediction of residual stresses in carbon-fibre/polymer composites. *Composites Science and Technology*, 57(1):1445–1455, 1997.

[170] J.P. Nobre, A.C. Batista, A. Nau, W. Van Paepegem, and B. Scholtes. Using the incremental hole-drilling technique for measuring residual stresses in fibre-reinforced polymer. In *ECCM15 - 15TH Europen Conference on Composite Materials, Venice, Italy, 24-28*, 2012.

[171] L. Khoun, R. de Oliveira, V. Michaud, and P. Hubert. Investigation of process-induced strains development by fibre Bragg grating sensors in resin transfer moulded composites. *Composites Part A: Applied Science and Manufacturing*, 42(3):274–282, 2011.

[172] N. Lammensa, D. Kinetb, K. Chahb, G. Luyckxa, C. Caucheteurb, J. Degriecka, and P. Mégretb. Residual strain monitoring of out-of-autoclave cured parts by use of polarization dependent loss measurements in embedded optical fiber Bragg gratings. *Composites Part A: Applied Science and Manufacturing*, 52:38–44, 2013.

[173] M.R. Wisnom, M. Gigliotti, N. Ersoy, M. Campbell, and K.D. Potter. Mechanisms generating residual stresses and distortion during manufacture of polymer-matrix composite structures. *Composites Part A: Applied Science and Manufacturing*, 37(4):522–529, 2006.

[174] W.A. Schulz, D.G. Myers, T. N. Singer, P.G. Ifju, and R.T. Haftka. Determination of residual stress and thermal history for IM7/977-2 composite laminates. *Composite Science and Technology*, 65:2014–2024, 2005.

[175] P. Hofslagere. Residual Stress Measurement on Fibre-Metal-Laminates. *Journal of Neutron Research*, 11(4):215–220, 2003.

[176] H.S. Kim, S.W. Park, H.Y. Hwang, and D.G. Lee. Effect of the smart cure cycle on the performance of the co-cured aluminium/composite hybrid shaft. *Composite Structures*, 75(1-4):276–288, 2006.

[177] H.S. Kim, S.W. Park, and D.G. Lee. Smart cure cycle with cooling and reheating for co-cure bonded steel/carbon epoxy composite hybrid structures for reducing thermal residual stress. *Composites Part A: Applied Science and Manufacturing*, 37(10):1708–1721, 2006.

[178] S.R. White and H.T. Hahn. Cure cycle optimization for the reduction of processing-induced residual stresses in composite materials. *Journal of Composite Materials*, 27(14):1352–1378, 1993.

[179] N. Ersoy, T. Garstka, K. Potter, M.R. Wisnom, D. Porter, M. Clegg, and G. Stringer. Development of the properties of a carbon fibre reinforced thermosetting composite through cure. *Composites Part A: Applied Science and Manufacturing*, 41(3):401–409, 2010.

[180] G. Fernlund, N. Rahman, R. Courdji, M. Bresslauer, A. Poursartip, K. Willden, and K. Nelson. Experimental and numerical study of the effect of cure cycle, tool surface, geometry, and lay-up on the dimensional fidelity of autoclave-processed composite parts. *Composites Part A: Applied Science and Manufacturing*, 33(3):341–351, 2002.

[181] J. Xue, W.-X. Wang, Y. Takao, and T. Matsubara. Reduction of thermal residual stress in carbon fiber aluminum laminates using a thermal expansion clamp. *Composite Part A: Science and Manufacturing*, 42(8):986–992, 2011.

[182] D.H. Cho and D.G. Lee. Manufacturing of Co-Cured Composite Aluminium Shafts with Compression to Reduce Residual Thermal Stresses. *Journal of Composite Materials*, 32(12):1221–1241, 1998.

[183] G. Twigg, A. Poursartip, and G. Fernlund. Tool-part interaction in composites processing. Part I: experimental investigation and analytical model. *Composites Part A: Applied Science and Manufacturing*, 35(1):121–133, 2004.

[184] L. Khoun and P. Hubert. Investigation of the dimensional stability of carbon epoxy cylinders manufactured by resin transfer moulding. *Composites Part A: Applied Science and Manufacturing*, 41(1):116–124, 2010.

[185] V. Kaushik and J. Raghavan. Experimental study of tool-part interaction during autoclave processing of thermoset polymer composite structures. *Composites Part A: Applied Science and Manufacturing*, 41(9):1210–1218, 2010.

[186] N. Ersoy, K. Potter, M.R. Wisnom, and M.J. Clegg. An experimental method to study the frictional process during composites manuacturing. *Composites Part A: Applied Science and Manufacturing*, 36(11):1536–1544, 2005.

[187] K.D. Potter, M. Campbell, C. Langer, and M.R. Wisnom. The generation of geometrical deformations due to tool/part interaction in the manufacture of composite components. *Composites Part A: Applied Science and Manufacturing*, 36(2):301–308, 2005.

[188] P. Hubert and A. Poursartip. Aspects of the compaction of composite angle laminates: an experimental investigation. *Journal of Composite Materials*, 35(1):2–26, 2001.

[189] C.J. Martin and J.C. Seferis. Frictional resistance of thermoset prepregs and its influence on honeycomb composites processing. *Composites Part A: Applied Science and Manufacturing*, 27(10):943–951, 1996.

[190] Y.R. Larberg and M. Akermo. On the interply friction of different generations of carbon/epoxy prepreg systems. *Composites Part A: Applied Science and Manufacturing*, 42(9):1067–1074, 2011.

[191] J.M. Svanberg and J.A. Holmberg. An experimental investigation on mechanisms for manufacturing induced shape distortions in homogenous and balanced laminates. *Composites Part A: Applied Science and Manufacturing*, 32(6):827–838, 2001.

[192] R.J. Roark. *Roark's formulas for stress and strain.* McGraw-Hill Professional, 7 edition, 2001.

[193] H.J. Oel and V.D. Frechette. Stress distribution in multiphase systems: composites with planar interfaces. *Journal of the American Ceramic Society*, 50:542–549, 1967.

[194] A. Baker, S. Dutton, and D. Kelly. *Composite Materials for Aircraft Structures.* American Institute of Aeronautics and Astronautics, Inc., 2004.

[195] DIN Deutsches Institut für Normung e.V. *Aerospace series - Fibre reinforced plastics - Test method - Determination of the compression strength after impact EN 6038:2015*, 02 2016.

[196] AIRBUS. *AITM1-0010 Determination of Compression Strength After Impact*. AIRBUS, 2005.

[197] ASTM. *ASTM D7137/D7137M - 07(2007) Standard Test Method for Compressive Residual Strength Properties of Damaged Polymer Matrix Composite Plates*, 11 2007.

[198] D.D.R. Cartié and P.E. Irvin. Effect of resin and fibre properties on impact and compression after impact performance of CFRP. *Composites Part A: Applied Science and Manufacturing*, 33(4):483–493, 2002.

[199] S. Sanchez-Saez, E.J. Barbero, R. Zaera, and C. Navarro. Compression after impact of thin composite laminates. *Composites Science and Technology*, 65(13):1911–1919, 2005.

[200] K. Tanaka and K. Kageyama. Manualization Study on Compression After Impact Test for CFRPs in Japan. In *Proceedings of European Conference for Composite Testing and Manualization, Woodhead Publishing*, pages 469–477, 1994.

[201] M. Remacha, S. Sánchez-Sáez, B. López-Romano, and E. Barbero. A new device for determining the compression after impact strength in thin laminates. *Composite Structures*, 127:99–107, 2015.

[202] M.O.W. Richardson and M.J. Wisheart. Review of low-velocity impact properties of composite materials. *Composites Part A: Applied Science and Manufacturing*, 27(12):1123–1131, 1996.

[203] H. Saito, M. Morita, K. Kawabe, M. Kanesaki, H. Takeuchi, M. Tanaka, and I. Kimpara. Effect of ply-thickness on impact damage morphology in CFRP laminates. *Journal of Reinforced Plastics and Composites*, 30(13):1097–1106, 2011.

[204] P. Rahmé, C. Bouvet, S. Rivallant, V. Fascio, and G. Valembois. Experimental investigation on impact on composite laminates with protective layers. *Composites Science and Technology*, 72:182–189, 2012.

[205] W.J. Cantwell. Geometrical effects in the low velocity impact repsonse of GFRP. *Composite Science and Technology*, 67:1900–1908, 2007.

[206] G. Wu, J.-M. Yang, and T. Hahn. The impact properties and damage tolerance and of bi-directionally reinforced fiber metal laminates. *Journal of Materials Science*, 42(3):948–957, 2007.

[207] F.D. Morinière, R.C. Alderliesten, and R. Benedictus. Energy Distribution in GLARE and 2024-T3 Aluminium during Low-Velocity Impact. In *ICAS 2012 - 28th International Congress of the Aeronautical Sciences*, 2012.

[208] J. Fan, W.J. Cantwell, and Z.W. Guan. The low velocity impact response of fiber-metal laminates. *Journal of Reinforced Plastics and Composites*, 30(1):26–35, 2011.

[209] S.A. Hitchen and R.M.J. Kemp. The effect of stacking sequence on impact damage in a carbon fibre/epoxy composite. *Composites*, 26:207–214, 1995.

[210] T.A. Sebaey, E.V. González, C.S. Lopes, N. Blanco, and J. Costa. Damage resistance and damage tolerance of dispersed CFRP laminates: Design and optimization. *Composite Structures*, 95(1):569–576, 2013.

[211] L. Onal and S. Adanur. Effect of Stacking Sequence on the Mechanical Properties of Glass-Carbon Hybrid Composites Before and After Impact. *Journal of Industrial Textiles*, 31:255–271, 2002.

[212] E. Fuoss, P.V. Straznicky, and C. Poon. Effects of stacking sequence on the impact resistance in composite laminates - Part 1: paramteric study. *Composite Structures*, 41:67–77, 1998.

[213] G. Caprino, V. Lopresto, C. Scarponi, and G. Briotti. Influence of material thickness on the response of carbon-fabric/epoxy panels to low velocity impact. *Composite Science and Technology*, 59:2279–2286, 1999.

[214] Y. Liu and B. Liaw. Effects of Constituents and Lay-up Configuration on Drop-Weight Tests of Fiber-Metal Laminates. *Applied Composite Materials*, 14(1):43–62, 2010.

[215] E.V. Gonzáles, P Maimí, J.R. Sainz de Aja, P. Cruz, and P.P. Camanho. Effects of interply hybridization on the damage resistance and tolerance of composite laminates. *Composite Structures*, 108:319–331, 2014.

[216] H. Zarei, M. Fallah, G. Minak, and H. Bisadi A. Daneshmer. Low velocity impact analysis of Fiber Metal Laminates (FMLs) in thermal environments with various boundary conditions. *Composite Structures*, 149:170–183, 2016.

[217] D. Ghelli and G. Minak. Low velocity impact and compression after impact tests on thin carbon/epoxy laminates. *Composites Part B: Engineering*, 42(7):2067–2079, 2011.

[218] G. Minak and D. Ghelli. Influence of diameter and boundary conditions on low velocity impact response of CFRP circular laminated plates. *Composites Part B: Engineering*, 39(6):962–972, 2008.

[219] AIRBUS. *AITM1-0008 Determination of Plain, Open Hole and Filled Hole Compression Strength*, 2010.

[220] ASTM. *D6641/D6641M - 16 Standard Test Method for Determining the Compressive Properties of Polymer Matrix Composite Laminates Using a Combined Loading Compression (CLC) Test Fixture*, 2016.

[221] ASTM. *D3410/D3410M - 16 Standard Test Method for Compressive Properties of Polymer Matrix Composite Materials with Unsupported Gage Section by Shear Loading*, 2016.

[222] DIN Deutsches Institut für Normung e.V. *DIN EN ISO 14126 Faserverstärkte Kunststoffe - Bestimmung der Druckeigenschaften in der Laminatebene*, 12 2000.

[223] DIN Deutsches Institut für Normung e.V. *DIN EN 2850 Unidirektionale Laminate aus Kohlenstoffasern und Reaktionsharz - Druckversuch parallel zur Faserrichtung*, 1998.

[224] DIN Deutsches Institut für Normung e.V. *DIN 65380:1991-11 Prüfung von unidirektionalen Laminaten und Gewebe-Lamianten Druckversuch*, 11 1991.

[225] PerkinElmer Technologies GmbH & Co. KG. XRD 1620 xN CS Flat Panel X-ray Detector - Product Note, 2012.

[226] B. Jähne. *Digital Image Processing*. Springer-Verlag, 2005.

[227] P. Soille. *Morphological Image Analysis*. Springer-Verlag, 2nd edition edition, 2004.

[228] J. F. Barrett and N. Keat. Artifacts in CT: Recognition and Avoidance. *RadioGraphics*, 24(6):1479–1691, 2004.

[229] ASTM. *ASTM D7136/D7136M - 07(2007) Standard Test Method for Measuring the Damage Resistance of a Fiber-Reinforced Polymer Matrix Composite to a Drop-Weight Impact Event*, 11 2007.

[230] H. Schürmann. *Konstruieren mit Faser-Kunststoff-Verbunden.* Springer-Verlag Berlin Heidelberg, 2007.

[231] W. Schnell, D.Gross, and W. Hauger. *Technische Mechanik Band 2: Elastostatik.* Springer-Verlag Berlin Heidelberg, 2002.

[232] A. Vlot. *Low-Velocity IImpact Loading on Fibre Reinforced Aluminium Laminates (ARALL and GLARE.* PhD thesis, Technische Univ. Delft (Netherlands), 93.

Appendix

A Simplified shear solution by *Bednarcyk et al.*

This shear solution is provided by *Bednarcyk et al.* [116] and reproduced in the following for the sake of completeness.
The original width of each layer b is transformed to $b\ n_k$ with:

$$n_k = \frac{E_x^k}{\overline{E_x}} \tag{7.1}$$

where n_k is defined for each ply and describes the ratio of the ply's stiffness and the average laminates stiffness. The neutral axis of the laminate is located at the center of the transformed laminate's cross section and - with respect to the laminate midplane coordinate system - given by:

$$z^* = \frac{\sum_{k=1}^{N} \frac{1}{2}\ (z_k + z_k - 1)\ A_k}{\sum_{k=1}^{N} A_k} = \frac{\sum_{k=1}^{N} \frac{1}{2}\ (z_k + z_k - 1)\ t_k\ n_k}{\sum_{k=1}^{N} t_k\ n_k} \tag{7.2}$$

A_k and t_k represent the area and the thickness of the layer, respectively. The distance of a point from the neutral axis is denoted by $\hat{z} = z - z^*$.
The normal stress distribution at an arbitrary vertical cross section is - according to the beam theory - given by:

$$\sigma_x = -\frac{M\hat{z}}{I} \tag{7.3}$$

where I is the transformed cross section and M is the moment applied to the vertical cross section. Equilibrium dictates $M = -Px$, hence:

$$\sigma_x = -\frac{P\ x\ \hat{z}}{I} \tag{7.4}$$

The shear force H acting on an arbitrary cross section located at $\hat{z} = \hat{z}_c$, with the ply number k results in:

$$-H + \int \sigma_x\ \mathrm{d}A = 0 \tag{7.5}$$

with dA defining a differential area of the cross section. With $c = \hat{z}_N$ denoting the distance form the neutral axis to the laminate's bottom surface and $\mathrm{d}A = b\ n_k\ \mathrm{d}\hat{z}$, the following can be obtained:

$$H = \frac{Px}{I}\int_{\hat{z}_N}^{\hat{z}_c} \hat{z}\ \mathrm{d}A = \frac{Px}{I}\int_{\hat{z}_N}^{\hat{z}_c} b\ n_k\ \hat{z}\,\mathrm{d}\hat{z} \tag{7.6}$$

The right integral is denoted as $Q'(k,\hat{z})$ and can be formulated as follows:

$$\begin{aligned} Q'(k,\hat{z}) = \int_{\hat{z}_N}^{\hat{z}_c} b\ n_k\ \hat{z}\,\mathrm{d}\hat{z} &= \int_{\hat{z}_k}^{\hat{z}_c} b\ n_k\ \hat{z}\,\mathrm{d}\hat{z} + \int_{\hat{z}_{k+1}}^{\hat{z}_c} b\ n_{k+1}\ \hat{z}\,\mathrm{d}\hat{z} + ... + \int_{\hat{z}_N}^{\hat{z}_{N-1}} b\ n_N\ \hat{z}\,\mathrm{d}\hat{z} \\ &= \frac{b\ n_k}{2}(\hat{z}_c^2 - \hat{z}_k^2) + \frac{1}{2}\sum_{m=k+1}^{N} b\ n_m\ (\hat{z}_{m-1}^2 - \hat{z}_m^2) \end{aligned} \tag{7.7}$$

In formula 7.7, b describes the width, k the ply number, c the distance from the neutral plane to the bottom surface and N the total number of plies. The shear stress τ at an arbitrary position $\hat{z}$ within an arbitrary layer k is given by:

$$\tau(k, \hat{z}) = -\frac{Q}{I}\, Q'(k, \hat{z}) \tag{7.8}$$

where the moment of inertia of the transformed beam cross section is described by:

$$I = \sum_{k=1}^{N} \left[\frac{1}{12} b\, n_k\, t_k^3 + b\, n_k\, t_k \left(\frac{\hat{z}_k + \hat{z}_{k-1}}{2} \right)^2 \right] \tag{7.9}$$

B Failure geometries - CFRP-UD-steel CT plots

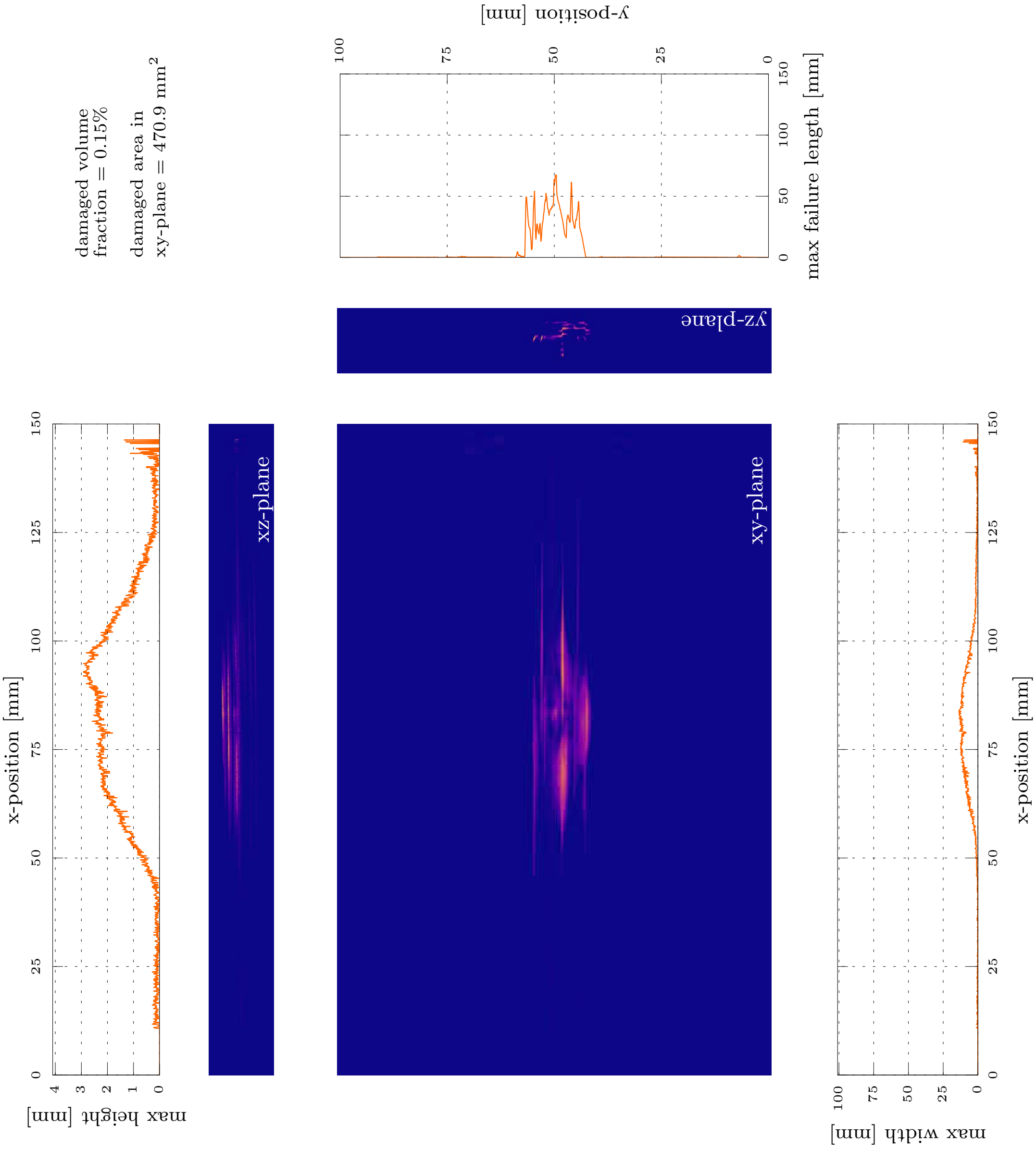

Figure 7.1: CT damage intensity plot UD-St-0.03-low/4 specimen 1

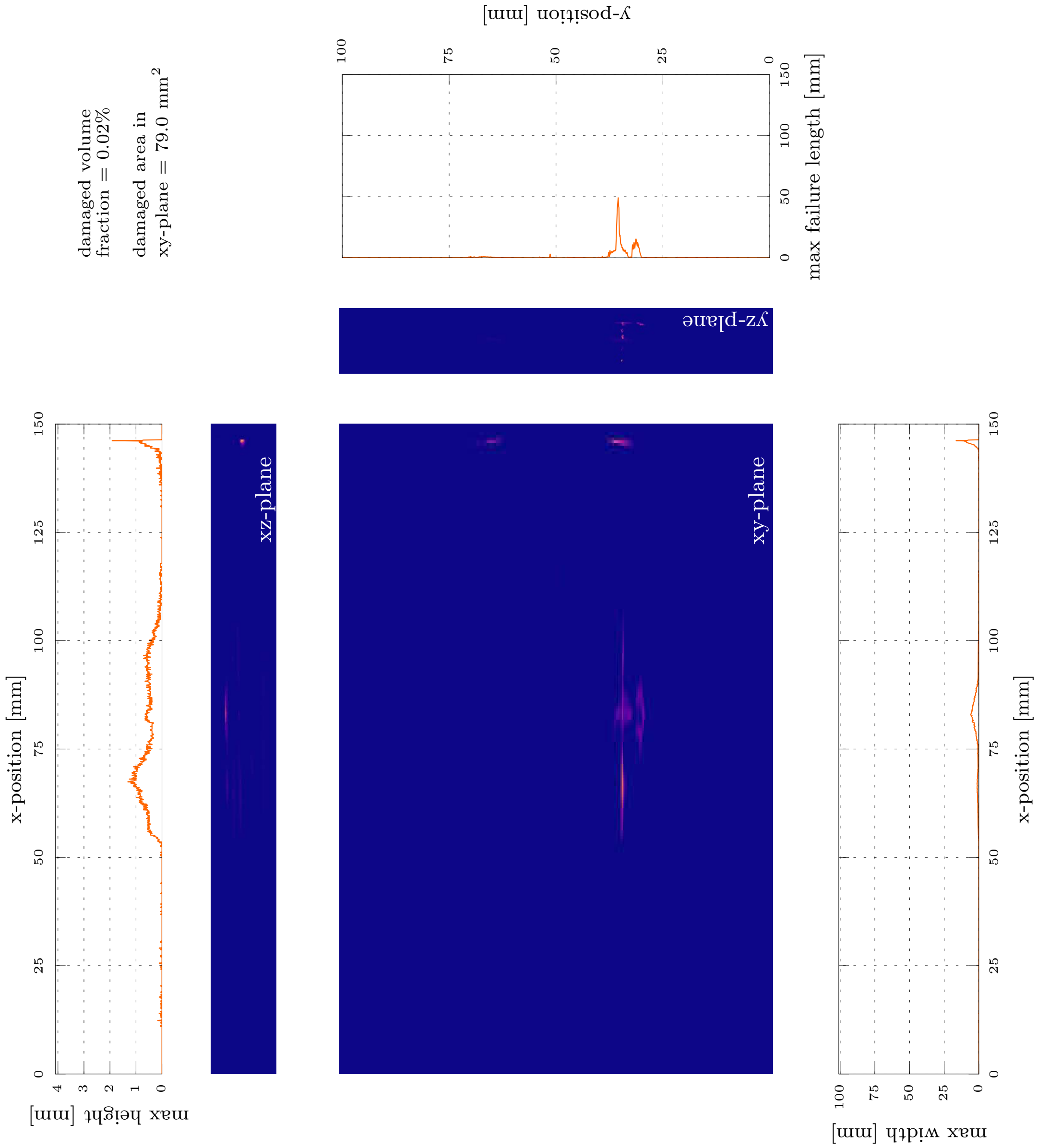

Figure 7.2: CT damage intensity plot UD-St-0.03-low/4 specimen 2

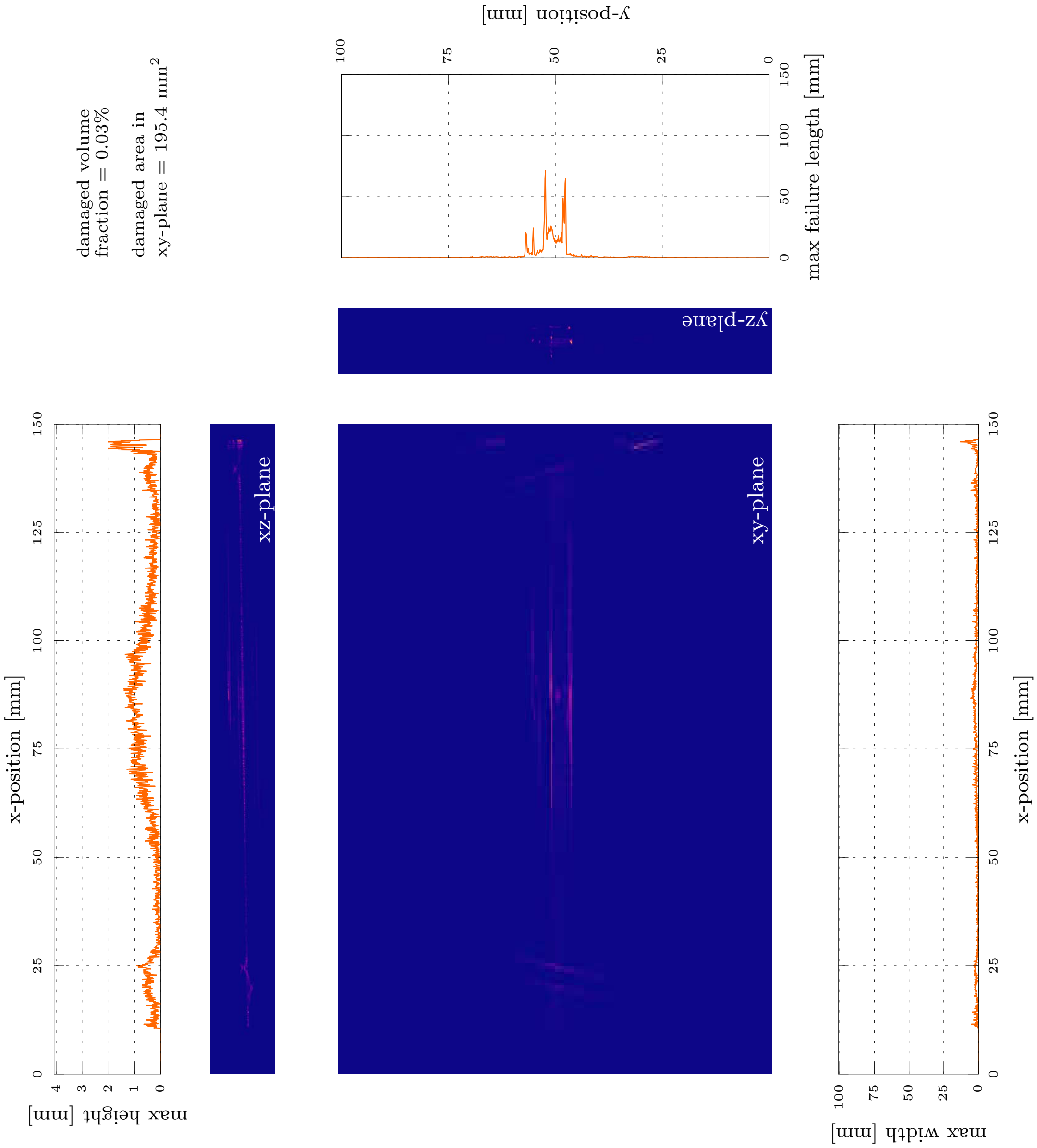

Figure 7.3: CT damage intensity plot UD-St-0.03-low/4 specimen 3

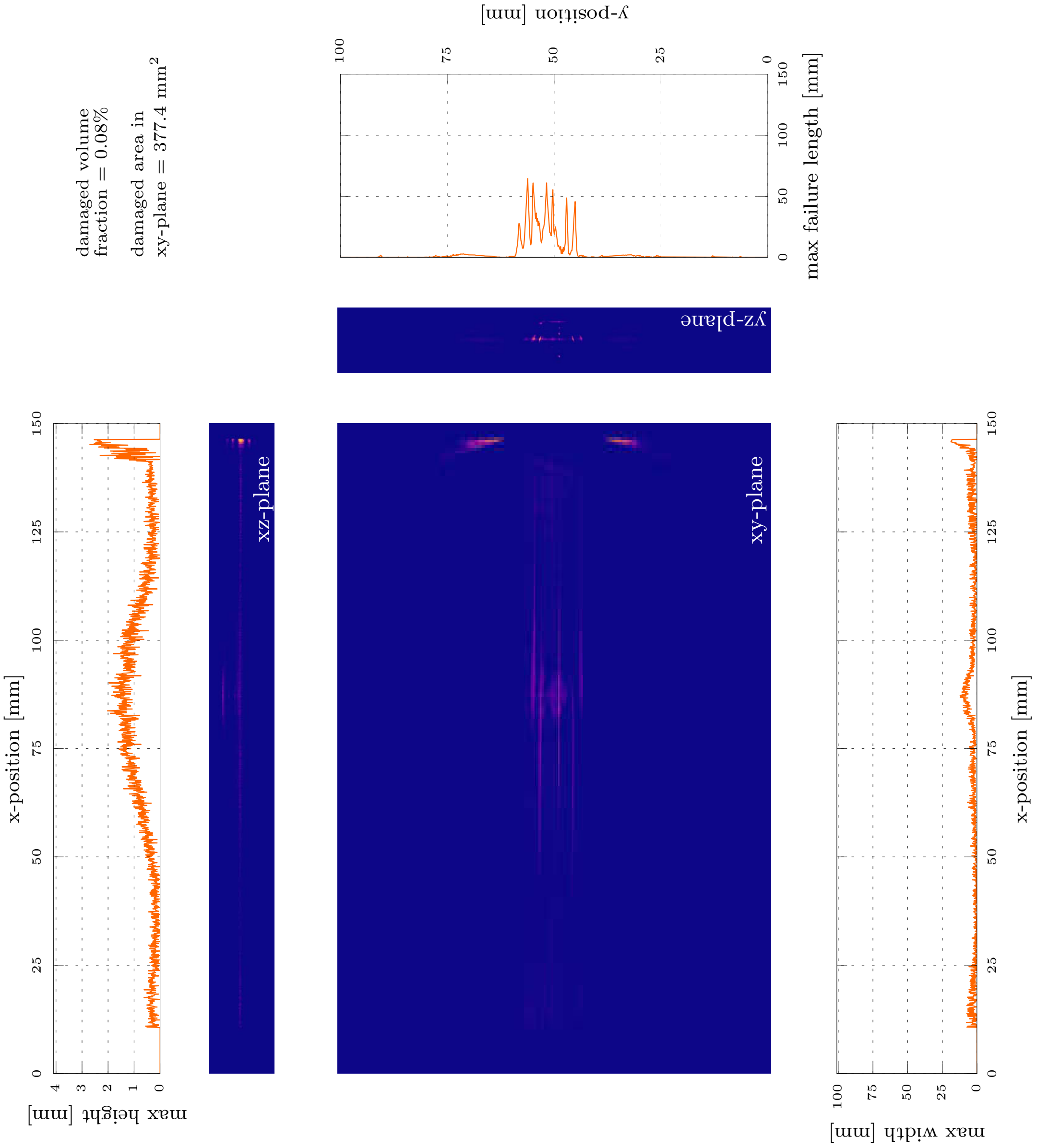

Figure 7.4: CT damage intensity plot UD-St-0.03-low/4 specimen 4

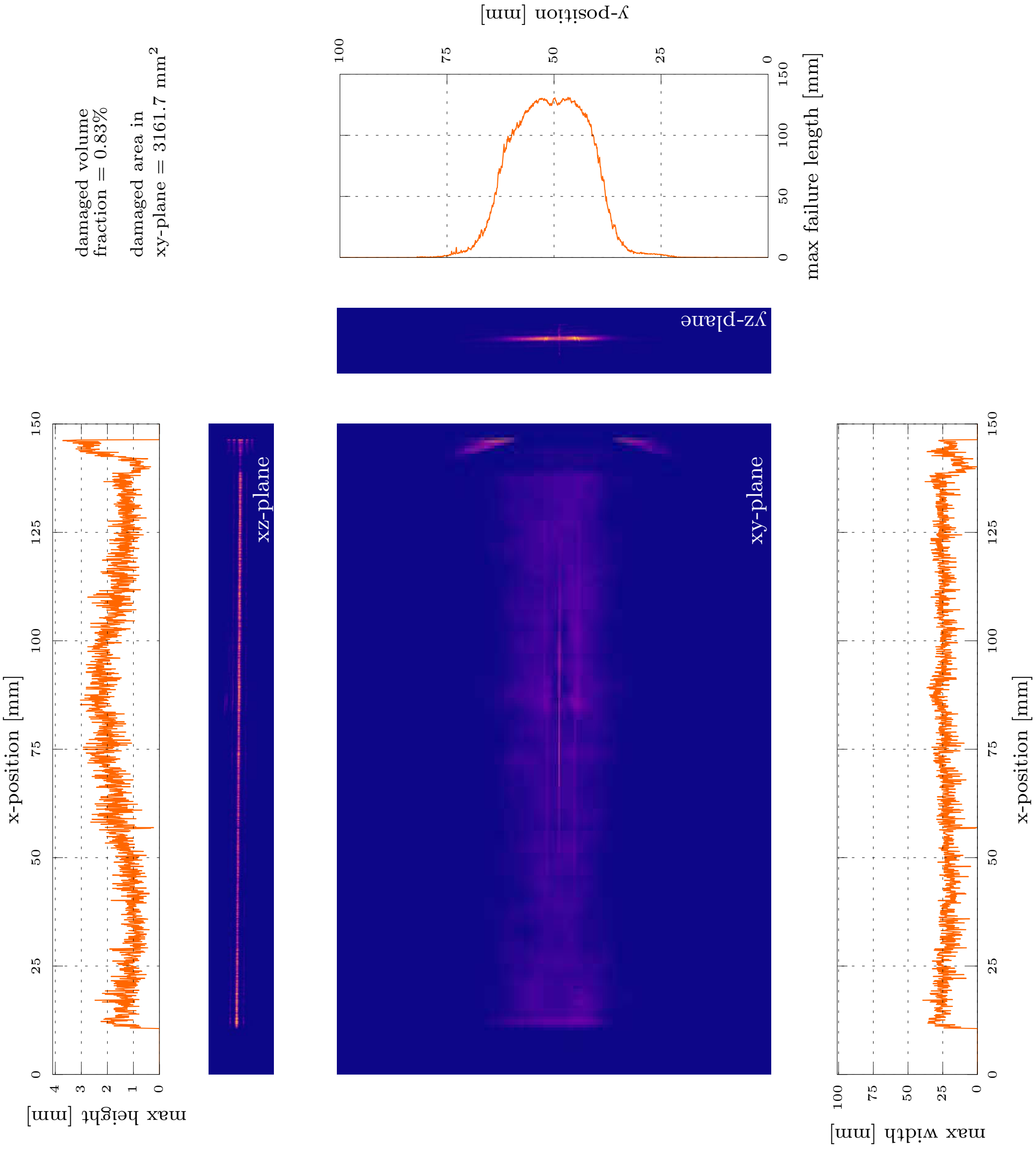

Figure 7.5: CT damage intensity plot UD-St-0.05-low/7 specimen 1

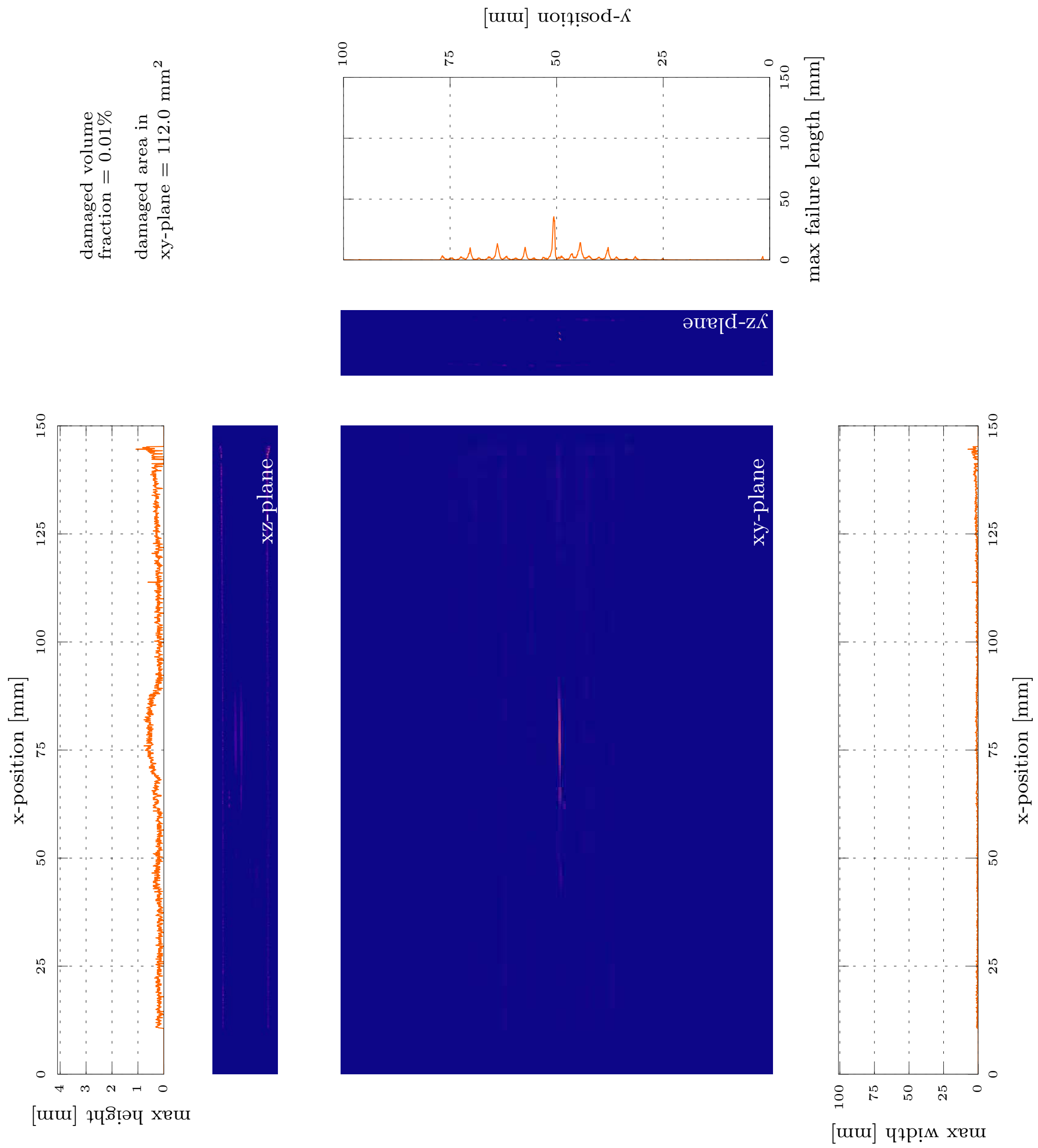

Figure 7.6: CT damage intensity plot UD-St-0.05-low/7 specimen 2

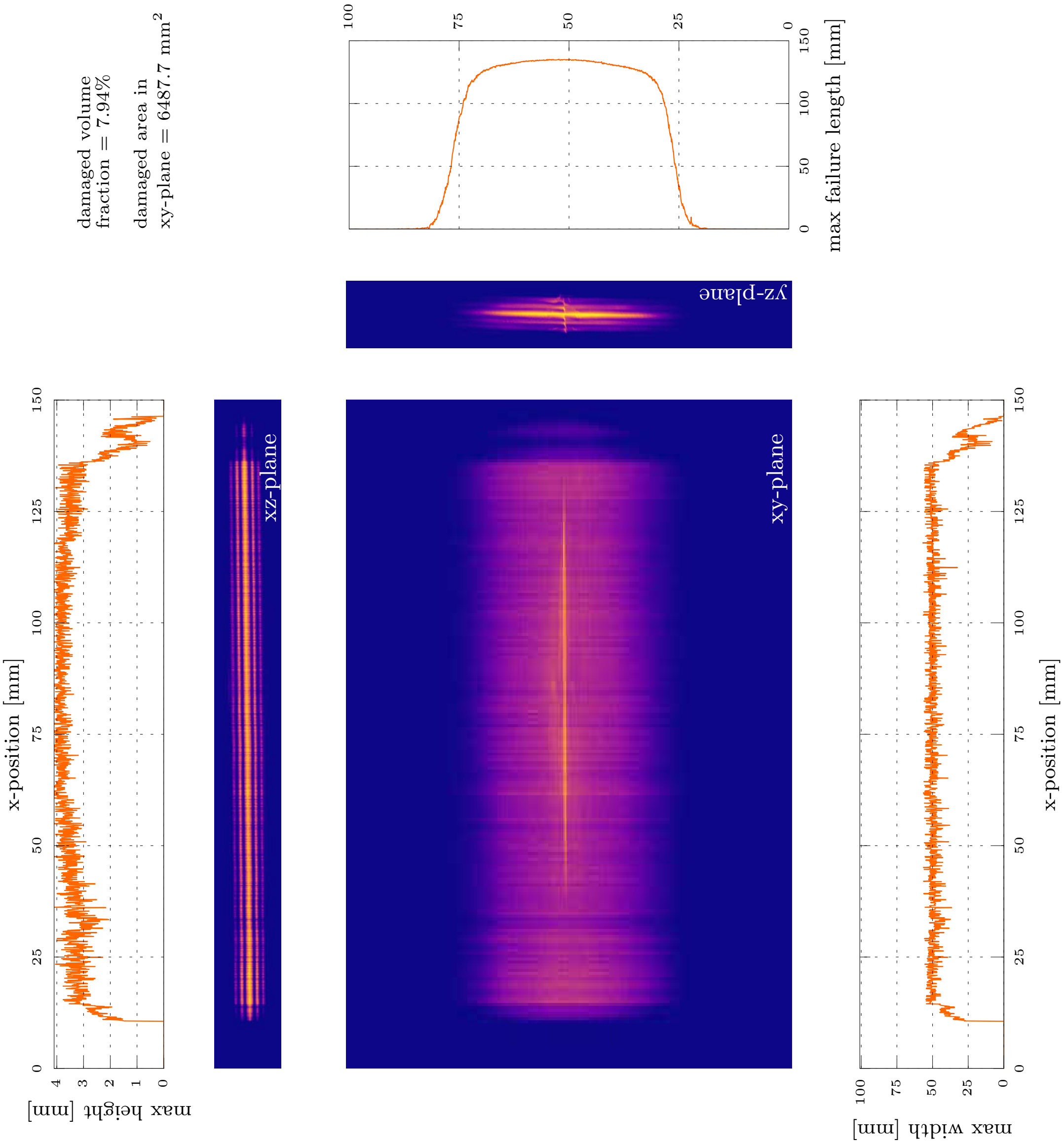

Figure 7.7: CT damage intensity plot UD-St-0.05-low/7 specimen 3

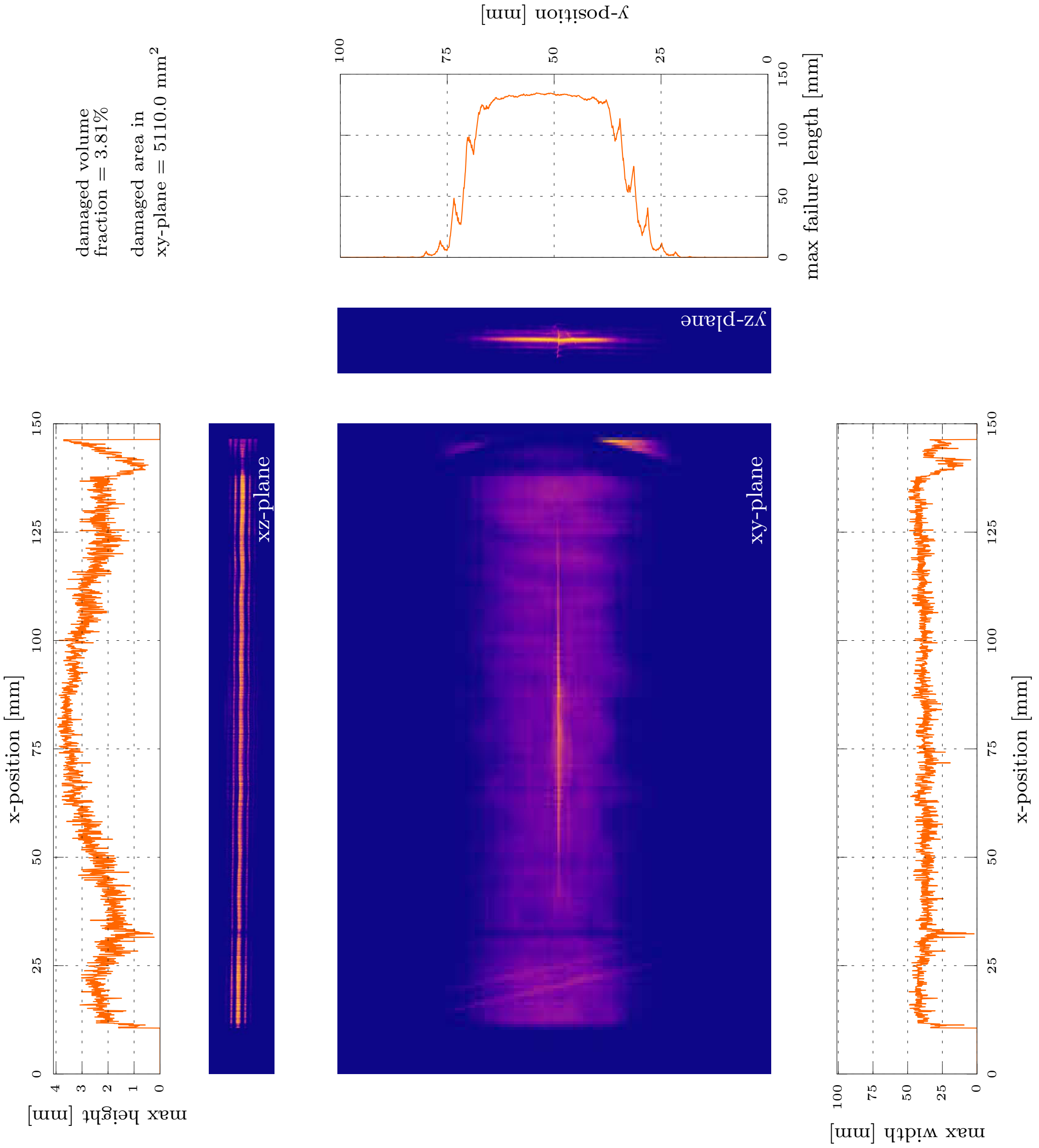

Figure 7.8: CT damage intensity plot UD-St-0.05-low/7 specimen 4

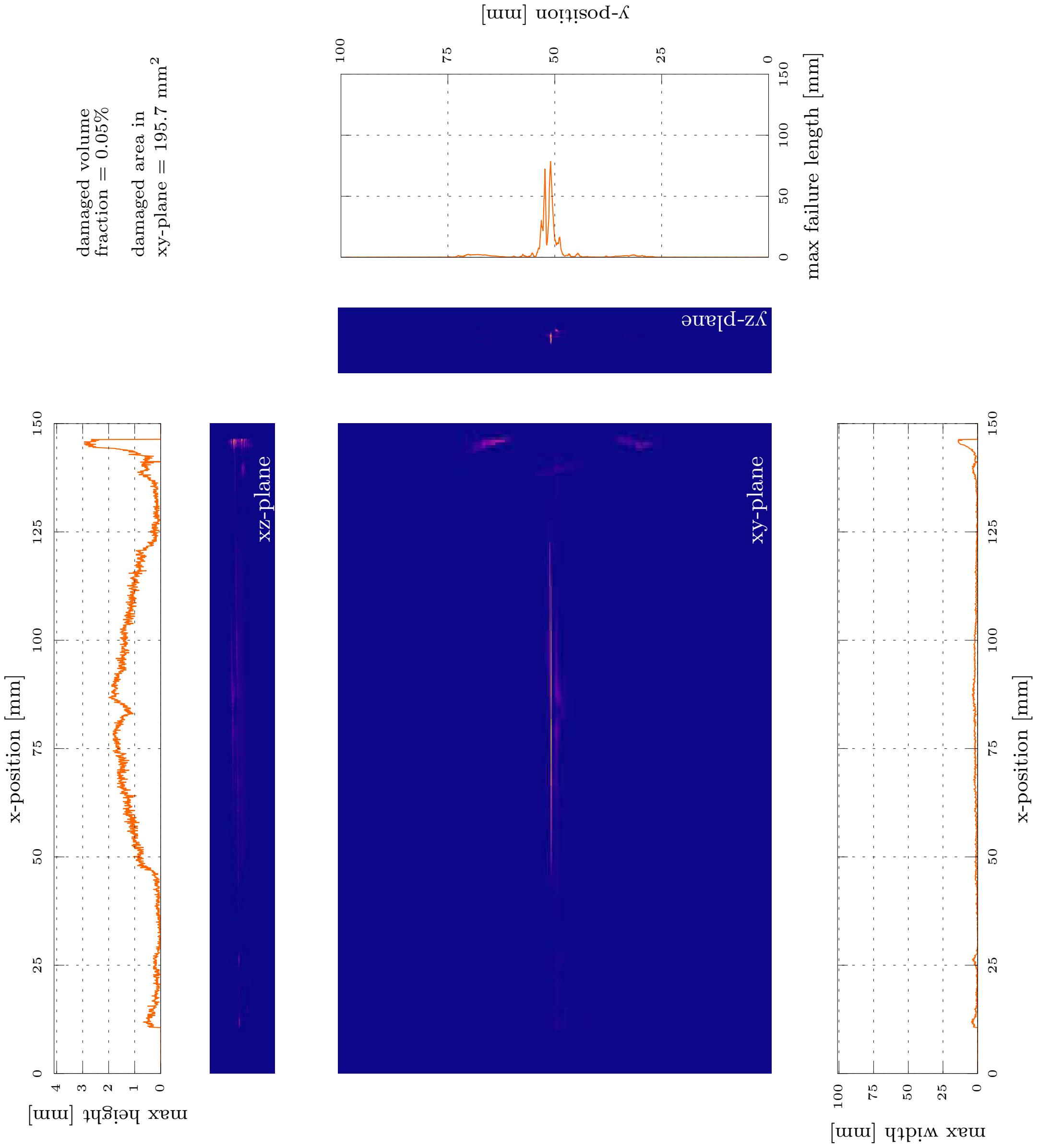

Figure 7.9: CT damage intensity plot UD-St-0.03-inner/11 specimen 1

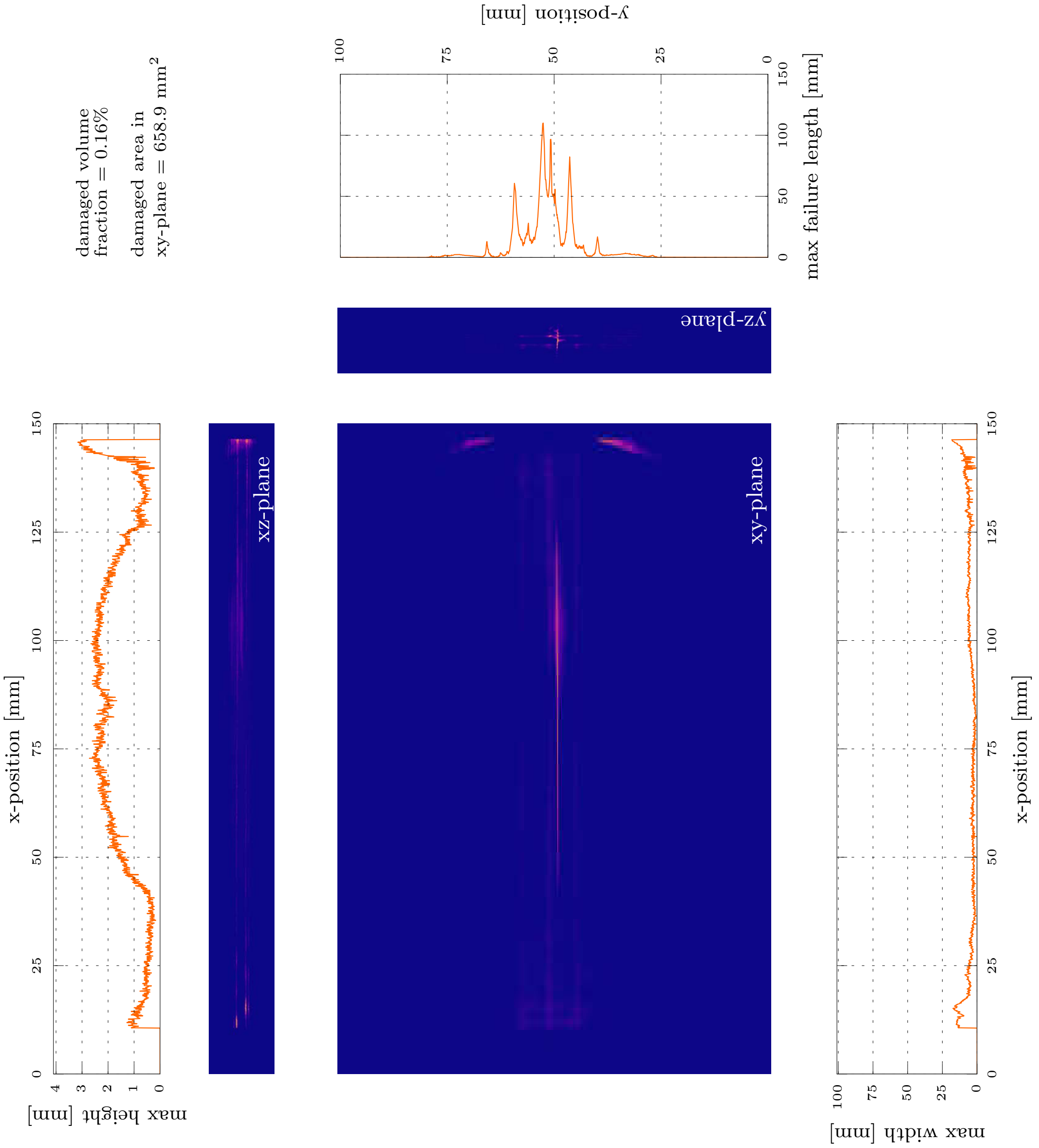

Figure 7.10: CT damage intensity plot UD-St-0.03-inner/11 specimen 2

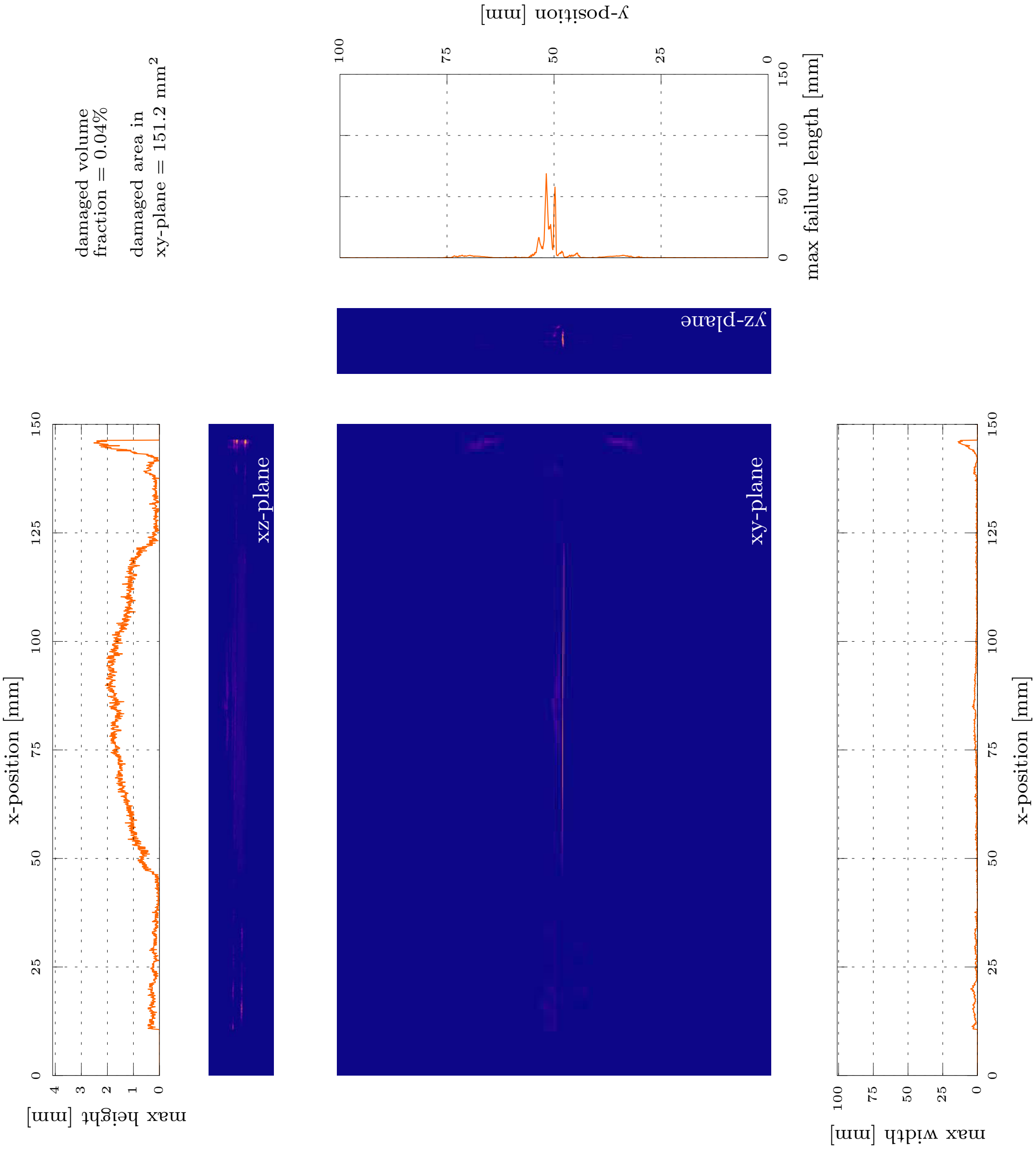

Figure 7.11: CT damage intensity plot UD-St-0.03-inner/11 specimen 3

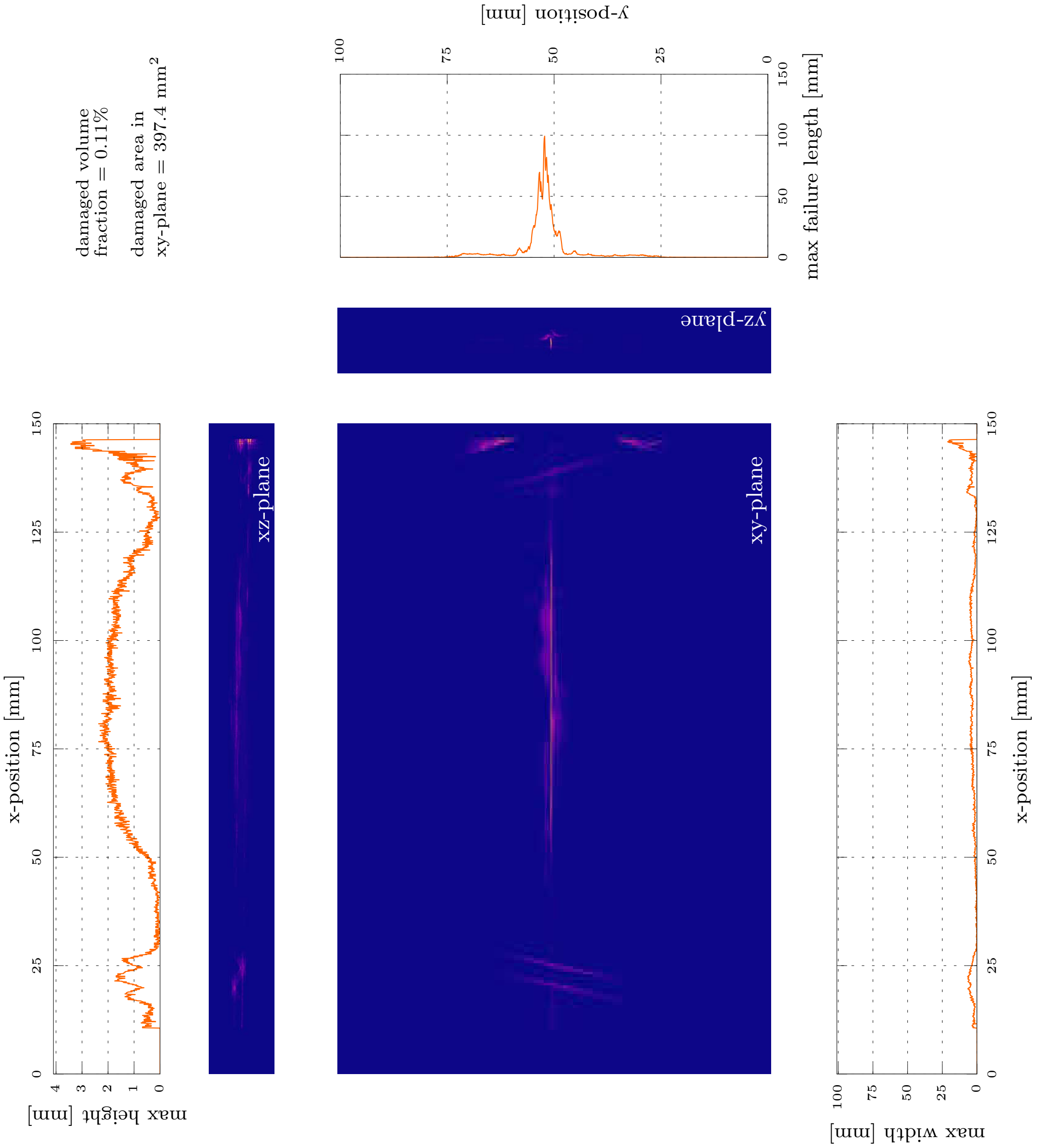

Figure 7.12: CT damage intensity plot UD-St-0.03-inner/11 specimen 4

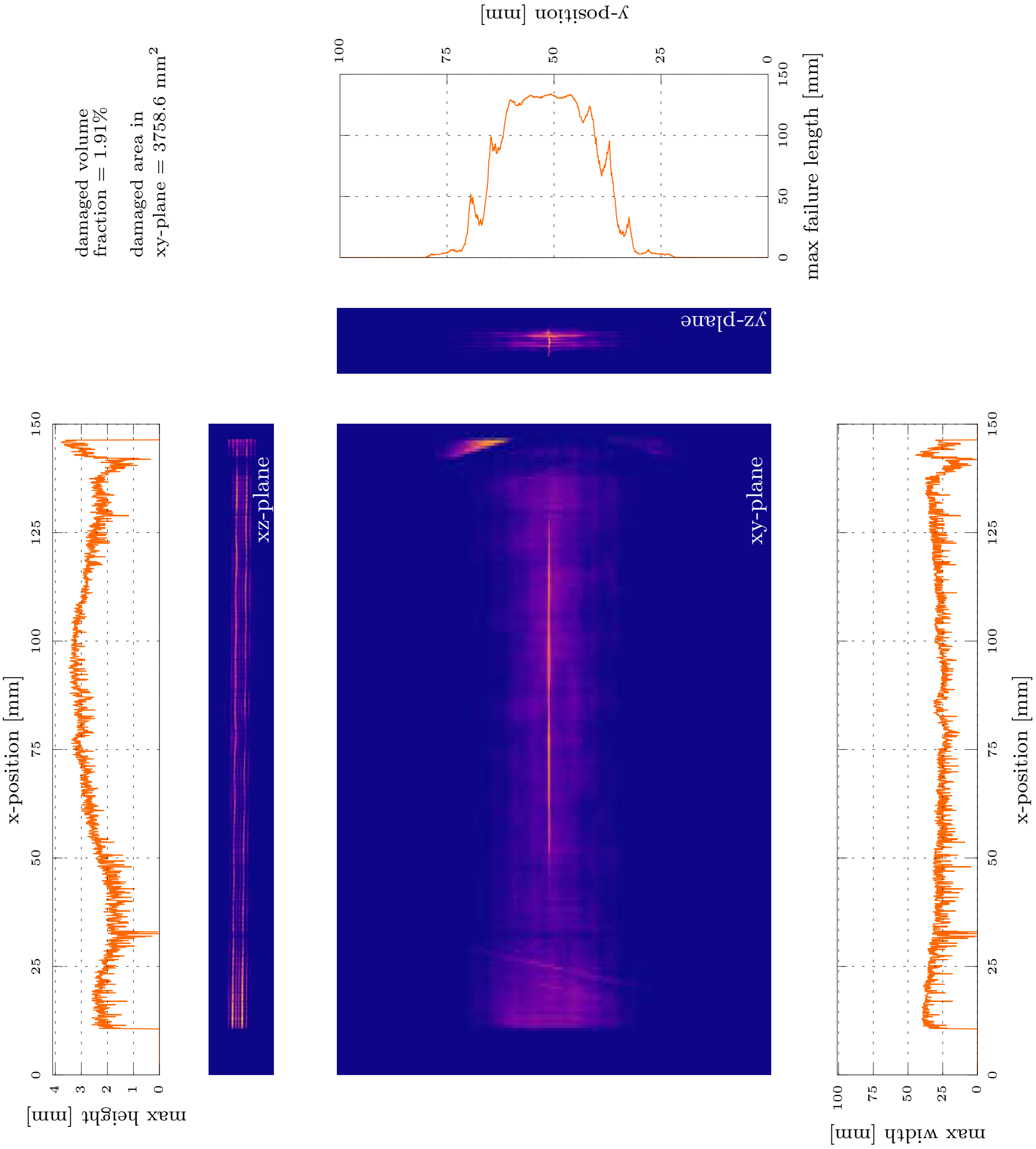

Figure 7.13: CT damage intensity plot UD-St-0.05-equal/11 specimen 1

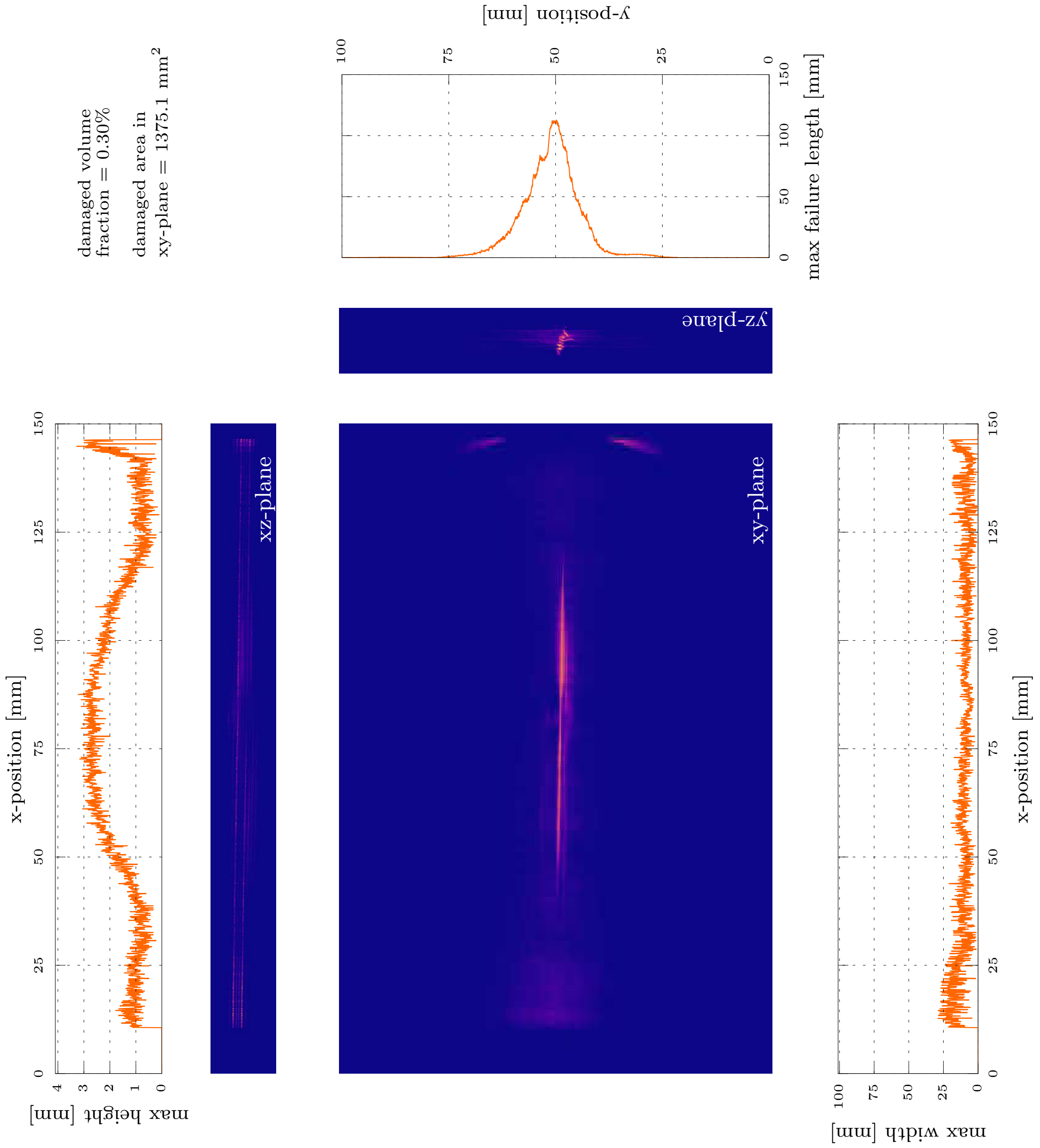

Figure 7.14: CT damage intensity plot UD-St-0.05-equal/11 specimen 3

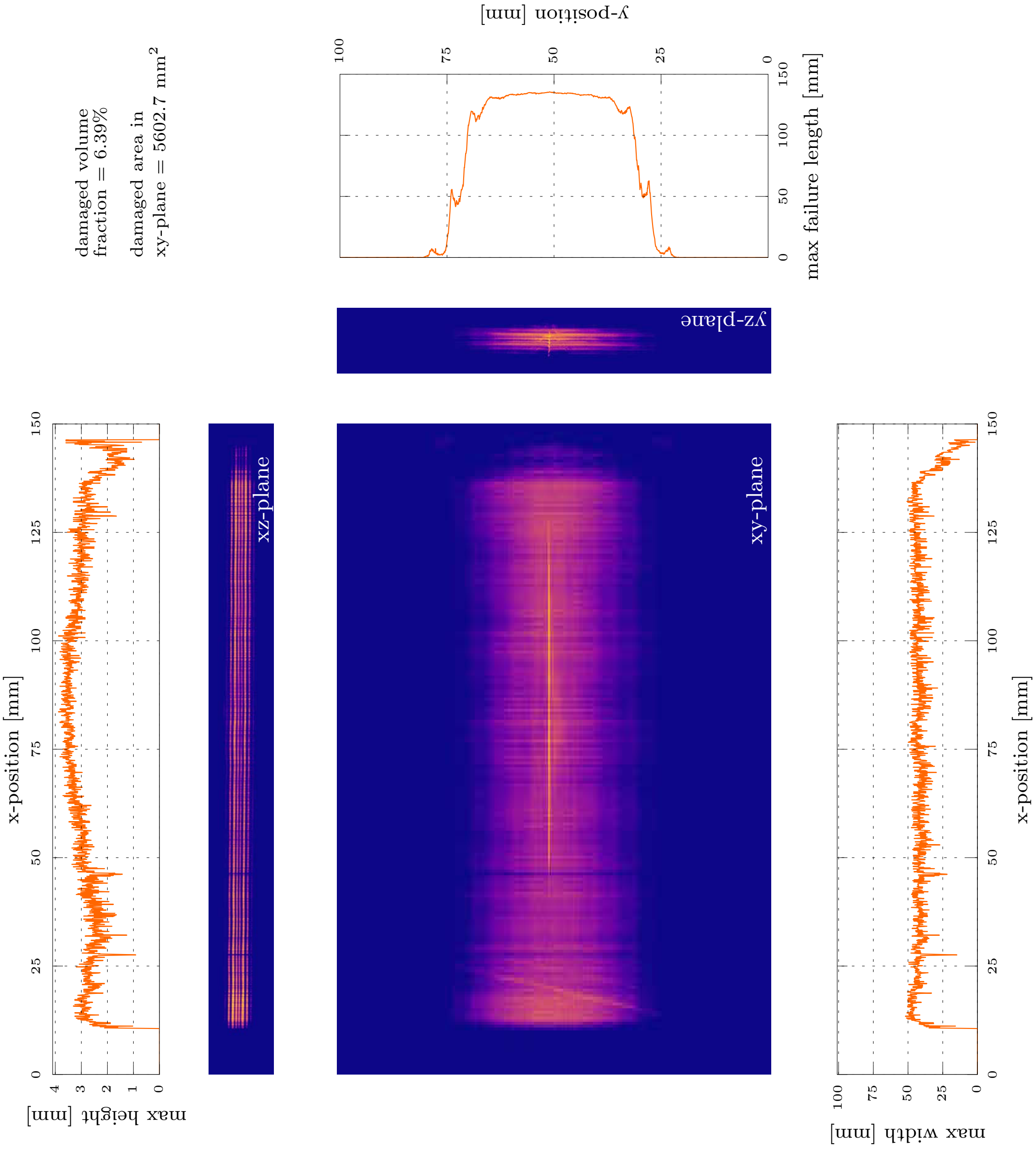

damaged volume fraction = 6.39%

damaged area in xy-plane = 5602.7 mm^2

Figure 7.15: CT damage intensity plot UD-St-0.05-equal/11 specimen 3

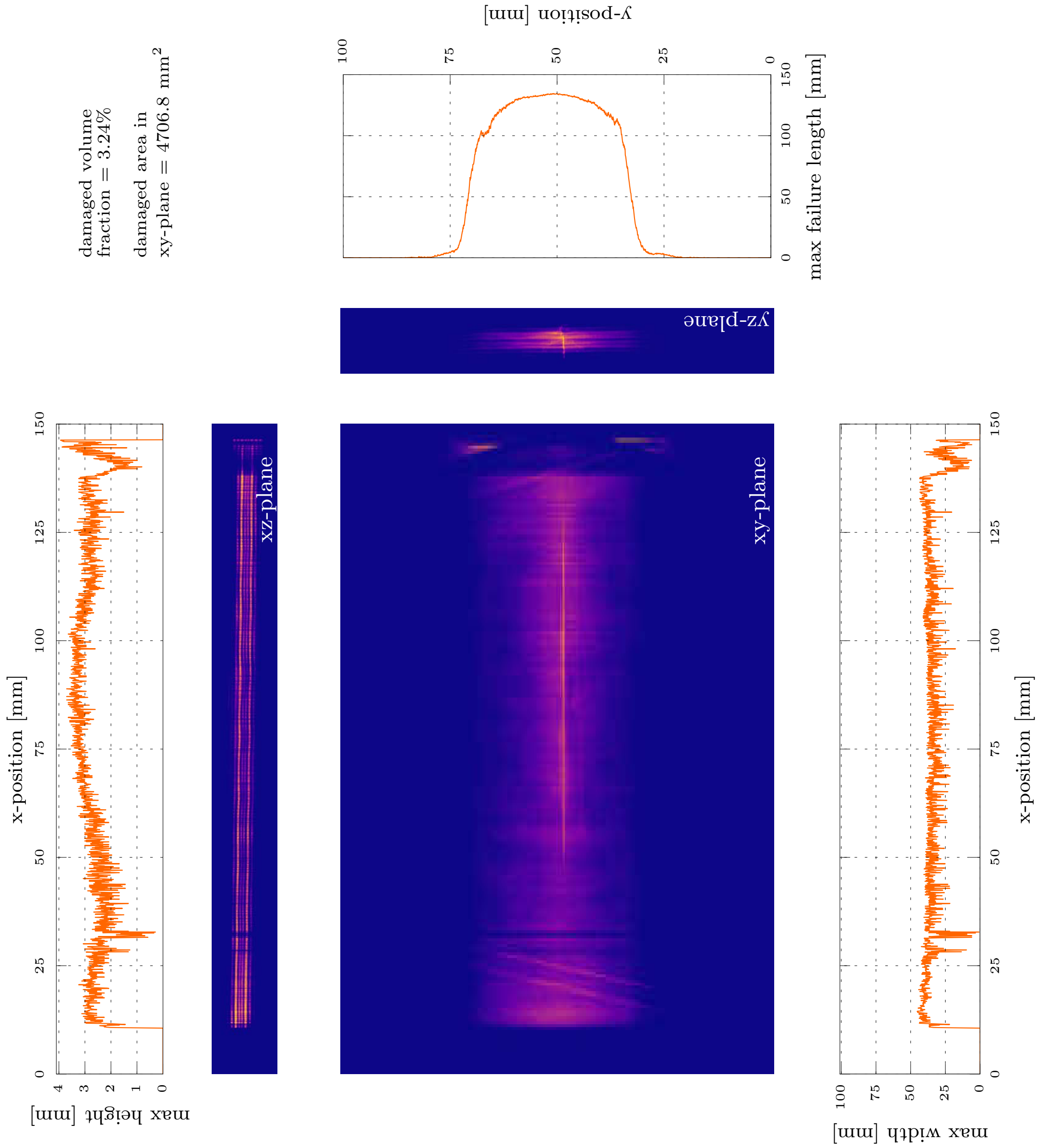

Figure 7.16: CT damage intensity plot UD-St-0.05-equal/11 specimen 4

Own publications

Journal Publications

Lopes J. Reis L. **Stefaniak D.** Freitas M. Camanho P.P. *Mechanical characterisation of CFRP-steel hybrid composites*, Int. J. Automotive Composites, Vol. 2, No. 2 (2016), pp.139-154.

Viandier A. **Stefaniak D.** Schröder D. Krewer U. Hühne C. and Sinapius M. *Degradation analysis of fibre-metal laminates under service conditions to predict their durability.* U.P.B. Sci. Bull., Series D, Vol. 1, Iss. 1, 2016

Lopes J. **Stefaniak D.** Reis L. Camanho P.P. *Single lap shear stress in hybrid CFRP/Steel composites.* Procedia Structural Integrity. 2016; 01:58-65

Düring D. Weiß L. **Stefaniak D.** Jordan N. Hühne C. *Low-velocity impact response of composite laminates with steel and elastomer protective layer.* Composite Structures, Vol. 134, pp. 18-26, 2015

Prussak R. **Stefaniak D.** Hühne C. and Sinapius M. *Residual stresses in intrinsic UD-CFRP-steel-laminates – Experimental, determination, identification of sources, effects and modification approaches.* Materials Science Forum Vols. 825-826 (2015) pp 369-376

Lopes J. **Stefaniak D.** Camanho P.P Freitas M. *Inter-laminar shear stress in hybrid CFRP/Austenitic Steel.* Fracture and Structural Integrity. 2015; 31:67-79

Kappel E, **Stefaniak D**, Fernlund G. *Predicting process-induced distortions in composite manufacturing: A pheno-numerical simulation strategy.* Composite Structures, Vol. 120, pp. 98-106, 2015

Kappel E. **Stefaniak D.** Hühne C. *Process distortions in prepreg manufacturing – An experimental study on CFRP L-profiles.* Composite Structures 2013; 106: 615-625

Rohwer K. Kappel E. **Stefaniak D.** Wille T. *Spring-in and Warpage – Progress in Simulating Manufacturing Aspects.* Machanics of Composite Materials 2013; 49; 2: 193-200.

Stefaniak D. Kappel E. Spröwitz D. Hühne C. *Experimental identification of parameters inducing warpage of autoclave-processed CFRP parts.* Composites Part A 2012; 43:1081-1091.

Kappel E. **Stefaniak D.** Spröwitz T. and Hühne C. *A semi-analytical simulation strategy and its application to warpage of autoclave-processed CFRP parts.* Composites Part A. 2011;42:1985-1994.

Kappel E. **Stefaniak D.** Holzhüter D. Hühne C. Sinapius M. *Manufacturing distortions of a CFRP box-structure – A semi-numerical prediction approach.* Composites Part A 2012; 51: 89-98.

Conference contributions

Stefaniak D. Prussak R. Viandier A. Hühne C. *Faser-Metall-Laminate – Ziele, Anreize und Herausforderungen bei der Verwendung als Strukturwerkstoff und in der Verbindungstechnik*; Faszination Hybrider Leichtbau Symposium, 2016 Wolfsburg

Prussak R. **Stefaniak D.** Hühne C. and Sinapius M. E*xperimentelle Untersuchungen zur Entstehung von Eigenspannungen in intrinsischen CFK-Stahl-Laminaten während des Herstellungsprozesses*, Euro Hybrid - Materials and Structures 2016, 2016, Kaiserslautern

Koch S.F. Barfuss D. Bobbert M. Groß L. Grützner R. Riemer M. **Stefaniak D**. Wang Z. *Intrinsic hybrid composites for lightweight structures – New process chain approaches*. 6th Congress of German Academic Society for Production Engineering, Hamburg, September 2016

Petersen, E. **Stefaniak D.** Hühne C. *Konzentrierte Lasteinleitungen in Faserverbund - werkstoffe unter Anwendung der lokalen Metallhybridisierung.* Werkstoff- und Leichtbau-Forum, Hannover Messe, 2016, Hannover

Viandier A. **Stefaniak D.** Hühne C. and Sinapius M. *Degredation analysis of fiber-metal laminates under service conditions to predict their durability*, The 6th International Conference on Structural Analysis of Advanced Materials, 2015, Porto, Portugal

Prussak R. **Stefaniak D.** Hühne C. and Sinapius M. *Residual stresses in intrinsic UD-CFRP-steel-laminates – Experimental, determination, identification of sources, effects and modification approaches*, 20. Symposium Verbundwerkstoffe und Werkstoffverbunde, 2015, Vienna, Austria

Masania K. Geissberger R. **Stefaniak D.** and Dransfeld C. *Steel foil reinforced composites: study of strength, plasticity and ply size effects*, 20th International Conference on Composite Materials, 2015, Copenhagen, Denmark

Düring D. **Stefaniak D.** Hühne C. *Influence of the elastomer layer position on the low velocity impact behavior of composite/steel/elastomer laminates,* 10th International Conference on Composite Science and Technology, 2015 Lisbon, Portugal

Lopes J. **Stefaniak D.** Camanho P.P. Freitas M. and Reis L. *Fatigue behaviour of CFRP/steel hybrid composites*, 10th International Conference on Composite Science and Technology, 2015 Lisbon, Portugal

Masania K. Geissberger R. **Stefaniak D.** and Dransfeld C. S*teel foil reinforced composites: Experimental and numerical study of strength, plasticity and ply size effects*, 5th International workshop on Aircraft System Technologies 2015, Hamburg, Germany.

Masania, K. Geissberger R. **Stefaniak D.** and Dransfeld C. *Steel foil reinforced composites: Experimental and numerical study of strength, plasticity and ply size effects*, SAMPE SETEC 14, (2014): Tampere, Finland.

Masania K. Leone R. Geissberger R. Studer J. Dransfeld C. **Stefaniak D.** *Steel Foil Reinforced Composites Produced by B stage Curing: Experimental and Numerical Study of Strength, Plasticity and Ply Size Effects;* Euro Hybrid – Materials and Structures 2014

Stefaniak D. Kappel E. Kolotylo M. Hühne C. *Experimental identification of sources and mechanisms inducing residual stresses in multi-layered Fiber-Metal- Laminates* ; Euro Hybrid – Materials and Structures 2014, Stade

Kappel, E. **Stefaniak D.** and Hühne C, *Process-induced distortions in CFRP manufacturing: A bottleneck for high-rate production scenarios*, CFK-Valley Convention 2014, Stade

Petersen E. **Stefaniak D.** Hühne C. *Efficient joint design using metal hybridization in fiber reinforced plastics*; Euro Hybrid – Materials and Structures 2014

Niewerth D. **Stefaniak D.** Hühne C. *The response of hybrid composite structures to low-velocity impact*; 16th International Conference on Experimental Mechanics, Cambridge 2014

Lopes J. **Stefaniak D.** Camanho P.P Freitas M. *Inter-laminar shear stress in hybrid CFRP/Austenitic Steel,* XIV Portuguese Conference on Fracture, 2014

Stefaniak D. Kolesnikov B. Huehne C. I*mproving the mechanical performance of unidirectional CFRP by metal-hybridization.* 15th European Conference on Composite Materials, Venice, June 2012

Stefaniak D. Kolesnikov B. Huehne C. *Improving specific material properties of impact endangered CFRP structures by metal-hybridization.* European Conference on Spacecraft Structures, Materials & Environmental Testing, Nordwijk, March 2012

Stefaniak D. Fink A. Kolesnikov B. Hühne C. *Improving the mechanical properties of CFRP by metal-hybridization.* International Conference on Composite Structures ICCS16, Porto, June 2011

Liebers N. **Stefaniak D.** Kleineberg M. Wiedemann M. *Sensor guided process – A study of productivity and quality optimization potential.* Conference on Composite Materials (ICCM 19) Montreal, August 2013

Kappel E. **Stefaniak D.** *Prediction of manufacturing-induced distortions of an integral stiffened panel using a novel semi-numerical approach*, 6th International Symposium on Manufacturing Technology for Composite Aircraft Structures ISCM 2012, Stade, October 2012

Kappel E. **Stefaniak D.** Hühne C. *Semi-analytical spring-in analysis counteract CFRP manufacturing deformations due to tool compensation*, 28th International Congress of the Aeronautical Sciences, Brisbane, September 2012

Rohwer K. Kappel E. **Stefaniak D**. Wille T. *Spring-In and warpage – progress in simulating manufacturing aspects.* International Conference on Mechanics of Composite Materials MCM, Riga, Latvia, May 2012

Fink A. Kolesnikov B. **Stefaniak D.** Hühne C. *Local CFRP/metal hybrid material improving composite bolted joints.* International Conference on Composite Structures ICCS16, Porto, June 2011

Book chapters

Kolesnikov B. **Stefaniak D.** Wölper J. Payload Adapter Made from Fiber-Metal-Laminate Struts, Adaptable, efficient and tolerant composite structures. Springer, 2012

Kappel E. **Stefaniak D.** Hühne C. About the Spring-In Phenomenon: Quantifying the Effects of Thermal Expansion and Chemical Shrinkage, Adaptable, efficient and tolerant composite structures. Springer, 2012

Hühne C. Kappel E. **Stefaniak D.** Compliant Aggregation of Functionalities, Adaptable, efficient and tolerant composite structures. Springer, 2012

Curriculum Vitae

Education:

2015 *Hagener Masterstudium Management* at 'The Faculty of Business Administration and Economics of the FernUniversität Hagen', Master of Science (M.Sc.)

2010 *Mechanical Engineering* at Leibniz University Hanover, Diplom-Ingenieur (Dipl.-Ing.)
Diploma Thesis: Experimental investigation of 'warpage'-distortion of plane CFRP-prepreg laminates with varying fiber directions

Career:

2010 - 2013 *Research Engineer* at 'at 'DLR German Aerospace Center - Composite Design Department'

since 2014 *Teamleader: Multimaterial Systems* at 'DLR - German Aerospace Center - Composite Design Department'

since 2016 *Lecturer* at 'PFH - Private University of Applied Sciences'

Awards:

2015 AVK - Industrievereinigung Verstärkte Kunststoffe e. V., Innovation Award - Innovative processes/procedures - 2nd

2012 DLR - Deutsches Zentrum für Luft- und Raumfahrt e.V., DLR Idea Award - 1st